Vehicle Biofuels

MARK HOLTZAPPLE
Department of Chemical Engineering, Texas A&M University, College Station, TX, USA

Article Outline

Glossary

Biodiesel Methyl or ethyl ester of fatty acids.

Biomass Biological material from living or recently living organisms.

Bio-oil The liquid resulting from biomass pyrolysis.

Equivalence ratio The actual oxygen fed to the reactor divided by the stoichiometric oxygen needed for complete combustion.

Gasohol A mixture of gasoline and ethanol, typically 90% gasoline and 10% ethanol.

Lignocellulose Biomass composed of lignin, cellulose, and hemicellulose.

Oleaginous microorganisms Microorganisms that accumulate triacylglycerol (TAG) within their cells.

Saccharification Hydrolysis of polysaccharides to produce sugar.

Synthesis gas Mixture of carbon monoxide and hydrogen.

Triacylglycerol (TAG) A natural product containing three fatty acids linked to glycerol via ester bonds.

Definition of the Subject

Vehicle biofuels are solid, liquid, and gaseous fuels derived from biomass (e.g., corn, sugarcane, grasses, and wood) used for transportation (e.g., automobiles, trucks, planes, and trains). Among biofuels, liquids are the most valuable because they are easily stored, have a high energy density, and are readily metered into engines. Biofuels are infinitely renewable provided appropriate agricultural practices are followed.

Introduction

Historically, biological feedstocks have been used to ‘power transportation. For example, early steam-powered trains were fueled by wood, Rudolph Diesel designed his engine to run on peanut oil, and Henry Ford designed the Model T to run on ethanol.

From 1880 to 1973, the price of crude oil was \$15–30/bbl (current dollars), so it was very difficult for biofuels to compete. As a consequence, during this time period, very few vehicles were powered by biofuels. However, during crisis situations, biofuels were employed. For example, during World War II, Europeans had difficulty obtaining gasoline, so millions of vehicles were adapted to run on gasified wood. The Arab Oil Embargo (1973) and Iranian Hostage Crisis (1979) caused the price of crude oil to rise to about \$90/bbl (current dollars), which precipitated interest in biofuels. In 1978, the US Energy Tax Act provided tax credits for ethanol (\$0.54/gal ethanol), which promoted the conversion of corn into biofuel. This act was designed to reduce dependence on foreign oil (36% imports in 1978) and to create a new market for corn, which had depressed prices at the time. In 2005, the US government provided a tax subsidy for biodiesel (\$1.00/gal). In 2008, the Farm Bill included a subsidy for cellulosic ethanol (\$1.01/gal).

Through these subsidies, the US government is promoting the use of biofuels for the following reasons:

- Energy security – In 2009, the United States imported 59% of its net crude oil consumption, which makes its economy vulnerable to supply disruptions.
- Balance of trade – When crude oil sells for about \$90/bbl, the United States spends about \$1 billion per day on imports. If retained within the United States, this money would help develop domestic jobs.
- Rural economic development – The sale of biofuels will bring additional revenue to rural economies.

M. Ehsani et al. (eds.), *Transportation Technologies for Sustainability*, DOI 10.1007/978-1-4614-5844-9,

Originally published in
Robert A. Meyers (ed.) Encyclopedia of Sustainability Science and Technology, © 2012, DOI 10.1007/978-1-4419-0851-3

- Environment – The production of biofuels from polluting biomass feedstocks (e.g., manure, municipal solid waste) removes these hazards from the environment.
- Global warming – The combustion of biofuels does not contribute net carbon dioxide to the atmosphere; any CO_2 released from the combustion of biofuels is fixed via photosynthesis which recycles it as plant matter.

Vehicle Fuels

For transportation, liquid fuels are preferred because of their high energy density, ease of transport, and controllability; therefore, they command a premium price as described below:

- Liquid (e.g., gasoline, jet fuel, diesel) – $15 to $25/GJ.
- Gaseous (e.g., methane) – $2 to $5/GJ.
- Solid (e.g., coal) – $1 to $3/GJ.

Conventional Fuels

Gasoline is used primarily in spark-ignited piston engines (Otto cycle). It is composed of hydrocarbons containing 4–12 carbon atoms (average about 7–8). Gasoline grades are determined by the *octane number*, which characterizes the tendency of the fuel to *knock*, i.e., prematurely detonate. Gasoline-powered engines have a compression ratio (maximum: minimum gas volume) of about 7:1–12:1. During the compression of the air–fuel mixture, the temperature increases. Fragile molecules (e.g., large linear hydrocarbons) readily detonate whereas stable molecules (e.g., branched hydrocarbons, aromatics, oxygenates) resist detonation. High-compression engines are more efficient and powerful, and require high-octane fuels to prevent knocking. Because knocking pressurizes the gas at the wrong point in the engine cycle, it can rob efficiency and potentially cause damage. (Note: A fuel with an octane number of 100 has knocking characteristics identical to an idealized fuel containing 100% iso-octane and 0% *n*-heptane. Similarly, a fuel with an octane number of 0 has knocking characteristics identical to an idealized fuel containing 0% iso-octane and 100% *n*-heptane. Other fuel octane numbers correspond to other idealized mixtures.)

Jet fuel is used primarily in jet engines (Brayton cycle). It is composed of hydrocarbons containing 8–16 carbon atoms (average of about 12), which is similar to kerosene. Jet fuel formulations are adjusted to ensure the fuel does not freeze at high altitudes, where the temperature is cold. Also, the composition is adjusted to reduce smoke formation.

Diesel fuel is used primarily in diesel engines. It is composed of hydrocarbons containing 10–22 carbon atoms (average of about 16). Diesel engines have a high compression ratio (typically 14:1–24:1), which greatly increases the air temperature during the compression stroke. To ignite the fuel, they do not employ a spark; rather, they rely on the high temperature of the compressed air. When atomized diesel fuel is injected into the hot compressed air, it decomposes and ignites. The burn characteristics of diesel fuel are determined by the *cetane number*, which quantifies how quickly the fuel starts to auto-ignite in a diesel engine. Analogous to octane rating, the cetane rating assigns a value of 100 to a fuel that behaves like cetane (*n*-hexadecane) whereas a value of 0 is assigned to a fuel that behaves like 1-methyl napthalene.

Biofuels

Biofuels come in many forms, as described in Table 1. Table 2 provides properties of both biofuels and conventional fuels.

In the United States, ethanol is the dominant biofuel. Figure 1 shows the US ethanol capacity from 1980 to 2010. In 2010, the US ethanol capacity was 13.2 billion gallons per year and US gasoline consumption was 138.5 gal per year (Fig. 2); thus, about 8.7% of the gasoline–ethanol pool was ethanol. In 2010, approximately 40% of the US corn crop was converted to fuel ethanol. Table 3 shows global ethanol production in 2009.

In 2009, the US biodiesel capacity was 2.0 billion gallons per year [4] and US diesel consumption was 55.7 billion gallons per year [5]; thus, about 3.5% of the diesel pool was biodiesel.

Biofuel Blends

Biofuels are often blended with other components. Common designations are described below.

Vehicle Biofuels. Table 1 Examples of biofuels

<table>
<tr><th>Fuel type</th><th>Generic</th><th>Examples</th><th></th></tr>
<tr><td rowspan="2">Primary alcohols</td><td rowspan="2">R–OH</td><td>H_3C–OH</td><td>methanol</td></tr>
<tr><td>H_3CH_2C–OH</td><td>ethanol</td></tr>
<tr><td>Secondary alcohols</td><td>OH
|
R–C–R’</td><td>OH
|
H_3C–C–CH_3</td><td>isopropanol</td></tr>
<tr><td rowspan="2">Ethers</td><td rowspan="2">R–O–R’</td><td>H_3C–O–CH_3</td><td>dimethyl ether</td></tr>
<tr><td>H_3CH_2C–O–CH_2CH_3</td><td>diethyl ether</td></tr>
<tr><td>Ketones</td><td>O
||
R–C–R’</td><td>O
||
H_3C–C–CH_3</td><td>Acetone</td></tr>
<tr><td>Esters</td><td>O
||
R–CO–R’</td><td>O
||
$H_{34}C_{18}$–CO–CH_3</td><td>Biodiesel</td></tr>
</table>

E10 *E10* is a blend of 10% ethanol and 90% gasoline, and is commonly described as *gasohol*. It is widely used in the United States; nearly the entire gasoline pool contains ethanol. Modern gasoline engines are designed to be compatible with E10 without the need for modifications.

Addition of ethanol to gasoline has some benefits, such as (1) reducing gasoline imports, (2) improving the fuel octane rating, and (3) improving combustion. Regarding the latter point, the 1990 US Clean Air Act required the addition of oxygenates to *reformulated gasoline* in cities that could not attain carbon monoxide or ozone standards. In those cities, fuels were required to contain 2.7% oxygen, which could be met by adding oxygenates such as methyl tertiary butyl ether (MTBE) or ethanol. When MTBE was found to contaminate groundwater, its use was banned so the demand for ethanol increased dramatically.

Addition of ethanol to gasoline also has some detriments, such as (1) reducing fuel economy because of its lower energy content (~3%); (2) raising the fuel vapor pressure, which reduces the amount of low-cost, high-octane butanes that can be added to fuel; (3) increasing production of formaldehyde and acetaldehyde in tail-pipe emissions; and (4) absorbing water into the fuel. Regarding the latter point, ethanol is very polar compared to gasoline and attracts water, which is also polar. Common-carrier pipelines that transport hydrocarbon fuels often contain water. If ethanol-containing fuel were transported through these pipelines, it would absorb water, which adversely affects fuel quality. To avoid this problem, anhydrous ethanol is transported via rail or trucks and is “splash blended” at the fuel terminal.

E15 *E15* is a blend of 15% ethanol and 85% gasoline. As ethanol is increasingly added to the gasoline pool, the United States will soon reach a “blend wall” for E10. The US Environmental Protection Agency has authorized the use of E15 in certain vehicles (e.g., automobiles, SUVs, light-duty trucks) after model year 2001, which potentially would allow the percentage of ethanol to increase by 50%. The ruling has spurred controversy regarding potential damage to engines, emission systems, and air quality. Further, E15 would need to be sold in a manner to prevent it from being used in unauthorized vehicles (e.g., motorcycles, heavy-duty vehicles, off-road vehicles, and vehicles older than model year 2000).

E85 *E85* is a blend of 85% ethanol and 15% gasoline. Because ethanol has lower energy content than gasoline, the fuel mileage of E85 decreases by

Vehicle Biofuels. Table 2 Properties of fuels[a]

Fuel	Heat of combustion[b] (MJ/kg)	Density (kg/L)	Heat of combustion[b] (MJ/L)	Octane rating[c]
Hydrocarbons				
Diesel	44.8	0.83	37.2	15–25
Jet	46.6	0.81	37.7	
Gasoline	47.3	0.74	35.0	91–99
Esters				
Biodiesel	39.9	0.88	35.1	
Alcohols				
Methanol	19.9	0.79	15.7	106
Ethanol	28.9	0.79	22.8	108
n-Propanol	30.7	0.80	24.6	
Isopropanol	30.5	0.80	24.4	
n-Butanol	33.1	0.81	26.8	96
Isobutanol	33.0	0.80	26.4	
Tertbutanol	32.6	0.78	25.4	103
n-Pentanol	34.7	0.81	28.1	
Ethers				
Dimethyl ether	28.7	0.67	19.2	
Diethyl ether	33.9	0.71	24.1	
Dipropyl ether	36.4	0.74	26.9	
Dibutyl ether	37.8	0.77	29.1	
Ketones				
Acetone	28.6	0.78	22.3	
Methyl ethyl ketone	31.5	0.80	25.2	
Diethyl ketone	35.7	0.82	29.3	

[a]Data derived from Wikipedia
[b]Higher heating value (i.e., water product is a liquid)
[c]Research Octane Number (RON)

25–30%. Compared to gasoline, ethanol has a higher latent heat of vaporization and lower vapor pressure; thus, it is potentially difficult to start the engine during cold weather. To overcome this problem, gasoline is a component of E85. During very cold weather, fuel retailers will increase the percentage of gasoline to 30%. Conventional spark-ignited engines are not designed to combust E85; however, flexible-fuel vehicles (FFVs) can accept any ratio of E0 to E85. In FFVs, the metals, polymers, and elastomers in the fuel system and engine components must be compatible with the range of fuels. Further, engine sensors detect the fuel composition and automatically adjust the fuel injector and spark timing. For the automobile manufacturer, the marginal cost of producing an FFV is about $150 per vehicle.

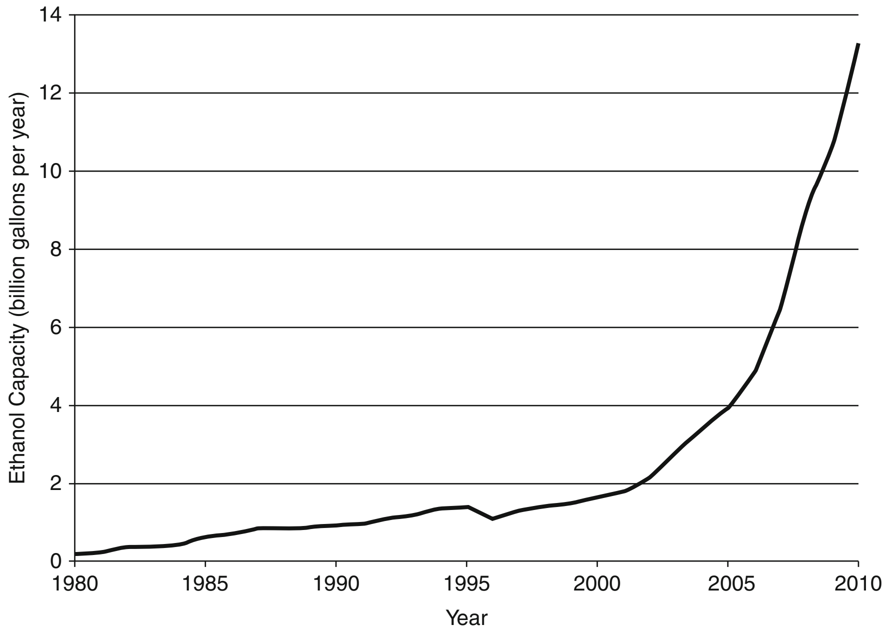

Vehicle Biofuels. Figure 1
US ethanol capacity [1]

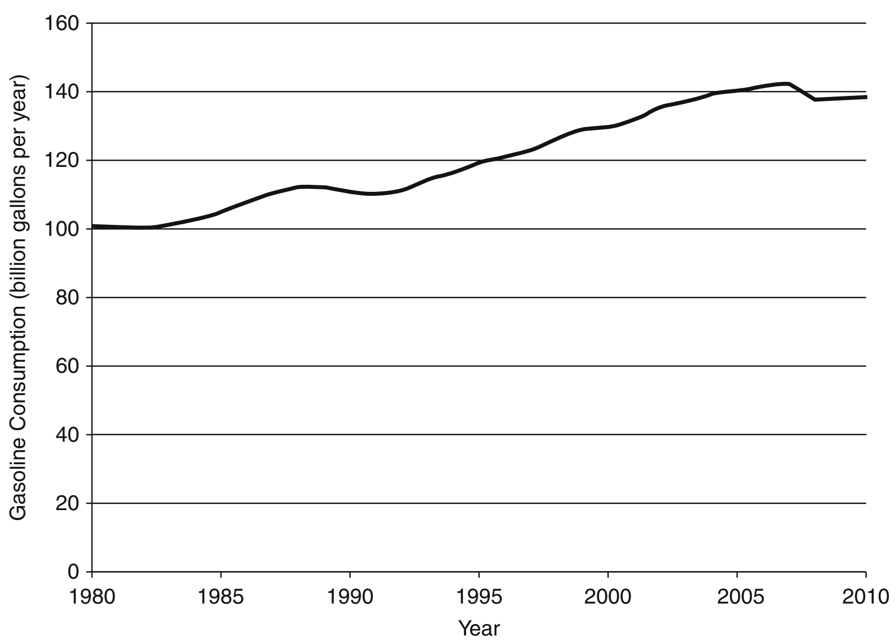

Vehicle Biofuels. Figure 2
US gasoline consumption [2]

Vehicle Biofuels. Table 3 Global fuel ethanol production in 2009 [3]

Country	Annual Production (million gallons)
United States	10,600.00
Brazil	6,577.89
European Union	1,039.52
China	541.55
Thailand	435.20
Canada	290.59
India	91.67
Colombia	83.21
Australia	56.80
Other	247.27
Total	19,963.70

E100 *E100* is 100% ethanol and 0% gasoline. The previously discussed fuels (E10, E15, E85) contain ethanol blended with gasoline. In these fuels, only anhydrous ethanol can be used; otherwise, water will phase out when the gasoline is added. However, E100 is a *neat fuel* (i.e., it contains no additives), so it can contain water. In the production of ethanol, it must be distilled from water. The top of the distillation column reaches the *azeotrope*, where the composition of the liquid and vapor are identical (95.63% ethanol and 4.37% water, by weight). To break the azeotrope requires additional technology (e.g., the use of molecular sieves to remove water from the solution), which adds cost. In Brazil, many vehicles operate on azeotropic ethanol; therefore, the cost of the final dehydration step is eliminated. To overcome potential cold-start problems, it is common practice to start the engine on gasoline and then switch to E100 once the engine is warmed. Direct injection of ethanol into the engine shows an effective octane rating of 130. With appropriate engine controls, it is possible to burn neat ethanol in engines with a compression ratio up to 19.5:1, which has a thermal efficiency similar to diesel engines. The higher efficiency of the high-compression engine compensates for the lower energy content of ethanol, so the fuel mileage is similar to gasoline.

Biodiesel *Biodiesel* is produced from vegetable oil or animal fats. It has a carbon number similar to petroleum-derived diesel fuel, so it can be combusted in conventional diesel engines. Common blends include B2, B5, B10, and B100, which contain 2%, 5%, 10%, and 100% biodiesel, respectively. Disadvantages of biodiesel include the following: (1) potential cold-start problems (not unlike conventional diesel), which can be overcome using additives that prevent clogging of filters; (2) deposits and clogging from low-quality or oxidized fuel; (3) slightly higher NO_x emissions; and (4) lower energy content. Regarding the latter point, because biodiesel contains oxygen, B100 has 3–5% less energy content than petroleum-derived diesel. Advantages of biodiesel include the following: (1) better lubricity (short-term studies with biodiesel show that it has less wear than conventional diesel) and (2) lower emissions. Regarding the latter point, because of its oxygen content, biodiesel burns more completely. Further, it has no sulfur or aromatic emissions.

Although biodiesel is more commonly used in diesel engines, it can be used in aircraft engines as well. Usually, it is blended with conventional jet fuel; however, there are some reports of aircraft operating with B100.

E-Diesel Because of its hydroxyl group, ethanol has hydrophilic properties and is completely soluble in water in any ratio. Because of its ethyl group, ethanol has oleophilic properties and is completely soluble in diesel fuel in any ratio. However, if a small amount of water (0.2%) is present in the fuel, two phases form: one ethanol-rich and the other diesel-rich [6]. To prevent phase separation, additives (e.g., surfactants, emulsifiers, and co-solvents) can be included in the fuel. The addition of biodiesel to petroleum-derived diesel allows significant quantities (5–15%) of ethanol to be added to the fuel [7]. Rather than adding ethanol directly to diesel fuel, ethanol can be stored in a separate tank and introduced as a fog or vapor into the air intake of the engine.

Biomass

Biomass is biological material from living or recently living organisms. In the context of biofuels, usually

biomass is used to describe plant matter such as wood, grass, agricultural residues, energy crops, and algae. The dominant components of biomass are described below.

Free Sugars

Free sugars are found in fruits and plant juices. Figure 3 shows examples including glucose, fructose, and sucrose (a disaccharide of glucose and fructose).

Starch

As shown in Fig. 4, starch is a polymer of glucose joined by α bonds. It occurs in two forms: amylose (unbranched) and amylopectin (branched). In plants, starch is used primarily as an energy-storage compound.

Cellulose

As shown in Fig. 5, cellulose is an unbranched polymer of glucose joined by β bonds. Because of extensive internal hydrogen bonds (Fig. 6), cellulose is crystalline and rigid; therefore, it is used as a structural component of roots, stems, and leaves. Because these components are so common in plants, cellulose is the most abundant biological material produced on earth.

Hemicellulose

As shown in Fig. 7, hemicellulose is a polymer with a backbone of xylose (a five-carbon sugar) joined by β bonds. In addition to xylose, hemicellulose contains glucose, mannose, galactose, rhamnose, arabinose, mannuronic acid, and galacturonic acid.

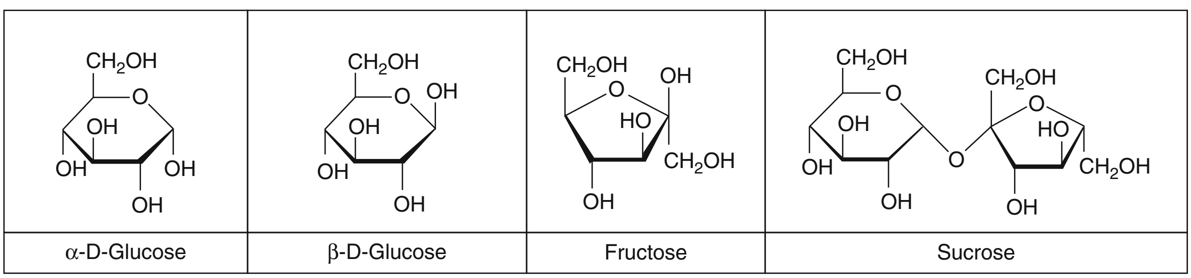

Vehicle Biofuels. Figure 3
Free sugars. (Note: For simplicity, the hydrogens bonded to carbon are not shown)

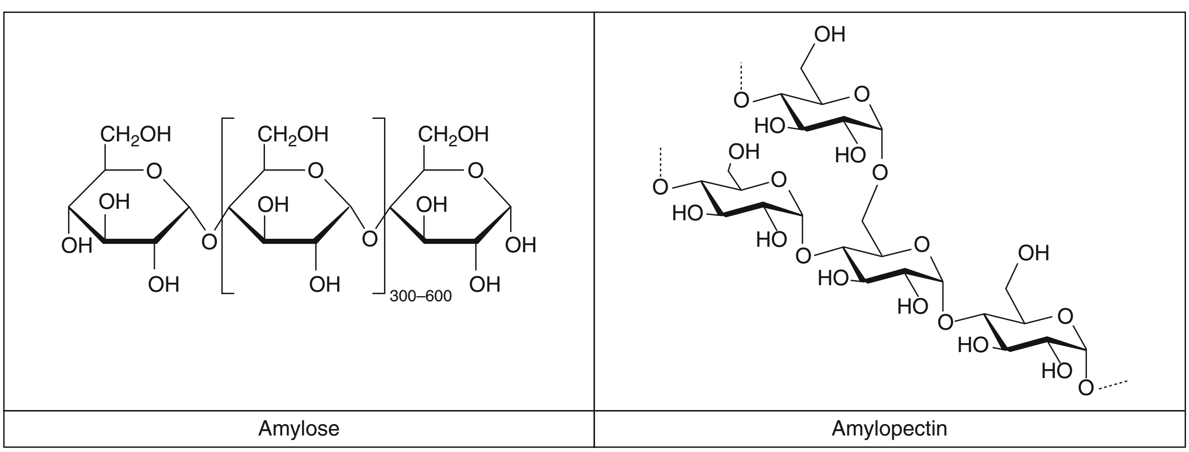

Vehicle Biofuels. Figure 4
Two forms of starch. (Note: For simplicity, the hydrogens bonded to carbon are not shown)

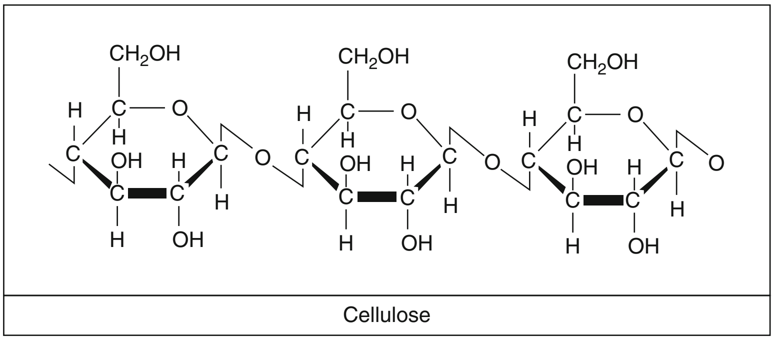

Vehicle Biofuels. Figure 5
Cellulose structure

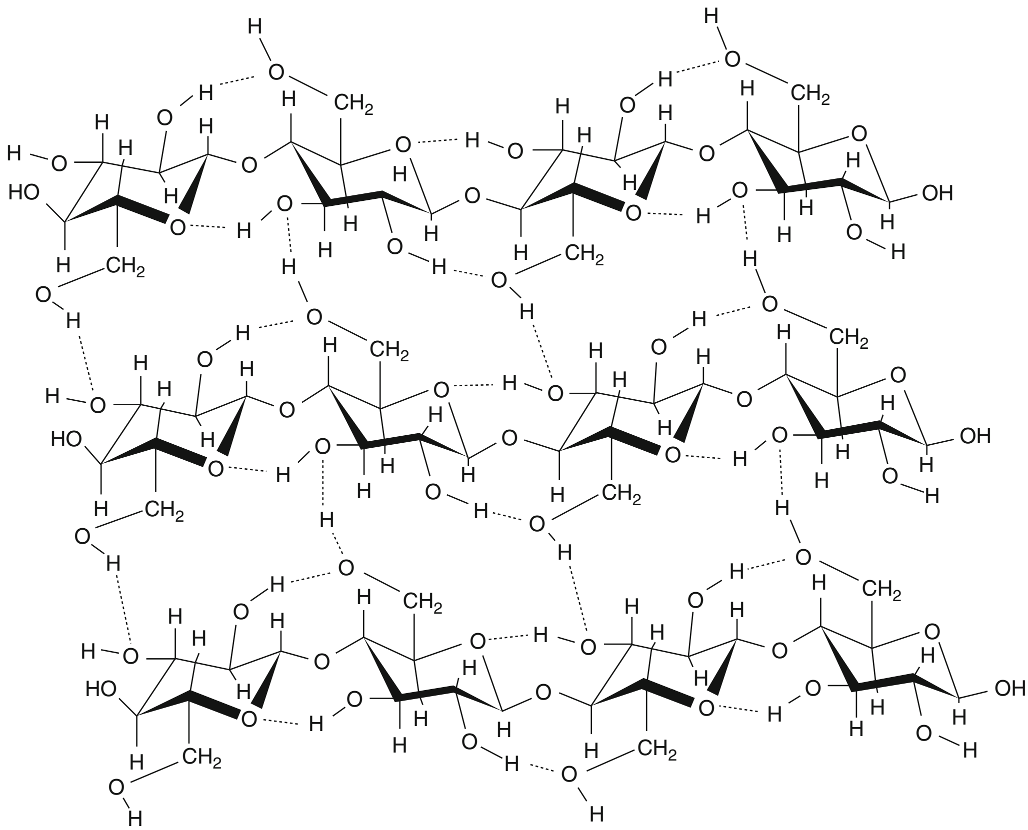

Vehicle Biofuels. Figure 6
Cellulose has extensive hydrogen bonds, shown as *dotted lines*

Hemicellulose is randomly acetylated, which helps it resist degradation by sterically hindering hemicellulose enzymes.

Lignin

Lignin is a complex polymer composed of three monomers (Fig. 8), which are highly cross-linked (Fig. 9).

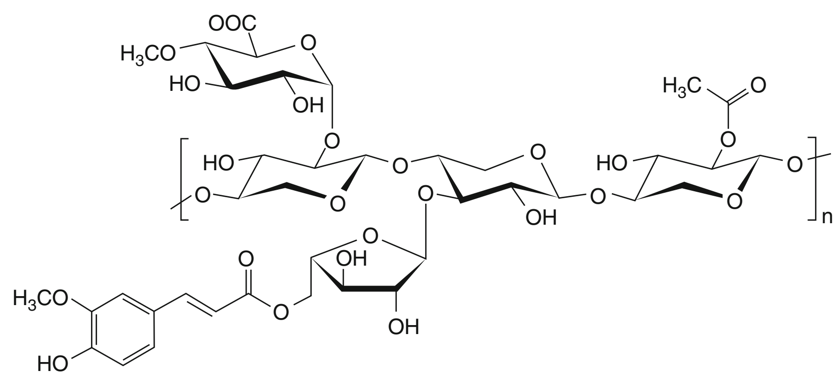

Hemicellulose

Vehicle Biofuels. Figure 7
Hemicellulose structure

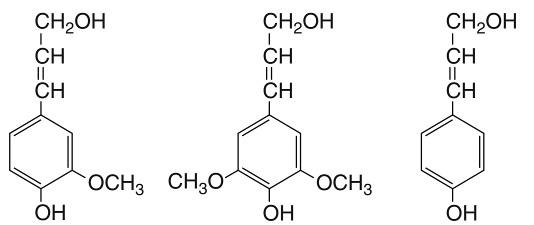

coniferyl alcohol sinapyl alcohol *p*-coumaryl alcohol

Vehicle Biofuels. Figure 8
Lignin monomers

Lignin is the "glue" that holds biomass together. By analogy to fiberglass composites, lignin functions like epoxy resin whereas cellulose functions like glass fibers. Lignin is hydrophobic and reduces evaporation of water from plant vessels. Further, lignin resists biological attack by insects and microorganisms.

Triacylglycerol

Triacylglycerol (TAG) is the main component of vegetable oil and animal fats and is composed of fatty acids bonded to glycerol via ether linkages (Fig. 10). In Fig. 10, the value of *n* typically ranges from 14 (palmitic acid) to 16 (oleic and stearic acids). Although Fig. 10 shows the hydrocarbon chain is fully saturated with hydrogen, naturally occurring fatty acids often have some unsaturated bonds as well.

Proteins

Figure 11 shows the chemical structure of an amino acid, which contains an amine group ($-NH_2$) and a carboxylic acid ($-COOH$). In naturally occurring amino acids, there are 20 standard R groups, which are coded by DNA. By eliminating water, the amine and carboxylic acid groups form a peptide bond, thus creating a protein polymer. In nature, proteins have many functions, including catalyzing reactions (enzymes) and providing mechanical structure.

Biomass Processing

Figure 12 shows an overview of processes that convert biomass into fuels, which is described in more detail below.

Raw Materials

Lignocellulose includes wood, grass, agricultural residues, and aquatic plants. Lignocellulose is the structural component of biomass and is composed of cellulose (30–50%), hemicellulose (20–40%), and lignin (20–30%). By far, lignocellulose is the dominant form of biomass produced on earth. Table 4 catalogs the land available in the United States. Table 5 summarizes the potential lignocellulose resources in the United States. Tables 6 and 7 focus on waste

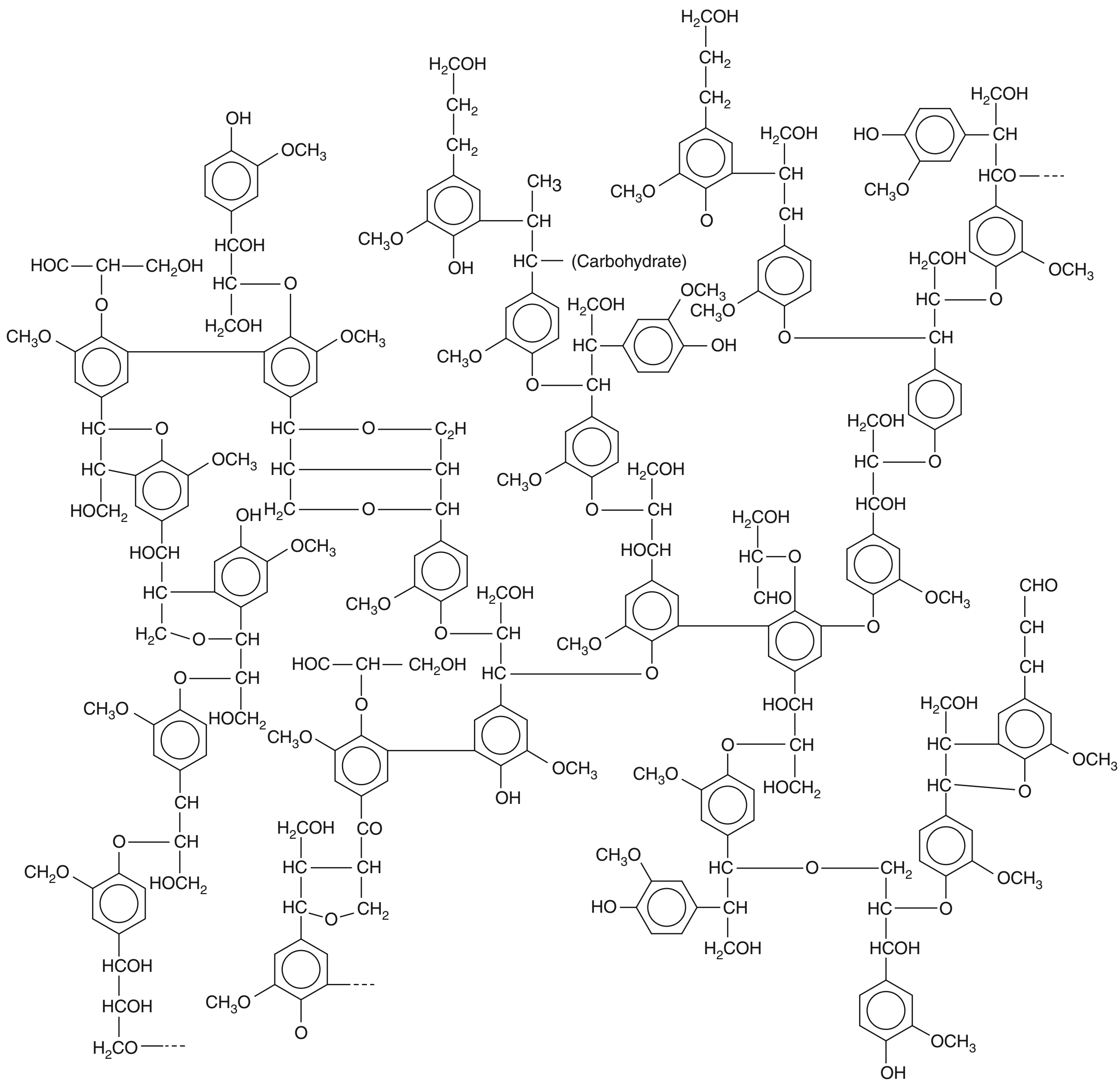

Vehicle Biofuels. Figure 9
Lignin structure

biomass whereas Table 8 describes the productivity of energy crops.

Sugar crops include sugarcane, sweet sorghum, and sugar beets. The dominant sugar is sucrose with minor amounts of glucose and fructose. Table 9 shows the productivity of sugar crops.

Starch crops include grains (e.g., corn, grain sorghum) and tubers (e.g., potatoes, cassava). Table 10 shows the productivity and abundance of US grain crops. Figure 13 shows the historical increase in US corn productivity.

Oil crops include palm, soybeans, rape, and Chinese tallow. Also, animal fats and waste frying oil can be used as raw material. Table 11 shows the productivity of oil crops.

Algae include primarily microalgae (e.g., cyanobacteria, diatoms) but also macroalgae (e.g., kelp, seaweed). Table 12 shows the range of lipid contents and

biomass productivities of microalgae grown under laboratory conditions. Table 13 shows lipid contents, biomass productivities, and lipid productivities for microalgae grown in outdoor ponds.

Intermediates

Figure 12 describes the following intermediates:

Bio-oil is the liquid resulting from biomass pyrolysis. Visually, it looks like crude oil; however, the composition is very different. Unlike crude oil, bio-oil contains a substantial amount of oxygen and is water soluble. A typical composition includes saccharides (2.4–3.3%), anhydrosugars (6.5–6.8%), aldehydes (10.1–14.0%), furans (0.35%), ketones (1.24–1.4%), alcohols (1.2–2.0%), carboxylic acids (8.5–11.0%), and pyrolytic lignin (16.2–20.6%). Because of the acids, the pH is low (1.5–3.8) [27].

Synthesis gas is the common name for a mixture of carbon monoxide and hydrogen, so named because it can be catalytically converted to a wide variety of products.

Acid degradation products result when biomass is heated with strong mineral acids. Components include acetaldehyde, formic acid, 2-furfural, glucose, 5-hydroxymethyl-furfural, 5-methyl-2-furfural, levulinic acid, saccharinic acid, and 2-furoic acid [28, 29].

Sugar intermediates include glucose, xylose, arabinose, galactose, mannose, rhamnose, and fructose, which are derived from sucrose, starch, cellulose, and hemicellulose.

Carboxylates are salts of carboxylic acids and include salts of volatile fatty acids (e.g., acetate, propionate, butyrate, valerate, caproate, heptanoate) and fatty acids (e.g., palmitate, stearate, oleate).

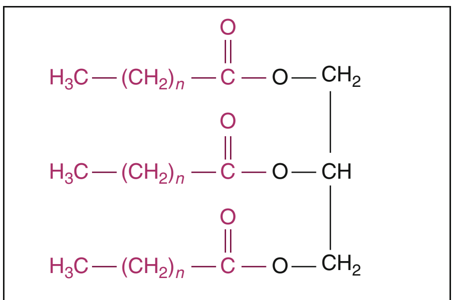

Triacylglycerol

Vehicle Biofuels. Figure 10
Structure of triacylglycerol

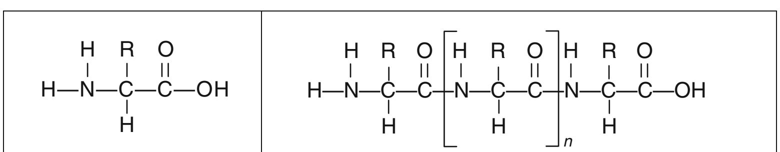

Amino acid | Protein

Vehicle Biofuels. Figure 11
Structure of amino acids and proteins

Raw Material	**Intermediate**	**Fuel**
(1) Lignocellulose	(a) Bio-oil	(A) Hydrocarbon
(2) Sugar crops	(b) Synthesis gas	(B) Alcohol
(3) Starch crops	(c) Acid degradation products	(C) Ether
(4) Oil crops	(d) Sugar	(D) Ester
(5) Algae	(e) Carboxylate	(E) Ketone

Vehicle Biofuels. Figure 12
Overview of processes that convert biomass to fuels

Vehicle Biofuels. Table 4 US land categories [8]

Land categories	Percentage (%)	Land (million acre)	Land (million hectare)
Forest	33	747	302
Grassland pasture and range	26	588	238
Crop	20	453	183
Special use (e.g., public facilities)	8	181	73
Misc. (e.g., urban, swamp, desert)	13	294	119
Total	100	2,263	916

Vehicle Biofuels. Table 5 Summary of potential lignocellulose feedstocks [8]

Biomass resource	Availability (million dry ton/ year)	Potential gasoline[a] (billion gal/ year)
Woody		
Logging and other residues	64	4.5
Fuel treatments	60	4.2
Urban wood residues	47	3.3
Fuelwood	52	3.6
Sub-total	223	15.6
Herbaceous		
Perennial crops	377	26.4
Crop residues	446	31.2
Process residues	87	6.1
Sub-total	910	63.7
Grand total	1,133	79.3

[a]Assumed yield = 70 gal/t

Products

Figure 12 describes the following products: hydrocarbons, alcohols, ethers, esters, and ketones. All of these products have been described previously.

Vehicle Biofuels. Table 6 Residues that are sustainably recovered under moderate crop yield increases without land use changes [8]

Biomass resource	Yield (dry ton/ (acre·year))	Availability (million dry ton/year)	Potential gasoline[a] (billion gal/ year)
Crop residues			
Corn	4.1	169.7	11.88
Sorghum, grain	1.7	1.3	0.09
Barley	2.2	2.8	0.20
Oats	1.9	0.7	0.05
Wheat, winter	2.3	27.4	1.92
Wheat, spring	1.4	7.4	0.52
Soybeans	1.8	0.0	0.00
Rice	5.1	10.3	0.72
Cotton lint	1.1	5.5	0.39
Other crops	1.2	20.8	1.46
Wastes			
Manure	–	43.5	3.05
Fats and grease	–	2.0	0.14
Municipal solid waste	–	29.4	2.06

[a]Assumed yield = 70 gal/t

Conversion Processes

Biomass is converted to fuels using either thermochemical or biological processes [30].

Thermochemical

At elevated temperatures, thermochemical conversion processes react biomass with air or oxygen to form solid (char), liquid, and gaseous products. Except for minor amounts of nitrogen and sulfur, the elemental composition of biomass is dominated by carbon, hydrogen, and oxygen (Table 14). Free of ash, nitrogen, or sulfur, a typical formula for woody biomass is $CH_{1.4}O_{0.59}$ [31].

Vehicle Biofuels. Table 7 Maximum potential of municipal solid waste (2009) [9]

	Percentage (%)	Wet weight (mill ton/year)	Assumed moisture (%)	Dry weight (mill ton/year)	Gasoline potential (bill gal/year)
Organic					
Wood	6.5	15.8	7	14.7	1.03
Yard trimmings	13.7	33.3	70	10.0	0.70
Food scraps	14.1	34.3	80	6.9	0.48
Paper & paperboard	28.2	68.5	6	63.7	4.46
Inorganics					
Glass	4.8	11.7	0	11.7	0
Metal	8.6	20.9	0	20.9	0
Plastic	12.3	29.9	0	29.9	0
Rubber/leather/textiles	8.3	20.2	0	20.2	0
Other	3.5	8.5	0	8.5	0
Total	100.0	243.0		186.5	6.67

Vehicle Biofuels. Table 8 High-yield lignocellulosic crops

Crop	Yield (dry ton/(acre·year))	Potential gasoline[a] (gal/(acre·year))	Potential gasoline[a] (L/(ha·year))
Mixed prairie grass [10]	1.64–2.67	115–187	1,070–1,740
Switchgrass [11]	2.3–4.9	161–343	1,500–3,200
Poplar [12]	4.5–6.7	315–469	2,940–4,380
Willow [12]	4.5–6.7	315–469	2,940–4,380
Miscanthus [12]	5.3–13.4	371–938	3,460–8,760
Photoperiod-sensitive sorghum [13]	8–17	560–1,190	5,230–11,100
Conventional sugarcane [14]	17	1,190	11,100
Giant cane (*Arundo donax*) [15]	25	1,720	16,300
Energy cane [16]	30	2,100	19,600
Elephant grass (*Pennisetum purpurcum*) [17]	37–47	2,590–3,290	24,200–30,700
Water hyacinth [18]	111	7,770	72,500
Water hyacinth with enriched CO_2 [18]	146	10,220	95,400

[a]Assumed yield = 70 gal/t

The *equivalence ratio* ϕ is defined as the actual oxygen fed to the reactor divided by the stoichiometric oxygen needed for complete combustion. Using a typical formula for woody biomass, the stoichiometric amount of oxygen is calculated as follows:

$$CH_{1.4}O_{0.59} + 1.055O_2 \rightarrow CO_2 + 0.7H_2O.$$

Vehicle Biofuels. Table 9 US sugar crops (2010)

Crop	Land harvested (acre)	Yield (wet ton/(acre·year))	Sugar content (ton sugar/t wet biomass)	Yield (ton sugar/(acre·year))	Potential ethanol yield (gal/(acre·year))
Sugarcane [8]	1,766,400	31.8	0.12	3.8	536
Energy cane [16]	Negligible	100	0.09	9	1,270
Sugar beets [8, 19]	1,155,700	27.6	0.15	4.1	578
Sorghum, sweet [20, 21]	negligible	13–20	0.06	0.78–1.2	110–169

Ton = 2,000 lb
Assumed yield = 141 gal per ton of sucrose

Vehicle Biofuels. Table 10 US grain crops (2010) [22]

Crop	Land harvested (acre)	Yield	Bushel weight (lb)	Water (%)	Yield (ton/(acre·year))	Yield (tonne/(ha·year))
Corn	81,446,000	152.8 bu/acre	56	15.5	3.62	8.11
Wheat	47,637,000	46.4 bu/acre	60	13.5	1.20	2.69
Sorghum, grain	4,808,000	71.8 bu/acre	56	13.0	1.75	3.92
Rice	3,615,000	6,725 lb/acre	NA	14.0	2.89	6.47
Oats	1,263,000	64.3 bu/acre	32	12.0	0.91	2.04

Tonne = 1,000 kg
Ton = 2,000 lb

As a function of equivalence ratio, Fig. 14 shows the equilibrium energy content of the char and gases exiting an air-fired thermochemical reactor [31]. Under *pyrolysis* conditions ($\phi < 0.1$), char is about 40–55% of the energy content of the raw biomass with the remaining energy in the form of gases. Under *gasification* conditions ($0.2 < \phi < 0.4$), char is less than 15% of the energy content of the raw biomass; most of the energy is in the form of gases. Figure 15 shows the equilibrium composition of the gases exiting an air-fired thermochemical reactor. Other than char, the only equilibrium products are CH_4, CO, H_2, CO_2, and N_2. Real thermochemical reactors also produce complex tars and bio-oils; however, these are non-equilibrium products.

Combustion A biomass combustor can be as simple as a bonfire or a sophisticated as a fluidized bed. The objective of the combustion process is to produce heat (Table 14), which typically is used to generate steam. To ensure that there is negligible carbon monoxide in the combustion gas, a biomass combustor is typically operated at an equivalence ratio of 1.05–1.10. In an air-fired combustor, the combustion temperature is about 2,050°C and in an oxygen-fired combustor, combustion temperature is about 2,800°C [31].

As a solid fuel, biomass competes with coal. Because of its lower oxygen content, coal has higher energy content than biomass. Heating biomass in an oxygen-free environment drives off volatiles to produce charcoal, which has lower oxygen content than biomass and hence its heating value is similar to coal. Compared to coal, biomass has fewer impurities (N, S), so less treatment of stack gases is required, which lowers the capital cost of the combustor.

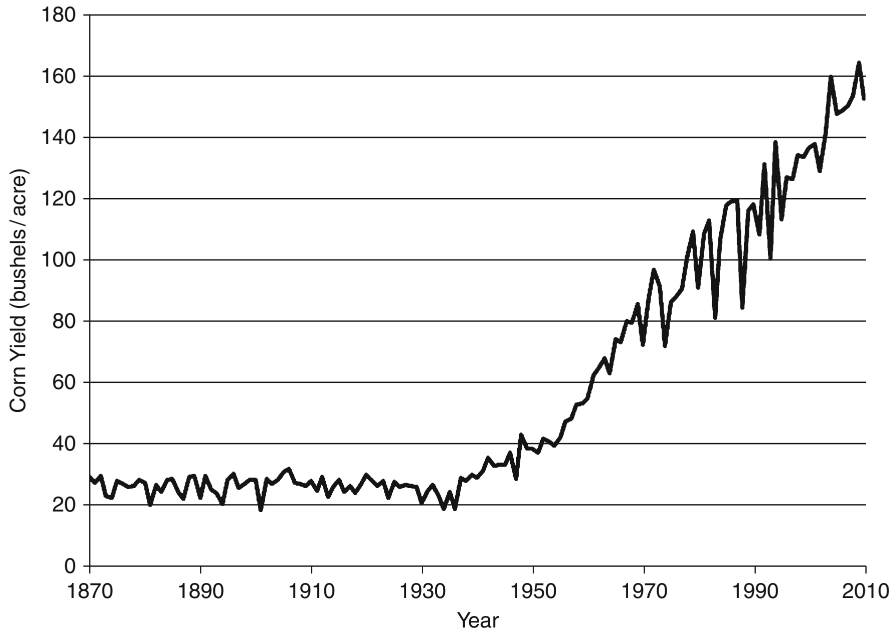

Vehicle Biofuels. Figure 13
Historical corn productivity [22]

Gasification Commonly, gasifiers are operated at an equivalence ratio of about 0.25 (1.6 g air/g biomass). Gasification typically occurs at temperatures of 700–1,100°C with air and about 100°C higher with oxygen [31]. Table 15 shows the energy content of the gases exiting a gasifier fired with air or oxygen. In Europe during World War II, the low-energy gas from air-fired gasifiers was fed to millions of vehicles.

The mechanical design of gasifiers follows [31]:

Updraft gasifiers employ a bed of biomass in which fresh biomass is introduced at the top. Air (or oxygen) is introduced at the bottom of the bed and is blown upward. The bottom zone is richest in oxygen, which is where combustion reactions occur thereby releasing heat and increasing the temperature. As the hot gases flow upward through the upper zone of fresh biomass, gases and liquids are generated. Ideally, to prevent liquid condensation, the hot products are burned directly.

Downdraft gasifiers also employ a bed of biomass in which fresh biomass is introduced at the top. Air (or oxygen) is introduced at an intermediate zone in the bed. The gas flows downward with the biomass and passes through the hot combustion zone. Because the gas exits at very high temperatures, less tar and bio-oil is produced. The hot product gas can be used to preheat the incoming biomass feed.

Fluidized-bed gasifiers mix high-velocity air and steam with the biomass to create an ebullating bed. Unlike fixed-bed gasifiers, fluidized-bed gasifiers can employ a wider range of particle sizes and have a higher throughput because of the uniformly high temperature. To maintain high velocities, the hot product gas is often recycled into the fluidized-bed gasifier. These gasifiers often employ a solid heat transfer agent, such as sand or catalyst.

The primary product from gasifiers is a mixture of carbon monoxide and hydrogen, often called *synthesis gas*. The hydrogen content of the synthesis gas can be enriched using the *shift reaction*

$$CO + H_2O \rightarrow CO_2 + H_2.$$

Commonly, the process employs two stages: high-temperature shift (350°C, iron oxide catalyst) and low-temperature shift (190–210°C, copper catalyst).

Vehicle Biofuels. Table 11 Productivity of oil-producing crops

Crop	Latin Name	Productivity (gal/(acre·year))	Productivity (L/(ha·year)
Corn [23]	*Zea mays*	18	168
Soybean [23]	*Glycine max*	46	429
Peanut [23]	*Ariachis hypogaea*	109	1,020
Rape seed [23]	*Brassica napus*	122	1,140
Castor bean [23]	*Ricinus communis*	145	1,350
Jojoba [23]	*Simmondsia chinensis*	186	1,740
Jatropha [23]	*Jatropha curcas*	194	1,810
Coconut [23]	*Cocos nucifera*	276	2,580
Macauba palm [23]	*Acrocomia aculeata*	461	4,300
Oil palm [23]	*Elaeis guineensis*	610	5,700
Chinese tallow [24]	*Triadica sebifera*	645	6,020

Vehicle Biofuels. Table 12 Productivity of microalgae [25]

Algae species	Lipid content (%)	Biomass productivity (tonne/(ha·year))
Ankistrodesmus sp.	24–31	42–63
Botryoccus braunii	25–75	11
Chlorella emersonii	25–63	3.3–3.5
Chlorella vulgaris	5–58	2.1–3.5
Chlorella sp.	10–48	5.9–91
Chlorella pyrenoidosa	2	264–474
Chlorella	18–57	13–51
Dunaliella salina	6–25	5.8–131
Dunaliella primolecta	23	51
Haematococcus pluvialis	25	37–133
Monallanthus salina	20–22	43
Nannochloropsis sp.	12–53	7–19
Nitzchia sp.	16–47	32–79
Oocystis pusilla	11	148–167
Phaeodactylum tricornutum	18–57	8.8–77
Porphyridium cruentum	9–61	91
Scenedesmus sp.	20–21	8.9–49
Spirulina platensis	4–17	1.5–186
Spirulina maxima	4–9	91
Tetraselmis suecica	8–23	69

Synthesis gas can be converted to a variety of products, as described below.

Methanol ($1 \rightarrow b \rightarrow B$) (*Note:* Codes are described in Fig. 12) Using ZnO catalyst operating at 240–400°C and 50–300 atm, methanol can be produced from synthesis gas according to the following reaction [31]:

$$CO + 2H_2 \rightarrow CH_3OH.$$

Mixed Alcohols ($1 \rightarrow b \rightarrow B$) Using Mo_2C catalyst operating at 300°C and 80 atm, mixed alcohols (e.g., C2 to C7) can be produced from synthesis gas [32]. A representative reaction is the formation of ethanol [32]

$$CO + 4H_2 \rightarrow C_2H_5OH + H_2O.$$

Hydrocarbons ($1 \rightarrow b \rightarrow A$) Fischer–Tropsch catalysts (e.g., cobalt, iron) typically operate at 150–300°C and produce hydrocarbons according to the following reaction:

$$(2n + 1)H_2 + nCO \rightarrow C_nH_{(2n+2)} + nH_2O.$$

The product distribution tends to be very wide and includes heavy waxes. Although waxes are valuable products, the market is small, so they often must be refined into lighter fuels (e.g., gasoline, jet fuel, diesel). During World War II, Fischer–Tropsch chemistry was used by the Germans to produce liquid fuels from coal. Currently, South African SASOL uses Fischer–Tropsch chemistry to produce hydrocarbons from coal. A number of commercial plants (Malaysia, Qatar) use

Vehicle Biofuels. Table 13 Productivity of microalgae grown in outdoor ponds [26]

Algae species	Lipid content (%)	Biomass productivity (tonne/(ha·year)	Lipid productivity (L/(ha·year))	Lipid productivity (gal/(acre·year))
Amphora	40	142	64,500	6,910
Chaetoceros muelleri	26	95	28,100	3,010
Cyclotella cryptica	24	99	27,000	2,890
Isochrysis galbana	22	102	25,500	2,730
Nannochloropsis	21	55	13,100	1,410
Nannochloropsis salina	16	91	16,500	1,770
Tetraselmis suecica	22	69	17,200	1,850

Fischer–Tropsch chemistry to produce hydrocarbons from natural gas.

Hydrocarbons (1 → b → B → A) Through an alternative route, methanol (or higher alcohols) can be converted to hydrocarbons using zeolite catalysts, such as ZSM-5 [31].

$$n\mathrm{CH_3OH} \rightarrow \mathrm{C}_n\mathrm{H}_{2n} + n\mathrm{H_2O}$$

Ethers (1 → b → B → C) Methanol can also be converted to dimethyl ether (DME) using a zeolite catalyst, such as ZSM-5 [33].

$$2\mathrm{CH_3OH} \rightarrow \mathrm{H_3COCH_3} + \mathrm{H_2O}$$

DME can be used in diesel engines as a clean-burning fuel [34].

Pyrolysis (1 → a → A) As stated previously, liquids are not thermodynamically stable products from thermochemical reactors; however, they are produced as reaction intermediates. *Fast pyrolysis* involves rapidly heating biomass (less than 1–5 s) to 450–600°C and then rapidly cooling the products to "freeze" the reaction [35]. On a weight basis, a typical product spectrum consists of the following:

- Char = 10–25%
- Gas = 8–30%
- Bio-oil = 45–65%
- Water = 8–15%

Although the bio-oil physically looks like crude petroleum, its properties are very different [36]. It has high water content (15–30%) that is difficult to remove via distillation. Further, it has high oxygen content (35–40%) and low pH (~2.5). Crude bio-oil can be used directly in boilers and engines (e.g., diesel, gas turbines); however, there are issues with fuel stability and corrosiveness. Using processes similar to those used to refine crude oil (e.g., hydrotreating and catalytic vapor cracking), the bio-oil can be upgraded to products similar to those obtained from petroleum [36]. At the moment, upgrading bio-oil is expensive and energy yields are low.

Acid Degradation (1 → c → C) To produce fuels using acid degradation, lignocellulose is thermochemically treated in a multi-step process [37]:

- *Step 1* – The biomass is hydrolyzed at 210–230°C for 13–25 s using 1–5% mineral acid. This produces primarily hydroxymethylfurfural, which is removed continuously.
- *Step 2* – The hydroxymethylfurfural is hydrolyzed further at 195–215°C for 15–30 min to produce primarily levulinic acid, which is continuously removed.
- *Step 3* – Through a series of dehydration and reduction reactions, levulinic acid is converted to methyltetrahydrofuran, an oxygenate that can be added to conventional gasoline.

Biodiesel (4 → e → D or 5 → e → D) A component of oil seeds and algae, triacylglycerol (TAG) can be extracted using a solvent (e.g., hexane). TAG can

Vehicle Biofuels. Table 14 Elemental composition and energy content of solid fuels [31]

Feedstock	Elemental composition (wt%)						Higher heating value[a]	
	C	H	N	S	O	ash	(Btu/lb)	(MJ/kg)
Coal								
Pittsburg seam coal	75.5	5.0	1.2	3.1	4.9	10.3	13,650	31.754
West Kentucky No. 11 coal	74.4	5.1	1.5	3.8	7.9	7.3	13,460	31.312
Utah coal	77.9	6.0	1.5	0.6	9.9	4.1	14,170	32.963
Wyoming Elkol coal	71.5	5.3	1.2	0.9	16.9	4.2	12,710	29.567
Lignite	64.0	4.2	0.9	1.3	19.2	10.4	10,712	24.919
Charcoal	80.3	3.1	0.2	0.0	11.3	3.4	13,370	31.102
Biomass								
Douglas fir	52.3	6.3	0.1	0.0	40.5	0.8	9,050	21.053
Douglas fir bark	56.2	5.9	0.0	0.0	36.7	1.2	9,500	22.010
Pine bark	52.3	5.8	0.2	0.0	38.8	2.9	8,780	20.425
Western hemlock	50.4	5.8	0.1	0.1	41.4	2.2	8,620	20.052
Redwood	53.5	5.9	0.1	0.0	40.3	0.2	9,040	21.030
Beech	51.6	6.3	0.0	0.0	41.5	0.6	8,760	20.378
Hickory	49.7	6.5	0.0	0.0	43.1	0.7	8,670	20.169
Maple	50.6	6.0	0.3	0.0	41.7	1.4	8,580	19.959
Poplar	51.6	6.3	0.0	0.0	41.5	0.6	8,920	20.750
Rice hulls	38.5	5.7	0.5	0.0	39.8	15.5	6,610	15.377
Rice straw	39.2	5.1	0.6	0.1	35.8	19.2	6,540	15.214
Sawdust pellets	47.2	6.5	0.0	0.0	45.4	1.0	8,814	20.504
Paper	43.4	5.8	0.3	0.2	44.3	6.0	7,572	17.615
Redwood wood waste	53.4	6.0	0.1	0.1	39.9	0.6	9,163	21.316
Alabama oak waste wood	49.5	5.7	0.2	0.0	41.3	3.3	8,266	19.229
Animal waste	42.7	5.5	2.4	0.3	31.3	17.8	7,380	17.168
Municipal solid waste	47.6	6.0	1.2	0.3	32.9	12.0	8,546	19.880

[a]Water product is assumed to be liquid

be used directly in diesel engines; however, its high viscosity causes operational problems in the fuel injectors. To overcome this problem, the diesel engine can be modified to include fuel-line heaters that lower the TAG viscosity. Rather than modify the engine, the fuel itself can be modified to lower its viscosity. Typically, this is accomplished by converting TAG to esters ("biodiesel") by a base-catalyzed reaction with an alcohol [38, 39]. Because of its low cost, methanol is the preferred alcohol; however, other alcohols (e.g., ethanol) can be used as well. A by-product of biodiesel production is glycerol.

Biological Processes

Biological processing of biomass involves the use of fermentation to convert biomass to fuels.

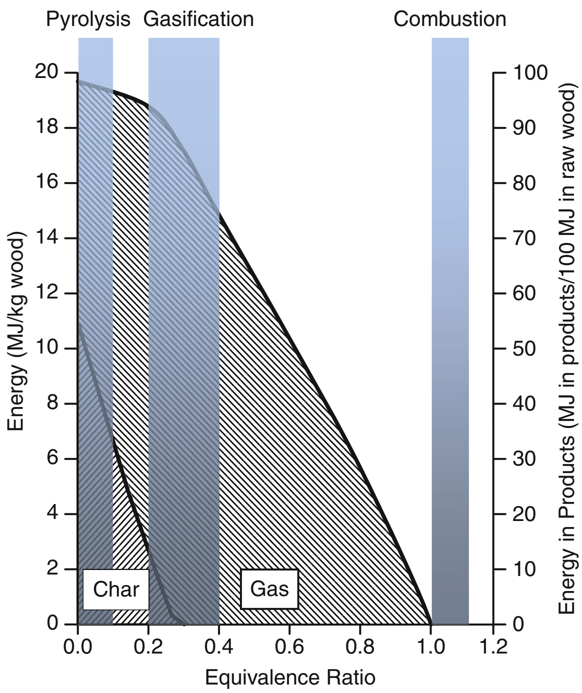

Vehicle Biofuels. Figure 14
Equilibrium energy content of gas and char exiting a thermochemical reactor using air as the oxidant. The equivalence ratio is the actual air employed compared to the stoichiometric amount needed for complete combustion [31]

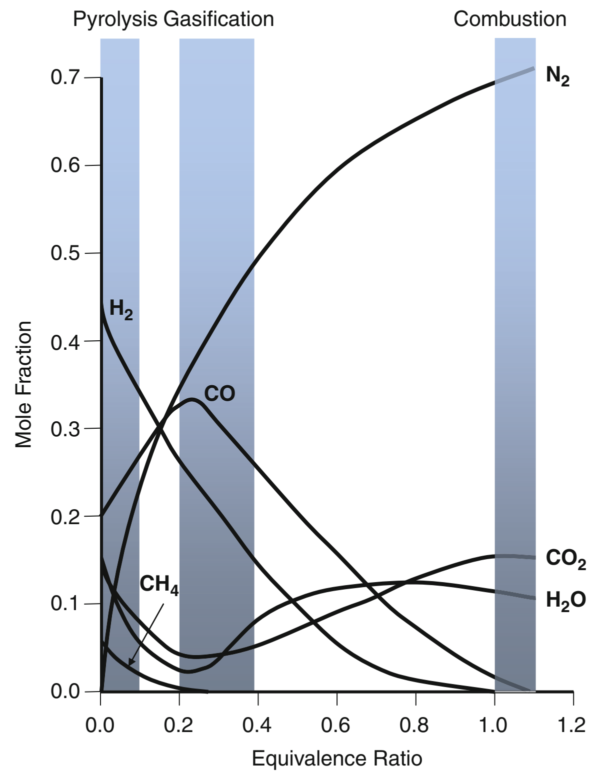

Vehicle Biofuels. Figure 15
Equilibrium gas composition exiting a thermochemical reactor using air as the oxidant. The equivalence ratio is the actual air employed compared to the stoichiometric amount needed for complete combustion [31]

Sugar Platform The sugar platform employs processes that convert sugar to fuel (typically alcohol) via fermentation (Fig. 16).

Sugar Crop (2 → d → B) In Brazil, the dominant sugar crop is sugarcane (*Saccharum officinarum*). Traditionally, prior to harvest, the sugarcane field is set afire to burn off leaves, which contain negligible amounts of sugar. (*Note:* Because of the pollution that results from burning sugarcane fields, many governments are banning this practice.) After the fire, the stalks are brought to the sugar mill for processing. On a wet basis, the harvested plant contains 68–72% moisture and 12–17% total sugars that are 90% sucrose and 10% glucose or fructose [40].

To extract the sugar, the sugarcane stalks are chopped using a hammer mill and washed countercurrently with water in a multi-stage operation. The most common extraction method uses roller mills that intensely squeeze the fiber to recover the maximum juice per stage. Typically three to four stages are employed. Another common extraction method employs diffusers in which the fiber is

Vehicle Biofuels. Table 15 Energy content of gaseous fuels [31]

Name	Source	Energy content (Btu/scf)[a]
Low-energy gas	Air gasifier	150–200
Medium-energy gas	Oxygen gasifier Pyrolyzer	300–500
Biogas	Anaerobic digestor	600–700
High-energy gas	Natural gas	1,000

[a]*scf* standard cubic foot (ft^3) where $T = 60°F$ and $P = 1$ atm

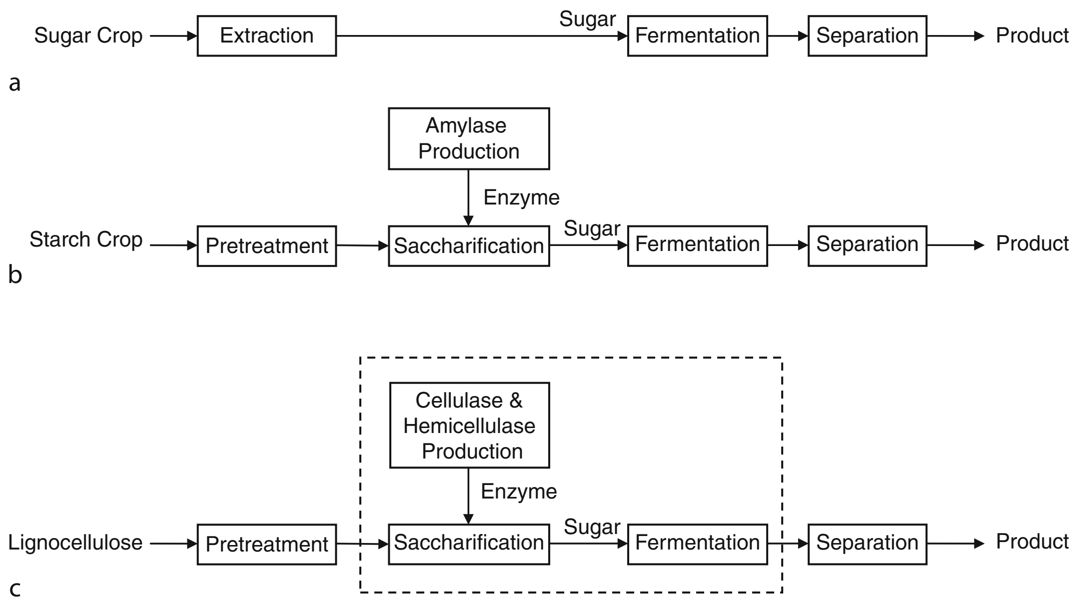

Vehicle Biofuels. Figure 16
Sugar platform. (**a**) sugar crop; (**b**) starch crop; (**c**) lignocellulose

placed on a conveyor belt and is repeatedly washed in a countercurrent manner with water that has ever-lower sugar concentrations. Typically, 10–18 washing stages are employed [40]. The extraction process usually recovers >95% of the sugar in fiber. The washed fiber is called *bagasse*, and is used to fuel boilers that power the sugar mill.

Commercial sugarcane varieties are bred to have high sugar concentrations, which reduces the amount of fiber that must be processed by the sugar mill. In contrast, energy cane varieties are bred to have high per-acre yields of both fiber and sugar, at the expense of lower sugar concentrations. To economically recover sugar from energy cane, a novel screw-press conveyor extraction system can be employed that uses a "gentle squeeze" between extraction stages [41]. Typically eight extraction stages would be employed.

In Brazil, both continuous and batch fermentations are employed [42]. Continuous fermentations are more productive; however, they are more prone to contamination, thus batch fermentations are preferred. In both processes, centrifuges recover yeast (*Saccharomyces cerevisiae*) from the fermentation broth and recycle it to subsequent fermentations. Yeast grow at acid pH whereas bacteria prefer neutral pH; therefore, to reduce bacterial contamination, the recycled yeast is contacted with dilute sulfuric acid. Typical fermentations employ the following conditions: cell density 8–17% v/v, temperature 33–35°C, ethanol concentration 8–11% v/v, ethanol yield 90–92% of theoretical, and fermentation time 6–10 h. Contaminants are unable to take over the fermentation because of the short residence time, high ethanol concentrations, and addition of antibiotics.

The ethanol product is distilled to the azeotrope (95.5% v/v) and then can be dehydrated using molecular sieves [42]. In Brazil, azeotropic ethanol is sold as a neat fuel; however, it cannot be blended into gasoline or diesel fuel because the water will form a separate phase.

Starch Crop $(3 \rightarrow d \rightarrow B)$ The most common starch crop is corn, which has a typical composition shown in Table 16. Corn is processed by wet mills and dry mills (Fig. 17). Wet mills fractionate corn into oil, fiber, gluten (i.e., protein), and starch; the later which may be fermented into ethanol. Purpose-built ethanol plants use dry milling, which is less capital intensive and produces the majority of corn ethanol in the United States.

In dry mills [43], the corn is hammer-milled and then is mixed with water, lime, and ammonia at 88–110°C for 75 min. During this cooking process, the starch hydrates and swells. To reduce the viscosity, thermo-stable α-amylase is added which begins the *saccharification* (i.e., sugar-production) process. After cooking, the temperature is lowered to 61°C and glucoamylase is added, which completes the saccharification of starch to glucose in about 5 h. After saccharification, the temperature is lowered to 32°C to begin the fermentation using yeast (*Saccharomyces cerevisiae*). Typically, batch fermentations are used with a residence time of about 68 h. The final ethanol concentration in the beer is about 10.8% ethanol (w/w). To recover the ethanol, the beer is distilled. The bottoms of the first distillation column contain solids (e.g., yeast, gluten, fiber, and germ), which are recovered by centrifugation and evaporation and sold as distiller's dried grains with solubles (DDGS). The DDGS has high protein content (about 28%) and is sold as animal feed. The tops from the first distillation column contain ethanol and water, which is further distilled and finally dehydrated using molecular sieves.

In wet mills [44], first the corn is *steeped*, i.e., soaked in water containing 0.06–0.2% sulfur dioxide at about 51°C for about 36 h. The steeping softens the kernels and breaks the protein matrix allowing the corn to be separated into its various components (germ, fiber, gluten, starch). From the germ, corn oil is extracted

Vehicle Biofuels. Table 16 Typical corn composition [43]

Component	Wet basis (g/100 g wet corn)	Dry basis (g/100 g dry corn)
Starch	59.5	70.0
Fiber	7.0	8.2
Ash and other	6.7	7.9
Protein	8.4	9.9
Oil	3.4	4.0
Water	15.0	0.0
Total	100.0	100.0

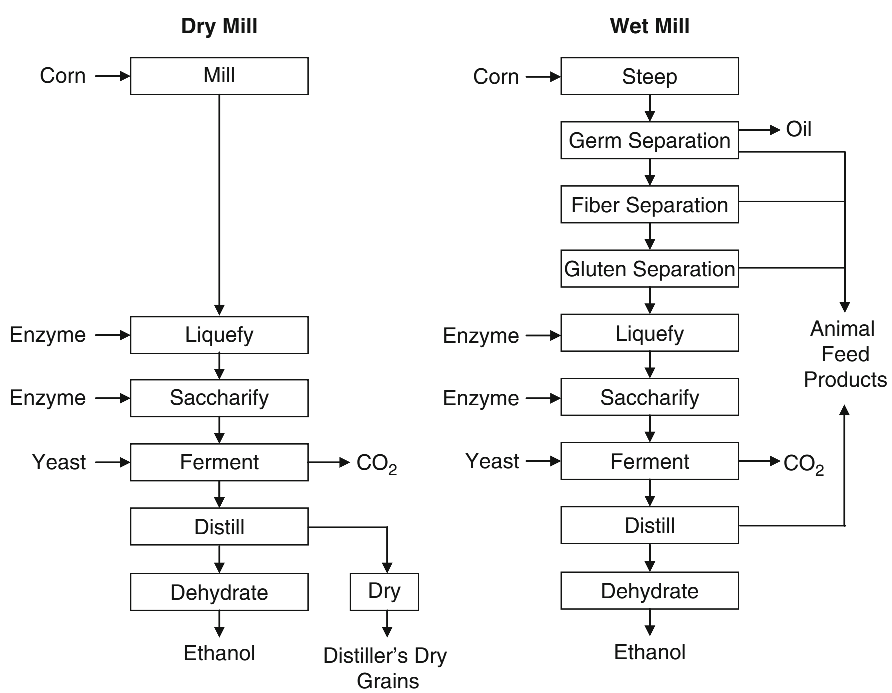

Vehicle Biofuels. Figure 17
Corn-to-ethanol processes

leaving germ meal. The germ meal, corn fiber, and gluten are formulated into various animal feed products (e.g., gluten meal, gluten feed). The corn starch has numerous uses (e.g., production of high-fructose syrup) and can be used to produce ethanol in a process similar to that used in dry mills.

Although ethanol is the dominant alcohol produced from starch, butanol is also being produced [45].

Lignocellulose (1 → d → B) In lignocellulose, the dominant polysaccharide is cellulose, which is composed of β-linked glucose monomers. Because of its similarity to starch (α-linked glucose), many lignocellulose-conversion processes are modeled after starch-conversion processes (Fig. 16). In starch-conversion processes, the pretreatment step involves soaking in water, which swells the starch rendering it more susceptible to enzymatic hydrolysis. In lignocellulose-conversion processes, a more aggressive pretreatment is required.

The enzymatic digestibility of lignocellulose is affected by the following factors: lignin content, acetyl content of hemicellulose, cellulose crystallinity, degree of polymerization, pore volume, and accessible surface area. To increase its enzymatic digestibility, lignocellulose may be treated with steam, alkali (e.g., ammonia, lime, sodium hydroxide), dilute acids (e.g., sulfuric), liquid hot water, solvents (e.g., ethanol, acetone, butanol, ionic liquids), oxidants (e.g., hydrogen peroxide, oxygen, ozone), and machines (e.g., ball mill, two-roll mill) [46].

After pretreatment, the lignocellulose is saccharified using cellulase and hemicellulase enzymes, which produce primarily glucose and xylose [47]. Traditional yeast (*Saccharomyces cerevisiae*) can ferment only the glucose, so xylose-fermenting microorganisms (e.g., *Pichia stipitis*) are required to utilize all sugars. Using genetic engineering, microorganisms have been developed that ferment both glucose and xylose to ethanol [48]. Economies can be realized via *consolidated bioprocessing* in which enzyme production, saccharification, and fermentation occur in the same vessel using a single microorganism, as shown in the dotted box of Fig. 16 [49]. Although genetic engineering is being used to develop consolidated bioprocessing microorganisms, naturally occurring microorganisms have been identified as well [50].

The conversion of lignocellulose to ethanol has not been commercialized, so typical industrial fermentation conditions have not yet been established. Compared to starch, lignocellulose is much less reactive; therefore, lignocellulose fermentations are likely to take much longer and produce lower ethanol concentrations.

Lignocellulosic ethanol will be recovered via distillation, much like ethanol from conventional starch or sugar processes.

The main impediments to lignocellulosic ethanol are the high cost of pretreatment and enzymes. Some processes overcome this barrier by using dilute acids to saccharify lignocellulose [51]. In the early and mid twentieth century, this process was used commercially in Germany and the former Soviet Union, and was piloted in the United States during World War II. The main obstacle to widespread commercialization is sugar degradation, which reduces yields and inhibits the fermentation. Another process option is the use of concentrated acid to saccharify lignocellulose [52]. Compared to dilute-acid hydrolysis, sugar degradation is much less; however, acid recovery is a challenge. One promising approach is industrial-scale chromatography.

Carboxylate Platform (1 → e → B) The carboxylate platform is a type of consolidated bioprocessing in which lignocellulose is biologically converted to carboxylate salts (e.g., calcium acetate) that are subsequently chemically converted to fuels and chemicals [53, 54]. Generally, a mixed culture of microorganisms is used, which has a great operational advantage: sterile operating conditions are not required. Nonetheless, because they have greater control over the products and yields, some processes use a monoculture and do require sterile operating conditions [55].

Figure 18 shows a schematic of the carboxylate platform, which has routes to secondary and primary alcohols.

In the secondary alcohol route [56], the biomass is pretreated to enhance its digestibility. In principle, any pretreatment can be used; however, alkaline pretreatments (e.g., lime) are favored because the cations help neutralize the carboxylic acids produced in the fermentation. The biomass is then fed to a mixed culture of microorganisms that ferments biomass components

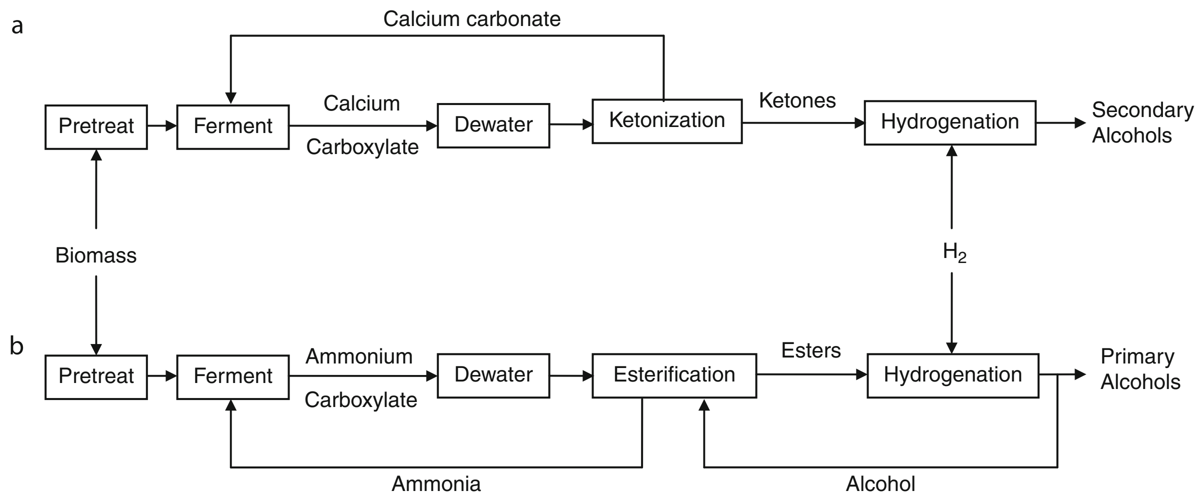

Vehicle Biofuels. Figure 18
Carboxylate platform. (**a**) secondary alcohol route; (**b**) primary alcohol route

(e.g., cellulose, hemicellulose, starch, free sugars, pectin, protein, fats) into carboxylic acids (e.g., acetic, propionic, butyric acids) and hydrogen. To maintain a near-neutral pH, a buffer is added (e.g., calcium carbonate). The mixed culture of microorganisms can originate from a variety of sources, such as cattle rumen or marine swamps. An inhibitor (e.g., iodoform) is added to suppress the generation of methane, an unwanted by-product. Via vapor-compression evaporation, the carboxylate salts in the fermentation broth are dewatered. The concentrated carboxylate salts (e.g., calcium acetate) are thermally converted to ketones (e.g., acetone). The ketones are hydrogenated using a hydrogenation catalyst (e.g., Raney nickel) to produce secondary alcohols (e.g., isopropanol). Potential sources of hydrogen include the fermentor gas, gasified undigested residues, reformed methane, and water electrolysis.

In the primary alcohol route [57], the early steps (pretreatment, fermentation, and dewatering) are nearly identical to the secondary alcohol route. After dewatering, the concentrated carboxylate salts (e.g., ammonium acetate) react with a recycled high-molecular-weight alcohol (e.g., hexanol) to form esters (e.g., hexyl acetate), which is subsequently hydrogenated to form two alcohols (e.g., ethanol and hexanol). The high-molecular-weight alcohol is recycled and the low-molecular-weight alcohol is harvested as product.

Syngas Platform (1 → b → B) As described previously, syngas ($CO + H_2$) is produced by gasifying biomass. The syngas can be fermented to acetate, butyrate, ethanol, and butanol [58–60].

Biomass to Hydrocarbons Because of their high energy density, hydrocarbons are the preferred source of transportation fuels. Various routes to hydrocarbons are described below.

Biogas (1 → e → A) As described previously, the carboxylate platform uses a mixed culture of microorganisms to produce carboxylate salts and hydrogen. If no methanogen inhibitor is included, these products are converted to biogas ($CH_4 + CO_2$), which simply bubbles out of the fermentation broth [61]. Because of its simplicity, this process is used all over the world, including developing countries, to convert waste biomass into fuel. Normally, this fuel is used for stationary applications (e.g., cooking, electricity production); however, it could be purified by removing carbon dioxide using acid-gas absorbents (e.g., triethanol amine). The resulting pure methane could be cryogenically liquefied and used for transportation purposes.

Hydrocarbons from Alcohols (B → A) Fermentation-derived alcohols can be converted to hydrocarbons using zeolite catalysts, such as H-ZSM-5 [62].

$$nC_2H_5OH \rightarrow C_{2n}H_{4n} + nH_2O$$

The reaction proceeds by dehydrating the alcohol to form an alkene (olefin), which then oligomerizes to form higher molecular weight hydrocarbons (e.g., olefins, aromatics). If desired, the final product can be hydrogenated to saturate the bonds. Compared to low-molecular-weight alcohols, high-molecular-weight alcohols retain a greater percentage of their combustion energy within the hydrocarbon product [63].

Oleaginous Microorganisms *Oleaginous microorganisms* accumulate triacylglycerol (TAG) within their cells, typically as a result of environmental stress such as nutrient limitations (e.g., nitrogen, phosphorous). As with algae and oil crops, the TAG can be extracted from the cell and converted to methyl esters (biodiesel) or hydrotreated to hydrocarbons [64]. In some cases, the TAG floats to the top of the fermentor and can be removed by skimming.

Hydrocarbons from Sugar (d → A) Under appropriate fermentation conditions, naturally occurring microorganisms accumulate TAG. For example, the yeast *Rhodosporidium toruloides* ferments sugar and accumulates 67% of its cellular dry weight as lipids and can produce TAG concentrations over 70 g/L in the fermentor [64]. To enhance TAG production, researchers are applying genetic engineering techniques to *Saccharomyces cerevisiae* and *Escherichia coli* [65].

Hydrocarbons from Lignocellulose (1 → A) Some microorganisms that grow directly on lignocellulose accumulate TAG within their cells [66].

Hydrocarbons from Carboxylates (e → A) Some microorganisms (e.g., *Alcanivorax borkumensis* SK2) accumulate and secrete TAG when growing on acetate [67].

Future Directions

For biofuels to make a significant impact on transportation, it is necessary to minimize land area requirements, which is accomplished by (1) growing the most productive crops and (2) utilizing the whole plant.

Crop Productivity

Among oil-producing land crops, Chinese tallow is one of the most productive and it can grow on marginally productive lands. Despite these advantages, it is not a significant source of biodiesel. In the United States, soybean oil dominates, yet it is among the least productive oil-seed crops. Chinese tallow is not widely grown because it is an invasive species and governments restrict its growth; however, the very properties that make it invasive (rapid growth, robust) make it an ideal biomass source. Perhaps plant breeders can create varieties that maintain the desirable traits, yet eliminate its invasive properties. For example, it might be possible to create varieties in which the seeds are sterile.

Among aquatic plants, water hyacinth has the highest productivity and rivals algae, which are the most productive photosynthetic organisms. Water hyacinth is also an invasive species; therefore, production systems must be developed to prevent its release into local rivers and lakes.

Among land crops, lignocellulose is the most productive. Further, numerous lignocellulosic wastes (municipal solid waste, manure, agricultural residues) are inexpensive and many are already collected.

Whole Plant Utilization

In recent years, much attention has been paid to algae because they do not compete with agricultural land, and they produce high concentrations of TAG, which is readily converted to biodiesel or hydrocarbons. Nonetheless, only a portion of the algae is TAG. Rather than focusing only on TAG, greater yields will be realized by converting the entire organism to fuel. Given the diverse composition and high water content of algae, the best process candidate is the carboxylate platform.

Lignocellulose conversion processes use the whole plant, not just the seed or the root. Although many lignocellulose conversion processes are being developed, the technology is still immature so no processes have been fully commercialized.

Closing Thoughts

Although biofuels currently contribute to the global supply of transportation fuels, the industry is in its

infancy. Once lignocellulose conversion technology is perfected, the full potential of biofuels will be realized.

Bibliography

Primary Literature

1. Renewable Fuels Association. http://www.ethanolrfa.org/pages/statistics#A
2. Energy Information Administration. http://www.eia.gov/dnav/pet/hist/LeafHandler.ashx?n=PET&s=MGFUPUS2&f=A
3. Renewable Fuels Association (2010) Ethanol industry outlook: climate of opportunity. http://www.ethanolrfa.org/page/-/objects/pdf/outlook/RFAoutlook2010_fin.pdf?nocdn=1
4. Energy Information Administration. http://www.eia.doe.gov/cneaf/solar.renewables/page/biodiesel/biodiesel.html
5. Energy Information Administration. http://www.eia.gov/dnav/pet/pet_cons_psup_dc_nus_mbblpd_a.htm
6. Zhang RD, He H, Shi XY, Zhang CB, He BQ, Wang JX (2004) Preparation and emission characteristics of ethanol-diesel fuel blends. J Environ Sci (China) 16:793–796
7. Subbaiah GV, Gopal KR, Hussain SA, Prasad BD, Reddy KT (2010) Rice bran oil biodiesel as an additive in diesel-ethanol blend for diesel engines. Int J Res Rev Appl Sci 3:334–342
8. Perlack RD, Wright LL, Turhollow AF, Graham RL, Stokes BJ, Erbach DC (2005) Biomass as feedstock for a bioenergy and bioproducts industry: the technical feasibility of a billion-ton annual supply. Oak Ridge National Laboratory, Oak Ridge. DOE/GO-102995–2135, ORNL/TM-2005/66
9. US Environmental Protection Agency (2010) Municipal solid waste generation, recycling, and disposal in the United States: facts and figures for 2009. Franklin Associates, EPA530-R-10–012. http://www.epa.gov/epawaste/nonhaz/municipal/pubs/msw2009-fs.pdf
10. Tilman D, Hill J, Lehman C (2006) Carbon-negative biofuels from low-input high-diversity grassland biomass. Science 314:1598–1600
11. Schmer MR, Vogel KP, Mitchell RB, Perrin RK (2008) Net energy of cellulosic ethanol from switchgrass. Proc Nat Acad Sci USA 105:464–469
12. McKendry P (2002) Energy production from biomass (part 1): overview of biomass. Bioresour Technol 83:37–46
13. McCollum III T, McCuistion K, Brent B (2005) Brown mid-rib and photoperiod-sensitive forage sorghums. AREC 05–20. Agricultural Program, Texas A&M University, Amarillo
14. Waclawovsky AJ, Sato PM, Lembke CG, Moore PH, Souza GM (2010) Sugarcane for bioenergy production: an assessment of yield and regulation of sucrose content. Plant Biotechnol J 8:263–276
15. Westlake DF (1963) Comparisons of plant productivity. Biol Rev 38:385–425
16. Alexander AG (1985) The energy cane alternative, vol 6, Sugar series. Elsevier, Amsterdam
17. Klass DL (1998) Biomass for renewable energy, fuels, and chemicals. Academic, San Diego, 70
18. Spencer W, Bowes G (1986) Photosynthesis and growth of water hyacinth under CO_2 enrichment. Plant Physiol 82:528–533
19. http://waterquality.montana.edu/docs/irrigation/sugarbeet101.shtml
20. Freeman KC, Broadhead DM, Zummo N, Westbrook FE (1986) Sweet sorghum culture and syrup production. U.S. Department of Agriculture, Washington, DC, Handbook No. 611, 55 pp
21. Reddy BVS, Ramesh S, Reddy PS, Ramaiah B, Salimath PM, Kachapur R (2005) Sweet sorghum – a potential alternate raw material for bio-ethanol and bioenergy. SAT eJournal 1(1). www.ejournal.icrisat.org
22. US Department of Agriculture, National Agricultural Statistics Service. http://www.nass.usda.gov/
23. Tickell J (2000) From the fryer to the fuel tank: the complete guide to using vegetable oil as an alternative fuel, 3rd edn. Tickell Energy Consulting, Tallahassee, 162
24. Breitenbeck GA (2008) Chinese tallow trees a potential bioenergy crop for Louisiana. Louisiana Agr 51:10–12
25. Mata TM, Martins AA, Caetano NS (2010) Microalgae for biodiesel production and other applications: a review. Renew Sust Energy Rev 14:217–232
26. Griffiths MJ, Harrison STL (2009) Lipid productivity as a key characteristic for choosing algal species for biodiesel production. J Appl Phycol 21:493–507
27. Piskorz J, Scott DS, Radlein D (1988) Composition of oils obtained by fast pyrolysis of different woods. In: Soltes EJ, Milne TA (eds) Pyrolysis oils from biomass, vol 376, ACS symposium series. American Chemical Society, Washington, DC, pp 167–178
28. Emsley AM, Stevens GC (1994) Kinetics and mechanisms of the low-temperature degradation of cellulose. Cellulose 1:26–56
29. Klinke HB, Thomsen AB, Ahring BK (2004) Inhibition of ethanol-producing yeast and bacteria by degradation products produced during pre-treatment of biomass. Appl Microbiol Biotechnol 66:10–26
30. Wu X, McLaren J, Madl R, Wang D (2010) Biofuels from lignocellulosic biomass. In: Singh OV, Harvey SP (eds) Sustainable biotechnology: sources of renewable energy. Springer, New York, pp 19–41
31. Reed TB (1981) Biomass gasification: principles and technology. Noyes Data Corporation, Park Ridge
32. Woo HC, Park KY, Kim YG, Nam I-S, Chung JS, Lee JS (1991) Mixed alcohol synthesis from carbon monoxide and dihydrogen over potassium-promoted molybdenum carbide catalysts. Appl Catal 75:267–280
33. Xu M, Lunsford JH, Goodman DW, Bhattacharyya A (1997) Synthesis of dimethyl ether (DME) from methanol over solid-acid catalysts. Appl Catal A Gen 149:289–301

34. Semelsberger TA, Borup RL, Greene HL (2006) Dimethyl ether (DME) as an alternative fuel. J Power Source 156:497–511
35. Bridgwater AV, Meier D, Radlein D (1999) An overview of fast pyrolysis of biomass. Org Geochem 30:1479–1493
36. Czernik S, Bridgwater AV (2004) Overview of applications of biomass fast pyrolysis oil. Energy Fuels 18:590–598
37. Bozell JJ, Moens L, Elliott DC, Wang Y, Neuenscwander GG, Fitzpatrick SW, Bilski RJ, Jarnefeld JL (2000) Production of levulinic acid and use as a platform chemical for derived products. Resour Conserv Recycl 28:227–239
38. Balat M, Balat H (2010) Progress in biodiesel processing. Appl Energy 87:1815–1835
39. Chisti Y (2007) Biodiesel from microalgae. Biotechnol Adv 25:294–306
40. Rein PW (1995) A comparison of cane diffusion and milling. In: Proceedings of the South African sugar technologists' association, pp 196–200
41. Granda CB, Holtzapple MT (2006) Low-pressure sugar extraction with screw-press conveyors. Int Sugar J 108:555–568
42. Wheals AE, Basso LC, Alves DMG, Amorim HV (1999) Fuel ethanol after 25 years. Trends Biotechnol 17:482–487
43. Kwiatkowski JR, McAloon AJ, Taylor F, Johnston DB (2006) Modeling the process and costs of fuel ethanol production by the corn dry-grind process. Ind Crop Prod 23:288–296
44. Ramirez EC, Johnston DB, McAloon AJ, Yee W, Singh V (2008) Engineering process and cost model for a conventional corn wet milling facility. Ind Crops Prod 27:91–97
45. Manzer LE (2010) Recent developments in the conversion of biomass to renewable fuels and chemicals. Topics Catal 53:1193–1196
46. Sierra R, Smith A, Granda C, Holtzapple MT (2008) Producing fuels and chemicals from lignocellulosic biomass. Chem Eng Prog 104:S10–S18
47. Sun Y, Cheng J (2002) Hydrolysis of lignocellulosic materials for ethanol production: a review. Bioresour Technol 83:1–11
48. Zaldivar J, Nielsen J, Olsson L (2001) Fuel ethanol production from lignocellulose: a challenge for metabolic engineering and process integration. Appl Microbiol Biotechnol 56:17–34
49. Lynd LR, van Zyl WH, McBride JE, Laser M (2005) Consolidated bioprocessing of cellulosic biomass: an update. Curr Opin Biotechnol 16:577–583
50. Warnick TA, Methe BA, Leschine SB (2002) *Clostridium phytofermentans* sp. nov., a cellulolytic mesophile from forest soil. Int J Syst Evol Microbiol 52:1155–1160
51. Lee YY, Iyer P, Torget RW (1999) Dilute-acid hydrolysis of lignocellulosic biomass. Adv Biochem Eng Biotechnol 65:93–114
52. Lindsey TC (2010) Conversion of existing dry – mill ethanol operations to biorefineries. In: Blaschek HP, Ezeji TC, Scheffran J (eds) Biofuels from agricultural wastes and byproducts. Wiley-Blackwell, Oxford
53. Agler MT, Wrenn BA, Zinder SH, Angenent LT (2011) Waste to bioproduct conversion with undefined mixed cultures: the carboxylate platform. Trends Biotechnol 29:70–78
54. Chang HN, Kim N-J, Kang J, Jeong CM (2010) Biomass-derived volatile fatty acid platform for fuels and chemicals. Biotechnol Bioprocess Eng 15:1–10
55. Verser D, Eggeman T (2003) Process for producing ethanol. US Patent 6,509,180 B1
56. Pham V, Holtzapple M, El-Halwagi M (2010) Techno-economic analysis of biomass to fuel conversion via the MixAlco process. J Ind Microbiol Biotechnol 37:1157–1168
57. Granda CB, Holtzapple MT, Luce G, Searcy K, Mamrosh DL (2009) Carboxylate platform: the MixAlco process. Part 2: process economics. Appl Biochem Biotechnol 156:537–554
58. Datar RP, Shenkman RM, Cateni BG, Huhnke RL, Lewis RS (2004) Fermentation of biomass-generated producer gas to ethanol. Biotechnol Bioeng 86:587–594
59. Younesi H, Najafpour G, Mohamed AR (2005) Ethanol and acetate production from synthesis gas via fermentation processes using anaerobic bacterium, *Clostridium ljungdahlii*. Biochem Eng J 27:110–119
60. Vega JL, Prieto S, Elmore BB, Clausen EC, Gaddy JL (1989) The biological production of ethanol from synthesis gas. Appl Biochem Biotechnol 20(21):781–797
61. Santosh Y, Sreekrishnan TR, Kohli S, Rana V (2004) Enhancement of biogas production from solid substrates using different techniques – a review. Bioresour Technol 95:1–10
62. Oudejans JC, Van den Oosterkamp PF, Van Bekkum H (1982) Conversion of ethanol over zeolite H-ZSM-5 in the presence of water. Appl Catal 3:109–115
63. Holtzapple MT, Granda CB (2009) Carboxylate platform: the MixAlco process. Part 1: comparison of three biomass conversion platforms. Appl Biochem Biotechnol 156:525–536
64. Li Q, Du W, Liu D (2008) Perspectives of microbial oils for biodiesel production. Appl Microbiol Biotechnol 80:749–756
65. Rude MA, Schirmer A (2009) New microbial fuels: a biotech perspective. Curr Opin Microbiol 12:274–281
66. Hui L, Wan C, Hai-tao D, Xue-jiao C, Qi-fa Z, Zhao Yu-hua (2010) Direct microbial conversion of wheat straw into lipid by a cellulolytic fungus of *Aspergillus oryzae* A-4 in solid-state fermentation. Bioresour Technol 101:7556–7562
67. Manilla-Pérez E, Lange AB, Hetzler S, Steinbüchel A (2010) Occurrence, production, and export of lipophilic compounds by hydrocarbonoclastic marine bacteria and their potential use to produce bulk chemicals from hydrocarbons. Appl Microbiol Biotechnol 86:1693–1706

Books and Reviews

Bungay HR (1981) Energy, the biomass options. Wiley-Interscience, New York

Cheremisinoff NP, Cheremisinoff PN, Ellerbusch F (1980) Biomass: applications, technology, and production, vol 5, Energy, power, and environment. Marcel Dekker, New York

Klass DL (1981) Biomass as a nonfossil fuel source, vol 144, ACS symposium series. American Chemical Society, Washington, DC

Klass DL (1998) Biomass for renewable energy, fuels, and chemicals. Academic, San Diego

Moo-Young M, Blanch HW, Drew S, Wang DIC (1985) Comprehensive biotechnology, vol 3, The practice of biotechnology: current commodity products. Pergamon, New York

Saha BC, Woodward J (1997) Fuels and chemicals from biomass, vol 666, ACS symposium series. American Chemical Society, Washington, DC

Sarkanen KV, Tillman DA (1979) Progress in biomass conversion, vol 1. Academic, New York

Smil V (1983) Biomass energies: resources, links, constraints. Plenum, New York

Stafford DA, Hawkes DL, Horton R (1980) Methane production from waste organic matter. CRC Press, Boca Raton

Waldron K (2010) Bioalcohol production: biochemical conversion of lignocellulosic biomass, vol 3, Woodhead publishing series in energy. CRC Press, Boca Raton

Zaborsky OR, McClure TA, Lipinsky ES (1981) Handbook of biosolar resources, vol II, Resource materials. CRC Press, Boca Raton

Vehicle Detection, Tightly Coupled LIDAR and Computer Vision Integration for

LILI HUANG, MATTHEW BARTH
Department of Electrical Engineering, University of California, Riverside, CA, USA

Article Outline

Glossary

Calibration Comparison and alignment between two or more measurements or coordinates; coordinate systems are defined for different devices and the relationships between systems are established through calibration.

Computer vision Technology using computers to extract information from an image, a series of images, or video sequences to aid sensing applications.

Intelligent transportation system (ITS) System of technologies including information processing, control, communications, and system management applied to vehicles and infrastructure to improve transportation. ITS aims to improve safety, transportation efficiency, and reduce environmental impacts.

Laser range finder (LIDAR) A device that uses laser beams to determine the distance to an object. The most common technique used for distance measurement works on the time-of-flight principle.

Vehicle detection Detect, count, and classify vehicles using video camera, loop sensors, or wireless sensors. Vehicle detection systems are typically "nonintrusive" to traffic.

Vehicle tracking A combination of techniques to track a vehicle's location, record position data, and deliver data to an owner or a third party. Devices used in vehicle tracking include GPS, and possibly a video camera and other electronic devices.

Definition of the Subject

The demand on today's transportation systems is growing quite rapidly, with an estimated 30% travel demand increase predicted over the next decade [1]. Transportation infrastructure growth is not keeping pace with this traffic demand, therefore researchers and practitioners have turned to intelligent transportation systems (ITS) to improve overall traffic efficiency, thereby maximizing the current infrastructure's capacity.

ITS uses sensors, communication, and traffic control technologies to better handle the increased demands in traffic, to enhance public safety, and to reduce environmental impacts of transportation [2]. One key ITS function that is important for many applications is the ability to gather traffic information using vehicle detection and surveillance techniques. Vehicle detection technology is widely used to provide information for vehicle counting, classification, and traffic characterization. Further, when it is implemented on a moving vehicle, it can even be utilized for vehicle navigation purposes [3]. The generalized vehicle detection problem from a moving vehicle is challenging, which aims to determine the surrounding vehicle's (relative) position, speed, and trajectory. A driver is able to determine a short-term and long-term trajectory based on the vehicle's current position and information about the surrounding vehicles.

In the case where vehicle detection is carried out on a moving vehicle, the surrounding vehicles' information is commonly collected by various sensing systems. These sensing systems typically consist a suite of sensors that can provide real-time measurements, and play an important role in the development of driver assistant systems (DAS).

One of the most common sensing techniques used is computer vision. Computer vision sensors provide a large amount of information on the surrounding environment. However, the computer vision sensors often suffer from intensity variations, narrow fields of

M. Ehsani et al. (eds.), *Transportation Technologies for Sustainability*, DOI 10.1007/978-1-4614-5844-9,

Originally published in
Robert A. Meyers (ed.) Encyclopedia of Sustainability Science and Technology, © 2012, DOI 10.1007/978-1-4419-0851-3

view, and low-accuracy depth information [4]. In contrast, a laser ranging method (i.e., LIDAR) measures distance and relative angle from the sensor to the target by calculating time of flight of the laser. Its measurements depend on the size and reflectivity of the target, so the probability of detection decreases with distance [5]. Since their characteristics of computer vision and LIDAR complement each other, it is useful to integrate both computer vision and LIDAR for detecting different objects around the vehicle's environment.

A tightly coupled LIDAR and computer vision system is proposed in this entry to solve the vehicle detection problem. This sensing system is mounted on a test vehicle, as is shown in Fig. 1. A pair of LIDAR sensors is mounted on the front bumper of the vehicle, and a camera is mounted behind the front windshield.

Since sensor fusion systems are commonly used to integrate sensory data from disparate sources, the output will be more accurate and complete in comparison to the output of a single sensor. In order to effectively extract and integrate 3D information from both computer vision and LIDAR systems, the relative position and orientation between these two sensor modalities should be obtained. A sensor calibration process is used to identify the parameters that describe the relative geometric transformation between sensors [6, 7], which is a key step in the sensor fusion process. However, current calibration methods work only for visible beam LIDAR, 3D LIDAR, and 2D LIDAR [8–12]. To date, there does not exist any convenient calibration methods for multi-planar "invisible-beam" LIDAR and computer vision systems.

A novel calibration approach of a camera with a multi-planar LIDAR system is proposed in this entry, where the laser beams are invisible to the camera. The camera and LIDAR are required to observe a planar pattern at different positions and orientations. Geometric constraints of the "views" from the LIDAR and camera images are resolved as the coordinate transformation coefficients. The proposed approach consists of two stages: solving a closed-form equation, followed by applying a nonlinear algorithm based on a maximum likelihood criterion. Compared with the classical methods which use "beam-visible" cameras or 3D LIDAR systems, this approach is easy to implement at low cost.

The combination of LIDAR and camera is employed in vehicle detection since the geometric transformation between two sensors is known from calibration. In the sensor fusion system, LIDAR sensor estimates possible vehicle positions. This information is transformed into the image coordinates. Different regions of interest (ROIs) in the imagery are defined based on the LIDAR object hypotheses. An Adaboost object classifier is then utilized to classify the vehicle in ROIs. A classifier error correction approach chooses an optimal position of the detected vehicle. Finally, the vehicle's position and dimensions

Vehicle Detection, Tightly Coupled LIDAR and Computer Vision Integration for. Figure 1
The mobile sensing platform. This probe vehicle carries one camera and two IBEO ALASCA XT LIDAR sensors

are derived from both the LIDAR and image data. This sensor fusion system can be used in ITS applications such as traffic surveillance and roadway navigation tasks.

This entry is organized as follows: section "Introduction and Background" reviews background and related work, including the calibration methods for LIDAR and camera, and sensor fusion–based vehicle detection algorithms. Section "A Novel Multi-Planar LIDAR and Computer Vision Calibration Procedure Using 2D Patterns" focuses on the calibration of LIDAR and camera system. The coordinate systems of the LIDAR and camera sensors are introduced, followed by the mathematical derivation of geometric relations between the two sensors. The equations are then solved in two stages: a closed-form solution, followed by applying a nonlinear algorithm based on a maximum likelihood criterion. Section "Tightly Coupled LIDAR and Computer Vision Integrated System for Vehicle Detection" describes the sensor fusion–based vehicle detection system. Both hardware and data processing software of the sensor fusion system are introduced in this section. Finally, future work is discussed in section "Conclusions and Future Work".

Introduction and Background

During the past decade, a variety of research has been carried out in the traffic surveillance area, where numerous techniques have been developed to obtain parameters such as vehicle counts, location, speed, trajectories and classification data, for both in-vehicle navigation and freeway traffic surveillance applications [13].

As one of the most popular traffic surveillance techniques, computer vision-based approaches are one of the most widely used and promising techniques. LIDAR is another attractive technology due to its high accuracy in ranging, wide-area field of view, and low data processing requirements [5]. The other sensors used in vehicle detection include radar and embedded loop sensors. A brief comparison of the sensor technologies and their advantages as well as disadvantages is given in Table 1.

Sensor fusion systems in the vehicle detection application aim to gather information from the far-field as well as near-field sensors, and combine them in a meaningful way [15]. The output of the sensor fusion system should be the states of objects around the test vehicle.

In this section, a few of the most popular LIDAR sensors that are available commercially today are introduced. This is followed by a discussion of current LIDAR and computer vision calibration methods. The calibration methods include the visible LIDAR beam–based calibration, 3D LIDAR and the 2D single planar LIDAR calibration. Sensor fusion techniques for vehicle detection and tracking systems are also discussed here.

Laser Range Finder (LIDAR)

The vehicle detection solution aims to estimate the states of surrounding vehicles. Vehicle state includes position, orientation, speed, and acceleration. State estimation addresses the problems of estimating quantities from sensors that are not directly observable [16].

LIDAR sensors are commonly utilized in vehicle navigation for detecting surrounding vehicles, infrastructure, and pedestrians. It can also be used in vehicle localization, either as the only sensor or in some combination with GPS and INS.

One of the most popular LIDAR sensors is the SICK LMS 2xx series [17]. A SICK LIDAR operates at distance up to 80 m with an angular resolution of 0.5° and a measurement accuracy of typically 5 cm. The distance between the sensor and an object is calculated by measuring the time interval between an emitted laser pulse and a reception of the reflected pulse. Amplitude of the received signal is used to determine reflectivity of the object surface. The SICK LIDAR is able to detect dark objects at long ranges. Moreover, compared to the CCD cameras and RADAR systems, the view angle of SICK LIDAR is larger, e.g., 180°. Figure 2a illustrates the SICK LMS200 LIDAR.

The HOKUYO UXM-30LN LIDAR is another single planar range sensor for intelligent robots and vehicles [18]. Its detection range is up to 60 m, and the horizontal field of view is 190°. The distance accuracy is 30 mm when the range is less than 10 m, and 50 mm when the range is between 10 and 30 m. The angular resolution is 0.25°. The device is shown in Fig. 2b.

Vehicle Detection, Tightly Coupled LIDAR and Computer Vision Integration for. Table 1 Performance comparison of existing sensor technologies used in ITS [14]

Sensor technology	Advantage	Disadvantage
LIDAR	Detect distance and angle with high accuracy	High cost
	Low data processing requirement	Limited detection range
	Operational in fog and rain	Difficult to classify the object
Radar	Direct measurement of speed or distance	Relatively low precision
	Compact size	Limited field of view
	Low data processing requirement	May have identification problem in multilane applications
		Medium cost
Video camera	Provide real-time image of traffic	High requirement for data processing and storage
	Low cost	
	Multiple lanes observed	Different algorithms required for day- and nighttime
	No traffic interruption for installation and repair	
	Large field of view	Susceptible to atmospheric obscurants and weather change
Infrared camera	Day and night operation	High requirement for data processing
	Operational in fog	Susceptible to weather change
Inductive loop detector	Low cost per unit	Installation and maintenance require traffic disruption
	Large experience base	Easily damaged

Vehicle Detection, Tightly Coupled LIDAR and Computer Vision Integration for. Figure 2
A variety of LIDAR sensors: (**a**) SICK LMS LIDAR, (**b**) HOKUYO UXM-30LN LIDAR, (**c**) IBEO ALASCA XT LIDAR, and (**d**) Velodyne HDL-64E LIDAR

As another example, the ALASCA XT laser scanner made by IBEO is a multi-planar LIDAR, which splits the laser beam into four vertical layers. The aperture angle is 3.2°. The distance range is up to 200 m, and the horizontal field of view is 240° [19]. Figure 2c shows the IBEO sensor.

The Velodyne HDL-64E LIDAR is a 3D sensor which is specifically designed for autonomous vehicle navigation [20]. With 360° horizontal by 25° vertical field of view, 0.09° angular resolution, and 10 Hz refresh rate, Velodyne provides surrounding 3D traffic information with high accuracy (<5 cm resolution) and efficiency. The detection range is 100 m for cars, and the latency is less than 0.05 ms. Figure 2d illustrates the Velodyne sensor.

LIDAR sensors were initially used by automatic guided vehicles in indoor environments. More recently, the performance of these ranging sensors has been improved, so that they now can be used in outdoor environments on vehicles. A primary application example is the DARPA Urban Challenge in 2007, in which autonomous vehicles were capable of driving in traffic and performing complex maneuvers such as acceleration and deceleration, lane change, and parking [13]. IBEO and SICK LIDARs were used in many of the finalists for object detection and localization. The Velodyne sensor was used by the five out of six of the finishing teams.

LIDAR and Computer Vision Calibration

Sensor fusion systems are commonly used to combine the sensory data from disparate sources, so that the result will be more accurate and complete in comparison to the output of one sensor. As an example, the winner of the 2007 DARPA Urban Grand Challenge performed sensor fusion between a GPS receiver, long- and short-range LIDAR sensors, and stereo cameras [21].

In order to effectively extract and integrate 3D information from both computer vision and LIDAR systems, the relative position and orientation between these two sensor modalities can be obtained. The relative geometric transformation can be solved through a calibration process [6, 7]. Several approaches have been defined and utilized for LIDAR and computer vision calibration. These techniques can be roughly classified into three categories.

Visible Beam Calibration Visible beam calibration is performed by using cameras to observe the LIDAR beams or reflection points. The calibration system usually consists of an active LIDAR and some infrared or near-infrared cameras. The LIDAR system typically projects stripes with a known frequency, while these stripes are visible to the camera [8–10]. For example, the LIDAR beams used in [9] are captured by a 955fps high-speed camera. However, the image of the high-speed camera is not suitable for monitoring. Color image of the LIDAR beams is generated by letting the vision output go through a beam splitter.

This approach requires a high-cost infrared camera, which should be sensitive to the spectral emission band of the LIDAR. Therefore, this method is not suitable for the low-cost sensor fusion systems.

Three-Dimensional (3D) LIDAR-Based Calibration The 3D LIDAR-based calibration method calibrates the computer vision system with a 3D LIDAR system. Various features are captured by both the camera and the LIDAR. These features are usually in the form of planes, corner, or edges of specific calibration object. An elaborate setup is required. Moreover, dense LIDAR beams in both the vertical and horizontal directions are necessary for the calibration.

The 3D calibration algorithm presented in [11] uses checkerboard in calibration, which is commonly used for camera calibration. Coefficients of the checkerboard plane are first calculated by LIDAR, and then the coefficients are computed by camera in computer vision coordinates. A two-stage optimization procedure is implemented to minimize the distance between the calculated results and the measurement output.

When the features are edges or corners, accuracy of the calibration method depends on the accuracy by which features are localized [22]. When the features are planes, the LIDAR beams must be sufficiently dense [11]. Therefore, these methods cannot easily be applied to single planar or sparse multi-planar LIDAR systems.

Two-Dimensional (2D) Planar-Based Calibration This approach works for the calibration of camera and 2D LIDAR integration system. The calibration system proposed in [23] consists of a monochrome CCD camera and a LIDAR. The camera and the

LIDAR have been pre-calibrated so that their coordinates are parallel to each other. A "V"-shaped pattern is designed to obtain the translation between these two sensors. The calibration procedure is implemented in two steps: the LIDAR detects the "V" shape and finds the vertex, and camera detects the intersection line which cuts the pattern into two parts.

Another calibration approach is proposed in [12] using a checkerboard for calibration. This method is based on observing a plane of an object and solving distance constraints from the camera and LIDAR systems. This approach works for a single planar LIDAR only, e.g., the SICK LMS 2xx series LIDAR.

To date, there does not exist any convenient calibration methods for multi-planar "invisible-beam" LIDAR and computer vision systems. Section "A Novel Multi-Planar LIDAR and Computer Vision Calibration Procedure Using 2D Patterns" proposes a method to handle this case, which is the first calibration method for this system as to the author's best knowledge.

Sensor Fusion–Based Vehicle Detection and Tracking

Computer vision is generally used on mobile platform–based object detection and tracking systems, either separately or along with LIDAR sensors [24]. Most of the computer vision techniques utilize a simple segmentation method such as background subtraction or temporal difference to detect objects [25]. However, these approaches suffer with the fast background changes due to camera motion. A trainable object detection method is proposed in [26] based on a wavelet template, which defines the shape of an object in terms of a subset of the wavelet coefficients of the image. However, the application of vision sensors in vehicle navigation is far from sufficient: clustering, illumination, occlusion, among many other factors, affect the overall performance. Fusion of camera and active sensors such as LIDAR or RADAR, is being investigated in the context of on-board vehicle detection and classification.

A LIDAR and a monocular camera–based detection and classification system is proposed in [27]. Detection and tracking are implemented in the LIDAR space, and the object classification work both in LIDAR space (Gaussian Mixture Model classifier) and in computer vision system (Adaboost classifier). A Bayesian decision rule is proposed to combine the results from both classifiers, and thus a more reliable classification is achieved.

Another integration structure is proposed in [28], in which a LIDAR is integrated with a far-infrared camera and an ego motion sensor. LIDAR-based shape extraction is employed to select region of interests (ROIs). This system combines a straightforward methodology with a backward loop one. Kalman filtering is used as the data fusion algorithm.

A similar technique is presented in [29], which makes use of RADAR, velocity, and steering sensors to generate position hypotheses. Examination of the hypotheses is implemented by a computer vision sensor. Classification is performed using a shape model for either the monocular camera vision or the infrared spectrum images.

A Novel Multi-planar LIDAR and Computer Vision Calibration Procedure Using 2D Patterns

In this section, a novel calibration approach is proposed for a LIDAR and computer vision sensor fusion system. This system consists of a camera with a multi-planar LIDAR, where the laser beams are invisible to the camera. This calibration method also works for computer vision and 3D LIDAR systems.

Although several calibration methods have been developed to obtain the geometric relationship between two sensors, only a few of them have provided a complete sensitivity analysis of the calibration procedure (see section "LIDAR and Computer Vision Calibration"). As part of the calibration method proposed in this section, the effects of LIDAR noise level as well as total number of poses on calibration accuracy are also discussed.

This section is organized as follows: section "Sensor Alignment" gives the setup using planar planes and defines the calibration constraint. Section "Calibration Solutions" describes in detail how to solve this constraint in two steps. Both a closed-form solution and a nonlinear minimization solution based on maximum likelihood criterion are introduced. Experimental results with different poses are provided in section "Experimental Results". Finally, a brief summary is given in section "Summary".

Sensor Alignment

The setup for a multi-planar LIDAR and camera calibration is described here.

Sensor Configuration In the calibration system, an instrumented vehicle is equipped with two IBEO ALASCA XT LIDAR sensors which are mounted on the front bumper. The LIDAR sensor scans with four separate planes. The distance range is up to 200 m, the horizontal field of view angle of a single LIDAR is 240°, and the total vertical field of view for the four planes is 3.2°. A camera is mounted on the vehicle behind the front windshield, as is shown in Fig. 1.

In order to use the measurements from different kinds of sensors at various positions on the vehicle, the measurements should be transformed from their own coordinate into some common coordinate system. This section focuses on obtaining the spatial relationship between video and LIDAR sensors. The geometric sensor model is shown in Fig. 3.

Vision, LIDAR, and World Coordinate Systems There are several coordinate systems in the overall system to be considered: the camera coordinates, the LIDAR coordinates, and the world coordinate systems.

A camera can be represented by the standard pinhole model. One 3D point in the camera coordinate denoted by $\mathbf{P}_c = [\mathbf{X}_c \quad \mathbf{Y}_c \quad \mathbf{Z}_c]^T$ is projected to a pixel $\mathbf{p} = [u \quad v]^T$ in the image coordinate. The pinhole model is given as [30]:

$$s\mathbf{p} \sim \mathbf{A}[\mathbf{R} \quad \mathbf{t}]\mathbf{P}_c \quad \text{with} \quad \mathbf{A} = \begin{bmatrix} \alpha & \gamma & u_0 \\ 0 & \beta & v_0 \\ 0 & 0 & 1 \end{bmatrix} \tag{1}$$

where s is an arbitrary scale factor. $\mathbf{A}$ is the camera intrinsic matrix defined by coordinates of the principal point $(u_0 \quad v_0)$, scale factors α and β in image u and v axes, and skewness of the two image axes γ. $(\mathbf{R}, \quad \mathbf{t})$ are called extrinsic parameters. The 3×3 orthonormal rotation matrix $\mathbf{R}$ represents the orientation of world coordinates to the camera coordinate system. The translation matrix $\mathbf{t}$ is a three-vector representing origin of world coordinates in the camera's frame of reference. In the real world, lens of the camera may also have image distortion coefficients, which include radial and tangential distortions and are usually stored in a five-vector [31]. In this entry, the lens is assumed to have no significant distortion, or the distortion has already been eliminated.

The LIDAR sensor provides distance and direction of each scan point in LIDAR coordinates. Distances and directions can be converted into a 3D point denoted by $\mathbf{P}_l = [X_l \quad Y_l \quad Z_l]^T$ [19]. The origin of LIDAR coordinates is the equipment itself. X, Y, and Z axes are

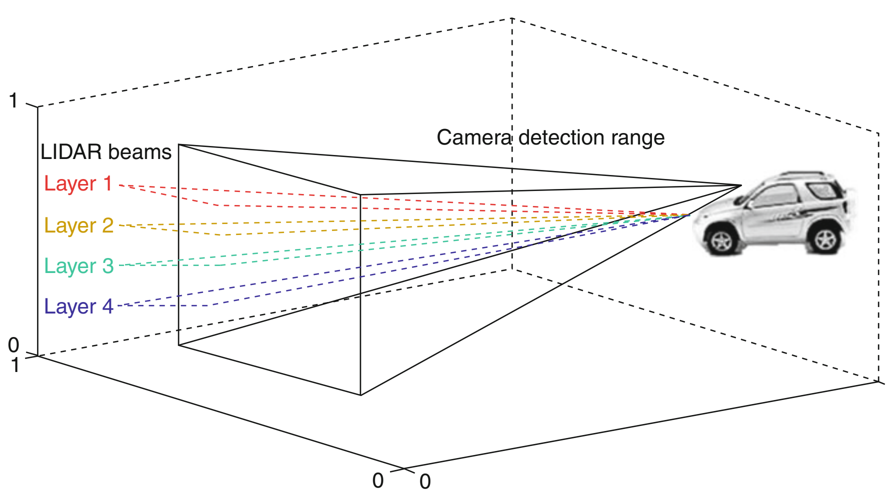

Vehicle Detection, Tightly Coupled LIDAR and Computer Vision Integration for. Figure 3
Geometric model with the camera and the LIDAR

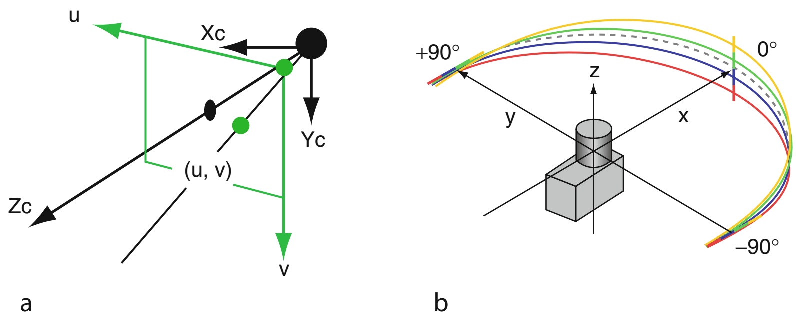

Vehicle Detection, Tightly Coupled LIDAR and Computer Vision Integration for. Figure 4
Two coordinate systems. (**a**) The camera coordinates and screen coordinate systems, and (**b**) the LIDAR coordinate system

defined as forward, leftward, and upward from the equipment, respectively. The camera and LIDAR reference systems are shown in Fig. 4.

In addition to the camera and LIDAR reference systems, another coordinate system is used in the calibration procedure: the world frame of reference. In the calibration process, a checkerboard is placed in front of the sensors. The first grid on the upper-left corner of this board is defined to be the origin of the world coordinates [31].

Suppose a fixed point $\mathbf{P}$ is denoted as $\mathbf{P}_c = [X_c \quad Y_c \quad Z_c]^T$ in the camera coordinates, and $\mathbf{P}_l = [X_l \quad Y_l \quad Z_l]^T$ in the LIDAR coordinates. The transformation from LIDAR coordinate to camera coordinate is given as:

$$\mathbf{P}_c = \mathbf{R}_l^c \mathbf{P}_l + \mathbf{t}_l^c \tag{2}$$

where $\left(\mathbf{R}_l^c, \quad \mathbf{t}_l^c\right)$ are the rotation and translation parameters which relate LIDAR coordinate system to the camera coordinate system.

The purpose of this calibration method is to solve Eq. 2 and obtain coefficients $\left(\mathbf{R}_l^c, \quad \mathbf{t}_l^c\right)$, so that any given point in the LIDAR reference system can be transformed to the camera coordinates.

Basic Geometric Interpretation A checkerboard visible to both sensors is used for calibration. In the following sections, the planar surface defined by the checkerboard is called the *checkerboard plane*. Without loss of generality, the checkerboard plane is assumed to be on $Z = 0$ in the world coordinates. Let $\mathbf{r}_3$ denotes the i-th column of the rotation matrix $\mathbf{R}$. $\mathbf{r}_3$ is also the surface normal vector of the calibration plane in camera coordinate systems [31].

Note the origin of world coordinate is the upper-left corner of the checkerboard, and the origin of camera coordinate is the camera itself. The translation vector $\mathbf{t}$ represents relative position of the checkerboard's upper-left corner in the camera's reference system. Since both $\mathbf{t}$ and $\mathbf{P}_c$ are points on the checkerboard plane denoted in camera coordinates, a vector $\vec{v}$ is defined as $\vec{v} = \mathbf{P}_c - \mathbf{t}$. Note that $\vec{v}$ is a vector on the checkerboard plane, and $\mathbf{r}_3$ is orthogonal to this plane, so:

$$\mathbf{r}_3 \cdot \vec{v} = 0 \tag{3}$$

where $\cdot$ denotes the inner product. The geometric interpretation for Eq. 3 is illustrated in Fig. 5.

By substituting Eq. 2 into Eq. 3, Eq. 3 becomes:

$$\mathbf{r}_3^T \left(\mathbf{R}_l^c \mathbf{P}_l + \mathbf{t}_l^c - \mathbf{t}\right) = 0 \tag{4}$$

Since point $\mathbf{P}_l$ in LIDAR coordinates is $[X_l \quad Y_l \quad Z_l]^T$, from Eq. 4:

$$\mathbf{r}_3^T \left[\mathbf{R}_l^c \quad \mathbf{t}_l^c - \mathbf{t}\right] \begin{bmatrix} X_l \\ Y_l \\ Z_l \\ 1 \end{bmatrix} = 0 \tag{5}$$

For each LIDAR point on the checkerboard plane, Eq. 5 explains the geometric relationships and constraints on $\left(\mathbf{R}_l^c, \quad \mathbf{t}_l^c\right)$. This is the basic constraints for the calibration from the LIDAR to the vision coordinate system.

Calibration Solutions

This subsection provides the method to efficiently obtain calibration coefficients $\left(\mathbf{R}_l^c, \quad \mathbf{t}_l^c\right)$. An analytical

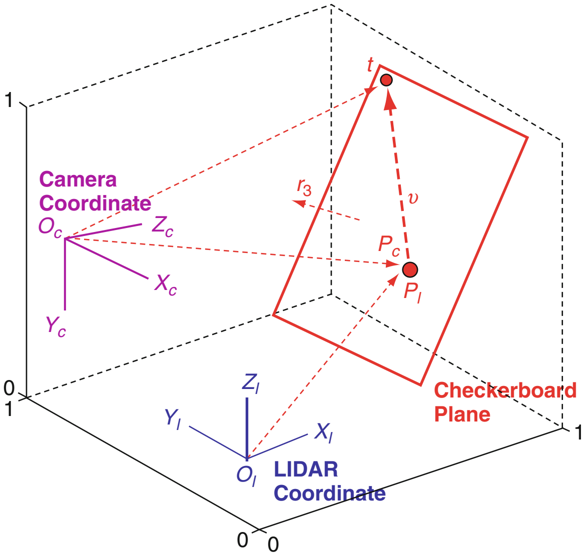

Vehicle Detection, Tightly Coupled LIDAR and Computer Vision Integration for. Figure 5
Geometric interpretation of the camera coordinates, the LIDAR coordinates, and checkerboard

solution is proposed, followed by a nonlinear optimization technique based on the maximum likelihood criterion.

Closed-Form Solution Initially, the camera's intrinsic parameters are calibrated using a standard Camera Calibration Toolbox [31]. For each pose of the checkerboard, there is one set of camera extrinsic parameters $(\mathbf{R}, \ \mathbf{t})$. Each $(\mathbf{R}, \ \mathbf{t})$ is determined also using the toolbox, after which $\mathbf{r}_3$ and $\mathbf{t}$ in Eq. 5 are obtained.

For simplicity, it is defined that $\mathbf{r}_3 = [r_{31} \quad r_{32} \quad r_{33}]^T$, $\Delta_i = \mathbf{t}_l^c - \mathbf{t} = [\Delta_x \quad \Delta_y \quad \Delta_z]^T$, and m_{ij} is the element on the i-th row, j-th column in matrix $\mathbf{R}_l^c$. Suppose for one pose of the checkerboard, there are p LIDAR points on the checkerboard plane, denoted as $\mathbf{P}_{l,1} = [X_{l,1} \quad Y_{l,1} \quad Z_{l,1}]^T$, $\mathbf{P}_{l,2} = [X_{l,2} \quad Y_{l,2} \quad Z_{l,2}]^T, \ldots, \mathbf{P}_{l,p} = [X_{l,p} \quad Y_{l,p} \quad Z_{l,p}]^T$. The geometric interpretation becomes a $\mathbf{Ax} = \mathbf{0}$ problem, where $\mathbf{A}$ is a $N \times 12$ matrix, and $\mathbf{x}$ is a 12-vector to be solved. $\mathbf{A}$ and $\mathbf{x}$ are given in Eq. 6.

$$\begin{aligned} \mathbf{A} &= [r_{31}\mathbf{P}_{l,p} \, r_{31}\mathbf{E} \; r_{32}\mathbf{P}_{l,p} \; r_{32}\mathbf{E} \; r_{33}\mathbf{E}_{l,p} \, r_{33}\mathbf{E}] \\ \mathbf{x} &= [\mathbf{m}_1 \, \Delta_x \, \mathbf{m}_2 \Delta_y \, \mathbf{m}_3 \, \Delta_z]^T \end{aligned} \tag{6}$$

where $\mathbf{P}_{l,p} = \left[\mathbf{P}_{l,1} \;\; \mathbf{P}_{l,2} \;\; \ldots \;\; \mathbf{P}_{l,p}\right]^T$, $[\mathbf{E} = [1 \;\; 1 \;\; \cdots \;\; 1]^T$ is a $(p \times 1)$ vector, and $\mathbf{m}_i = [m_{i1} \;\; m_{i2} \;\; m_{i3}]$, $i = 1, 2, 3$.

By getting the LIDAR points $\mathbf{P}_{l,1}, \mathbf{P}_{l,2}, \ldots, \mathbf{P}_{l,p}$, $\mathbf{x}$ is estimated using the least square method. In order to avoid the solution $\mathbf{x} = \mathbf{0}$, normalization constraints are proposed. Faugeras and Toscani suggested the constraint $m_{31}^2 + m_{32}^2 + m_{33}^2 = 1$, which is singularity free [32]. This restriction is proposed from the coincidence that $[m_{31} \quad m_{32} \quad m_{33}]$ is the third row of the rotation matrix $\mathbf{R}_l^c$. Thus solving the equation $\mathbf{Ax} = \mathbf{0}$ is transformed into minimizing the norm of $\mathbf{Ax}$, i.e., minimizing $|\mathbf{Ax}|$ with the restriction $m_{31}^2 + m_{32}^2 + m_{33}^2 = 1$.

$|\mathbf{Ax}|$ can be minimized using a Lagrange method [33]. Let $\mathbf{m}_3 = [m_{31} \; m_{32} \; m_{33}]$ and $\mathbf{m}_9$ be a vector containing the remaining nine elements in $\mathbf{x}$. The Lagrange equation is written as:

$$L = \mathbf{A}_9 \cdot \mathbf{m}_9 + \mathbf{A}_3 \cdot \mathbf{m}_3 + \lambda\left(\mathbf{m}_3^T \mathbf{m}_3 - 1\right) \tag{7}$$

where $\mathbf{A}_3$ contains the 9th to 11th columns of $\mathbf{A}$, and $\mathbf{A}_9$ contains the remaining nine columns corresponding to $\mathbf{m}_9$.

The closed-form linear solution is:

$$\begin{aligned} \lambda \mathbf{m}_3 &= \left(\mathbf{A}_3^T \mathbf{A}_3 - \mathbf{A}_3^T \mathbf{A}_9 \left(\mathbf{A}_9^T \mathbf{A}_9\right)^{-1} \mathbf{A}_9^T \mathbf{A}_3\right) \mathbf{m}_3 \\ \mathbf{m}_9 &= -\left(\mathbf{A}_9^T \mathbf{A}_9\right)^{-1} \mathbf{A}_9^T \mathbf{A}_3 \mathbf{m}_3 \end{aligned} \tag{8}$$

It is well known that $\mathbf{m}_3$ is the eigenvector of the symmetric positive definite matrix $\mathbf{A}_3^T \mathbf{A}_3 - \mathbf{A}_3^T \mathbf{A}_9 \left(\mathbf{A}_9^T \mathbf{A}_9\right)^{-1} \mathbf{A}_9^T \mathbf{A}_3$ associated with the smallest eigenvalue. $\mathbf{m}_9$ is obtained after $\mathbf{m}_3$. Once $\mathbf{m}_3$ and $\mathbf{m}_9$ are known, the rotation and translation matrix $\left(\mathbf{R}_l^c, \mathbf{t}_l^c\right)$ is available.

Because of data noise, the rotation matrix $\mathbf{R}_l^c$ may not in general satisfy $\left(\mathbf{R}_l^c\right)^T \mathbf{R}_l^c = \mathbf{I}$. One solution is to obtain $\hat{\mathbf{R}}_l^c$, which is the best approximation of given $\mathbf{R}_l^c$. This $\hat{\mathbf{R}}_l^c$ has the smallest Frobenius norm of the difference $\hat{\mathbf{R}}_l^c - \mathbf{R}_l^c$, subject to $(\hat{R}_l^c)^T \hat{\mathbf{R}}_l^c = \mathbf{I}$ [30].

Maximum Likelihood Estimation The closed-form solution is obtained by minimizing an algebraic distance $|\mathbf{Ax}|$, which is not physically meaningful. In this subsection, the problem is refined through maximum likelihood function using multi-pose checkerboard planes, which is more meaningful.

In the proposed camera calibration approach, differences of image points and the corresponding projection of the ground truth point in an image are minimized [30]. This method is also valid for visible-beam LIDAR calibration [12]. In the test, the Euclidean distances from camera to the checkerboard are checked. Note that Eq. 4 can be written as:

$$\mathbf{r}_3^T\left(\mathbf{R}_l^c\mathbf{P}_l+\mathbf{t}_l^c\right)=\mathbf{r}_3^T\mathbf{t} \tag{9}$$

where both $\mathbf{R}_l^c\mathbf{P}_l+\mathbf{t}_l^c$ and $\mathbf{t}$ are points on the calibration plane surface, and $\mathbf{r}_3$ is the normal vector to this surface. Therefore, both the left and right sides of Eq. 9 are the distance between the checkerboard plane and the origin of the camera reference system.

Suppose there are totally n poses of the calibration plane. For the i-th pose, there is a set of $(\mathbf{r}_3, \mathbf{t})$ denoted as $\left(\mathbf{r}_3^i, \mathbf{t}^i\right)$. LIDAR points are assumed to be corrupted by Gaussian distributed noise. The maximum likelihood function is defined by minimizing sum of the difference between $\mathbf{r}_3^T\left(\mathbf{R}_l^c\mathbf{P}_l+\mathbf{t}_l^c\right)$ and $\mathbf{r}_3^T\mathbf{t}$ for all the LIDAR points. Suppose for the i-th plane, there are p_i LIDAR points. The solution satisfies:

$$\arg\min_{\mathbf{R}_l^c,\mathbf{t}_l^c}\sum_{i=1}^{n}\frac{1}{p_i}\sum_{j=1}^{p_i}\left(\left(\mathbf{r}_3^i\right)^T\left(\mathbf{R}_l^c\mathbf{P}_{l,j}^i+\mathbf{t}_l^c\right)-\left(\mathbf{r}_3^i\right)^T\mathbf{t}^i\right)^2 \tag{10}$$

where $\mathbf{R}_l^{c,i}\mathbf{P}_{l,j}^i+\mathbf{t}_l^{c,i}$ is the coordinate of $\mathbf{P}_{l,j}^i$ in the camera reference system, according to Eq. 2.

By using Rodriguez formula [32], the rotation matrix $\mathbf{R}_l^c$ is transformed into a vector, which is parallel to the rotation axis and whose magnitude is equal to the rotation angle. Thus $\left(\mathbf{R}_l^c, \mathbf{t}_l^c\right)$ forms a vector. Equation 10 is solved using the Levenberg–Marquardt algorithm (LMA) [34, 35], which provides numerical solutions to the problem of minimizing nonlinear functions. LMA requires an initial guess for the parameters to be estimated. In this algorithm, $\left(\mathbf{R}_l^c, \mathbf{t}_l^c\right)$ in the closed form is used as this initial state. For each pose, a set of $\left(\mathbf{R}_l^c, \mathbf{t}_l^c\right)$ is obtained. The weighted average is used as an initial guess, where the scalar weight is normalized as a relative contribution of each checkerboard pose. Then LMA gives a robust solution even if the initial state starts far off the final solution.

Summary of Calibration Procedure The calibration procedure proposed in this approach can be summarized as:

1. Place the checkerboard in view of the camera and LIDAR systems. Make sure that the plane is within the detection zone of both sensors. The different poses of checkerboard cannot be parallel to each other, otherwise the parallel poses do not provide enough constraints on $\mathbf{R}_l^c$.
2. Take a few measurements (images) of the checkerboard under different orientations. For each orientation, read the LIDAR points on this plane from the output.
3. Estimate the coefficients using the closed-form solution given in section "Closed-Form Solution".
4. Refine all the coefficients using the maximum likelihood estimation in section "Maximum Likelihood Estimation".

Experimental Results

The proposed vision-LIDAR calibration algorithm has been tested on both a computer simulation platform and with real-world data.

Computer Simulations The camera is assumed to have been calibrated. It is simulated to have the following properties: $\alpha = 1,200$, $\beta = 1,000$, and the skewness coefficient $\gamma = 0$. The principal point is $(320, 240)$, and the image resolution is 640×480. The calibration checkerboard consists of 10×10 grids. The size of each square grid is 5cm $\times$ 5cm. The position and orientation of the LIDAR relative to the camera have also been defined. The LIDAR's position in camera coordinates is $\mathbf{t}_l^c = [10 \quad 150 \quad 100]^T$ centimeters, and the rotation matrix $\mathbf{R}_l^c$ is parameterized by a three-vector rotation vector $[-85^\circ \quad 10^\circ \quad -80^\circ]^T$.

The LIDAR points are calculated based on the location of the camera, and relative position as well as orientation of the checkerboard. Gaussian noise is added to the points.

Performance with respect to Gaussian Noise Level A checkerboard plane is placed in front of the camera and the LIDAR. Three poses are used here. All of them have $\mathbf{t} = [-20 \quad -20 \quad -550]^T$. Three rotation matrices are defined by the rotation vectors as

$\mathbf{r}_1 = [170^{\circ} \quad -5^{\circ} \quad 85^{\circ}]^T$, $\mathbf{r}_2 = [170^{\circ} \quad 15^{\circ} \quad 85^{\circ}]^T$, $\mathbf{r}_3 = [170^{\circ} \quad -25^{\circ} \quad 85^{\circ}]^T$, respectively. Gaussian noise with zero mean and standard deviation (from 1 to 10 cm) is added to the LIDAR points. The estimation results are then compared with ground truth. For each noise level, 100 independent random trials are delivered. The averaged calibration error is shown in Fig. 6, where the calculation results are denoted as $\hat{\mathbf{R}}_l^c$ and $\hat{\mathbf{t}}_l^c$, respectively. This figure illustrates that the calibration error increases with noise level, as expected. For $\sigma < 7$cm (which is larger than the normal standard deviation for most LIDAR sensors), the error of norm of $\mathbf{R}_l^c$ is less than 0.01. With three checkerboard poses, the relative translation error is less than 5% when $\sigma < 5$cm.

Performance with respect to the Number of Checkerboard Positions The checkerboard was originally setup as parallel to the image plane. Then it is rotated by, where the rotation axis is randomly selected in a uniform sphere. The number of checkerboards used for calibration varies from 4 to 20. Gaussian noise with zero mean and standard deviation $\sigma = 4$cm is added to the LIDAR points. For each position, 100 trials of independent rotation axes are implemented. The averaged result is illustrated in Fig. 7. This figure shows that when the number of checkerboard positions increases, the calibration error decreases.

Performance with respect to the Orientation of Checkerboard The checkerboard plane is initially set as parallel to the image plane. It is then rotated around a randomly chosen axis with angle θ. The rotation axis is randomly selected from a uniform sphere. The rotation angle θ varies from 10° to 80°, and 10 checkerboards are used for each θ. Gaussian noise with zero mean and standard deviation $\sigma = 4$cm is added to the LIDAR points. For each rotation angle, 100 trials are repeated and the average error is calculated. The simulation result is shown in Fig. 8. The calibration error decreases when the rotation angle increases. When the rotation angle is too small, the calibration planes are almost parallel to each other, which cause error. When the rotation angle is too large, the calibration plane is almost perpendicular to the image plane, which makes the LIDAR measurement less precise.

Real Data Calibration The calibration method has been tested using an IBEO ALASCA XT LIDAR system and a Sony CCD digital camera with a 6 mm lens.

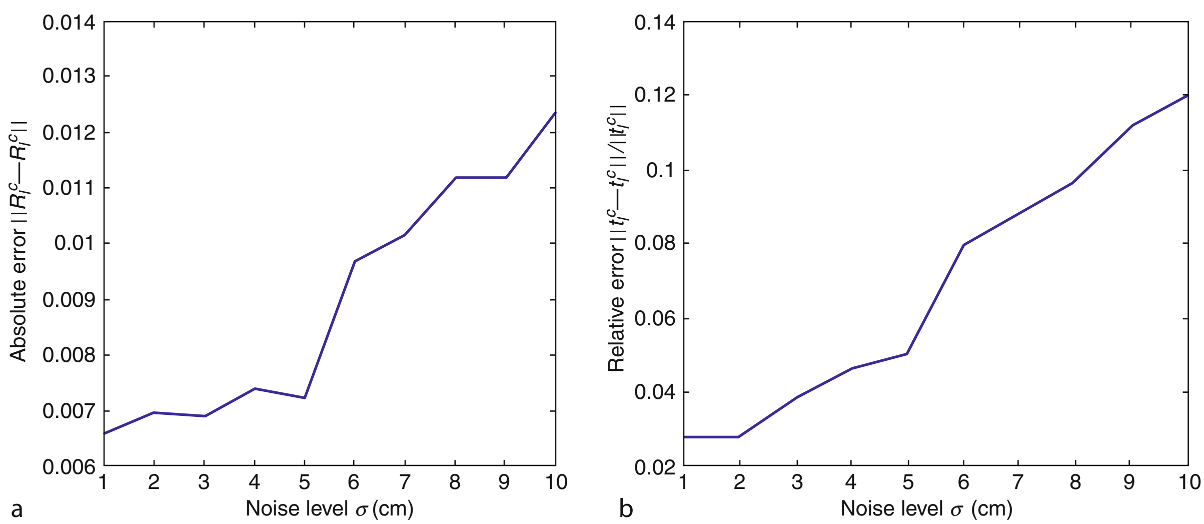

Vehicle Detection, Tightly Coupled LIDAR and Computer Vision Integration for. Figure 6
Rotation and translation error with respect to the noise level. (**a**) Rotation error with respect to noise level. (**b**) Translation error with respect to noise level

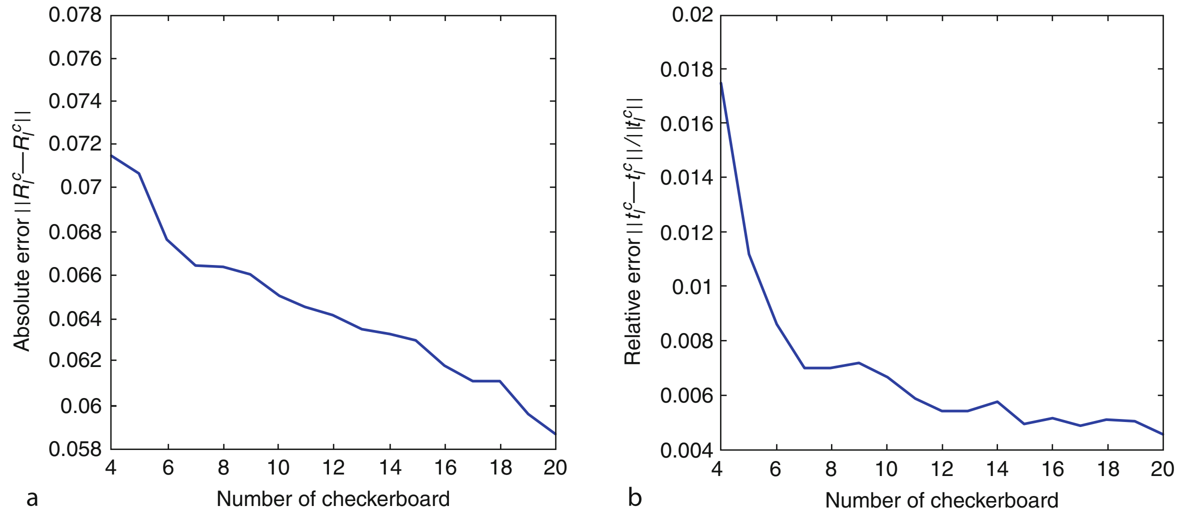

Vehicle Detection, Tightly Coupled LIDAR and Computer Vision Integration for. Figure 7
Rotation and translation error with respect to number of checkerboard positions. (**a**) Rotation error with respect to number of checkerboard. (**b**) Translation error with respect to number of checkerboard

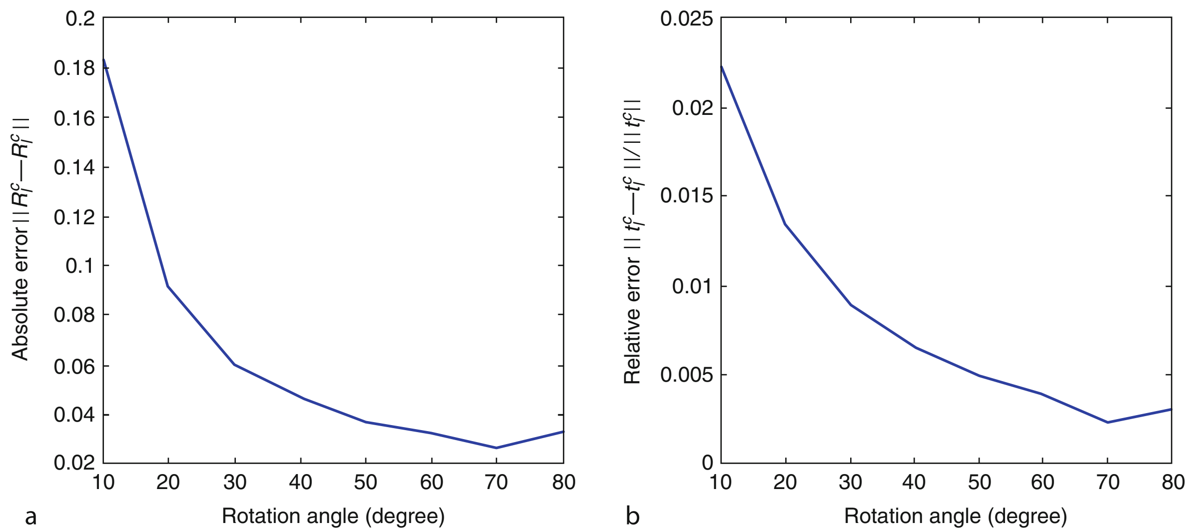

Vehicle Detection, Tightly Coupled LIDAR and Computer Vision Integration for. Figure 8
Rotation and translation error with respect to the orientation of the checkerboard plane. (**a**) Rotation error with respect to orientation of the checkerboard plane. (**b**) Translation error with respect to orientation of the checkerboard plane

The image resolution is 640×480. The checkerboard plane consists of a pattern of 16×16 squares, so there are totally 256 grids on the plane. The size of each grid is 2.54cm $\times$ 2.54cm (1×1 in.).

Twenty images of the plane were taken with different orientations, and the LIDAR points are recorded simultaneously. Two examples of the calibration results are shown in Fig. 9, where the LIDAR points are mapped to image reference system using estimated $\mathbf{R}_l^c$ and $\mathbf{t}_l^c$. Although the ground truth of $\mathbf{R}_l^c$ and $\mathbf{t}_l^c$ are not known, Fig. 9 shows that the estimation results are pretty reasonable.

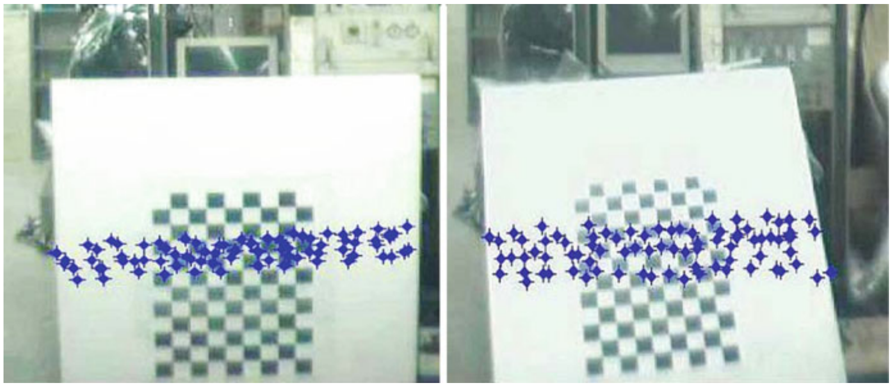

Vehicle Detection, Tightly Coupled LIDAR and Computer Vision Integration for. Figure 9
Two checkerboard positions. The LIDAR points are indicated by *blue dots*. The calibration method proposed in this entry is used to estimate $\mathbf{R}_l^c$ and $\mathbf{t}_l^c$

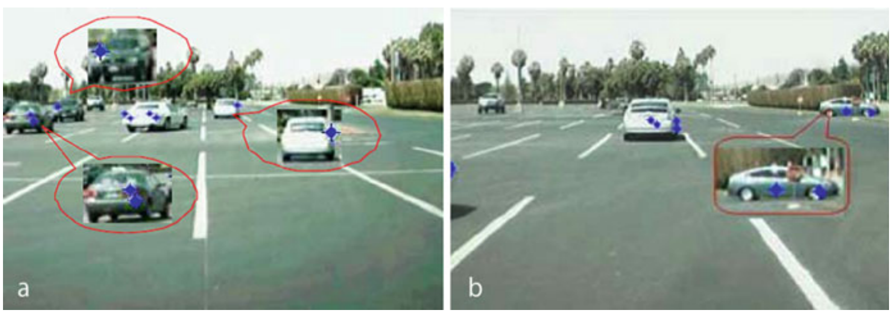

Vehicle Detection, Tightly Coupled LIDAR and Computer Vision Integration for. Figure 10
Two sensor fusion image frames. The *red rectangle* is an enlarged image of the detected area

Application in Vehicle Detection The calibration method has been integrated into a mobile sensing system. This mobile sensing system is designed to detect and track surrounding vehicles, which is the first and fundamental step for any of the automatic traffic surveillance systems. However, object detection is a big challenge for the moving platform. Both the foreground and the background are rapidly changing, which makes it difficult to extract the foreground regions from the background. The sensor fusion technique is used to compensate for the spatial motion of the moving platform. Figure 10 gives two images from the vehicle detection video.

In Fig. 10a, there are totally four vehicles detected by the LIDAR, where the farthest vehicle is 55 m away from the mobile sensing system. It is hard to obtain the vehicle's distance and orientation from an image alone. The LIDAR points provide a reliable estimation of this vehicle's position. In Fig. 10b, one car parallel to the probe vehicle is detected by the LIDAR. Meanwhile, it is partially visible in the image, together with its shadow on the ground. Although this vehicle is hardly recognizable in the image, with a wide angle of view, LIDAR data provide enough information to reconstruct the location of this vehicle.

The experiment results illustrate that the calibration algorithm provides good results. The sensor fusion system combining LIDAR and computer vision information sources presents distance and orientation information. This system is helpful for vehicle detection and tracking applications.

Summary

In this section, a novel calibration algorithm was developed to obtain the geometry transformation between a multi-plane LIDAR system and a camera vision system. This calibration method requires LIDAR and camera to observe a checkerboard simultaneously. A few checkerboard poses are observed and recorded. The calibration approach has two stages: closed-form solution followed by a maximum likelihood criterion–based optimization. Both simulation and real-world experiments have been carried out. The experiment results show that the calibration approach is reliable. This approach will be used in the vehicle detection and tracking system.

Tightly Coupled LIDAR and Computer Vision Integrated System for Vehicle Detection

Computer vision sensors are generally used in current mobile platform–based object detection and tracking systems. However, the application of vision sensors is far from sufficient: clustering, illumination, occlusion, among many other factors, affect the overall performance. In contract, a LIDAR sensor provides range and azimuth measurements from the sensor to the targets. However, the accuracy of its measurements depends on the reflectivity of the targets and the weather. The fusion of camera and active sensors such as LIDAR is being investigated in the context of on-board vehicle detection and tracking.

In this section, a tightly coupled LIDAR/CV system is proposed, in which the LIDAR scanning points are used for hypothesizing regions of interest and for providing error correction to the classifier, while the vision image provides object classification information. LIDAR object points are first transformed into image space. ROIs are generated using the LIDAR feature detection method. An Adaboost classifier based on computer vision systems [36] is then used to detect vehicles in the image space. Dimensions and distance information of the detected vehicles are calculated in body-frame coordinates. This approach provides a more complete and accurate map of surrounding vehicles in comparison to the single sensors used separately. One of the key features of this technique is that it uses LIDAR data to correct the Adaboost classification pattern. Moreover, the Adaboost algorithm is utilized both for vehicle detection and for vehicle distance and dimension extraction. Then the classification results provide compensatory information to the LIDAR measurements.

This section is organized as follows: in section "Overview of the Vehicle Detection System" a brief introduction of the vehicle detection system is given. Section "Vision-Based System" describes the vision-based system. The vehicle detection algorithm is introduced in section "Moving Vehicle Detection System". A vehicle tracking approach using particle filter is proposed in section "Vehicle Tracking System". Experimental results of vehicle detection are provided in section "Experiment Results", followed by conclusions and future work in section "Summary and Discussion".

Overview of the Vehicle Detection System

Vehicle detection is the first and fundamental step for any driver assistant system (DAS). With sensors mounted on a moving platform, the detected data change rapidly, making it difficult to extract objects of interest. In the proposed approach, spatial motion of the moving platform has been compensated by using the sensor fusion approach.

Multi-module Architecture The input of vehicle detection system consists of two LIDAR sensors and a single camera, as is shown in Fig. 1. The detection area is covered by two LIDAR sensors overlapping with each other. The camera is placed behind the rearview mirror. The field of view of this camera is fully covered by the LIDAR ranging space.

Figure 11 presents the flowchart of this vehicle detection system. It consists of four subsystems: a LIDAR-based subsystem, a coordinate transformation subsystem, a vision-based subsystem, and a vehicle detection subsystem.

LIDAR-Based Subsystem *The LIDAR Data Acquisition Module* uses IBEO External Control Unit (ECU) to communicate, collect, and combine data from a pair of LIDAR sensors.

The Prefiltering and Clustering Module aims to transform scan data from distances and azimuths to

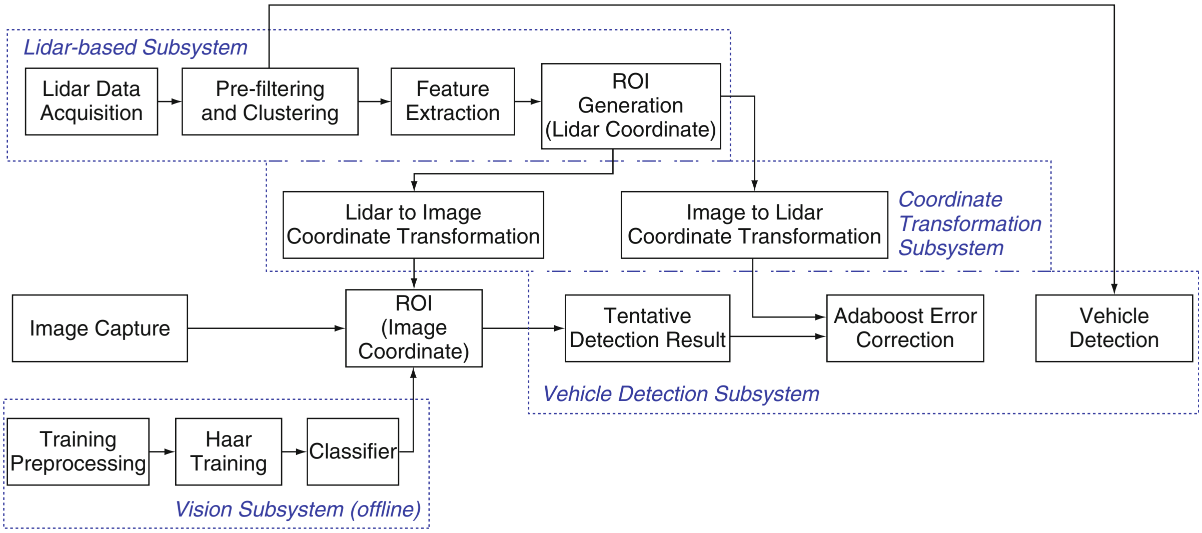

Vehicle Detection, Tightly Coupled LIDAR and Computer Vision Integration for. Figure 11
Flowchart of the mobile sensing system

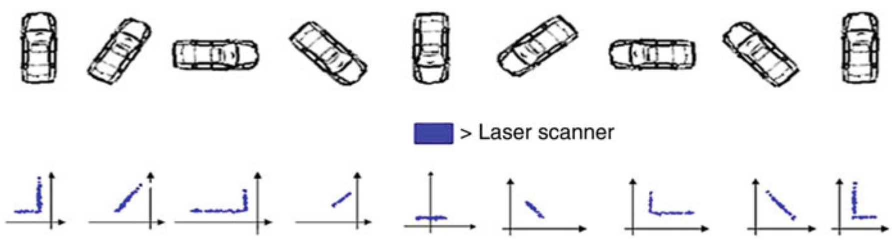

Vehicle Detection, Tightly Coupled LIDAR and Computer Vision Integration for. Figure 12
Orientation of the vehicle significantly changes its appearance in the scan data frame. The rectangles show position of the LIDAR

positions, and cluster the incoming data into segments using a Point-Distance-Based Methodology (PDBM) [12]. If there exists any segment consisting of less than three points, and the distance of this segment is greater than the given threshold, these points are considered as noise. The segment will be disregarded.

The Feature Extraction Module extracts primary features in the cluster. The main feature information in one segment is its geometrical representation, such as lines and circles. One of the advantages of geometrical features is that they occupy far less space than storing all the scanned points.

A vehicle may have any possible orientation. The contour of a vehicle is constructed by four sides: front, back, left side, and right side. The LIDAR sensor can capture one side, or two neighboring sides, as is shown in Fig. 12.

When the object is close to the probe vehicle, the extracted feature provides enough information for object classification. However, if the target is far away, it may be represented by only one or two scanning points. For those objects with only a few LIDAR points, it is difficult to get reliable size, location, and orientation information from the scan data alone. Note that the computer vision image also contains size and orientation information, which can be extracted by the object classification technique. By employing the sensor fusion technology, LIDAR

scan data and Adaboost output are complementary to each other.

The ROI Generation Module calculates positions of ROI bounding boxes in LIDAR coordinates. It is worth mentioning that the ROI is not defined by LIDAR points alone, since the scan points of one target may not be able to represent its full dimension. In this algorithm, the width and length of ROI are defined by both LIDAR data points and the maximum dimension of a potential vehicle.

Each ROI is defined as a rectangular area in the image. The bottom of the rectangle is the ground. The top of the rectangle is set to be the maximum height of a car. The left and right edges are obtained from the furthest left and right scanning points in a cluster, as well as the typical width of a car.

The LIDAR to Image Coordinate Transformation Module transforms all the LIDAR points into the image frame. The relative position and orientation between LIDAR and camera sensors should be obtained for the transformation. A unique multi-planar LIDAR and computer vision calibration algorithm is described in section "A Novel Multi-Planar LIDAR and Computer Vision Calibration Procedure Using 2D Patterns", which calculates the geometry transformation matrix between "multiple invisible beams" of LIDAR sensors and the camera. The calibration results are used in the sensor fusion system.

During the road test, each LIDAR scan point $\mathbf{P}_l$ is transformed into camera coordinate as $\mathbf{P}_c$. $\mathbf{P}_c$ is then transformed into point $\mathbf{p}_c$ in the image plane. Figure 13 illustrates LIDAR scan points and the transformation results in the image reference system.

After the LIDAR to image transformation coefficients are calculated, ROIs generated in the LIDAR-based subsystem is converted into image frame. A larger ROI is generated due to inaccuracy of the transformation from LIDAR data to image data.

The Image to LIDAR Coordinate Transformation Module is called to correct Adaboost classification result. More details are given in the following sections.

Vision-Based System

Object classification from the hypothesized ROIs is required for vehicle detection purpose. Feature representations are used for object classifiers by an Adaboost algorithm [36]. Viola et al. proposed that the object is detected based on a boosted cascade of feature classifiers, which performs feature extraction and combines features such as simple weak classifiers to a strong one.

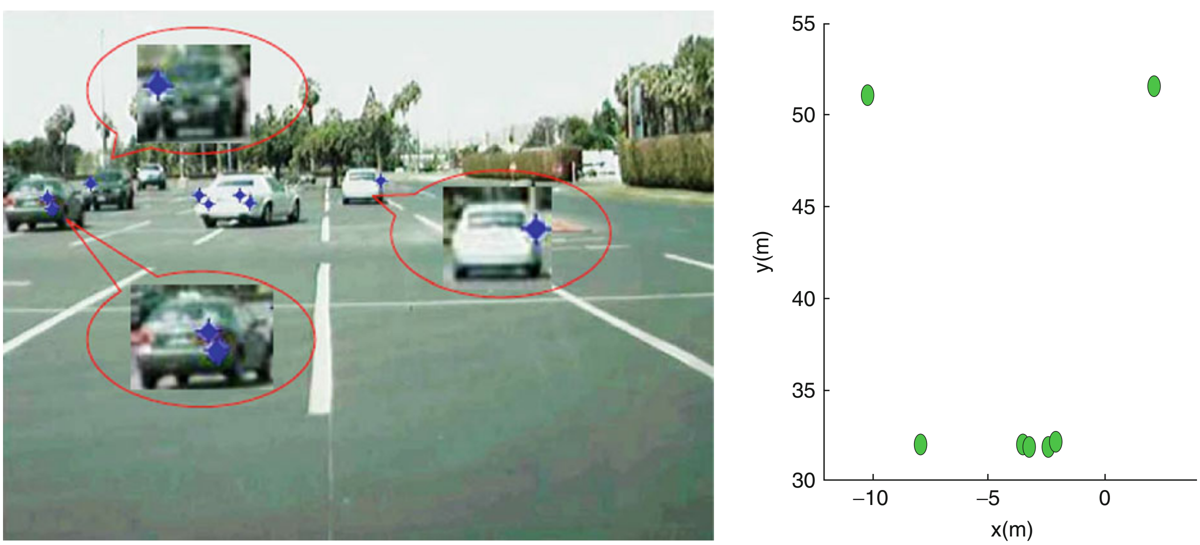

Vehicle Detection, Tightly Coupled LIDAR and Computer Vision Integration for. Figure 13
The LIDAR scan points. (**a**) Points in the LIDAR coordinate system. Each green dot is one scan point. (**b**) These points are transformed to the image frame. Each blue star in the image is one LIDAR point. Vehicles in the red circles are the enlarged image of the detected area

The Adaboost classifier requires off-line training using target as well as nontarget images. In the vehicle detection applications, the target images, i.e., the rearview of vehicles, are called positive samples; while the non-vehicles are named as negative samples. Figure 14 illustrates some of the positive as well as negative samples in the training dataset. Training samples are taken from both Caltech vehicle image dataset [37] and video collected by the test vehicle. The positive samples include passenger cars, vans, trucks, and trailers. The negative sample sets include roads, traffic signs, buildings, plants, and pedestrians.

Image Training Preprocessing Both the positive and negative samples are used by computer vision system for data training. All the samples are originally colored images. In order to remove the effects of various illumination conditions and camera differences, gray-level transformation is required as a preprocessing step. The gray-level normalization method is applied to the whole image dataset, which transforms gray level of the image to be in [0, 1] domain. The color image is transformed by [38]:

$$I^*(x,y) = \frac{I(x,y) - I_{\min}}{I_{\max} - I_{\min}} \tag{11}$$

where $I(x,y)$ is the intensity of pixel (x,y), $I_{\min}$ and $I_{\max}$ are the minimum and maximum values in this image, respectively. $I^*(x,y)$ is the normalized gray-level value.

The next step is to normalize the sizes of all the positive samples. It is implemented before training since different resolutions may cause different number of features to be counted. The sizes of the normalized positive samples determine the minimum size of objects that can be detected [39]. In this test, the normalized image size is set as 25×25 pixels.

Haar Training In the vision-based system, Haar-like features are used to classify objects [36]. This approach combines more complex classifiers in a "cascade" which quickly discard the background regions while spending more computation on the Haar-like area [36].

More specifically, 14 feature prototypes are utilized for the Haar training [40]. These features represent characteristic properties like edge, line, and symmetry.

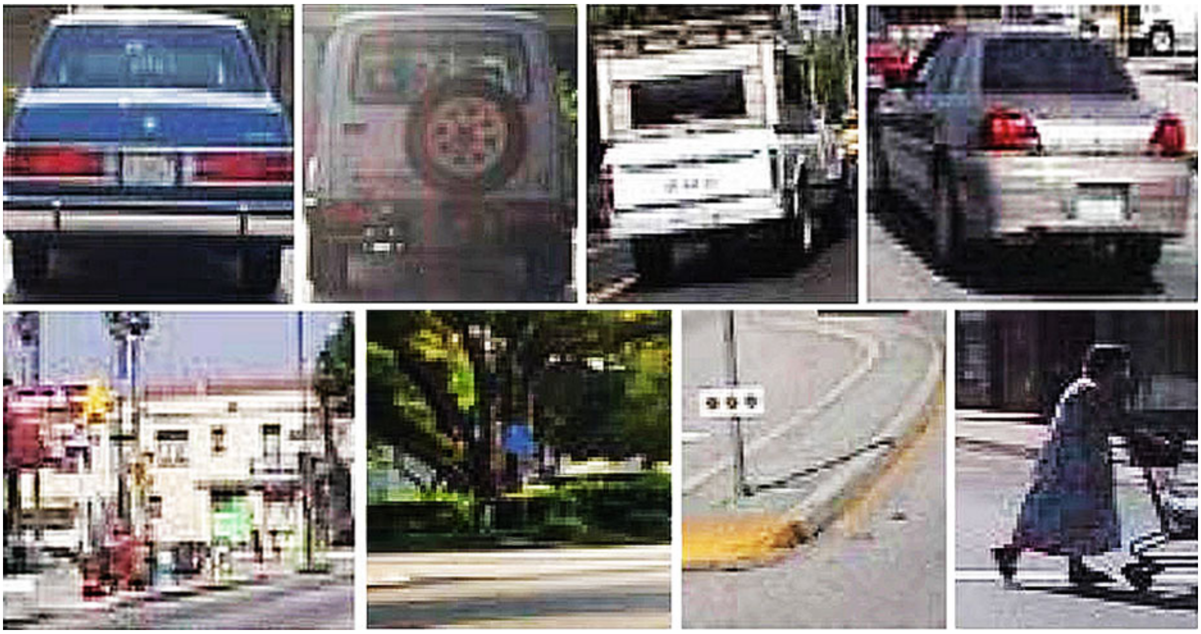

Vehicle Detection, Tightly Coupled LIDAR and Computer Vision Integration for. Figure 14
Positive and negative samples used in Adaboost training

The features prototypes can be grouped into three categories:

- Edge features: The difference between sums of the pixels within two rectangular regions

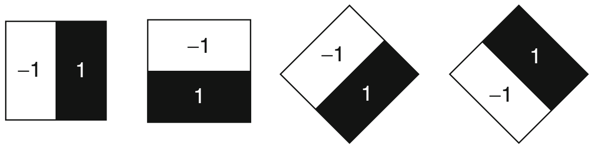

- Line features: The sum within two outside rectangular regions subtracted from the sum in the center rectangular

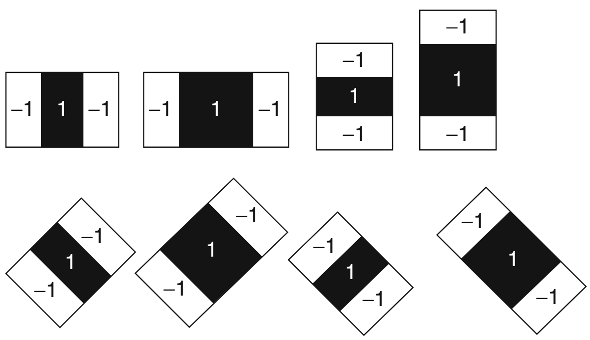

- Center-surround features: The difference between the sums of the center rectangular and the outside area

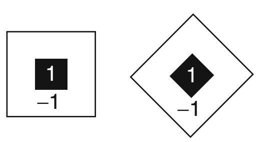

Here black areas with "–1" have negative weights, and white areas with "1" have positive weights.

After the weak classifier has been trained at each stage, the classifier is able to detect almost all the targets of interest while rejecting certain nontarget objects. A cascade of classifiers is generated to form a decision tree. The training process consists of totally 15 stages. Each stage is trained to eliminate 60% of the non-vehicle patterns, and the hit rate (HR) in each stage is set to be 0.998. Therefore, the total false alarm rate (FAR) for this cascade classifier is supposed to be $0.4^{15} \approx 1.07e - 06$, and the hit rate should be around $0.998^{15} \approx 0.97$.

Moving Vehicle Detection System

The Adaboost algorithm designs a strong classifier that can detect multiple objects in the given image. However, there is no guarantee that this strong classifier is optimal for the object detection. In contrast to the classic Adaboost algorithm, in this test there is only one vehicle in each ROI defined by the LIDAR clustering algorithm. Therefore, it is not necessary for the Adaboost algorithm to detect several possible targets in one ROI. A classification correction technique is proposed to utilize the LIDAR scanning data to reduce redundancy in the Adaboost detection results.

There are two kinds of redundancy errors in the classification results. Figure 15 gives some examples of these two cases. Both have detected more than one object, while the ground truth is that there is only one vehicle. One kind of error is that the Adaboost detects two possible targets, while the area of the smaller one is almost covered by the larger one, as is shown in Fig. 15a. Another error shown in Figure 15b is that all the detected areas belong to the same object, while none of them cover the full body of the target.

Suppose in the i-th ROI, there exists a LIDAR point cluster $\Re_i$, which has the following features in LIDAR coordinate system: c_i^{LIDAR} as the center of the cluster, w_i^{LIDAR} as the width of the object, and l_i^{LIDAR} as the possible length of the vehicle. On the image side, there are detected target candidates denoted as d_1, $d_2, \ldots, d_n$. Initially, $d_1, d_2, \ldots, d_n$ are transformed from image coordinate to camera coordinate, then to LIDAR coordinates.

The scan points in LIDAR coordinates are denoted as D_1, $D_2, \ldots, D_n$. The j-th candidate D_j has center $c_{i,j}^{DETECT}$, width $w_{i,j}^{DETECT}$, and height $h_{i,j}^{DETECT}$. In LIDAR coordinate frame, two vectors are defined as $\mathbf{m}_i^{LIDAR} = \left(c_i^{LIDAR}, w_i^{LIDAR}\right)$ and $\mathbf{m}_i^{DETECT} = \left(c_{i,1}^{DETECT}, w_{i,1}^{DETECT}, \cdots, c_{i,n}^{DETECT}, w_{i,n}^{DETECT}\right)$. Here $\mathbf{m}_i^{LIDAR}$ is the size information obtained by LIDAR, and $\mathbf{m}_i^{DETECT}$ consists of measurements in LIDAR coordinate systems which are transformed from the image reference system. The coefficient $\mathbf{w}_i$ for mapping multiple target areas to the LIDAR information satisfies:

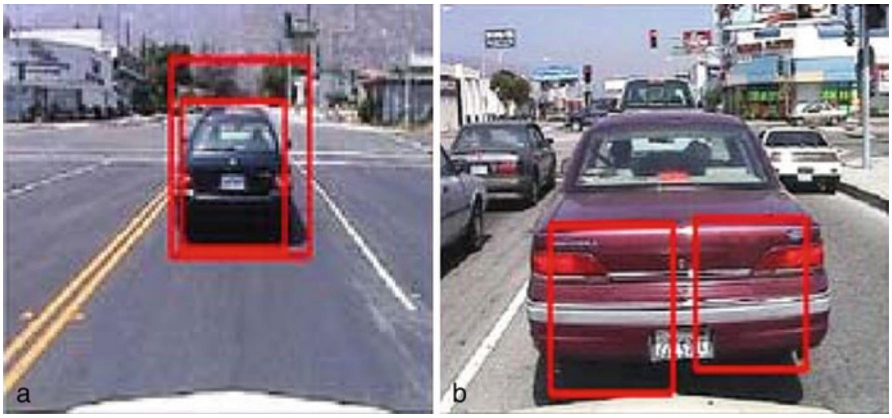

Vehicle Detection, Tightly Coupled LIDAR and Computer Vision Integration for. Figure 15
Two kinds of redundancy errors in Adaboost detection. (**a**) Two bounding boxes overlap on the same target. (**b**) Two bounding boxes detected with no overlap on the same target

$$\mathbf{w}_i = \arg\min \left\| \mathbf{m}_i^{LIDAR} - \sum\nolimits_{j=1:n} \mathbf{w}_{i,j} \mathbf{m}_{i,j}^{DETECT} \right\| \tag{12}$$

where $\|.\|$ is the Euclidean norm. $\mathbf{w}_i$ is used as a weight to recalculate the detected area, which is a combination of all the detected objects in one ROI.

LIDAR scanning points and Adaboost classification results are then combined to generate a complete map of vehicles. A summary of the vehicle detection process is given here:

Algorithm 1: Vehicle Detection. Given LIDAR points cluster $\Re_i$ with features $\left(c_i^{LIDAR}, w_i^{LIDAR}, l_i^{LIDAR}\right)$, detected target candidate $d_1, \ldots, d_n$ in the image;

if no object detected in the ROI
  enlarge ROI and search again
else
  define $\mathbf{m}_i^{LIDAR} = \left(c_i^{LIDAR}, w_i^{LIDAR}\right)$
  transform $d_1, \ldots, d_n$ in the image coordinate frame to LIDAR reference frame
  define $\mathbf{m}_i^{DETECT} = \left(c_{i,1}^{DETECT}, w_{i,1}^{DETECT}, \cdots, c_{i,n}^{DETECT}, w_{i,n}^{DETECT}\right)$
  calculate the weight vector which minimize $\left\| \mathbf{m}_i^{LIDAR} - \sum \mathbf{w}_{i,j} \mathbf{m}_{i,j}^{DETECT} \right\|$
end if

The detected vehicle is located at $\sum_{j=1:n} \mathbf{w}_{i,j} c_{i,j}^{DETECT}$.

The vehicle detection system proposed in this section can be summarized as:

- The Adaboost classifier training is implemented off-line with both positive and negative samples.
- ROI is defined by the LIDAR scan data. No more than one vehicle is assumed to exist in each ROI.
- Use the Adaboost classifier to make a preliminary vehicle detection.
- LIDAR data is used to correct the Adaboost redundancy error, and to merge detected areas in one ROI.
- Combine the Adaboost detected area (in LIDAR coordinate) and the LIDAR output to generate a complete vehicle distance and dimension map.

Vehicle Tracking System

LIDAR and computer vision sensors are integrated in a probabilistic manner for vehicle tracking. A sampling importance resampling (SIR) particle filter is used as the tracker, which is a sophisticated model estimation technique [41]. Unlike the commonly used Kalman filter and extended Kalman filter (EKF), this particle filter does not assume that the linear dynamic system is perturbed by Gaussian noise. The key idea of particle filter is to represent the estimation by a set of random samples (they are called *particles*) with associated weights.

Particle Filter Let $\mathbf{x}_t^{(i)}$ be the i-th sample of the position and velocity of the target at time t,

$i = 1, 2, \cdots, N_s$, where N_s is the total number of samples or particles in the particle filter. $w_t^{(i)}$ is the i-th weight at time $_t$ associated with $\mathbf{x}_t^{(i)}$. The procedure of SIR particle filter is defined as follows:

1. Initial Particle Generation
   Generate N_s particles $\left\{\mathbf{x}_0^{(i)},\ w_0^{(i)}\right\}$, $i = 1, 2, \cdots, N_s$. Here $\mathbf{x}_0^{(i)}$ is obtained from vehicle detection results and $w_0^{(i)} = 1/N_s$.
2. Particle Updating
   For each particle $\mathbf{x}_{t-1}^{(i)}$ at time $t-1$, generate a particle $\mathbf{x}_t^{(i)}$ at time t. This step corresponds to the prediction step in Kalman filter and EKF. However, in Kalman filter and EKF, at time t the state is updated only once. Here in the particle filter, each of the particles should be updated, so totally N_s particle updating calculations are implemented. In this system, $\mathbf{x}_t^{(i)} = \left[\mathbf{p}_t^{(i)} \quad \mathbf{v}_t^{(i)}\right]$ is the sample of the position and velocity, so a linear model is used to update the particles:

$$\mathbf{p}_t^{(i)} = \mathbf{p}_{t-1}^{(i)} + \mathbf{v}_{t-1}^{(i)} T + n \tag{13}$$

   where T is the time interval and n is the noise.
3. Particle Weighting
   Each particle $\mathbf{x}_0^{(i)}$ at time t is associated with the weight $w_t^{(i)}$, which is also called the *importance factor*. The weight at time t is a function of the weight at time $t-1$, and the probability function of measurements and states at time t. The importance factor is commonly calculated as [41]:

$$w_t^{(i)} = w_{t-1}^{(i)} p\left(\mathbf{z}_t \middle| \mathbf{x}_t^{(i)}\right) \tag{14}$$

   where $\mathbf{z}_t$ is the measurement at time t. In the proposed sensor fusion system, both LIDAR and computer vision sensors are utilized for vehicle tracking. Therefore, the measurement is $\mathbf{z}_t = \left\{{}^l\mathbf{z}_t;\ {}^c\mathbf{z}_t\right\}$, where ${}^l\mathbf{z}_t$ is the output of LIDAR and ${}^c\mathbf{z}_t$ is the measurement of the camera. This step corresponds to the update step in Kalman filter and EKF. The probability $p\left(\mathbf{z}_t \middle| \mathbf{x}_t^{(i)}\right)$ will be discussed in the following subsection.
4. Resampling
   A common problem with the particle filter is the degeneracy, which is the phenomenon that after a few iterations only one particle has non-negligible weight [41]. $\widehat{N_{eff}}$ has been defined to measure the degeneracy, which is calculated as [41]:

$$\widehat{N_{eff}} = \frac{1}{\sum_{i=1}^{N_s}\left(w_t^{(i)'}\right)^2} \tag{15}$$

where $w_t^{(i)'}$ is the normalized weight of the i-th particle at time t with $w_t^{(i)'} = \frac{w_t^{(i)}}{\sum_{i=1}^{N_s} w_t^{(i)}}$. If $\widehat{N_{eff}}$ is less than a given threshold N_T, the degeneracy is detected.

Resampling is performed at each iteration. It is designed to eliminate particles that have small weights and replicate particles that have large weights. Particles that have large weights are considered to be the "good" particles while the particles with small weights are "bad" particles. The resampled weights are set as $w_t^{(i)} = 1/N_s$.

After obtaining $w_t^{(i)}$, the posterior filtered density can be approximated as [41]:

$$p(\mathbf{x}_t|\mathbf{z}_{1:t}) \approx \sum_{i=1}^{N_s} w_k^i \delta\left(\mathbf{x}_t - \mathbf{x}_t^{(i)}\right) \tag{16}$$

The Sensor Model The sensor model describes the process by which sensor measurements are made in the physical world. It relates sensor output to the state of the vehicle. In the vehicle detection application it is defined as the conditional probability $p\left({}^l\mathbf{z}_t;\ {}^c\mathbf{z}_t \middle| \mathbf{x}_t^{(i)}\right)$, which is the probability of LIDAR and computer vision sensor measurements given the state of the vehicle.

A LIDAR sensor model is described in [42], which represents the probability as a mixture of four distributions corresponding to four types of measurement errors: the small measurement noise, errors due to unexpected objects or obstacles, errors due to failure to detect objects, and random unexplained noise.

Let $z_t^{(k)*}$ denote the true distance to an obstacle, $z_t^{(k)}$ denote the recorded measurement, and $z_{\max}$ denote the maximum possible reading. The small measurement error is defined as a Gaussian distribution p_{hit} over the range $[0,\ z_{\max}]$ with mean $z_t^{(k)*}$ and standard deviation σ_{hit}.

The LIDAR detection zone is often blocked by the moving vehicles, which leads to the measurement

whose length is shorter than the true length. This particular type of measurement error is modeled by a truncated exponential distribution p_{short} with the coefficient λ_{short}.

LIDAR sometimes fails to detect obstacles due to low reflectivity of the target. The errors due to failure to detect objects is defined as a pseudo point-mass distribution $p_{\max}$ centered at $z_{\max}$.

Finally, unexplainable measurements may be returned by the LIDAR sensor, which is caused by interference. This type of error is modeled by a uniform distribution p_{rand} over the entire measurement range.

$p\left({}^{l}\mathbf{z}_t \middle| \mathbf{x}_t^{(i)}\right)$ is calculated as a combination of the four types of errors as [42]:

$$\begin{aligned} p\left({}^{l}\mathbf{z}_t \middle| \mathbf{x}_t^{(i)}\right) = {} & \alpha_{\text{hit}} p_{\text{hit}}\left({}^{l}\mathbf{z}_t \middle| \mathbf{x}_t^{(i)}\right) \\ & + \alpha_{\text{short}} p_{\text{short}}\left({}^{l}\mathbf{z}_t \middle| \mathbf{x}_t^{(i)}\right) \\ & + \alpha_{\max} p_{\max}\left({}^{l}\mathbf{z}_t \middle| \mathbf{x}_t^{(i)}\right) \\ & + \alpha_{\text{rand}} p_{\text{rand}}\left({}^{l}\mathbf{z}_t \middle| \mathbf{x}_t^{(i)}\right) \end{aligned} \tag{17}$$

where α_{hit}, α_{short}, $\alpha_{\max}$, and α_{rand} are the weights for p_{hit}, p_{short}, $p_{\max}$, and p_{rand}, respectively. $\alpha_{\text{hit}} + \alpha_{\text{short}} + \alpha_{\max} + \alpha_{\text{rand}} = 1$. The parameters in Eq. 17 are commonly used as the a priori information, which are obtained by data training.

A camera weight model is proposed in [43] as:

$$p\left({}^{c}\mathbf{z}_t \middle| \mathbf{x}_t^{(i)}\right) = \begin{cases} S & \text{the object is in the camera detection zone.} \\ 1 - S & \text{the object is out of the camera detection zone.} \end{cases} \tag{18}$$

where S is a constant, $0 \leq S \leq 1$. This model is based on the assumption that the camera is able to detect all the objects in the detection zone.

The sensor fusion probability model is calculated based on the LIDAR probability model as well as the camera probability model. It is proposed in [43] that ${}^{l}\mathbf{z}_t$ and ${}^{c}\mathbf{z}_t$ are independent measurements. So

$$p\left({}^{l}\mathbf{z}_t; {}^{c}\mathbf{z}_t \middle| \mathbf{x}_t^{(i)}\right) = p\left({}^{l}\mathbf{z}_t \middle| \mathbf{x}_t^{(i)}\right) p\left({}^{c}\mathbf{z}_t \middle| \mathbf{x}_t^{(i)}\right) \tag{19}$$

However, in the proposed sensor fusion system, LIDAR and the camera are not two independent sensors. They have been calibrated to observe the same target, and the geometric relationships are given as a priori information. Moreover, the classification result of the camera is corrected by the LIDAR output.

In this section, a novel sensor fusion probability model is proposed. As defined in [42], LIDAR tracking process is modeled as a mixture of four types of errors: the small measurement noise, unexpected objects detection error, detection failure error, and random unexplained noise. In the field test, small measurement noise error is found to be the exclusive error source of the LIDAR sensor. The other types of errors are removed by integration of LIDAR and camera. The LIDAR tracking model is [42]:

$$p\left({}^{l}\mathbf{z}_t \middle| \mathbf{x}_t^{(i)}\right) = \begin{cases} \frac{1}{\sqrt{2\pi}\delta} \exp\left(-\frac{\left({}^{l}\mathbf{z}_t - {}^{l}\mathbf{z}_t^{*}\right)^2}{2\delta^2}\right) & 0 \leq {}^{l}\mathbf{z}_t \leq z_{\max} \\ 0 & \text{otherwiase} \end{cases} \tag{20}$$

The computer vision-based vehicle tracking is implemented by KLT tracking [36, 47]. A function $s\left(x_{t(i)}^{m}\right)$ is used to determine if a predicted corner $x_{t(i)}^{m}$ is close to an observed corner $z_{t(i)}$. $s\left(x_{t(i)}^{m}\right)$ is defined as $s\left(x_{t(i)}^{m}\right) = -\sum_{j=1}^{M} \exp\left(d_{t(i,j)}^{m}\right)^2$, where M is the total number of corners, $\left(d_{t(i,j)}^{m}\right)^2 = \left\| z_{t(j)} - x_{t(i)}^{m} \right\|^2$ is the Euclidean distance between i-th detected corner of the m-th particle $x_{t(i)}^{m}$ and j-th extracted corner $z_{t(j)}$ [47]. The camera model is defined as [47]:

$$p\left({}^{c}\mathbf{z}_t \middle| \mathbf{x}_t^{(i)}\right) = \exp\left(-\sum \left(s\left(x_{t(i)}^{m}\right) - 1\right)^2\right) \tag{21}$$

Finally, the sensor fusion tracing system has totally three measurement situations: (1) the vehicle is tracked by both the LIDAR and the camera. In this case, the single sensor tracking error is eliminated by sensor integration technique proposed in section "Moving Vehicle Detection System"; (2) the vehicle is out of camera detection zone, so it is tracked by the LIDAR alone; and (3) the vehicle is tracked by the camera but

not detected by the LIDAR sensor due to factors such as distance or weak reflection. The sensor fusion model is given as:

$$p\left({}^{l}\mathbf{z}_t;{}^{c}\mathbf{z}_t\middle|\mathbf{x}_t^{(i)}\right) = \begin{cases} \alpha p\left({}^{l}\mathbf{z}_t\middle|\mathbf{x}_t^{(i)}\right) + \beta p\left({}^{c}\mathbf{z}_t\middle|\mathbf{x}_t^{(i)}\right) \\ \text{target is tracked by both LIDAR and camara} \\ p\left({}^{l}\mathbf{z}_t\middle|\mathbf{x}_t^{(i)}\right) \\ \text{target is tracked by LIDAR alone} \\ p\left({}^{l}\mathbf{z}_t\middle|\mathbf{x}_t^{(i)}\right) \\ \text{target is tracked by camara alone} \end{cases} \tag{22}$$

where the weight $0 \leq \alpha \leq 1$ and $0 \leq \beta \leq 1$ are two coefficients obtained by data training, $\alpha + \beta = 1$, which allows to balance the LIDAR and computer vision information.

The weight $w_t^{(i)}$ can be calculated using Eq. 14. The particle filter is summarized in Algorithm 2. Unlike the Kalman filter or EKF, particle filter can track vehicle state with multi-model or arbitrary distributions.

Algorithm 2: Particle Filter for Sensor Fusion Systems. Input: $\left\{x_{t-1}^{(i)}, w_{t-1}^{(i)}\right\}$, $i = 1, 2, \cdots, N_s$: set of weighted particles at time $t - 1$
$\mathbf{z}_t = \left({}^{l}\mathbf{z}_t; {}^{c}\mathbf{z}_t\right)$: LIDAR and computer vision measurement at time t

Output: $\left\{x_t^{(i)}, w_t^{(i)}\right\}$, $i = 1, 2, \cdots, N_s$: set of weighted particles at time t

Process:

for $i = 1$ to N_s do
  Predict $\mathbf{x}_t^{(i)}$ as $\mathbf{p}_t^{(i)} = \mathbf{p}_{t-1}^{(i)} + \mathbf{v}_{t-1}^{(i)} T + n$
  $w_t^{(i)} = w_{t-1}^{(i)} p\left(\mathbf{z}_t\middle|\mathbf{x}_t^{(i)}\right)$
end for
calculate $\widehat{N_{eff}}$
if $\widehat{N_{eff}} < N_T$
  for $i = 1$ to N_s do
    computer $w_t^{(i)}$ using Eq. 14, in which $p\left({}^{l}\mathbf{z}_t; {}^{c}\mathbf{z}_t\middle|\mathbf{x}_t^{(i)}\right)$ is given in Eq. 20
    update the particle with $\left\{x_t^{(i)}, 1/N_s\right\}$
  end for
else
  $Z = \sum_{i=1}^{N_s} w_t^{(i)}$
  for $i = 1$ to N_s do
    update the particle with $\left\{x_t^{(i)}, Z^{-1} w_t^{(i)}\right\}$
  end for
end if

Experiment Results

The experiment results of vehicle detection are discussed in this section. To evaluate the performance of this system, a dataset of 377 images was used for training and testing. These images are taken from both the Caltech vehicle image dataset [37] and the video samples collected by probe vehicles. Another test dataset consists of 526 images with synchronized scanning data that are used for performance evaluation. The test dataset was recorded in a local parking lot on different days during different seasons.

Hit rate (HR), false alarm rate (FAR), and region detection rate (RDR) are used to evaluate the performance of this system. Here HR is the number of detected vehicles over total number of vehicles. RDA denotes the percentage of "real" vehicle detection rate. A "real" vehicle detection is that majority area of the vehicle is covered by a rectangle, and there is only one rectangle that covers this object. Therefore, a target that is hit may not be a region "really" detected; and a region detected object is always a hit. The higher the RDR is, the more accurate the detection result will be. Figure 16 illustrates several cases for hit, false alarm, and region detection. In this figure, TR represents the target region in the image, and DR is the detected region by the classifier.

Table 2 gives the detection performance of Adaboost classifier (detection with camera only), the classic LIDAR–camera sensor fusion system, and the proposed LIDAR and computer vision-based detection and error correction approach. Here in both the classic sensor fusion technique and the proposed approach, LIDAR data are utilized for ROI generation. The difference lies in the fact that in the proposed approach LIDAR data help correct the classification result. Table 2 shows that this approach both improves the hit rate and reduces the false alarm rate in comparison with Adaboost classifier. Compared with the classic

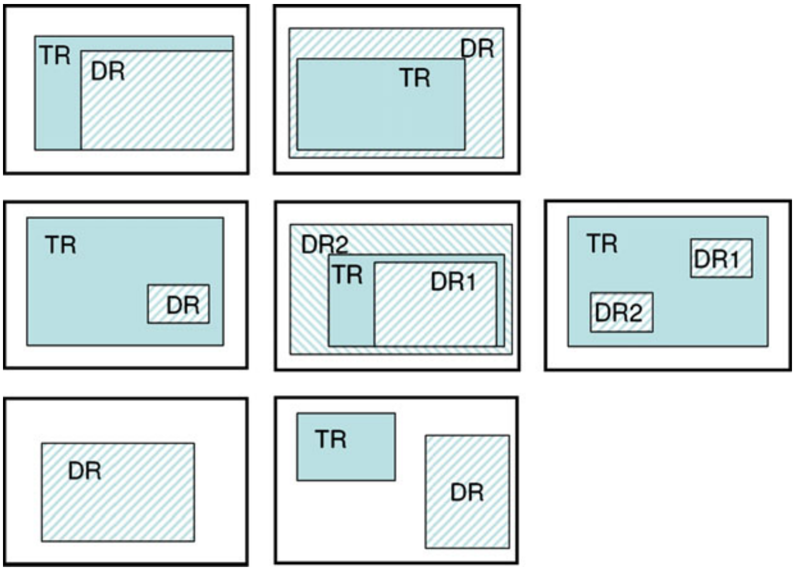

Vehicle Detection, Tightly Coupled LIDAR and Computer Vision Integration for. Figure 16
Three target detection cases. The first row is region detected, the second row is hit but not region detected, and the third row is false alarm

Vehicle Detection, Tightly Coupled LIDAR and Computer Vision Integration for. Table 2 Detection result

Type	HR (%)	FAR (%)	RDR (%)
Adaboost	84.17	3.27	78.00
Classic LIDAR–camera fusion	91.33	1.78	84.85
Proposed approach	91.33	1.78	89.32

LIDAR–camera fusion system, this approach improves the region detect rate from 84.85% to 89.32%, since for each hit but not accurately covered object the LIDAR scanning data helps to recomputed position of the target. Most of the overlapping or partial target detection areas are merged during the LIDAR correction process.

Figure 17 illustrates some of the vehicle detection results. The left column presents LIDAR scan points, and the right column illustrates camera images with information from the sensor fusion system. In Figure 7a, all the vehicles are detected and are marked with a rectangle. Figure 7b shows that the classifier found two vehicles only, which are bounded in a red rectangle. The other two ROIs (shown in blue rectangles) are classified to have non-vehicle objects. In fact, one of them is a trash can. The other is a vehicle at a distance of 92.78 m. This vehicle is too far away and too small in the image for the classifier to recognize.

During the test, the hit rate decreases when the distance between the probe vehicle and the target vehicles increases. The targets are detected frame by frame. Therefore, the target vehicles may not be recognized by the classifier in certain frames even if it was recognized in the last frame. Vehicle tracking technique helps solve this problem. By running a particle filter–based tracking algorithm, the target is initially detected in the initial frame or in several initial frames, after which it is tracked in the following frames. This approach both improves the detection accuracy and reduces the required amount of calculation. HR and RDR will be further improved by vehicle tracking.

Summary and Discussion

A novel vehicle detection system has been proposed based on tightly integrating LIDAR and computer

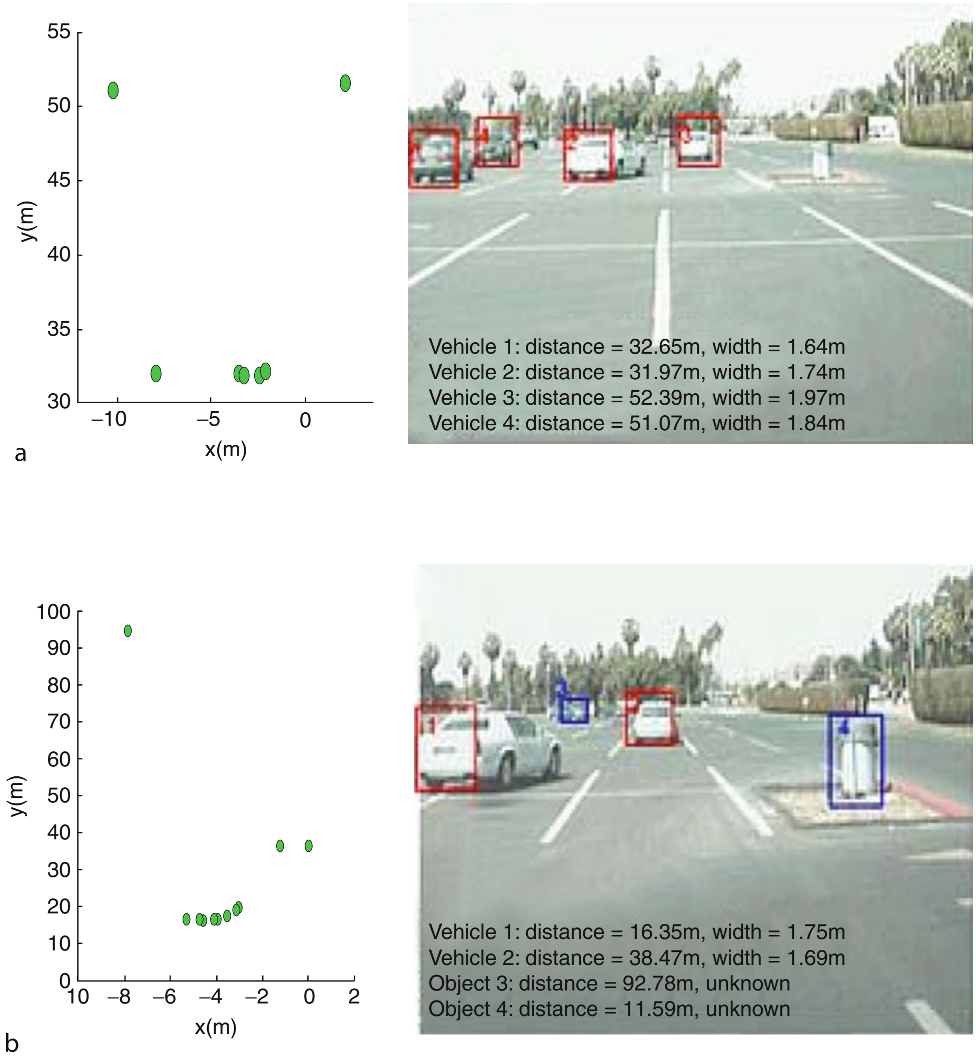

Vehicle Detection, Tightly Coupled LIDAR and Computer Vision Integration for. Figure 17
LIDAR scan points and the final vehicle detection results

vision sensors. Distances to the objects are first defined by the LIDAR sensors, and then the object is classified based on computer vision images. In addition, data from these two complementary sensors are combined for classifier correction and vehicle detection. The experimental results have indicated that, when compared with image-based and classic sensor fusion–based vehicle detection systems, this approach has a higher hit rate and a lower false alarm rate. It is quite useful for modeling and prediction of the traffic conditions over a variety of roadways. This system may be used in future autonomous navigation systems.

Conclusions and Future Work

This entry presents a multi-sensor equipped vehicle detection system that was developed to specifically obtain the state of surrounding vehicles. It involves the development of a tightly coupled LIDAR and

computer vision system, calibration of a pair of multi-planar LIDAR sensors and the camera system, and the methodology of sensor fusion-based vehicle detection technique.

This section provides a brief summary of this entry, as well as the possible future work.

Summary

Automatic vehicle detection techniques are becoming an essential part of our daily lives. They open up many potential opportunities but they also come with challenges in terms of sensing capability and accuracy. In this entry, the problem of vehicle detection is addressed, and some novel approaches have been demonstrated to solve the problem in a traffic environment.

The goal of this research is to provide a solution to measure the state of surrounding vehicles. State of the vehicle includes position, orientation, speed, and acceleration. Sensor fusion techniques are utilized to provide a direct measurement of the state. A variety of sensors have been used in this entry, including LIDAR and computer vision. The goal is to quantitatively show that the integration of sensors provides a more accurate and effective estimation of the vehicle state. The proposed system has successfully met this goal.

The developed multi-planar LIDAR and computer vision sensor calibration approach, as to the author's best knowledge, is the first calibration method for an "invisible-beam" multi-planar LIDAR and a camera. In comparison to the commonly used calibration methods that require a infrared camera to "see" the LIDAR beams or a special designed calibration shape, this approach is easy to implement with low cost. It has been theoretically and experimentally proven to be able to estimate the geometric relationships between the two sensors.

Based on this unique calibration method, a sensor fusion-based vehicle detection system is designed and implemented. It consists of three major components: (1) ROIs are generated by the LIDAR sensor; (2) vehicle classification using a computer vision-based Adaboost algorithm, and (3) vehicle position is verified using the output of the LIDAR sensor. A vehicle tracking model is also presented in this entry, which uses a joint probability model-based particle filter to predict state of the vehicle. The experiment result shows that the designed sensor fusion system achieves higher detection rate and lower positive as well as negative error rates, when compared with a single sensor-based detection method. The positions of detected vehicles have been represented in vehicle coordinates to generate a local traffic map.

Taken together, the tests in this entry demonstrate that a good vehicle detection performance can be achieved using a LIDAR and computer vision sensor-based moving platform. Such results are especially important for vehicle navigation systems, as well as traffic surveillance systems that are equipped with multiple sensors.

Future Directions

Although a sensor fusion system is developed in this entry for the on-board vehicle detection application, it is believed that the introduction of sensor fusion-based system in the automobile industry is still couple of years away. In the future driver assistance systems, sensor fusion techniques can be employed to support, even replace the driver. Moreover, falling costs of sensors, such as RADAR, GPS, inertial sensors (INS), and LIDAR, combined with increasing image processing capability provides a bright future for on-board intelligent transportation applications.

Disclaimer

Much of the material for this entry comes from the 2010 dissertation of Lili Huang, at the University of California-Riverside (see [44]). Portions of this entry have also appeared in [45] and [46].

Bibliography

1. Proper AT, Cheslow MD (1997) ITS benefits: continuing successes and operational test results. FHWA-JPO-98-002, Oct 1997
2. Mimbela L, Klein LA (2000) Summary of vehicle detection and surveillance technologies used in intelligent transportation systems. Report to Federal Highway Administrations (FHWA) Intelligent Transportation Systems Joint Program Office
3. Apogee/Hagler Bailly (1998) Intelligent transportation systems: real world benefits. FHWA-JPO-98-018, Jan 1998
4. Kim MY, Cho H, Lee H (2004) An active trinocular vision system for sensing mobile robot navigation environments. In: Proceedings of the IEEE intelligent robots and systems, Sendai, pp 1698–1703
5. Jung YK, Ho Y-S (1999) Traffic parameter extraction using video-based vehicle tracking. In: IEEE/IEEJ/JSAI international

conference on intelligent transportation systems, Tokyo, pp 764–769
6. Baltzakis H, Argyros A, Trahanias P (2003) Fusion of laser and visual data for robot motion planning and collision avoidance. Mach Vision Appl 12:431–441
7. Liu Y, Emery R (2001) Using EM to learn 3D environment models with mobile robots. In: Proceedings of the 18th international conference on machine learning, Williamston, 2001
8. Jokinen O (1999) Self-calibration of a light striping system by matching multiple 3-D profile maps. In: Proceedings of the second international conference on 3-D digital imaging and modeling, Ottawa, pp 180–190
9. Hayashibe M, Nakamura Y (2001) Laser-pointing endoscope system for Intra-operative 3D geometric registration. In: Proceedings of the international conference on robotics and automation, Seoul, pp 1543–1548
10. Mahlisch M, Schweiger R, Ritter W, Dietmayer K (2006) Sensorfusion using spatio-temporal aligned video and lidar for improved vehicle detection. In: Proceedings of intelligent vehicles symposium, Meguro-Kupp, pp 424–429
11. Unnikrishnan R, Hebert M (2005) Fast extrinsic calibration of a laser rangefinder to a camera. Technical report CMU-RI-TR-05-09, Robotics Institute, Carnegie Mellon University, July 2005
12. Zhang Q, Pless R (2004) Extrinsic calibration of a camera and laser range finder (Improves camera calibration). In: IEEE proceedings of international conference on intelligent robots and systems, Sendai, pp 2301–2306
13. DARPA urban challenge http://www.darpa.mil/grandchallenge/index.asp
14. Mahmassani HS, Haas C, Zhou S, Peterman J (1998) Evaluation of incident detection methodologies. Technical Report FHWA/TX-00/1795-1, Center of Transportation Research, The University of Texas at Austin, Oct 1998
15. University of Central Florida (2007) I2Lab, TeamUCF – DARPA urban challenge. Technical Report, June 2007
16. Thrun S (2003) Learning occupancy grid maps with forward sensor models. Autonomous Robots 15(2):111–127
17. SICK USA, see http://www.sick.com/us/en-us/home/Pages/Homepage1.aspx
18. HOKUYO UXM-30LN LIDAR, see http://www.hokuyo-aut.jp/02sensor/07scanner/uxm_30ln.html
19. The laser scanner product overview, see http://www.ibeoas.com/english/products.asp
20. Velodyne HDL-64E LIDAR, http://www.hizook.com/blog/2009/01/04/velodyne-hdl-64e-laser-rangefinder-lidar-pseudo-disassembled
21. Whittaker WR (2005) Red team DARPA grand challenge 2005 technical paper. Carnegie Mellon University, CSC Technical Report, Aug 2005
22. Cobzas D, Zhang H, Jagersand M (2002) A comparative analysis of geometric and image-based volumetric and intensity data registration algorithms. In: IEEE international conference on robotics and automation (ICRA), Washington, DC, 2002
23. Wasielewski S, Strauss O (1995) Calibration of a multi-sensor system laser rangefinder/camera. In: Proceedings of intelligent vehicles symposium, Detroit, pp 472–477
24. Neira J, Tard JD, Horn J, Schmidt G (1999) Fusing range and intensity images for mobile robot localization. IEEE Trans Robot Autom 15(1):76–84
25. Toyh D, Aach T (2003) Detection and recognition of moving objects using statistical motion detection and Fourier descriptors. In: 12th international conference on image analysis and processing, Mantova, pp 430–435
26. Oren M, Papageorgiou C, Sinha P (1997) Pedestrian detection using wavelet templates. In: IEEE proceedings on computer vision and pattern recognition, San Juan, 1997
27. Premebida C, Monteiro G, Nunes U, Peixoto P (2007) A lidar and vision-based approach for pedestrian and vehicle detection and tracking. In: IEEE intelligent transportation systems conference, Seattle, pp 1044–1049
28. Fardi B, Schuenert U, Wanielik G (2005) Shape and motion-based Pedestrian detection in infrared images: a multi sensor approach. In: Proceedings of the IEEE intelligent vehicles symposium Las Vegas, pp 18–23
29. Milch S, Behrens M (2001) Pedestrian detection with radar and computer vision. In: Proceedings of the conference on progress in automobile lighting, Darmstadt, 2001
30. Zhang Z (2000) A flexible new technique for camera calibration. IEEE Trans Patt Anal Mach Intell 22:1330–1334
31. Bouguet J-Y (2003) Camera calibration toolbox for matlab, 2003
32. Faugeras OD, Toscani G (1987) Camera calibration for 3D computer vision. In: Proceedings of the international workshop on industrial applications of machine vision and machine intelligence, Silken, Japan, pp 240–247
33. Ricolfe Viala C, Sanchez Salmeron AJ (2004) Performance evaluation of linear camera calibration techniques. In: IEEE Proceedings on world automation congress, Spain, vol 18, pp 49–54
34. Levenberg K (1944) A method for the solution of certain problems in least squares. Quart Appl Math 2:164–168
35. More J (1977) The Levenberg-Marquardt algorithm, implementation and theory. In: Numerical analysis. Lecture notes in mathematics, vol 630. Springer, Berlin
36. Viola P, Jones MJ (2001) Rapid object detection using a boosted cascade of simple features. In: Proceedings of the IEEE computer vision and pattern recognition, Hawaii, pp 511–518
37. Caltech vehicle image dataset, see http://www.vision.caltech.edu/htmlfiles
38. Haselhoff A, Kummert A, Schneider G (2007) Radar-vision fusion with an application to car-following using an improved adaboost detection algorithm. In: IEEE intelligent transportation systems conference, Seattle, pp 854–858
39. Tutorial OpenCV Haartraining, see http://sourceforge.net/projects/opencvlibrary
40. Lienhart R, Kuranov A, Pisarevsky V (2003) Empirical analysis of detection cascades of boosted classifiers for rapid object detection. In: 25th pattern recognition symposium, Madgeburg, Sep 2003, pp 297–304

41. Arulampalam MS, Maskell S, Gordon N, Clapp T (2002) A tutorial on particle filters for online nonlinear/non-Gaussian Bayesian tracking. IEEE Trans Signal Process 50(2):174–188
42. Thrun S, Burgard W, Fox D (2005) Probabilistic robotics. The MIT Press, Cambridge, MA
43. Kurazume R, Yamada H, Murakami K, Iwashita Y, Hasegawa T (2008) Target tracking using SIR and MCMC particle filters by multiple cameras and laser range finders. In: IEEE/RSJ international conference on intelligent robots and systems, Nice, pp 3838–3844
44. Huang L (2010) LIDAR, Camera and inertial sensors based navigation techniques for advanced intelligent transportation systems, PhD dissertation, University of California Riverside
45. Huang L, Barth M (2009) A novel multi-planar LIDAR AND computer vision calibration procedure using 2D patterns for automated navigation. In: IEEE intelligent vehicles symposium, Xi'an, pp 117–122
46. Huang L, Barth M (2009) Tightly-coupled LIDAR and computer vision integration for vehicle detection. In: IEEE intelligent vehicles symposium, Xi'an, pp 604–609
47. Dore A, Beoldo A, Regazzoni CS (2009) Multitarget tracking with a corner-based particle filter. In: IEEE 12th international conference on computer vision workshops, Kyoto, pp 1251–1258

Vehicle Dynamics and Performance

Yimin Gao
Department of Electrical and Computer Engineering, Texas A&M University, College Station, TX, USA

Article Outline

Glossary

Braking forces The forces acting on the contact area of the running wheels and ground, generated by the brake system.

Braking performance The vehicle behavior underlying braking, braking distance, and direction stability.

Braking system A vehicle subsystem that is used to slow the vehicle quickly.

Fuel consumption Fuel consumed in unit traveling distance.

Power plants The machines that supplies power for propelling vehicle.

Tractive effort The thrust force acting on the contact area of running wheels and ground that push the vehicle forward.

Transmissions Mechanical devices that transmit the powers of the power plants to vehicle wheels.

Vehicle performance The capability of a vehicle, in terms of speed, acceleration, and gradeability.

Vehicle resistance The forces that is against the vehicle motion.

Definition of the Subject

Vehicle system is a complex system that includes many mechanical and electric components and operates in very different traffic environments. There are many requirements, including traffic conditions, mission requirements, energy supplies, environmental protection, cost, etc. Vehicle dynamic and performance analysis supplies the basic methodologies for vehicle performance evaluation, design principle, and quantitative computation methods for system and component design.

Introduction

Vehicle dynamics and performance are broad topics that deal with vehicle's drivability, fuel economy, braking performance, handling characteristics, noise, vibration and harshness (NVH), etc. The research for improving vehicle dynamics and performance never ceased in 100 years since vehicles have been invented. The research in this area has been developed for the purposes of basic understanding of the system operation behaviors, system and components design, and development of more advanced control technologies, such as engine control, transmission control, traction control, braking control, vehicle stability control, etc. In recent years, more efficient and clean vehicle technologies have been developed quickly, especially, electric propulsion, fuel cell, and hybrid technologies. These require the research on vehicle dynamics and performance being extended beyond the scope of conventional vehicles that has focused on gasoline and diesel power vehicles. However, although there are many differences between conventional and electric-based vehicles, they share some similarities of drivability and braking performance. The fundamentals of vehicle dynamics and performance established for conventional vehicles are still, to a great degree, valid. This section reviews the fundamentals of vehicle's dynamics and performance for providing reference for electric, hybrid electric, and fuel cell vehicle design. The following sections focus on the traction and braking performance. Other performance, such as handling characteristics, noise, vibration and harshness (NVH), etc., will not be discussed in this entry.

Vehicle Performance

Vehicle performance discussed in this article will be restricted to propelling and braking performance in terms of vehicle speed, acceleration, gradeability, braking deceleration, and braking force distribution on front and rear wheels.

M. Ehsani et al. (eds.), *Transportation Technologies for Sustainability*, DOI 10.1007/978-1-4614-5844-9,

Originally published in
Robert A. Meyers (ed.) Encyclopedia of Sustainability Science and Technology, © 2012, DOI 10.1007/978-1-4419-0851-3

Overview of Vehicle Power Train Structure

Vehicle propelling performance is dictated by the power train structure, tractive power rating, and power plant operation characteristics and transmission design. Generally, vehicle power train consists of energy source (fuel, batteries), power plant (engine, electric motor), transmission, and drive wheels. The power train may be configured into front wheel drive, rear wheel drive, and all wheel drive, as shown in Fig. 1. The engine power is transmitted to drive wheels through clutch or torque converter, transmission, shaft, final drive, and transaxles. The torque on the drive wheels reacts with road surface to develop tractive effort to push the vehicle forward, as shown in Fig. 2.

The tractive effort developed on the drive wheel, together with the vehicle resistances, determines the vehicle performance (speed, acceleration, and gradeability).

Tractive Effort and Vehicle Speed

Tractive effort is produced on drive wheels by the reaction between the tractive torque and road surface as shown in Fig. 2. The tractive effort is proportional to the tractive torque, T_w, by

$$F_t = \frac{T_w}{r} \tag{1}$$

where T_w is the tractive torque on the drive wheels and r is the wheel radius.

The tractive torque acting on the drive wheels is produced by the engine or motor, transmitted through transmission gear box and final drive. It can be expressed as

$$T_w = T_e\, i_0\, i_g\, \eta_t \tag{2}$$

where T_e is the engine torque, i_0 is the gear ratio of the final drive, i_g is the gear ratio of the transmission, and η_t is the efficiency from the engine to the drive wheels. Combining (1) and (2), the tractive effort can be further expressed as

$$F_t = \frac{T_w\, i_0\, i_g \eta_t}{r} \tag{3}$$

The gear ratios of final drive and transmission are defined as the ratio of the input speed to the output speed. The transmission efficiency should include all the losses in the driveline components, such as, torque converter, transmission, torque distributor, final drive, etc. The typical efficiency values for individual components may be evaluated by [1, 2]

Clutch	99%
Each pair of meshed gears	95–97%
Bearing and joint	98–99%

It should be mentioned here that efficiency of torque converter is closely related to its operating point, that is, the speed ratio of the torque converter [1, 2].

Vehicle speed is related to the rotating speed of the drive wheels as

$$V = \omega_w\, r \quad (\mathrm{m/s}) \tag{4}$$

where ω_w is the rotating speed of the drive wheels in rad/s. In terms of revolution per second (rpm) N_w, the vehicle speed can be further expressed as

$$V = \frac{\pi N_w\, r}{30} \quad (\mathrm{m/s}). \tag{5}$$

The wheel rotating speed is related to the engine rotating speed by

$$N_w = \frac{N_e}{i_0\, i_g}, \tag{6}$$

where N_e is engine rpm.

It should be noted that gear ratio of torque converter should be included into the gear box gear ratio, i_g. Gear ratio of torque converter is the reciprocal of the speed ratio of the torque converter [1, 2].

Combining (5) and (6), the vehicle speed can be further expressed as

$$V = \frac{\pi N_e\, r}{30\, i_0\, i_g} \quad (\mathrm{m/s}) \tag{7}$$

Equation 3 is only valid while the vehicle is running on well-prepared road, where no obvious slip between tire and road surface occurs. For off-road operation, refer [1].

Torque (Power)-Speed Characteristics

For maximizing vehicle performance at a given power plant power capacity, the ideal power plant is one that

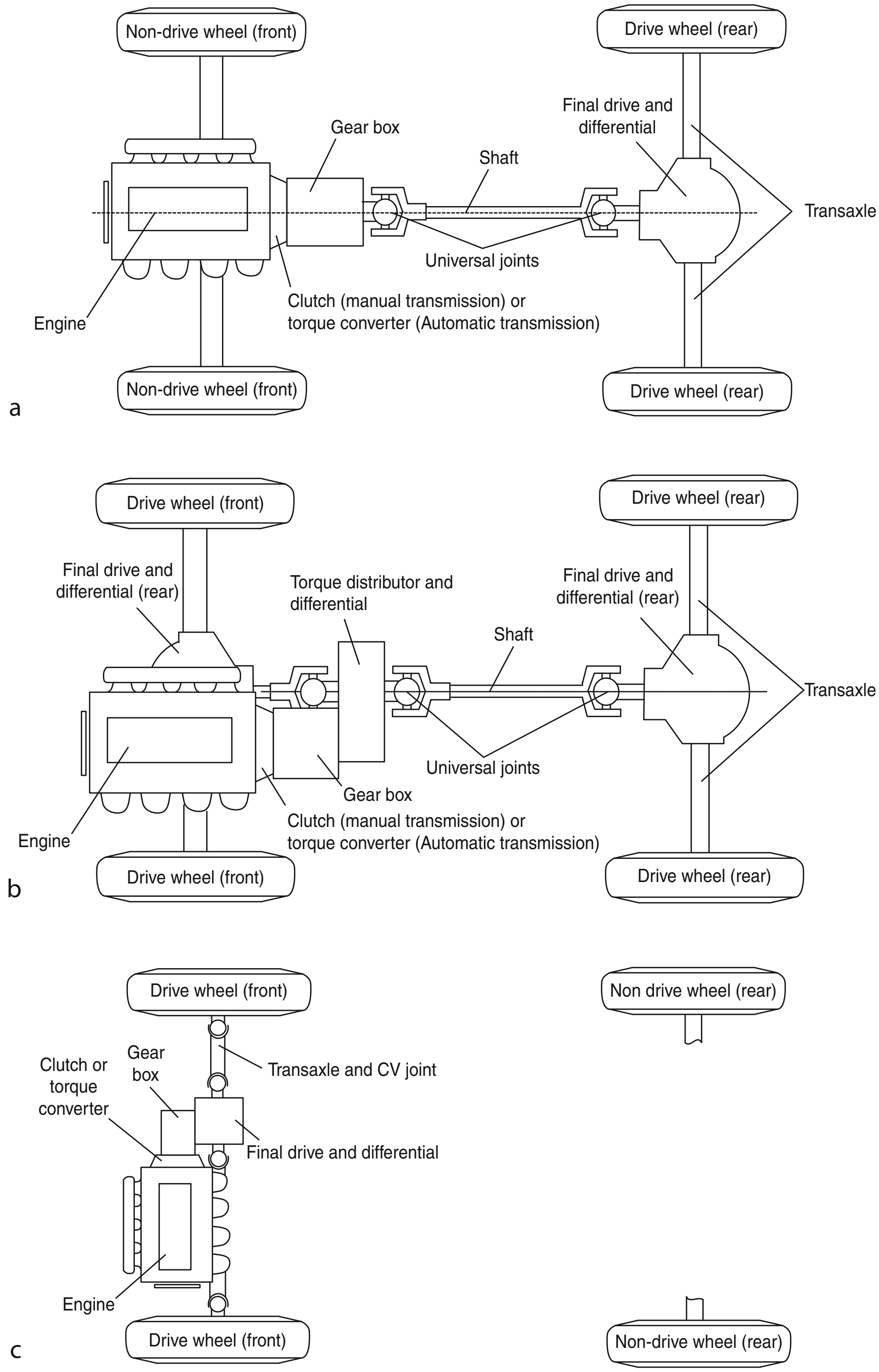

Vehicle Dynamics and Performance. Figure 1
Typical vehicle power trains: (**a**) rear wheel drive, (**b**) front wheel drive, and (**c**) all wheel drive

can produce a constant power in its full speed range. In this case, the power plant can apply its maximum power for propelling the vehicle in its whole speed range, yielding the highest vehicle performance. However, in practice, the maximum torque acting on drive wheels is limited by road adhesive capability. Beyond

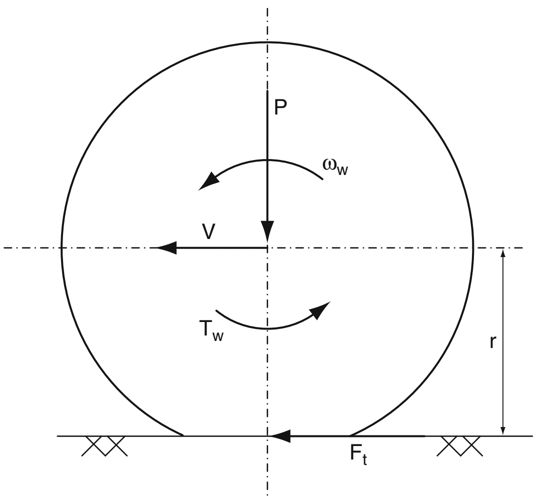

Vehicle Dynamics and Performance. Figure 2
Tractive effort, F_t, produced by wheel torque T_w

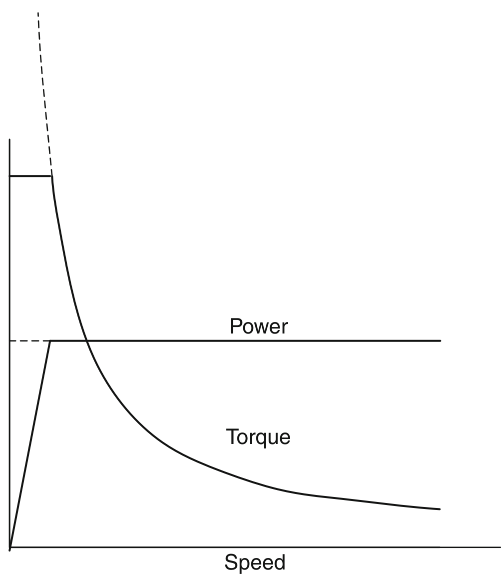

Vehicle Dynamics and Performance. Figure 3
Ideal torque (power)-speed performance of a vehicle power plant

this limitation, obvious tire slip will occurs. Therefore, at low speed, high torque is usually cut off with a constant torque as shown in Fig. 3.

For evaluating vehicle performance, such as maximum speed, acceleration, and gradeability, the maximum tractive torques in its whole speed range are used, that is, the torque produced by a fully opened throttle

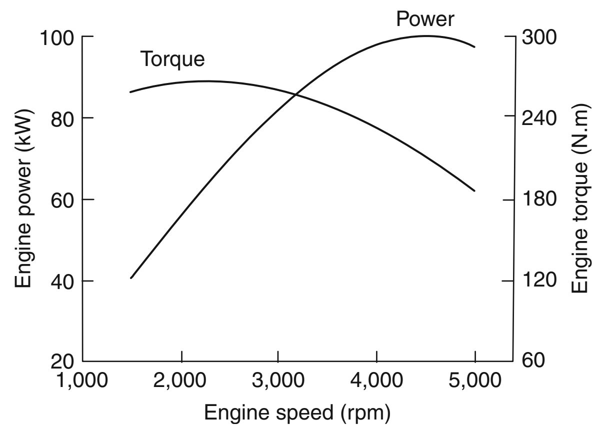

Vehicle Dynamics and Performance. Figure 4
Typical performance characteristics of gasoline engine with full open throttle [1]

engine. Figure 4 shows a typical gasoline engine operation characteristics with full open throttle [2]. Figure 5 shows the operation characteristics of a typical gasoline engine with partial open throttle.

The torque-speed profile of the engine is quit flat and is very different from the ideal profile shown in Fig. 3. Consequently, a multi-gear or continuous varying transmission (CVT) is required to modify this profile as shown in Fig. 6, in which, the envelope curve is a constant power curve as required.

Compared with the toque-speed profile of internal combustion engine, well-controlled electric motors possess the torque-speed profile much closer to the ideal as shown in Fig. 7. At low speeds, the motor develops constant torque, and at high speeds, constant power. The corner speed is called as base speed. A traction motor is usually controlled in such ways that terminal voltage is linearly increased from zero speed to its base speed; meanwhile, the magnetic field is kept constant. Beyond the base speed, the terminal voltage is kept constant and magnetic field is linearly weakened. Since its torque-speed profile is naturally closer to the required, an electric motor–driven vehicle usually needs fewer gears than that of an engine-driven vehicle. A single- or double-gear transmission may meet the performance requirement.

Transmission Characteristics

As discussed above, torque-speed characteristic of internal combustion engine is far away from the ideal

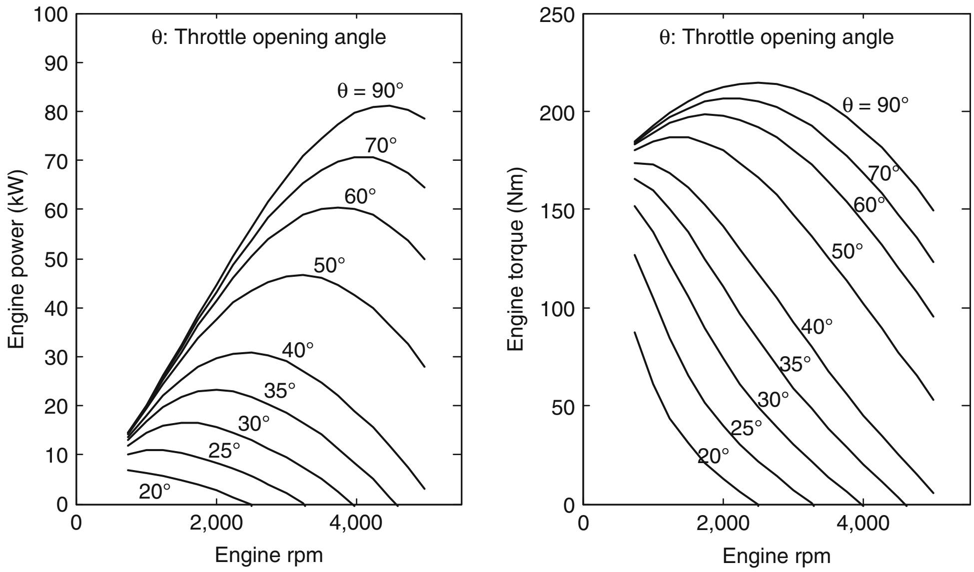

Vehicle Dynamics and Performance. Figure 5
Typical performance characteristics of gasoline engine with partial open throttle

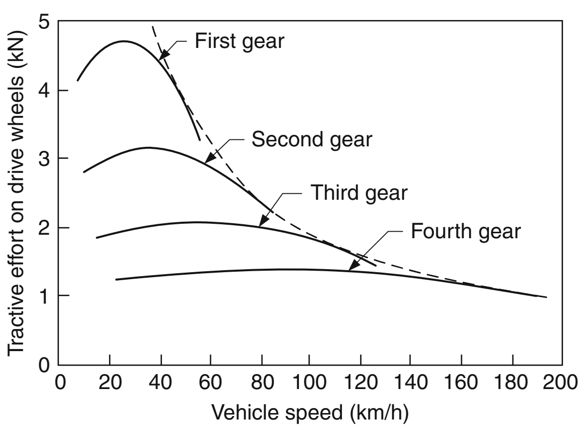

Vehicle Dynamics and Performance. Figure 6
Gasoline engine–powered tractive effort with a multi-gear transmission

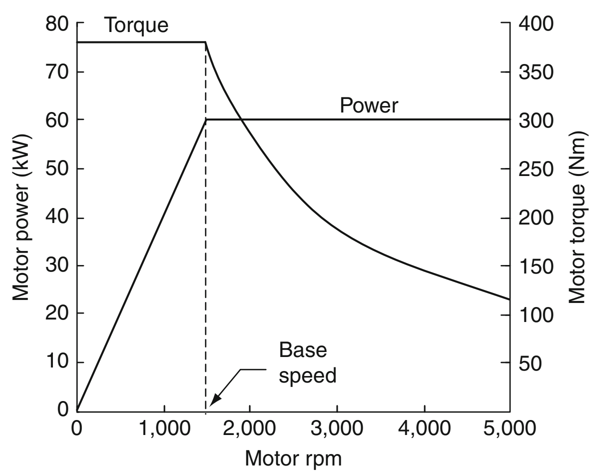

Vehicle Dynamics and Performance. Figure 7
Typical torque-speed profile of a well-controlled electric motor

one and the engine cannot be directly connected to wheels. A multi-gear transmission or continuous varying transmission (CVT) is installed between the engine and drive wheels for modifying the torque-speed characteristic of the engine output. A transmission is a gear box, in which there are several gear ratios for use. The gears are selected by driver based on real-time operation, such as vehicle speed and tractive effort requirement. This kind of transmission is referred to as manual transmission. The gear selection action may be performed automatically by a transmission control actuator, which is referred as automation or automatic transmission.

Transmission gear ratio design plays an importance role in vehicle performance. It should ensure the engine operating in its best speed range for torque producing and low fuel consumption.

Generally, there are several gears in a gear box. Each gear has a fixed gear ratio. Gear number depends upon vehicle performance requirements and specific power of the vehicle, which is defined as the power capacity per unit vehicle weight. More gear number results in a torque-speed profile closer to the ideal one, thus better vehicle performance can be obtained. However, more gears leads to complex transmission structure, and increased manufacturing difficulty, volume, weight, and cost. Therefore, the gear number design is usually a trade-off. In general, fewer gears are used in the vehicles that have large specific power. For passenger cars, four or five gears are common. For heavy-duty vehicles, over ten gears are common and two gear boxes are usually used.

Gear ratio design should ensure the engine operating in the best speed range. The design rule is interpreted as following.

As indicated by (7), for each gear, vehicle speed is proportional to engine speed. Gear changing procedure in acceleration driving is interpreted by Fig. 8 with a four-gear transmission.

1. Vehicle starts with first gear from zero speed to a speed, V_1 (point *a*), at which the engine speed reaches N_{e2}.
2. At point *a*, gear is changed from first to second (from point *a* to point *b*), in which vehicle speed does not change due to the very short gear change duration.

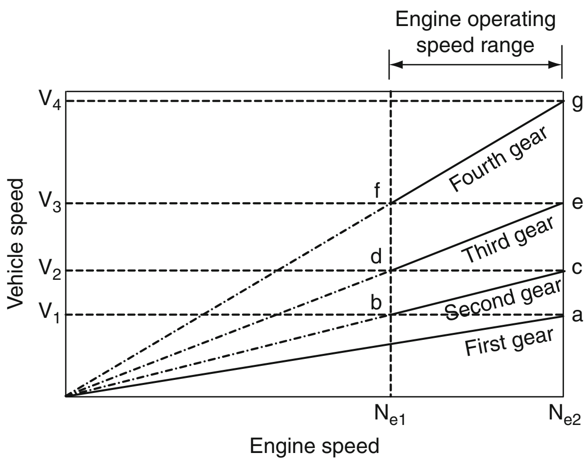

Vehicle Dynamics and Performance. Figure 8
Engine speed versus vehicle speed at each gear

3. Start from point *b*, second gear is engaged, and continuous acceleration to point *c*.
4. At point *c*, gear is changed to third (from point *c* to point *d*).

Using the speed relations, for example, the speed at point *a* equals to the speed at point *b*, the speed at point *c* equals to the speed at point *d*, and so on, and using (7), one obtains

$$V_1 = \frac{\pi N_{e2}\, r}{30\, i_0\, i_{g1}} = \frac{\pi N_{e1}\, r}{30\, i_0\, i_{g2}}$$
$$V_2 = \frac{\pi N_{e2}\, r}{30\, i_0\, i_{g2}} = \frac{\pi N_{e1}\, r}{30\, i_0\, i_{g3}} \tag{8}$$
$$V_3 = \frac{\pi N_{e2}\, r}{30\, i_0\, i_{g3}} = \frac{\pi N_{e1}\, r}{30\, i_0\, i_{g4}}$$

Equation 8 gives

$$\frac{N_{e2}}{N_{e1}} = \frac{i_{g1}}{i_{g2}} = \frac{i_{g2}}{i_{g3}} = \ldots\ldots = \frac{i_{g,n-1}}{i_{g,n}} = k \tag{9}$$

Equation 9 indicates that the ratios of two adjacent gears, *k*, is a constant, which determines the engine speed range, N_{e1}–N_{e2}. Small *k* allows engine operating in a narrow speed range, but more gears are needed.

When gear number and ratio, *k*, are determined, the gear ratio of each gear can be obtained using (9).

In transmission design, gear ratio of the highest speed gear is usually designed by selecting an engine speed, at which the vehicle has its top speed, that is,

$$i_{gh} = \frac{\pi\, N_{ed}\, r}{30\, i_0\, V_{\max}} \tag{10}$$

where i_{gh} is the gear ratio of highest speed gear, $V_{\max}$ is the top speed of the vehicle with the highest speed gear, N_{ed} is the desired engine speed with highest speed gear at maximum vehicle speed, and *r* is tire radius. After determination of the gear ratio of the highest speed gear, gear ratios of other gears can be determined by (9). It should be pointed out that the gear ratio of the lowest speed gear (first gear) should ensure the vehicle has its maximum tractive effort at low speed for meeting gradeability requirement.

In practice, gear ratio design may not exactly follow the rule of (9). For passenger cars, high-speed gears are used more often than low-speed gears in normal

driving, thus gear ratios are usually designed more "dense" than low-speed gears, that is,

$$\frac{i_{g1}}{i_{g2}} > \frac{i_{g2}}{i_{g3}} > \ldots.. > \frac{i_{g,n-1}}{i_{g,n}}. \tag{11}$$

Vehicle Resistance

In operation, the tractive effort needs to overcome vehicle resistances and inertias. In steady-state operation, vehicle resistance consists of rolling resistance, aerodynamic drag, and gravity component along the vehicle moving direction during climbing a grade. In acceleration, the tractive effort also needs to overcome the vehicle inertias for picking up its speed.

Rolling Resistance Rolling resistance stems from the energy loss inside tire due to hysteresis effect of rubber materials and deformation of road surface [1, 2]. When vehicle is running on well-prepared hard road, the rolling resistance is mainly caused by tire hysteresis effect. However, when vehicle is running off-road, the ground deformation becomes the major factor.

The rolling resistance is usually interpreted by a rolling coefficient, f_r defined as the horizontal force acting on the wheel rotating center, which maintains the wheel rotating on a road while unit load acting on the wheel center perpendicular to the road surface as shown in Fig. 9.

The rolling resistance of a vehicle is mathematically expressed as

$$F_r = M\,g\,f_r \cos\alpha, \tag{12}$$

where M is vehicle mass, g is gravity acceleration, 9.81 m/s^2, f_r is the rolling resistance coefficient, and α is the road grade angle as shown in Fig. 12.

The rolling coefficient is close to the tire and road conditions, such as tire material, tire structure, temperature, inflation pressure, tread geometry, road roughness, and presence of liquid on the road. In vehicle performance evaluation, at not very high speeds, rolling resistance can be taken as constant. Typical values on various roads are listed in Table 1 [1].

Vehicle speed should be taken in account for more accuracy at high speeds. Many experiments have been performed for determination of the effect of vehicle speed to the rolling resistance. Many empirical formulas have been proposed for

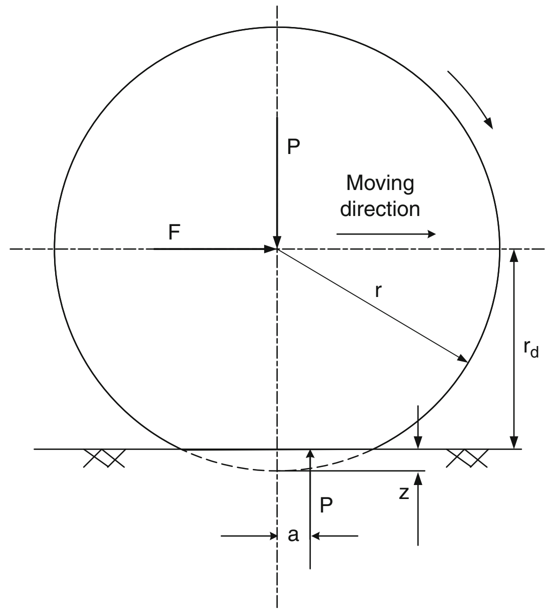

Vehicle Dynamics and Performance. Figure 9 Rolling resistance due to hysteresis effect inside tire material [2]

Vehicle Dynamics and Performance. Table 1 Rolling resistance coefficient [1]

Conditions	Rolling resistance coefficient
Car tire on a concrete or asphalt road	0.013
Car tire on a rolled gravel road	0.02
Tar macadam road	0.025
Unpaved road	0.05
Field	0.1–0.35
Truck tire on concrete or asphalt road	0.006–0.01
Wheel on iron rail	0.001–0.001

calculation of rolling resistance coefficient on hard road. For example, the rolling resistance coefficient for a passenger car running on concrete road may be calculated by [1]

$$f_r = f_0 + f_s\left(\frac{V}{100}\right)^{2.5}, \tag{13}$$

where V is vehicle speed in km/h, and f_0 and f_s depend on inflation pressure of the tire [1]. For most common range of tire pressure, the rolling resistance coefficient of passenger cars on hard concrete road may be estimated by [1]

$$f_r = 0.01\left(1 + \frac{V}{160}\right). \tag{14}$$

This equation is effective to predict acceptable accuracy for speeds up to 128 km/h [1].

Aerodynamic Drag A moving vehicle in air subjects a force that resists the vehicle's motion. This force is referred to as aerodynamic drag. The aerodynamic drag is mainly resulted from the pressure difference between front and back of the vehicle as shown in Fig. 10. When the vehicle is moving, high-pressure areas are formed ahead of the vehicle. On the other hand, low-pressure areas are also formed behind the vehicle. The pressure difference between the high pressure in front of the vehicle and low pressure behind the vehicle results in a resultant force that tries to stop the vehicle. One effective approach to reduce the aerodynamic drag is to design the vehicle body shape for minimizing the areas of both high pressure and low pressure.

Aerodynamic drag of a vehicle in Newton is calculated by

$$F_w = \frac{1}{2} C_D \rho_a A_f (V - V_w)^2, \tag{15}$$

where C_D is the aerodynamic drag coefficient that is determined by the vehicle body shape, ρ_a is the air density, 1.205 kg/m^3 for close earth surface, A_f is the front area of the vehicle body, V is the vehicle speed in m/s, and V_w is the wind velocity component in the vehicle moving direction, which has a positive value when this component in the same direction of the vehicle speed and negative when it is opposite to the vehicle speed. Typical values of aerodynamic drag for various types of vehicles are shown in Fig. 11 [3].

Grading Resistance The weight of a vehicle running on a grade produces a component that always directs toward downhill as shown in Fig. 12. This gravity weight component is a resistance for uphill and a drive force for downhill. For vehicle performance evaluation, only uphill operation is considered.

From Fig. 12, the grading resistance can be expressed as

$$F_i = M\,g\,\sin\alpha. \tag{16}$$

For simplifying calculation, $\sin\alpha$ is usually replaced by a grade value, i, with a small road angle. The road grade is defined as

$$i = \frac{H}{S} = \tan\alpha \approx \sin\alpha. \tag{17}$$

Further, the grading resistance can be expressed as

$$F_i = M\,g\,i. \tag{18}$$

Inertia Force When a vehicle is in acceleration, its translational and rotational inertias induce reaction force and reaction torque that are against the driving force and driving torque. For translational vehicle mass, the corresponding inertial force can be simply written as

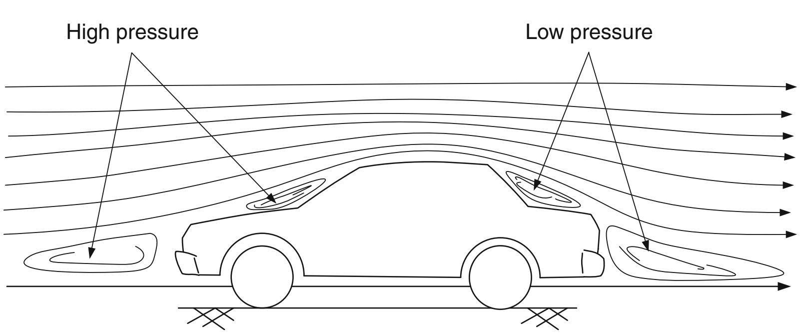

Vehicle Dynamics and Performance. Figure 10
Formation of aerodynamic drag

Vehicle type		Coefficient of aerodymanic drag
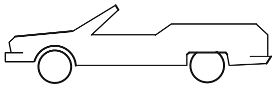	Open convertible	0.5–0.7
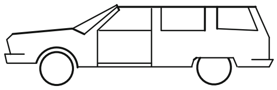	Van body	0.5–0.7
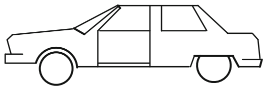	Ponton body	0.4–0.55
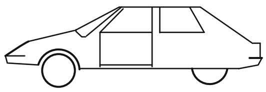	Wedged-shaped body; headlamps and bumper are integrated into the body, covered underbody, optimized cooling	0.3–0.4
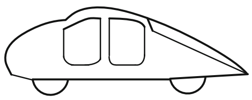	Headlamp and all wheels in body, covered underbody	0.2–0.25
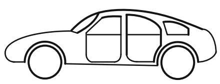	K-shaped (small reaksway section)	~ 0.23
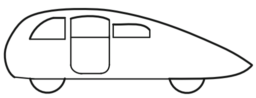	Optimum streamlined design	0.15...0.20
Trucks, road trains		0.8–1.5
Buses		0.6–0.7
Streamlined buses		0.3–0.4
Motorcycles		0.6–0.7

Vehicle Dynamics and Performance. Figure 11
Aerodynamic drag coefficients of various body shapes [3]

$$F_{a-l} = M\,\frac{dV}{dt}. \tag{19}$$

where dV/dt is the acceleration rate of the vehicle in m/s^2.

Along vehicle power line, there are many rotating components whose angular acceleration is related to the vehicle liner acceleration through gear ratios and wheel radius. For simplifying calculation, the rotational inertias are equivalently converted into translational inertia, which uses equal kinetic energy approach.

Suppose that a rotating component, i, in the drive line has the moment of inertia of J_i, and gear ratio of i_i to the drive wheel, using the equal kinetic energy principle, one obtains

$$\frac{1}{2}M_{i-e}V^2 = \frac{1}{2}J_i\omega_i^2. \tag{20}$$

where M_{i-e} is the equivalent linear mass inertia of rotating component i, V is the vehicle speed, and ω_i is the angular speed of the rotating component i. Thus, M_{i-e} can be expressed as

$$M_{i-e} = J_i\frac{\omega_i^2}{V^2}. \tag{21}$$

since ω_i and V have the relationship as

$$V = \frac{\omega_i\, r}{i_i} \tag{22}$$

Thus, (21) can be further expressed as

$$M_{i-e} = J_i\frac{i_i^2}{r^2} \tag{23}$$

where r is the radius of the drive wheel.

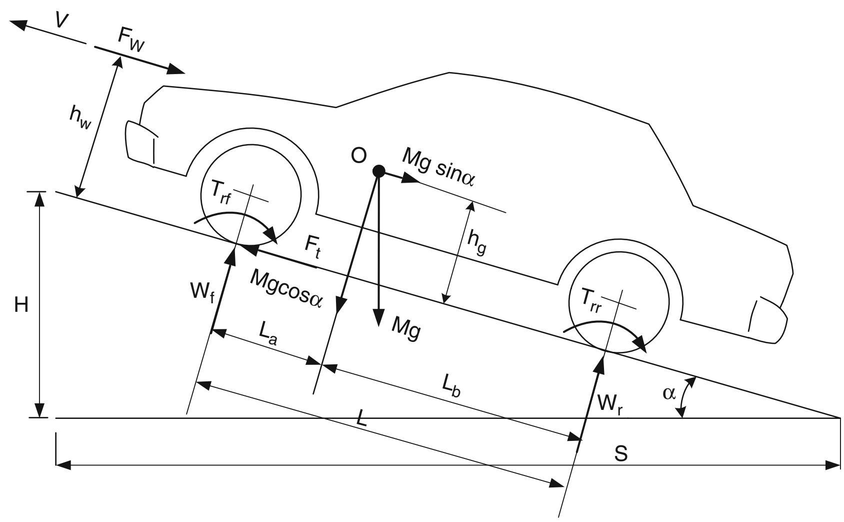

Vehicle Dynamics and Performance. Figure 12
Forces acting on uphill vehicle

In vehicle acceleration performance analysis, only relative large rotating inertias are considered, typically the engine shaft components, such as flywheel, and running wheels. The equivalent translational mass inertia can be expressed as

$$M_{eq} = \frac{J_e\, i_0^2\, i_g^2}{r^2} + \frac{J_w}{r^2} \tag{24}$$

where J_e is the moment of inertia of the rotating components that are attached on the engine shaft, i_0 and i_g are the final drive and transmission gear ratios, respectively, and J_w is the total moment of inertia of all wheels.

The total inertial force can be expressed as

$$F_a = (M + M_{eq})\frac{dV}{dt} = M(1 + \frac{M_{eq}}{M})\frac{dV}{dt} = M\delta\frac{dV}{dt} \tag{25}$$

where $\delta = (1 + M_{eq}/M)$ is defined as the equivalent mass factor.

Calculating equivalent mass factor, δ, needs to know the moments of inertia of all the rotating components. In the case of not knowing these values, δ of passenger cars would be estimated by empirical equation as

$$\delta = 1 + \delta_1 + \delta_2 i_0^2\, i_g^2 \tag{26}$$

where δ_1 represents the term that is related to the moment of inertia of running wheels with a estimated value of 0.04 and δ_2 represents the term that is related to the moments of inertia of the engine-attached components with an estimated value of 0.0025 [2].

Vehicle Performance

Vehicle performance represented by maximum speed, gradeability, and acceleration is completely determined by the vehicle tractive effort developed by the engine or electric motor and the resistance in the vehicle motion direction. Figure 12 illustrates the forces acting on a vehicle, which is running uphill.

The forces acting on the vehicle in the vehicle moving direction are tractive effort, F_t, and resistances including rolling resistance, aerodynamic drag, grading resistance, and inertial force induced by acceleration. All these forces are always in a balanced state, which can be described by

$$F_t = F_r + F_w + F_i + F_a, \tag{27}$$

or more detail

$$\begin{aligned} \frac{T_e\, i_0\, i_g \eta_t}{r} =& M\, g\, f_r \cos\alpha + \frac{1}{2} C_D \rho_a A_f V^2 \\ &+ M\, g\, \sin\alpha + M\,\delta\frac{dV}{dt}. \end{aligned} \tag{28}$$

When grade angle α is small, $\cos\alpha \approx 1$ and $\sin\alpha \approx \tan\alpha = i$. Equation 28 can further be written as

$$\frac{T_e\, i_0\, i_g \eta_t}{r} = M\,g\,f_r + \frac{1}{2} C_D \rho_a A_f V^2 + M\,g\,i + M\,\delta \frac{dV}{dt} \tag{29}$$

Equation 28 or 29 interprets the general operation behavior of a vehicle and is used to analyze vehicle performance. Depicting (29) using a tractive effort versus rolling resistance and aerodynamic drag on grade road is very helpful for vehicle performance analysis as shown in Figs. 13 and 14.

1. Maximum vehicle speed

   The maximum speed of a vehicle is defined as the speed that can be reached when the power plant operates with its maximum capability (full open throttle for an IC engine and maximum current for an electric motor) on a flat road. Running on its maximum speed, no grading resistance and inertia force exists. Thus, (29) becomes

$$\frac{T_e\, i_0\, i_g \eta_t}{r} = M\,g\,f_r + \frac{1}{2} C_D \rho_a A_f V^2. \tag{30}$$

   On the diagrams of Figs. 13 and 14, maximum speed of vehicle can be obtained as the intersection of the tractive effort curve and the resistance curve at zero grade road.

2. Gradeability

   Gradeability of a vehicle is defined as the road grade or grade angle that the vehicle can overcome at a specified speed, for example, 100 km/h, or the maximum grade at low speed. While running on an uphill grade with constant speed, 28 and 29 become

$$\frac{T_e\, i_0\, i_g \eta_t}{r} = M\,g\,f_r \cos\alpha + \frac{1}{2} C_D \rho_a A_f V^2 + M\,g \sin\alpha \tag{31}$$

and

$$\frac{T_e\, i_0\, i_g \eta_t}{r} = M\,g\,f_r + \frac{1}{2} C_D \rho_a A_f V^2 + M\,g\,i \tag{32}$$

The gradeability can be directly obtained by reading Figs. 13 and 14. For instance, for the gasoline engine–powered vehicle, running at 100 km/h, gradeabilities of 5.5° (9.6%) for fourth gear, 7.5°

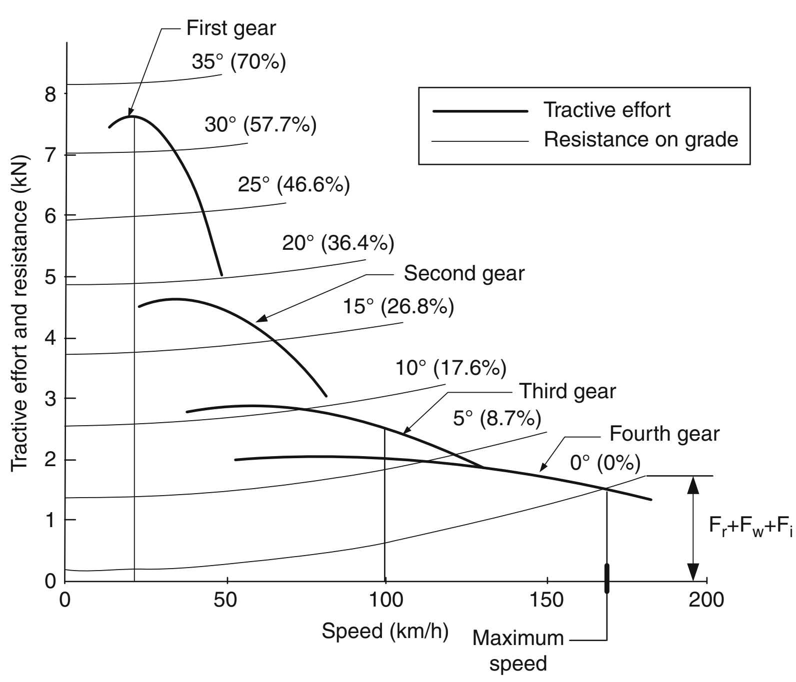

Vehicle Dynamics and Performance. Figure 13
Tractive effort versus vehicle resistance for a gasoline engine–powered vehicle [2]

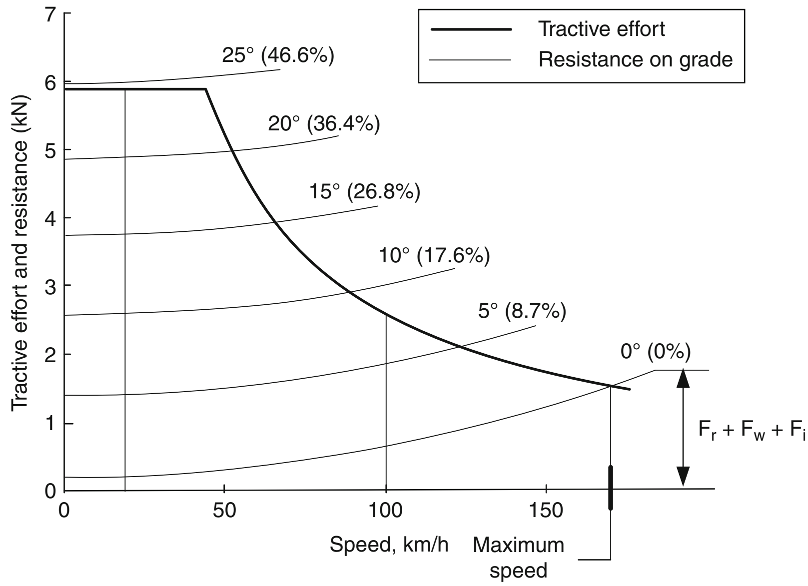

Vehicle Dynamics and Performance. Figure 14
Tractive effort versus vehicle resistance for an electric motor–powered vehicle [2]

(13%) for third gear, and 32.5° (63.7%) at speed of about 20 km/h are obtained. Similarly, for the electric motor–powered vehicle, around 8° (14%) at the speed of 100 km/h and 24° (44.5%) at speeds lower than 50 km/h are obtained.

3. Acceleration performance

Acceleration performance of a vehicle is interpreted by the time used for accelerating the vehicle from a low speed (general zero speed) to a specified high speed (e.g., 100 km/h) on a level road. The acceleration time can be calculated by

$$t = \int_0^{V_f} \frac{1}{a} dV. \quad (33)$$

where V_f is the specified final speed and a is the acceleration rate in m/s^2, which can be obtained from (29) as

$$a = \frac{dV}{dt} = \frac{\frac{T_e\, i_0\, i_g \eta_t}{r} - M\, g\, f_r + \frac{1}{2} C_D \rho_a A_f V^2}{M\, \delta} \quad (34)$$

The distance covered during acceleration can be calculated by

$$d = \int_0^{t_a} V dt \quad (35)$$

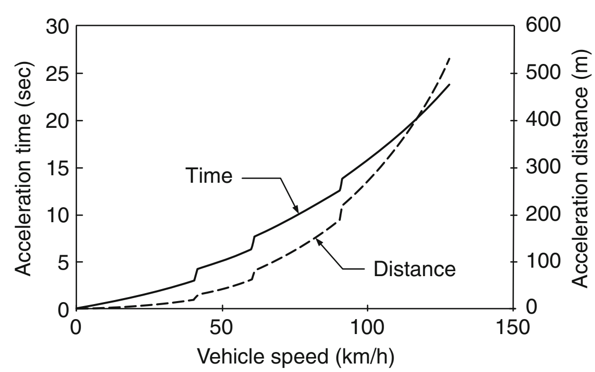

Vehicle Dynamics and Performance. Figure 15
Acceleration time and distance of a gasoline engine–powered vehicle with a four-gear transmission

A digital integration method may be used to solve (33)–(35). Figures 15 and 16 show the acceleration time and distance for a gasoline engine–powered and electric motor–powered vehicle.

Fuel Economy and Energy Consumption

Fuel economy is one of the most important performances of a vehicle, which is evaluated by the fuel consumed in number of liters per 100 km. In the

United States it is usually evaluated by the mileages per gallon fuel. In electric energy–driven vehicle, it is usually evaluated by kilowatt-hour (kWh) number of electric energy per unit traveling distance (km or mile). In plug-in hybrid vehicle, both fuel consumption and electric energy consumption are used at the same time.

Obviously, fuel and electric energy consumptions are associated with driving environments, typically, on highway and in urban. Highway driving is characterized by almost constant speeds. However, frequent stop-and-go is the common driving pattern in urban. These two very different driving patterns result in different fuel and energy consumptions. A vehicle specification usually lists the values for both highway and city driving.

Fuel and energy consumptions are determined by the energy consumed to overcome the vehicle resistances and the efficiency of the power train.

For engine-powered vehicle, the engine is the most inefficient component and its efficiency depends very much upon its operating points in terms of speed and torque or power. In practice, fuel usage efficiency of an engine is evaluated by fuel grams consumed per kWh energy output from its shaft, which is referred to as specific energy consumption (g/kWh). The typical fuel consumption characteristic of a gasoline engine is shown in Fig. 17 [2].

Fuel consumption varies with the operating points of the engine. The most efficient operating points are close to its full open throttle operation. At a given output power, the engine running at lower speed (point *a* in Fig. 17) results in lower fuel consumption than at higher speed (point *b* in Fig. 17). That is the reason that running in high-speed gear is more efficient than in low-speed gear. The transmission with more gears increases the chance for the engine operating close to its optimum operation line. Ideally,

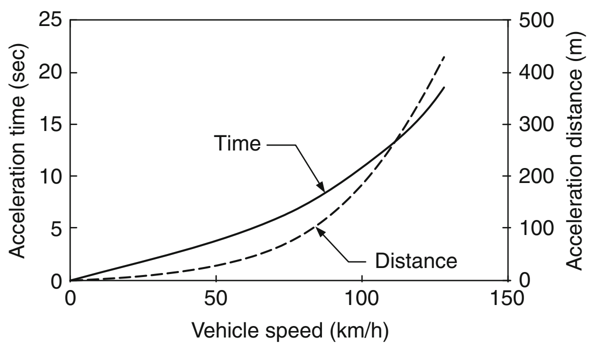

Vehicle Dynamics and Performance. Figure 16
Acceleration time and distance of an electric motor–powered vehicle with single-gear transmission

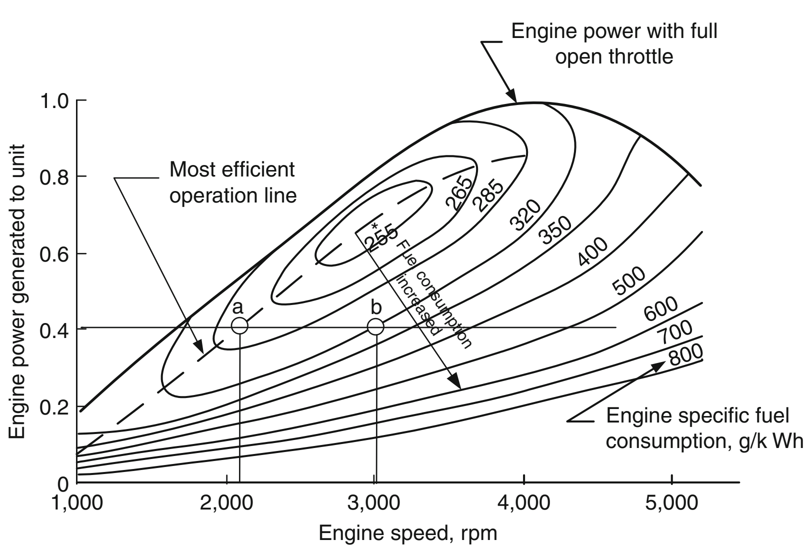

Vehicle Dynamics and Performance. Figure 17
Fuel consumption characteristics of a gasoline engine [2]

a continuous variable transmission (CVT) is capable of choosing a gear ratio that, at any driving condition, can operate the engine at its optimum line.

Based on the specific fuel consumption of engine, the fuel consumption rate (fuel amount consumed in unit time) of the engine can be determined by

$$Q_t = \frac{P_e\, g_e}{1000\gamma_f} \quad (\text{liter/h})\,, \tag{36}$$

where P_e is the engine power in kW, g_e is the specific fuel consumption (g/kWh) of the engine, which depends on its operating point (speed vs. power), and γ_f is the mass density of the fuel in kg/L. The engine power can be calculated by

$$P_e = \frac{V}{\eta_t}(F_a + F_w + F_i + F_a). \tag{37}$$

Specific fuel consumption of the engine, g_e, can be obtained on the fuel consumption characteristic map (Fig. 17) with respect to the engine speeds, which can be determined by the vehicle speed and gear ratio as

$$N_e = \frac{30\, i_0\, i_g}{\pi\, r} V. \tag{38}$$

With constant speed, fuel consumption of a vehicle in a driving distance, S, is obtained by

$$Q_t = \frac{P_e\, g_e}{1000\gamma_f}\frac{S}{V}. \tag{39}$$

Since the complexity of vehicle operation in real world, fuel consumption at constant speeds cannot reflect the real fuel consumption scenario. Various driving cycles have been developed to emulate the real operation of a vehicle in specific driving environments. Figure 18 shows some typical driving cycles.

Driving cycles are interpreted by vehicle speed profiles versus driving time. For calculation of vehicle fuel consumption in a cycle, numerical computing method is usually used. The whole cycle is divided into many time intervals, usually 1 s, then, the fuel consumption in each time interval is calculated. The fuel consumption in the whole cycle can be obtained by summation of the fuel used in all the time intervals.

Figures 19 and 20 show the fuel consumption of a vehicle and engine operating points overlapping the engine fuel consumption map in FTP 75 urban and highway driving cycles [2]. It can be seen from these two diagrams that the engine operating points are far away from its most efficient area. This is one of the major reasons why conventional vehicle is inefficient, which hybrid technologies intend to cure.

Vehicle Braking Performance

Braking performance of a vehicle is one of the most important requirements. The basic requirements of a vehicle brake system includes (1) fast reducing vehicle speed to complete stop, (2) braking effectiveness sustainability, and (3) maintaining vehicle stability during braking. Meanwhile, when a vehicle operates with stop-and-go pattern in urban areas, significant amount of energy is consumed, which is one of the major factors that result in low fuel efficiency. With more and more involvement of electric tractions, such as electric vehicle, hybrid electric vehicle, and fuel cell electric vehicle, braking energy recovery are becoming practice, in which, the kinetic energy of the vehicle body can be converted into electric energy by an electric machine. The recovered energy is charged into on-board energy storage, mostly chemical batteries, and can be reused in later traction. This is called regenerative braking. In vehicle brake system design, a new requirement is added, that is, recovering braking energy as much as possible. Nevertheless, braking safety is still the primary consideration.

Vehicle behavior during braking is determined by the reaction between the braking force and road. The basic requirements are to supply sufficient braking force to quickly stop the vehicle and at the same time, maintain the vehicle running direction stable and controllable.

Braking Force

Braking force of a vehicle determines the deceleration rate. Effective braking force is determined by two factors. One is the braking torque developed by the brake system and the other is the road adhesive condition. When braking force is not large enough to lock the vehicle wheels, the braking force is determined by the braking torque generated by the braking system. However, when the wheels are locked, the braking force depends solely on the road adhesive condition.

Figure 21 shows a braked wheel. The brake pad is pushed against the brake plate, generating a braking torque around the wheel's rotating center. This braking torque induces a braking force in the tire-ground

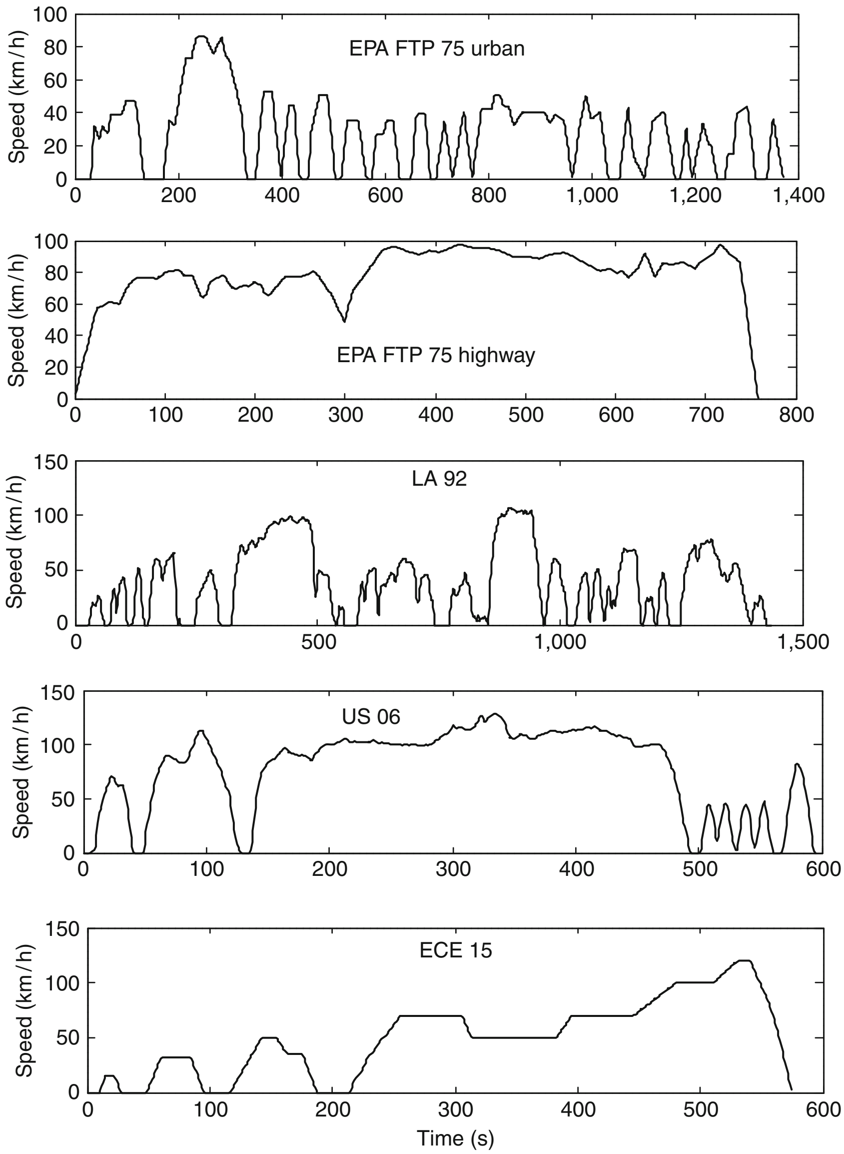

Vehicle Dynamics and Performance. Figure 18
Some typical driving cycles

contact area. In the case of unlocked wheel, the braking force is proportional to the braking torque as

$$F_b = \frac{T_b}{r}. \tag{40}$$

However, when the braking force goes up until locking the wheel, the braking force is completely determined by the road adhesive capability, as shown in Fig. 22, which is expressed as

$$F_{b\max} = \mu W, \tag{41}$$

where W is the vertical load between the wheel and ground and μ is the adhesive coefficient of the wheel to ground. A well-prepared road has high adhesive coefficient. Contrary, a slippery road has low adhesive coefficient. Generally, adhesive coefficient is a function of wheel slip, s, as shown in Fig. 23. The wheel slip is defined as

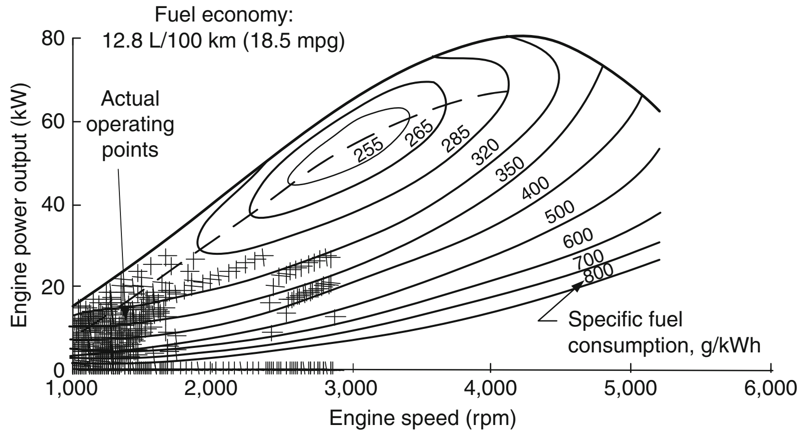

Vehicle Dynamics and Performance. Figure 19
Fuel consumption and engine operating points in EPA FTP 75 urban driving cycle [2]

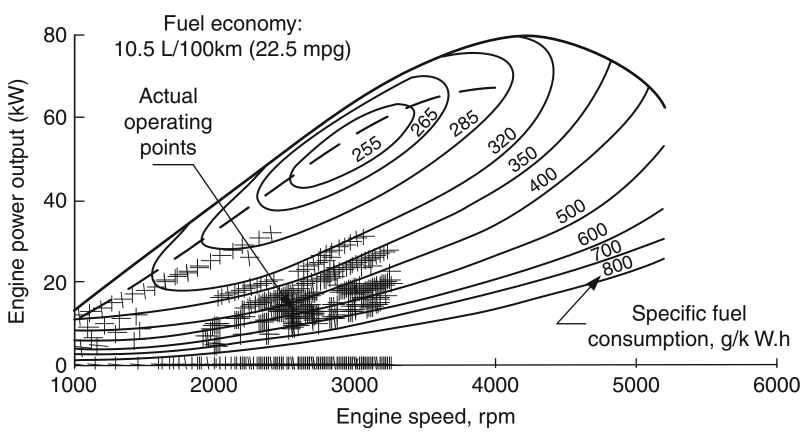

Vehicle Dynamics and Performance. Figure 20
Fuel consumption and engine operating points in EPA FTP 75 highway driving cycle [2]

$$s = \left(1 - \frac{r\,\omega}{V}\right) \times 100\%, \tag{42}$$

where V is vehicle speed (the translator speed of the wheel center), ω is angular speed of the wheel, and r is the wheel radius. With a free rotating wheel, $r\omega = V$ and $s = 0$. On the other hand, with a locked wheel, $\omega = 0$ and $s = 100\%$.

Figure 23 indicates that with a small slip (between 0 and A), the adhesive coefficient is almost linearly proportional to the slip value. In this case, no obvious slip occurs in the wheel-ground area. The small slip is caused by the elastic property of the tire. Further increase in the braking force will cause actual slip at some points in the contact area. With increase in the braking force, more and more points go into slipping. In this case, the relationship between the slip and adhesive coefficient is nonlinear with a small increase rate. The adhesive coefficient reaches its maximum at a slip of about 15–20%. Beyond this peak point, the wheel will become unstable and is quickly locked up, even no further increase in the braking force. The adhesive coefficient at complete slipping is generally named as slipping value, which is smaller than the peak value.

It should be noted that the adhesive coefficient in lateral direction drops monotonously with the increase

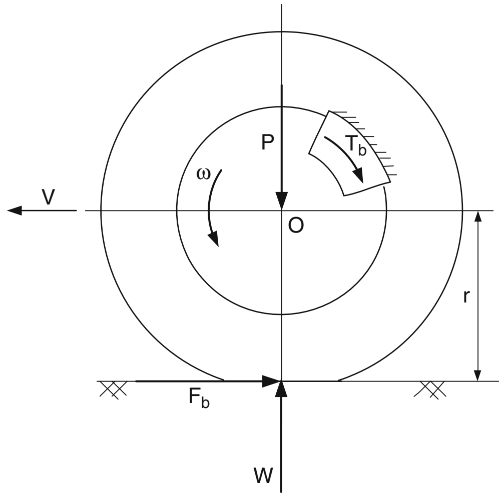

Vehicle Dynamics and Performance. Figure 21
Braking torque and braking force on a braked wheel

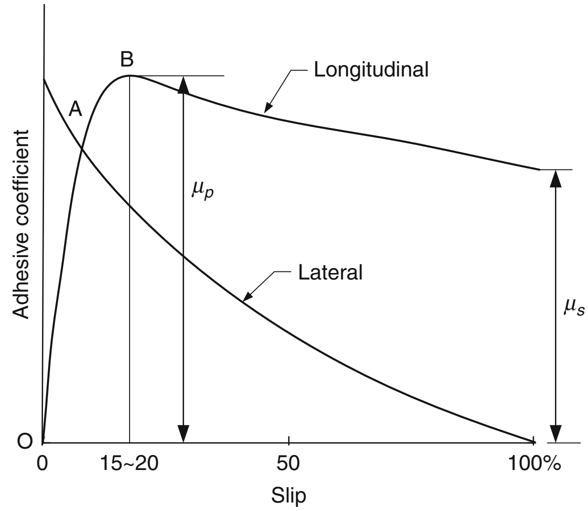

Vehicle Dynamics and Performance. Figure 23
Adhesive coefficient varying with wheel slip

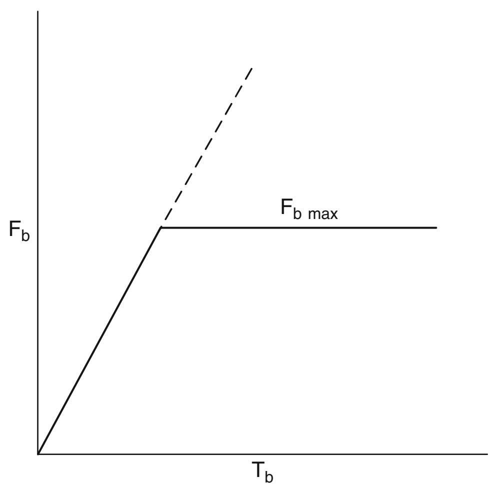

Vehicle Dynamics and Performance. Figure 22
Braking force versus braking torque

Vehicle Dynamics and Performance. Table 2 Average values of adhesive coefficient on various roads [1, 2]

Surface	Peaking values, μ_p	Slipping values, μ_s
Asphalt and concrete (dry)	0.8–0.9	0.75
Concrete (wet)	0.8	0.7
Asphalt (wet)	0.5–0.7	0.45–0.6
Grave	0.6	0.55
Earth road (dry)	0.68	0.65
Earth road (wet)	0.55	0.4–0.5
Snow (hard packed)	0.2	0.15
Ice	0.1	0.07

of wheel slip. At complete locked wheel, it becomes close to zero. Lateral adhesive coefficient represents the capability of resisting lateral disturbance. A completely locked wheel loses this capability, consequently, leading to unstable vehicle behavior during braking. Anti-lock brake systems (ABS) have been developed in order to prevent wheels from being completely locked, therefore improving vehicle braking stability.

Table 2 shows the average values of adhesive coefficients on various roads [1, 2].

Braking Strength and Braking Force Distribution on Front and Rear Wheels

Braking strength is defined as the deceleration rate, m/s^2 or g (g = 9.81 m/s^2), which is completely determined by the total forces acting on the vehicle in the opposite direction of the vehicle travel. Rolling

resistance and aerodynamic drag also functions as braking forces. However, they are quit small, compared to road braking force, and ignored in braking performance analysis.

Figure 24 shows all the forces acting on a vehicle during braking on a flat road, where j is the braking strength in m/s^2, and F_{bf} and F_{br} are the braking forces acting on the front and rear wheels, respectively. The braking strength, j can be expressed as

$$j = \frac{F_{bf} + F_{br}}{M}, \tag{43}$$

where M is the vehicle mass.

It is considered to be ideal design for distribution of the total braking force on front and rear wheels in such a way that the slips on the front and rear wheels are always equal. This strategy can ensure front and rear wheels reach their maximum road adhesion at the same time, consequently, achieving the shortest braking distance. This approach is interpreted as that the braking forces are proportional to their vertical loads, which is expressed as

$$\frac{F_{bf}}{W_f} = \frac{F_{br}}{W_r} \tag{44}$$

Referring to Fig. 24, the vertical loads on front and rear wheels can be obtained as

$$W_f = \frac{M\,g}{L}\left(L_b + h_g\frac{j}{g}\right), \tag{45}$$

and,

$$W_r = \frac{M\,g}{L}\left(L_b - h_g\frac{j}{g}\right). \tag{46}$$

Then, (44) can be further expressed as

$$\frac{F_{bf}}{F_{br}} = \frac{L_b + h_g j/g}{L_a - h_g j/g}. \tag{47}$$

Equations 43 and 47 dictate the ideal braking force distribution on front and rear wheels, which can further be written as

$$F_{br} = \frac{M\,g}{2h_g}\sqrt{L_b^2 + \frac{4h_g L}{M\,g}F_{bf}} - \left(F_{bf} + \frac{M\,g\,L_b}{2h_g}\right) \tag{48}$$

Figure 25 shows the ideal distribution curve (simply I curve), which has a parabolic shape. This figure also shows two sets of lines that represent (43) and (47) with respect to various braking strengths. When the braking forces reach their maximum values determined by the wheel-road adhesion, the maximum braking strength is achieved as

$$j_{\max} = \frac{F_{bf\,\max} + F_{br\,\max}}{M} = \frac{(W_f + W_r)\mu}{M} = g\mu. \tag{49}$$

Due to the nonlinear property of the ideal braking force distribution curve, design of a brake system to follow the ideal distribution curve becomes complicated. However, implementation of advanced electronic control may make this happen.

In practice, braking forces on front and rear wheels are usually designed to have a linear relationship.

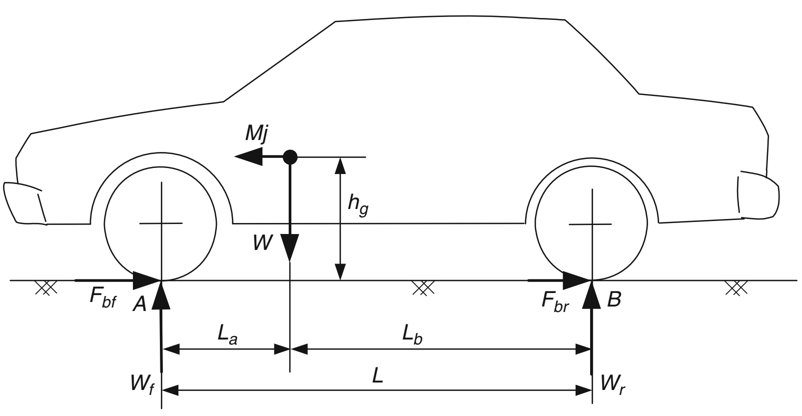

Vehicle Dynamics and Performance. Figure 24
Forces acting on a vehicle during braking

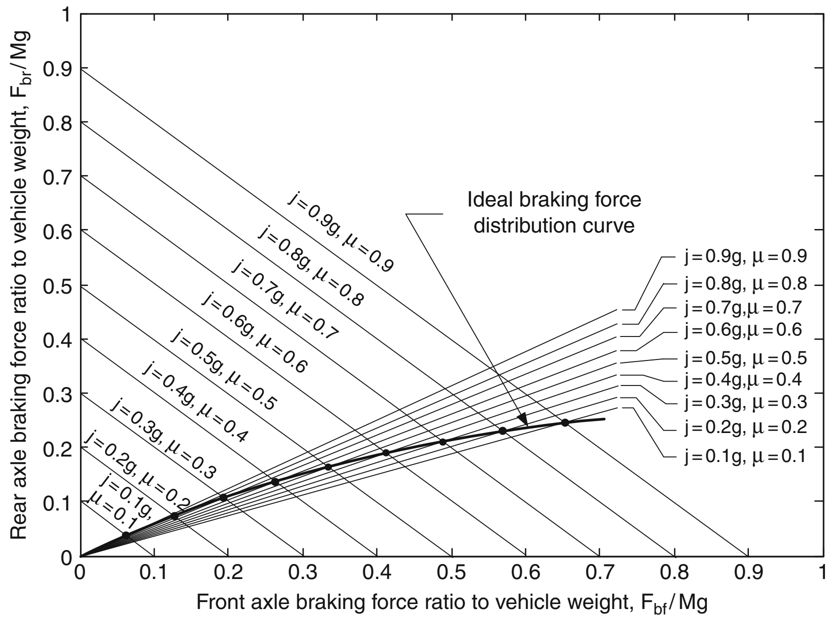

Vehicle Dynamics and Performance. Figure 25
Ideal braking force distribution on front and rear wheels [2]

The proportion is represented by a ratio of the braking force on front wheel to the total braking force of the vehicle, that is,

$$\beta = \frac{F_{bf}}{F_b} = \frac{F_{bf}}{F_{bf} + F_{br}}. \tag{50}$$

β is determined by the brake system design, such as the diameters of front and rear wheel cylinders. For a given β, the applied braking forces on the front and rear wheels can be expressed as

$$F_{bf} = \beta F_b, \tag{51}$$

and

$$F_{br} = (1 - \beta) F_b, \tag{52}$$

and then

$$\frac{F_{bf}}{F_{br}} = \frac{\beta}{1 - \beta} \tag{53}$$

The braking force distribution represented by (53) is different from that described by (48) as shown in Fig. 26. One intersection point of these two lines exists, at which both front and rear wheels have the same slips, or both wheels are locked at the same time. This point specifies a specific adhesive coefficient, μ_0. Referring to (47), in which j/g is replaced by μ_0, one obtains

$$\frac{\beta}{1 - \beta} = \frac{L_b + h_g \mu_0}{L_a - h_g \mu_0}. \tag{54}$$

From (54), one obtains

$$\mu_0 = \frac{L\beta - L_b}{h_g} \tag{55}$$

As shown in Fig. 26, μ_0 divides the whole range into two sections. While braking on the road with an adhesive coefficient less than μ_0, front wheels are locked prior to rear wheels. Otherwise, rear wheels are locked prior to front wheels.

Braking Stability

As discussed in a previous section, completely locked wheels will lose their capacity of resisting lateral disturbance. Consequently, any disturbance, such as wind, uneven road surface, and running along a curve road, would cause significant lateral movement and instability. Much more serious instability would occur with

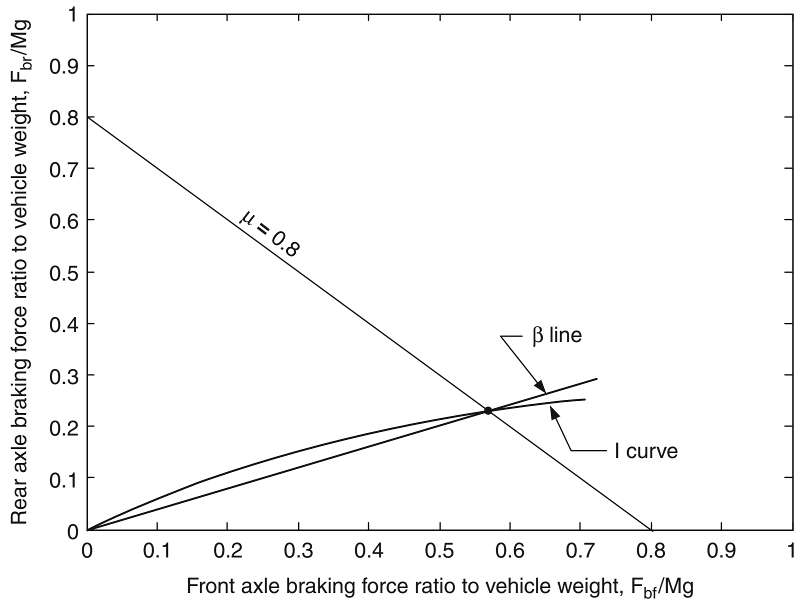

Vehicle Dynamics and Performance. Figure 26
Ideal and actual braking force distribution curve [2]

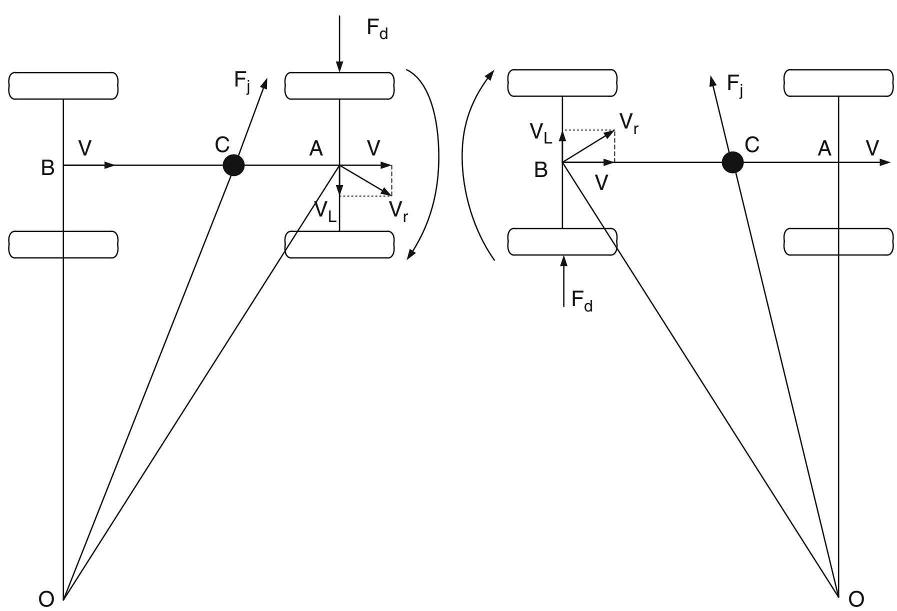

Vehicle Dynamics and Performance. Figure 27
Vehicle behaviors with (**a**) lateral slip on front wheels and (**b**) lateral slip in rear wheels

rear wheels locked than with front wheel locked. This can be interpreted in Fig. 27.

As shown in Fig. 27a, while a lateral slip on front wheels occurring, due to the lateral disturbance force F_d, the vehicle speed changes its motion from straight-forward direction V to a curved running speed, V_r, which causes the whole vehicle body rotating around the point O. At the same time, the curved running of

the vehicle body induces a centrifugal force, F_j, which acts on the gravity center, C, of the vehicle body. It can be seen from Fig. 27a that this centrifugal force has the effect of resisting against the lateral movement of the front wheel. When the disturbance force disappeared, the centrifugal force quickly brings the vehicle back to its straight motion.

While lateral slip occurs on rear wheels due to lateral disturbance, the induced centrifugal force augments the lateral slip, causing the vehicle very instable. Even after the lateral disturbance disappears, the lateral movement may continuous. Experiments have shown that when rear wheels are locked up over 0.5 s prior to the front wheels lockup, serious directional deviation would occur. In extreme case, vehicle body would swing 180° [1].

Front wheel lockup causes losing of steering capability. However, it can be detected more readily by the driver and correction can be made by the driver to release or partial release of the brake pedal. This is a less dangerous than rear wheel lockup swing.

Anti-lock brake system (ABS) can effectively present the wheels from lockup. This system monitors the wheel operation status. When it finds a wheel tending to be locked, a control system reduces the braking force for this wheel and therefore brings the wheels back to its rotation.

Brake Design Regulation

For maintaining braking stability, rear wheel lockup is required not prior to the front wheel lockup. This requirement results in the braking force distribution always below ideal braking force distribution curve (I curve) as shown in Fig. 26. This can be realized by increasing the front wheel braking force and decreasing the rear wheel braking force. However, when most of the braking forces are applied to the front wheels and very small to rear wheels, it would cause a problem of reduced utilization of road adhesive capability. That is, when front wheels are locked and rear wheels are not locked, the maximum braking force of rear wheels is never used. Consequently, the stop distance will be longer. For avoiding this situation, some brake design regulations have been developed. A typical one is the ECE R13 regulation.

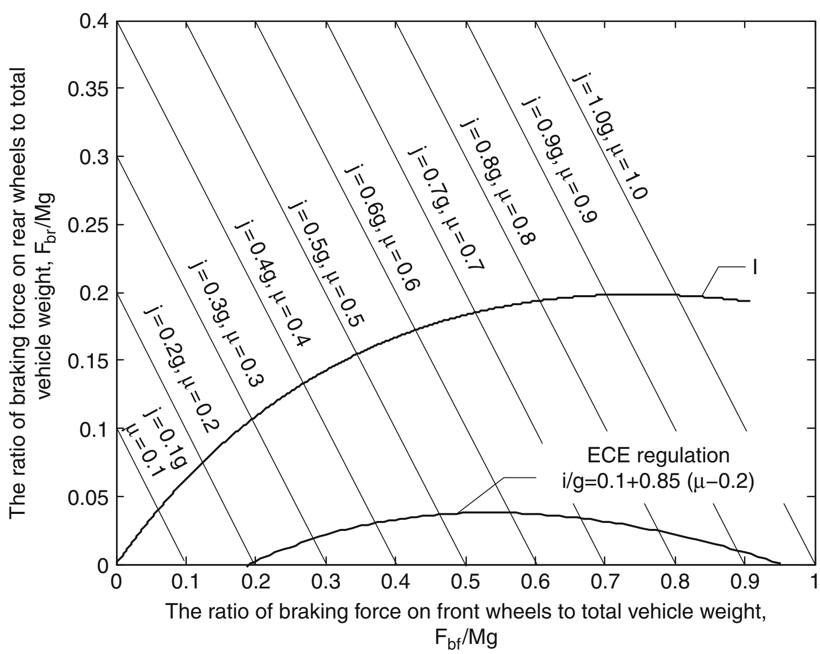

Vehicle Dynamics and Performance. Figure 28
The upper and low boundaries of braking force distribution dictated by ECE regulation

The ECE R13 regulation for passenger cars is represented by

$$\frac{F_{bf}}{W_f} \geq \frac{F_{br}}{W_r}, \tag{56}$$

and,

$$\frac{j}{g} \geq 0.1 + 0.85(\mu - 0.2). \tag{57}$$

Equation 56 dictates rear wheels being never locked prior to the front wheels, that is, β line is always below the I curve. Equation 57 dictates that, with locked front wheel, the braking force on rear wheels must be large enough to ensure to generate a braking strength j/g that is equal to or greater than a value dictated by (57).

Equations 56 and 57 are interpreted in a diagram as shown in Fig. 28. Obviously, the real braking force distribution design must fall into the area between the I curve and ECE regulation curve.

Future Directions

Vehicle system is a very complex system. With rapid development of computing technologies, the analysis methods of vehicle dynamics and performance are becoming more and more accurate and reliable by employing computer-based modeling and simulation. The advanced computing technologies allow solving much more complicated mathematical problems in real time, which was impossible before computer age. Advanced data accessing, acquisition, processing, and control technologies provide great opportunity for vehicle dynamic control to improve vehicle performances.

Advanced electrical propulsion and electric energy storage create a way for high efficiency and clean vehicles that include electric vehicles, hybrid vehicles, and fuel cell vehicles.

Bibliography

Primary Literature

1. Wong JY (1978) Theory of ground vehicles. Wiley, New York
2. Ehsani M, Gao Y, Emadi A (2010) Modern electric, hybrid electric and fuel cell vehicles—fundamentals, theory and design, 2nd edn. CRC press, Boca Raton
3. Bosch R (2000) Automotive handbook. Tobert Bosch GmbH, Karsruhe

Books and Reviews

Gillespie TD (1992) Fundamentals of vehicle dynamics. SAE international, Warrendale

Mizutani S (1992) Car electronics. Sankaido Co., Tokyo

Vehicle Energy Storage: Batteries

Y. S. Wong[1], C. C. Chan[2]
[1]State Grid Energy Research Institute, State Grid Corporation of China, China
[2]Department of Electrical and Electronic Engineering, University of Hong Kong, Hong Kong, China

Article Outline

Glossary

Battery A string of rechargeable electrochemical cells.

Battery electric vehicle An electric vehicle in which the electrical energy to drive the motor(s) is stored in an onboard battery.

Capacity The electrical charge that can be drawn from the battery before a specified cut-off voltage is reached.

Depth of discharge The ratio of discharged electrical charge to the rated capacity of a battery.

Electric vehicle A vehicle in which propulsion torque is delivered exclusively by one or more electric motors.

Energy capacity The electrical energy that can be drawn from the battery before a specified cut-off voltage is reached.

Fuel cell electric vehicle An electric vehicle in which the propulsion energy is delivered from an onboard fuel cell and battery hybrid system.

Hybrid electric vehicle A vehicle in which propulsion energy is provided from two or more kinds or types of energy stores, sources, or converters, and at least one of them delivers electrical energy.

Open circuit voltage The difference of electrical potential between two terminals of a battery when no external load is connected.

Vehicle energy source The onboard energy storage device of a vehicle.

Definition of the Subject

With ever-increasing concerns on energy efficiency, energy diversification, and environmental protection, electric vehicles (EVs), hybrid electric vehicles (HEVs), and low-emission vehicles are on the verge of commercialization. EVs not only offer higher energy efficiency than that of internal combustion engine (ICE) vehicles, but also mitigate one country's dependence on oil by diversifying the energy sources to renewable energies.

Vehicle energy source is bottleneck of EV and HEV commercialization. At present and in the foreseeable future, the viable energy sources for EVs and HEVs are batteries, fuel cells, and ultracapacitors (supercapacitors). The battery is the most mature energy source and it has been the most important component of an EV since commercialization of the first EV. This entry gives an overview of batteries for vehicle applications and discusses the research and development roadmap of next-generation batteries for vehicle applications.

Introduction

The EV has higher energy efficiency than that of the ICE vehicle and it also mitigates the one country's dependence on oil by diversifying the energy sources to renewable energies such as hydro, wind, and solar energies. The EV also facilitates load leveling of power systems and achieves zero local and minimal global vehicular emissions. At present, there is no economically viable energy source for commercialization of EVs.

The battery has been the most important component of an EV since commercialization of the first EV. In 1801, Richard Trevithick built a steam-powered carriage, opening the era of horseless transportation. The first battery-powered electric bicycle was built by Thomas Davenport in 1834. It was powered by a nonrechargeable battery and used on a short track. In 1838, Robert Davidson built a nonrechargeable battery-powered electric locomotive.

After the invention of lead-acid (Pb-Acid) battery in 1859, Sir David Salomons built a rechargeable battery-powered EV in 1874. The first petrol-powered ICE vehicle was built in 1885 and the first HEV was presented by J. Lohner and F. Porsche in 1901.

M. Ehsani et al. (eds.), *Transportation Technologies for Sustainability*, DOI 10.1007/978-1-4614-5844-9,

Originally published in
Robert A. Meyers (ed.) Encyclopedia of Sustainability Science and Technology, © 2012, DOI 10.1007/978-1-4419-0851-3

The ICE vehicle outperformed the EV and HEV in the automotive century because there was no high performance battery for EVs and HEVs to overcome four major barriers to commercialization of EVs and HEVs, namely, short driving range, long charge time, long recharge time, and high life-cycle cost [1].

The battery for EVs has evolved from flooded lead acid (Pb-Acid) battery in 1859 to lithium ion (Li-Ion) polymer in 1999. Table 1 lists some historic events of vehicle batteries. The EV has also evolved a lot but it still holds its position in niche areas, like postal services [2].

The HEV has been introduced as an interim solution before the full implementation of the EV when there is a breakthrough in vehicle energy sources. The HEV extends greatly the driving range of the EV by three to four times and offers rapid fuel refueling. There are several types of EVs and HEVs in the market [3–5].

Technical requirements of batteries for vehicle applications are discussed by analyzing vehicle topologies and energy management systems in EVs' and HEVs' electrical powertrain. Viable batteries for EV and HEV applications are reviewed and the research and development roadmaps are discussed at the end of this entry.

Vehicle Energy Storage: Batteries. Table 1 Vehicle battery history

Year	Inventor	Battery
1859	Raymond Gaston Planté	Planté lead-acid cell
1881	Camille Alphonse Faure	Improved lead-acid cell
1899	Waldmer Junger	Nickel-cadmium cell
1899	Waldmer Junger	Nickel-iron cell
1946	Union Carbide Company	Alkaline manganese secondary cell
1970	Exxon laboratory	Lithium-titanium cell
1980	Moli Energy	Lithium-molybdenum disulfide
1990	Samsung	Nickel-metal hydride
1991	Sony	Lithium ion
1999	Sony	Lithium ion polymer

Electrical Powertrain

Motor drive and battery are two major components of an electrical powertrain in EVs and HEVs. Energy efficiency of motor drives is, intrinsically, higher than that of an ICE. In addition, the electrical powertrain can absorb kinetic energy during braking and assist engine in acceleration in HEVs. Thus, the efficiency improvement of an EV or an HEV over an ICE vehicle depends on power ratings and functionality of the electric motor drive and the onboard batteries [6, 7]. Key motor drive features and battery characteristics are discussed in the following sections.

Motor Drive Features

Regenerative Braking Regenerative braking is a unique feature of an electrical powertrain. The motor drive converts vehicle's kinetic energy back to electrical energy during braking, deceleration, and downhill running. The converted electrical energy is stored in the receptive energy sources such as batteries or ultracapacitors to extend the driving range. If the receptive sources are fully charged up, regenerative braking can no longer be applied and the vehicle is braked by the conventional hydraulic braking system.

Power Boost The HEV allows both the engine and the electric motor to deliver power simultaneously to drive the vehicle. Generally, the engine and electric motor are coupled to the drive shaft of the wheel via two clutches, such that, the propulsion power may be supplied by the engine alone or by both of them. The motor cranks the engine and assists vehicle acceleration for maximization of engine fuel economy.

Battery Characteristics

Electrochemical Batteries The battery refers to the rechargeable electrochemical battery. Electrochemical cell is the basic element of each battery. A connection of a number of cells in series forms a battery. Figure 1 shows the basic components of an electrochemical cell in which both the positive and negative electrodes are immersed in the electrolyte. The electrolyte is an ion-conducting material, which can be in the form of aqueous, molten, or solid solution. The separator is a membrane that physically prevents direct contact

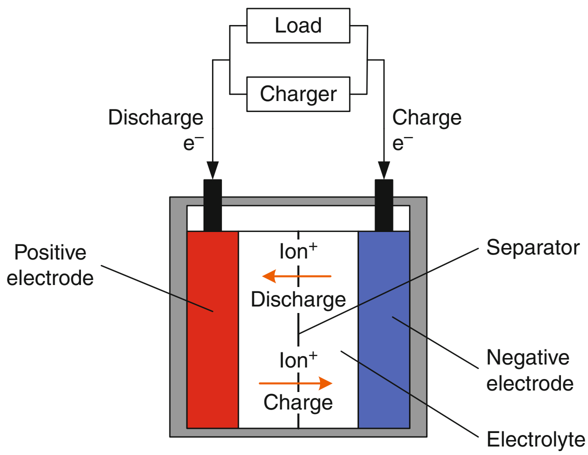

Vehicle Energy Storage: Batteries. Figure 1
Basic components of an electrochemical cell

between the two electrodes and allows ions, but not electrons, to pass through.

During discharge, the negative electrode performs oxidation reaction, which drives electrons to the external circuit, while the positive electrode carries out reduction reaction, which accepts electrons from the external circuit. During charge, the process is reversed so that electrons are injected into the negative electrode to perform reduction while the positive electrode releases electrons to carry out oxidation.

Battery Capacity Energy capacity (EC) of a battery refers to the electrical energy that can be drawn from the battery before a specified cut-off voltage is reached. EC is commonly presented in watt-hour (Wh). Coulometric capacity (C) refers to the total amount of electrical charge that can be drawn from the battery before the specified cut-off voltage is reached. C is typically measured in ampere-hour (Ah). C is widely employed to describe battery capacity, but EC is more common than C in addressing battery capacity in vehicle applications. Both EC and C, intrinsically, depend on the battery design, discharge current, temperature, and cyclic history.

Depth of Discharge and State of Charge Depth of discharge (DoD) and state of charge (SoC) are key parameters in battery energy management systems. DoD refers to the ratio of discharged electrical charge to the rated capacity. SoC refers to the ratio of usable charge to the rated battery capacity. SoC is an indicator of available electrical charge, while DoD is an indicator of discharged charge of a battery. Thus, sum of SoC and DoD of a battery is 100%. The SoC of a fully charged battery is 100% and the DoD is zero. When 20% of the stored charge is dissipated, SoC of this battery reduces to 80% and the DoD rises to 20% correspondingly.

Electrical Efficiency Energy efficiency of a battery refers the ratio of output electrical energy during discharging to the input electrical energy during charging. The energy efficiency is different from the charge efficiency, which is defined as the ratio of discharged charge to the charged charge. For vehicle applications, the energy efficiency is more informative than the charge efficiency. Typical energy efficiency of a battery is 55–75%.

Energy Density and Specific Energy Energy densities of an energy source refer to the usable energy capacity per unit mass or volume. The gravimetric energy density is usually named as the specific energy in watt-hour per kilogram (Wh/kg). The volumetric one is loosely named as energy density in watt-hour per litre (Wh/L). Specific energy is more instructive than the energy density for vehicle batteries because the battery weight is highly correlated with the vehicle fuel economy while the volume only affects the usable space. The specific energy is a key parameter to assess the pure electric driving range. The usable energy capacity greatly varies with discharge rate. The larger the discharge rate, the smaller the usable energy. Generally, specific energy and energy density are quoted with a discharge rate.

Power Density and Specific Power Power densities of a battery denote the deliverable rate of energy per unit mass or volume. The gravimetric power density is named specific power and measured in watt per kilogram (W/kg) and the volumetric power density is named power density and measured in watt per litre (W/L). The specific power changes with DoD. Thus, specific power and power density are quoted with DoD.

Cycle Life Cycle life is a key parameter to describe the service life of a battery based on the storage capacity of the battery. It is defined as the number of charge and

discharge cycles it can undergo before its capability falls to 80% of the rated capacity. Cycle life is greatly affected by DoD of each discharge cycle, thus, it is usually quoted with DoD. For example, a battery can be claimed to offer 500 cycles at 80% DoD and 1,000 cycles at 50% DoD [1].

Calendar Life Calendar life refers to life period of a battery until failure in years. The battery calendar life depends on charge rate, discharge rate, DoD, temperature, and chemistries of the battery.

Power and Energy Demands of EVs and HEVs

EVs and HEVs can be further divided into six types of vehicles according to the demands of energy and power on vehicle batteries. Instead of grouping HEVs by vehicle architecture, it is more informative to group them by functionality of the electrical powertrain, which affects the fuel economy significantly.

HEVs are classified into four specific hybrids: micro hybrid vehicle (MHV), mild hybrid electric vehicle (MHV), full hybrid electric vehicle (FHEV), and plug-in hybrid electric vehicle (PHEV). On the other hand, EVs are classified into battery EV (BEV) and fuel cell EV (FCEV). A BEV is an EV where the electrical energy to drive the motor(s) is stored in onboard rechargeable batteries while an FCEV is an EV making use of fuel cell and battery hybrid system as onboard energy sources [4, 8].

The battery is still the most important component of these vehicles but the requirements on power, energy, cycle life, and system voltage are different. Functionality of the electrical powertrain and the favorable battery voltages in these vehicles are shown in Fig. 2.

Hybrid Electric Vehicles

Energy management strategies of HEVs aim to satisfy four key goals: maximum fuel economy, minimum

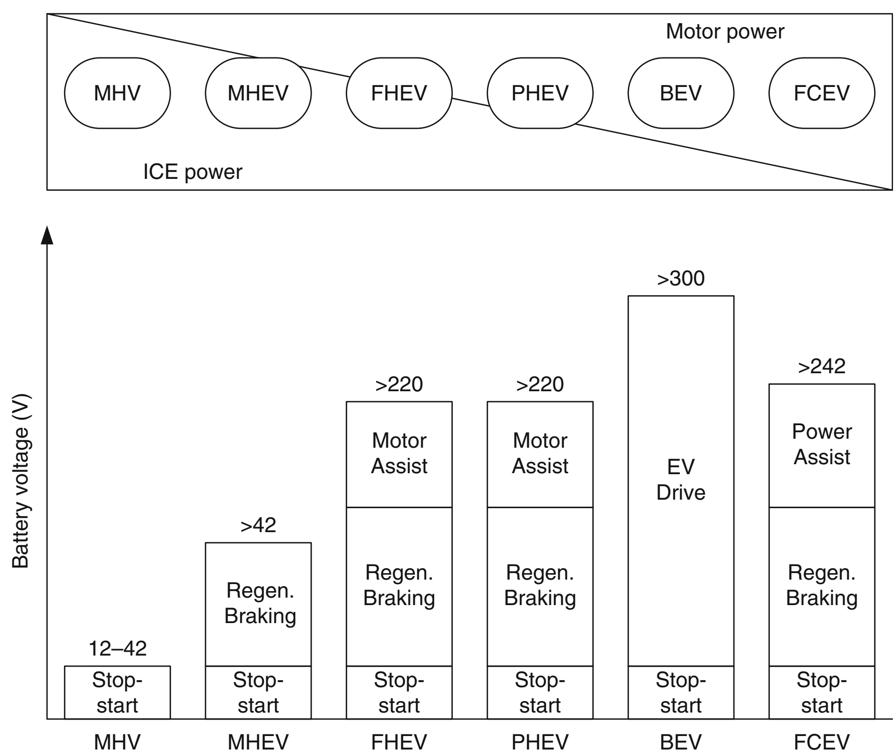

Vehicle Energy Storage: Batteries. Figure 2
Battery operating voltages in EVs and HEVs

emissions, minimum system costs, and high acceleration rate. The major challenges of HEV design are management of multiple energy sources, battery sizing, and battery management. HEVs take the advantages of electric drive to compensate the inherent weakness of engine. HEVs can avoid engine idling and increase the engine efficiency during starting, low-speed, and high-speed operations. HEVs can also absorb energy during regenerative braking [3, 9].

Hybrid Electric Vehicle Configuration The three basic hybrid architectures of HEVs are series, parallel, and series-parallel hybrids. Figure 3 shows the energy paths in these hybrids. The series hybrid couples the engine and the battery by a generator. Both the engine and the battery power the electric motor to propel the vehicle. The parallel hybrid couples the mechanical power from the engine and from the electric motor to propel the vehicle. The series-parallel hybrid is a direct combination of the series and parallel hybrids.

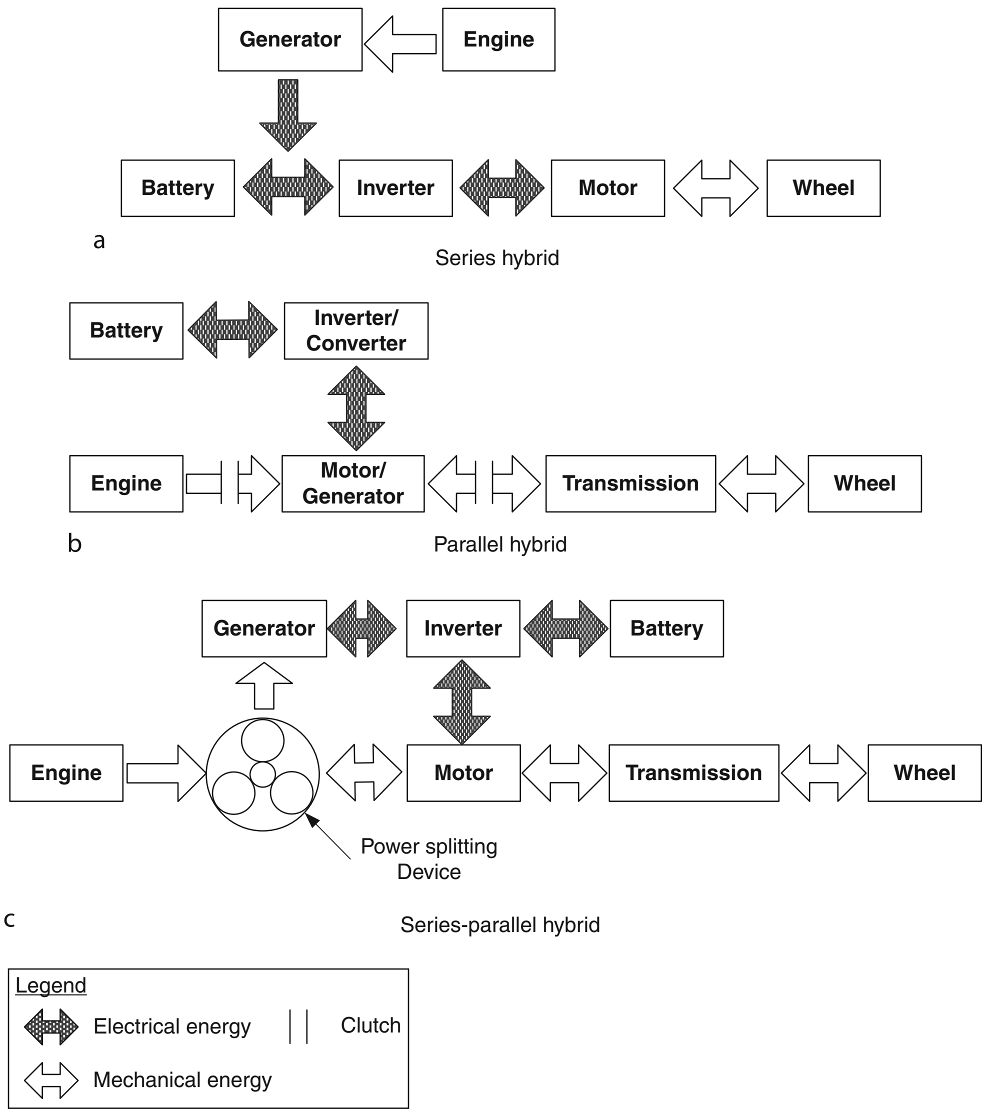

Vehicle Energy Storage: Batteries. Figure 3
Energy flow in series, parallel, and series-parallel HEVs

Vehicle Energy Storage: Batteries. Table 2 Technical data of batteries for MHVs

Parameters	Unit	MHV
Voltage	V	12–42
Discharge power	kW	4.2–6
Low temperature (−28°C) discharge power	kW	>3
Energy capacity	kWh	0.2–1
Operating temperature	°C	−30 to +52
Calendar life	Year	>3

Vehicle Energy Storage: Batteries. Table 3 Technical data of batteries for MHEVs

Parameters	Unit	MHEV
Voltage	V	42–200
Discharge power	kW	>15
Low temperature (−28°C) discharge power	kW	>4
Recharge power	kW	>15
SoC window	%	40–70
Recharge pulse power	kW	>20
Energy capacity	kWh	0.8–1
Operating temperature	°C	−30 to +52
Calendar life	Year	>10

Micro Hybrid Vehicles The MHV has an electric motor with peak power of about 2.5 kW. The electrical powertrain is driven by a battery system at 12–42 V. The motor is small and simple in structure. It can be an integration of starter and alternator in an ICE vehicle. The electrical and mechanical powertrains in an MHV are governed by an automatic stop-start mechanism, in which, the engine shuts down under vehicle braking and rest. The MHV is favorable for city driving, where there are frequent stops and starts. An MHV's fuel economy can be 5–10% higher than that of an ICE vehicle in city driving. The Citroen C3 is an MHV using the Valeo motor system.

The battery discharges frequently in cranking the engine in MHVs. Thus, there is a demand for high cycle life for batteries in MHVs. Table 2 lists some key technical data of batteries for MHVs.

Mild Hybrid Electric Vehicles The MHEV has a more powerful electrical powertrain than an MHV's. The typical electric motor power of a sedan MHEV is about 10–20 kW at 100–200 V. The motor is directly coupled with the engine. The motor has a large inertia such that it can replace the original flywheel of the engine. The motor and the engine are generally coupled in parallel hybrid configuration. Table 3 shows some technical data of batteries for MHEVs. The electrical powertrain is designed to crank the engine and perform regenerative braking during braking. There are demands of high specific power and long service life for batteries in MHEVs. Battery's charge and discharge power depend on its SoC. The battery's discharge power decreases with its SoC. The minimum operating SoC is around 40–50% to uphold sufficient power for launch and acceleration support. On the other hand, the battery's recharging power drops when the SoC is high, thus, the maximum operating SoC is regulated at around 70–80% to maintain sufficient recharge power for regenerative braking. Typically, the batteries operate in an SoC window between 40% and 70%.

Comparing with an ICE vehicle, the MHEV can boost the fuel economy by 20–30% in city driving. MHEVs in the market include Honda Insight Hybrid, Honda Civic Hybrid, and Ford Escape Hybrid.

Full Hybrid Electric Vehicles The FHEV has a high power electrical powertrain to drive the vehicle purely by electricity in a short driving range. The typical electric motor power for sedan FHEV is about 50 kW at 200–350 V. Generally, the motor, generator, and engine are coupled in series-parallel configuration. With the aid of power split devices, which are mainly built by planetary gear sets and clutches, the energy management system of the engine, motor, and generator is designed to maximize energy efficiency and minimize emissions.

The FHEV can be driven in pure EV mode and hybrid mode. The electrical powertrain assists the engine, not only at the starting, but also during acceleration in the hybrid model, which is also called

Vehicle Energy Storage: Batteries. Table 4 Technical data of batteries for FHEVs

Parameters	Unit	FHEV
Voltage	V	220–350
Discharge power	kW	>35
Low temperature (−28°C) discharge power	kW	>4
Recharge power	kW	>30
SoC window	%	40–80
Recharge pulse power	kW	>40
Energy capacity	kWh	1–2
Operating temperature	°C	−30 to +52
Calendar life	Year	>10

Vehicle Energy Storage: Batteries. Table 5 Technical data of batteries for PHEVs

Parameters	Unit	PHEV
Voltage	V	220–350
Discharge power	kW	>50
Low temperature (−28°C) discharge power	kW	>6
Recharge power	kW	>30
SoC window	%	20–100
Recharge pulse power	kW	>20
Energy capacity	kWh	5–20
Charge time	Hour	<5
Operating temperature	°C	−30 to +52
Calendar life	Year	>10

charge-sustaining mode. In this mode, the discharged energy of the battery is recharged not only during braking but also by the engine to maintain the SoC in high and narrow window. Table 4 shows the technical data of batteries for FHEVs.

The FHEV can achieve higher fuel economy than that of the ICE vehicle by 30–50% in city driving. FHEVs in the market include Toyota Prius, Highlander, and Lexus RX 400 h.

Plug-in Hybrid Electric Vehicles The electrical powertrain of a PHEV is similar to that of an FHEV. The key differences are the additional battery pack and the functionality of grid recharging. In addition to the charge-sustaining mode, the PHEV can also operate in the charge depletion mode, in which the PHEV operates in pure EV mode. Thus, the battery SoC drops in the charge depletion mode.

The electrical drivetrain of a PHEV works in a high voltage at 220–350 V. The battery energy capacity in PHEVs is the largest among all HEVs and it is determined by the targeted pure electric driving range. The PHEV operates in the charge depletion mode first and then the charge-sustaining mode. In the charge depletion mode, the batteries decline from 100% to a threshold SoC, which triggers the operation mode change. In the charge-sustaining mode, the battery SoC is regulated between the bottom of the SoC window and the threshold SoC. The battery is recharged from the grid at the end of the trip. Similar to the EV, the PHEV suffers from complexity and costliness. However, the PHEV delivers longer driving range than the EV's. Table 5 shows technical data of batteries for PHEVs.

The BYD F3DM is the world's first mass production PHEV, which went on sale to the government agencies and corporations in China in December 2008. Toyota also works on a plug-in version of the Prius. The plug-in Prius is converted from the Prius by adding additional 1.3 kWh battery pack into the car and a charging unit. The plug-in Prius and F3DM adopt the series-parallel hybrid powertrain.

A PHEV can also be implemented in a series hybrid topology. The GM Chevrolet Volt is a series PHEV, which is also called extended-range electric vehicle (EREV). The EREV is driven by one sole electrical powertrain, powered by the battery and a small engine.

Hybrid Electric Buses The battery in hybrid electric buses (HEBs) functions for engine start, power boost, and regenerative braking, which are very similar to the application in FHEVs. The HEB is heavier than a sedan HEV, such that the batteries needed for HEBs are a scale up of that in a sedan FHEV. The battery operates at a significantly higher voltage of 400–700 V. Table 6 shows the technical data of batteries for HEBs.

Electric Vehicles

Battery Electric Vehicles Battery is the sole energy source for the electrical powertrain and accessory systems in a BEV. The typical electric motor power for sedan BEV is about 50–80 kW and the battery operates in a high voltage, over 300 V. Figure 4 shows the bidirectional energy flow in the BEV powertrain and Table 7 lists some key data of batteries for BEVs. In city driving, the EV's fuel economy can be double that of an ICE vehicle [10, 11]. The Mitsubishi i-MiEV and Nissan Leaf are typical BEVs in the market.

Fuel Cell Electric Vehicles An FCEV is driven by a fuel cell and battery hybrid system. A fuel cell system consists of a fuel cell stack with plant components for air supply, fuel control, temperature control, and humidification control. Most FCEVs combine the fuel cell stack with a high-voltage battery in a hybrid system for regenerative braking and acceleration boost. The batteries operate in an SoC window between 40% and 70%. Figure 5 shows the energy flow in an FCEV and Table 8 shows technical data of batteries for FCEVs [5].

Batteries for Vehicle Applications

The battery has to be intrinsically tolerant to abuse conditions such as overcharge, short circuit, crush, fire exposure, and mechanical shock and vibration. Battery cells are connected in series and parallel in a vehicle battery system, thus, cells' SoCs have to be balanced to prevent undercharge and overcharge. The operating temperature range of the battery is wide such that active thermal management systems are needed [1, 12].

Key requirements for vehicle batteries are high specific energy and specific power, long cycle life, high efficiency, wide operating temperature, and low cost for commercialization. Figure 6 shows the power and energy requirements of battery for various EVs and HEVs.

Vehicle Energy Storage: Batteries. Table 6 Technical data of batteries for HEBs

Parameters	Unit	HEB
Voltage	V	400–700
Discharge power	kW	100–200
Low temperature (−28°C) discharge power	kW	>20
Recharge power	kW	50–100
SoC window	%	40–70
Energy capacity	kWh	>10
Operating temperature	°C	−30 to +52
Calendar life	Year	>5

Vehicle Energy Storage: Batteries. Table 7 Technical data of batteries for BEVs

Parameters	Units	BEV
Voltage	V	>300
Discharge power	kW	>50
Low temperature (−28°C) discharge power	kW	>40
Recharge power	kW	>30
SoC window	%	20–100
Energy capaciy	kWh	50–90
Charge time	Hour	<8
Operating temperature	°C	−30 to +52
Calendar life	Year	>10

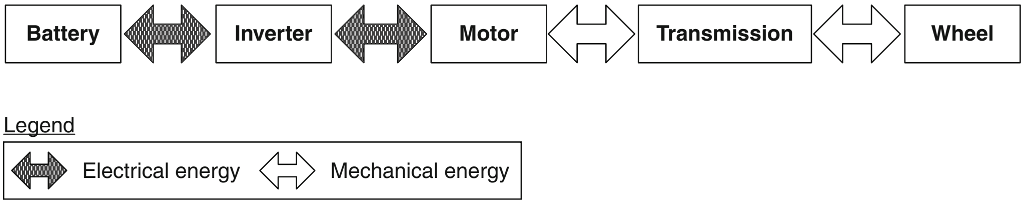

Vehicle Energy Storage: Batteries. Figure 4 Energy flow in a BEV

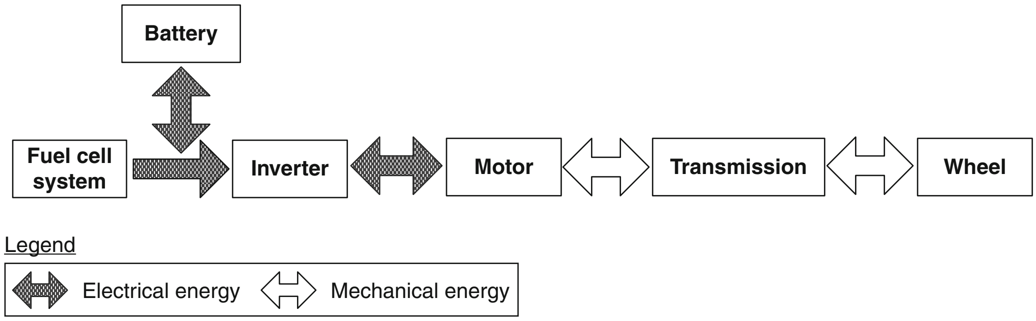

Vehicle Energy Storage: Batteries. Figure 5
Energy flow in an FCEV

Vehicle Energy Storage: Batteries. Table 8 Typical specification of batteries for FCEVs

Parameters	Unit	FCEV
Voltage	V	200–440
Discharge power	kW	>15
Low temperature (−28°C) discharge power	kW	>4
Recharge power	kW	>15
SoC window	%	40–70
Recharge pulse power	kW	>20
Energy capacity	kWh	0.6–1.5
Operating temperature	°C	−30 to +52
Calendar life	Year	>10

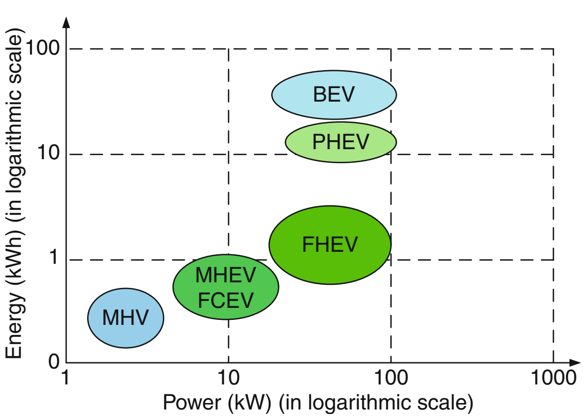

Vehicle Energy Storage: Batteries. Figure 6
Power and energy requirements of batteries for various EVs and HEVs

The United States Council for Automotive Research LLC (USCAR) and the United States Advanced Battery Consortium (USABC) have set technical targets for vehicle batteries. The MHVs need batteries with long cycle life. The MHEVs, FCEVs, FHEVs, and HEBs need batteries with high specific power for power boost and regenerative braking. Table 9 shows some USABC's key goals for batteries in HEV applications [12–15].

The EV needs batteries with high specific power for quick charge and with high specific energy for long driving range. Table 10 shows some USABC's key goals for batteries in EV applications. The EV commercialization goals were developed to provide lower and possibly reachable goals for car manufacturers to enter the EV market in the near future.

The PHEV needs batteries with high specific power but the requirements on specific energy vary with the targeted pure electric driving range. Table 11 shows some USABC's key goals for batteries in PHEV applications. The high power to energy ratio battery is required for PHEVs with 10-mile pure electric driving range, while the high energy to power ratio battery is required for a pure electric driving range of 40 miles.

The viable batteries for vehicle applications consist of the valve-regulated lead-acid (VRLA), nickel-cadmium (Ni-Cd), nickel-zinc (Ni-Zn), nickel-metal hydride (Ni-MH), zinc/air (Zn/Air), aluminium/air (Al/Air), sodium/sulfur (Na/S), sodium/nickel chloride ($Na/NiCl_2$), lithium metal-polymer (LiM-Polymer), and lithium-ion (Li-Ion) batteries. The specific energy and specific power of these batteries are shown in Fig. 7. These batteries are classified into lead-acid,

Vehicle Energy Storage: Batteries. Table 9 Typical USABC goals for batteries in HEV applications

Parameters	Unit	MHV	MHEV	FHEV	FCEV
Discharge pulse power	kW	6	13–25	40	20
Regenerative pulse power	kW	N.A.	8–20	35	25
Energy capacity	kWh	0.25	0.30	0.50	0.25
Calendar life	Year	15	15	15	15
Cycle life	Cycle	150,000	300,000	300,000	N.A.
Maximum operating voltage	V	48	400	400	440
Operating temperature	°C	−30 to +52	−30 to +52	−30 to +52	−30 to +52

N.A.: not applicable

Vehicle Energy Storage: Batteries. Table 10 Typical USABC goals for batteries in EV applications

Parameters	Unit	EV Commercialization goals	EV Long-term goals
Discharge specific power at 80% DoD for 30 s	W/kg	300	400
Regenerative specific power at 20% DoD for 10 s	W/kg	150	200
Power density	W/L	460	600
Onboard energy capacity	kWh	40	40
Specific energy at C/3 discharge rate	Wh/kg	150	200
Energy density at C/3 discharge rate	Wh/L	230	300
Calendar life	Year	10	10
Cycle life to 80% DoD	Cycle	N.A.	1,000
Operating temperature	°C	−40 to +50	−40 to +85
Selling price	USD/kWh	<150	<100
Normal recharge time	Hour	6	3 to 6
High recharge rate	Hour	0.5 (20–70% SoC)	0.25 (40–80% SoC)

N.A.: not applicable

nickel-based, zinc/halogen, metal/air, sodium-beta, and ambient-temperature lithium batteries, as shown in Fig. 8 [9–11].

Lead-Acid Batteries

The lead-acid (Pb-Acid) battery was invented in 1859. It has been a successful commercial product for over a century. The Pb-Acid battery is mature and has low cost. It has a nominal cell voltage of 2 V, specific energy of 35 Wh/kg, energy density of 90 Wh/L, and specific density of 200 W/kg. It uses metallic lead as the negative electrode and lead dioxide as the positive electrode. The electrolyte is a sulfuric acid solution [16].

On discharge, both lead and lead dioxide are converted into lead sulfate. On charge, the reactions are reversed. The overall electrochemical reactions are described in (1). The electrolyte, sulfuric acid, participates in the electrochemical reactions, and its concentration changes with SoC. Open-circuit voltage of the

Vehicle Energy Storage: Batteries. Table 11 Typical USABC goals for batteries in PHEV applications

Parameters	Unit	High power to energy ratio battery	High energy to power ratio battery
Reference equivalent electric range	Mile	10	40
Peak pulse discharge power for 2 s	kW	50	46
Peak regenerative power for 10 s	kW	30	25
Available energy for charge-depleting mode at 10 kW discharge rate	kWh	3.40	11.60
Available energy for charge-sustaining mode	kWh	0.50	0.30
Cold cranking power at −30°C	kW	7	7
Calendar life at 35°C	Year	15	15
Maximum system weight	kg	60	120
Maximum system volume	l	40	80
Maximum operating voltage	V	400	400
Operating temperature	°C	−30 to +52	−30 to +52

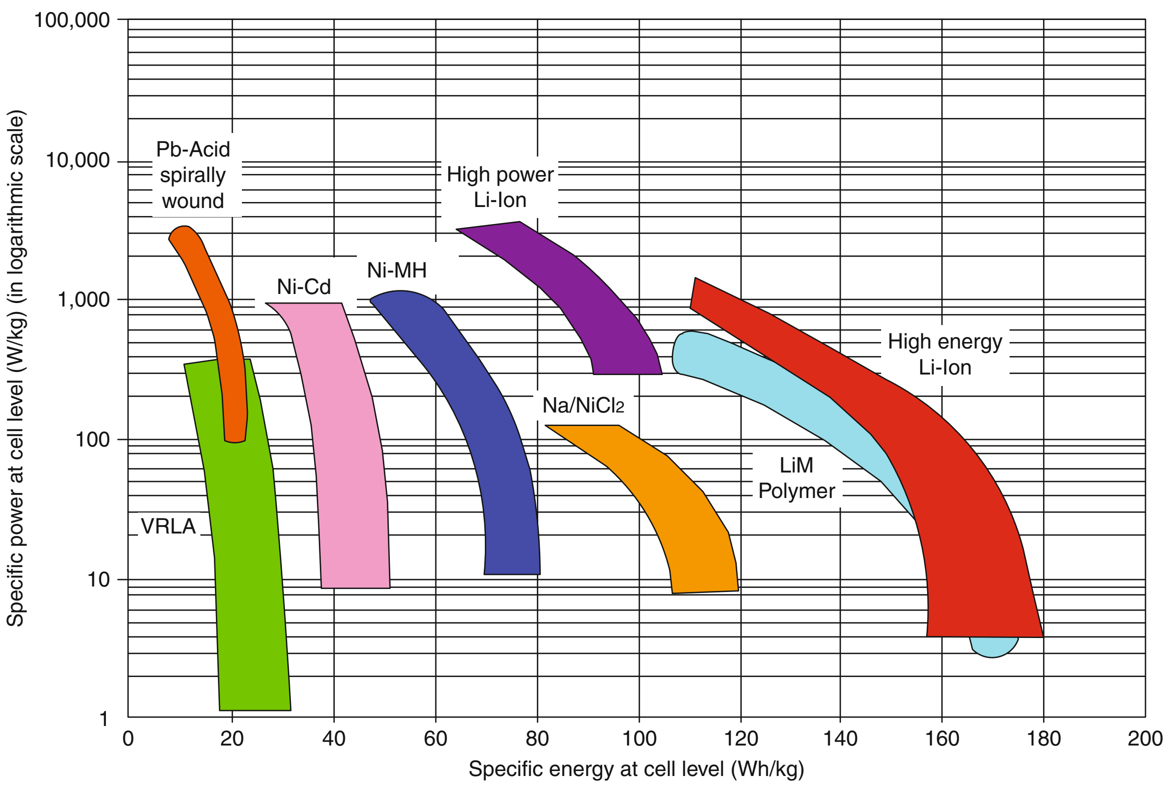

Vehicle Energy Storage: Batteries. Figure 7
Specific energy and specific power of vehicle batteries

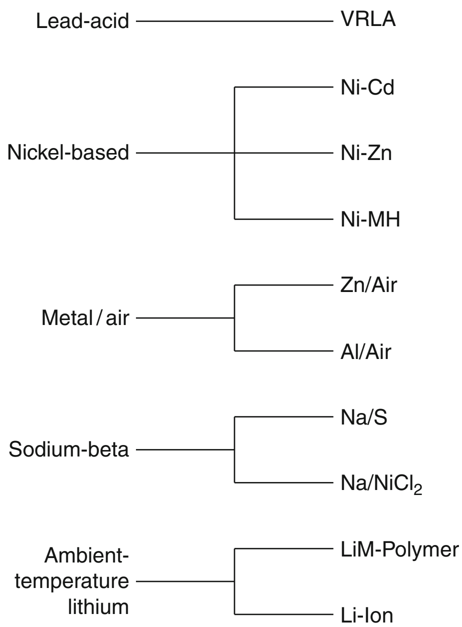

Vehicle Energy Storage: Batteries. Figure 8
Classification of vehicle batteries

Pb-Acid battery cell depends only on the acid concentration and is independent of the amount of lead, lead dioxide, or lead sulfate in the cell as long as these components are available. On discharge, the cut-off voltage at moderate rates is 1.75 V and can be as low as 1.0 V at extremely high rates at low temperature. On charge, the charge voltage is regulated below the gassing voltage, about 2.45 V, to avoid evolutions of hydrogen and oxygen gases with the loss of water.

$$Pb + PbO_2 + 2H_2O \underset{\text{charge}}{\overset{\text{discharge}}{\rightleftarrows}} 2PbSO_2 + 2H_2O \tag{1}$$

Valve-Regulated Lead-Acid Battery In the sealed Pb-Acid battery, a special porous separator is employed in the cell such that the evolved oxygen is transferred from the negative electrode to the positive electrode and then combines with hydrogen to form water. Thus, it provides a definite advantage of maintenance-free operation. Moreover, the immobilization of the gelled (Gel) electrolyte or absorbed electrolyte with absorptive glass mat (AGM) separators allows the battery to operate in different orientations without spillage. The sealed Pb-Acid battery is so-called valve-regulated lead-acid (VRLA) battery [16].

Absorptive Glass Mat The AGM separator in the VRLA batteries serves not only as a permeable electronic insulating diaphragm, resistant to strong acid and oxidation, but also as an acid reservoir for the electrochemical reactions. The separator also plays an active role and has a critical influence on the battery performance and service life. The AGM VRLA battery has penetrated the market of 12 V starting-lighting-ignition (SLI) batteries in premium cars and MHVs. They are attractive for HEBs and low-cost MHVs [17].

Gel Electrolyte In Gel VRLA batteries, the electrolyte is absorbed in a silica gel rather than an AGM. Ionic conductivity of the gelled electrolyte is low such that power density of the Gel VRLA battery is lower than that of the AGM or flooded Pb-Acid batteries. The Gel VRLA battery is not appropriate for starter batteries or power-optimized HEV batteries. Cycling capability of Gel VRLA battery is good but the discharge rate at low temperature is low. Therefore, Gel VRLA batteries are widely used in electric bicycles, BEVs, and in-house transportation systems, where cold cranking is not required but cyclic stress is extreme [18].

Bipolar Cell Stacks Conventional monopolar cell operates at approximately 2 V in its own plastic compartment and the system battery voltage is achieved by connecting a sufficient number of cells in series. In bipolar Pb-Acid batteries, the positive active material of a battery cell is pasted on one side of a conductive plate, so-called bipolar plate, and the negative active material is pasted on the other side. The positive material on one side of a bipolar plate faces the negative material of the neighboring plate with a separator between them. The battery capacity is determined by surface area of the bipolar plate and the paste material utilization [19]. Figure 9 shows the structure and conduction paths in a monopolar battery and in a bipolar Pb-Acid battery.

Bipolar Pb-Acid cells are favorable for high-voltage applications. In the bipolar Pb-Acid battery system, the system voltage increases by 2 V per unit of additional electrode. The bipolar construction shortens the

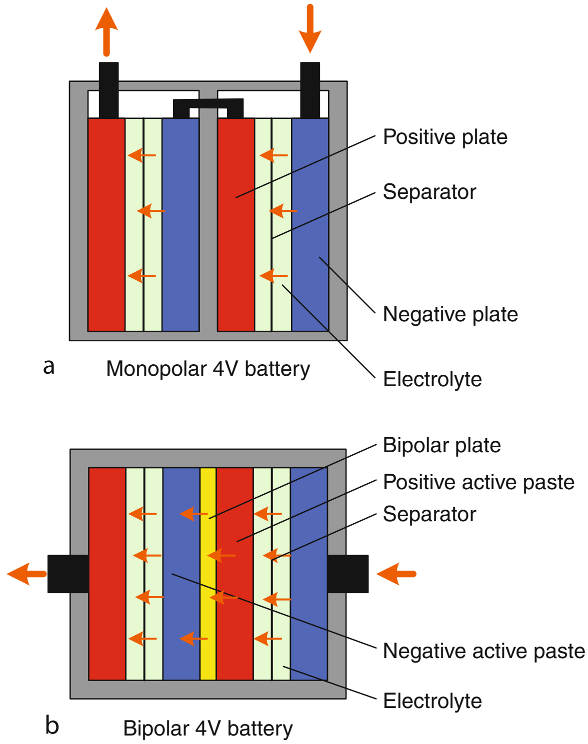

Vehicle Energy Storage: Batteries. Figure 9
Conduction paths inside a monopolar battery and inside a bipolar Pb-Acid battery

current path between the positive and negative terminals of adjacent cells of the battery. This reduces the battery's internal resistance and creates uniform current distribution such that the paste materials are utilized efficiently and the power intensity is improved.

UltraBattery™ The UltraBattery™ is a hybrid energy storage battery that integrates an asymmetric supercapacitor and a Pb-Acid battery in a single unit without extra electronic control. The Pb-Acid component comprises one positive plate, lead dioxide (PbO_2), and one negative plate, lead (Pb). The asymmetric supercapacitor consists of one lead dioxide positive electrode and one carbon-based negative electrode. Lead dioxide is the common material of the Pb-Acid cell and the asymmetric supercapacitor such that negative electrodes of the Pb-Acid cell and the asymmetric supercapacitor are connected in parallel and share the same positive electrode in the UltraBattery™ as shown in Fig. 10 [20].

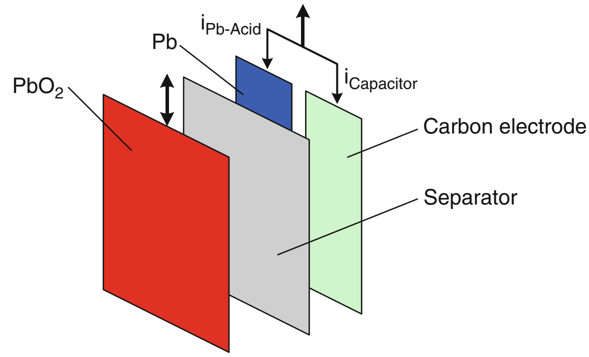

Vehicle Energy Storage: Batteries. Figure 10
Configuration of an UltraBattery™

The charge and discharge currents at the negative electrode consists of two components: capacitor current ($i_{Capacitor}$) and Pb-Acid negative electrode current ($i_{Pb\text{-}Acid}$). The capacitor electrode acts as buffer of the Pb-Acid electrode to mitigate peak charge and discharge currents in HEV applications.

The results from tests at the CSIRO laboratory demonstrated that the UltraBattery™ has greater charge and discharge power and significantly long cycle life than that of a traditional VRLA battery. The UltraBattery™ is at the preproduction stage and prototype batteries have been produced at the Furukawa Battery Co., Ltd, Japan for field testing in HEVs.

Vehicle Applications The VRLA battery has maintained its prime position for more than a century. There are a number of advantages contributing to this outstanding position: proven technology and mature manufacturing, low cost, high cell voltage, good high-rate performance that is suitable for vehicle applications, good low-temperature and high-temperature performances, high energy efficiency (75–80%), and availability in a variety of sizes and designs.

The VRLA battery still suffers from some disadvantages and needs continual development. Its specific energy and energy density are relatively low, typically, 35 Wh/kg and 70 Wh/L. Its self-discharge rate is relatively high at about 1% per day at 25°C.

Advanced Pb-Acid batteries with improved performance are being developed for vehicle applications. Improvements of the VRLA battery in specific energy over 40 Wh/kg and energy density over 80 Wh/L with the possibility of rapid recharge

have been attained. The bipolar VRLA battery and UltraBattery^{TM} are promising Pb-Acid batteries for vehicle applications.

Nickel-Based Batteries

There are many kinds of electrochemical batteries using nickel oxyhydroxide as the active material for the positive electrode, including the Ni-Cd, Ni-Zn, and Ni-MH. Among them, the Ni-MH battery has been well accepted for EV and HEV applications because of its proven technology and good performance. The Ni-Zn battery is still under development.

Ni-Cd Battery For more than 90 years, the Ni-Cd battery has been successfully utilized in heavy-duty industrial applications. Due to the resurgence of interest in EVs in the late 1970s and early 1980s, it led to further development of the Ni-Cd battery for EV applications. The Ni-Cd battery possesses the nominal parameters of 1.3 V, 56 Wh/kg, 110 Wh/L, and 225 W/kg. Its active materials are metallic cadmium for the negative electrode and nickel oxyhydroxide for the positive electrode. The alkaline electrolyte is an aqueous potassium hydroxide solution [21].

The electrochemical reactions of discharge and charge are described in (2). On discharge, metallic cadmium is oxidized to form cadmium hydroxide and nickel oxyhydroxide is reduced to nickel hydroxide with consumption of water. On charge, the reverse reactions occur. In contrast to the sulfuric acid electrolyte used in the Pb-Acid battery, the potassium hydroxide electrolyte in the Ni-Cd battery is not significantly changed in density or composition during discharge and charge.

$$2NiOOH + Cd + 2H_2O \underset{\text{charge}}{\overset{\text{discharge}}{\rightleftharpoons}} 2Ni(OH)_2 + Cd(OH)_2 \tag{2}$$

The Ni-Cd battery has gained enormous technical importance because of the advantages of high specific power (over 220 W/kg), long cycle life (up to 2,000 cycles), highly tolerant of electrical and mechanical abuse, flat voltage profile over a wide range of discharge currents, rapid recharge capability (about 40–80% in 18 min), wide operating temperature range (from −40°C to 85°C), low self-discharge rate (less than 0.5% per day), excellent long-term storage due to negligible corrosion, and available in a variety of sizes and designs. The Ni-Cd battery has some disadvantages which offset its wide acceptance for vehicle applications, namely, low cell voltage, memory effect, and the carcinogenicity and environmental hazard of cadmium.

The Ni-Cd battery can be divided into vented and sealed types. The vented sintered-plate type has higher specific energy but is more expensive. It is characterized by its flat discharge profile and superior high-rate and low-temperature performance. Similar to the sealed Pb-Acid battery, the sealed Ni-Cd battery incorporates a specific cell design feature to prevent build-up of pressure in the cell caused by gassing during overcharge. As a result, the battery can be sealed and requires no maintenance other than recharging.

Major manufacturers of the Ni-Cd battery for vehicle applications are SAFT and VARTA. EVs powered by the Ni-Cd battery included the Chrysler TE Van, Citroën AX, Mazda Roadster, Mitsubishi EV, Peugeot 106, Renault Clio, and HKU U2001.

Ni-Zn Battery Starting from the 1930s, the Ni-Zn battery has been studied for vehicle applications. The Ni-Zn battery has high specific energy and low material cost; however, it has not achieved any commercial importance because of the short life in the zinc electrode [22].

The Ni-Zn battery nominally operates at 1.6 V and has energy and power densities of 60 Wh/kg, 120 Wh/L, and 300 W/kg. It uses zinc as the negative electrode and nickel oxyhydroxide as the positive electrode. The electrolyte is an alkaline potassium hydroxide solution. The discharge and charge reactions are described in (3).

$$Zn + 2NiOOH + 2H_2O \underset{\text{charge}}{\overset{\text{discharge}}{\rightleftharpoons}} Zn(OH)_2 + 2Ni(OH)_2 \tag{3}$$

On discharge, metallic zinc in the negative electrode is oxidized to form zinc hydroxide and nickel

oxyhydroxide in the positive electrode is reduced to nickel hydroxide. On charge, the reactions are reversed.

Among the nickel-based batteries, the Ni-Zn battery has the advantages of higher specific energy and specific power than the Ni-Cd battery's, high cell voltage (the highest of the nickel-based family), nontoxicity (more environmental friendliness than the Ni-Cd), tolerance of overcharge and overdischarge, capability of high discharge and recharge rates, and wide operating temperature (from $-20^{\circ}C$ to $60^{\circ}C$). However, the major and serious drawback of the Ni-Zn battery is its short cycle life (about 300 cycles). It is mainly due to the partial solubility of zinc species in the electrolyte.

Ni-MH Battery The Ni-MH battery has been on the market since 1992. Its characteristics are similar to the Ni-Cd battery. The principal difference between them is the use of hydrogen, absorbed in a metal hydride, for the active negative electrode material in the Ni-MH battery [23].

Active materials of Ni-MH batteries are hydrogen in the form of metal hydride for the negative electrode and nickel oxyhydroxide for the positive electrode. The metal hydride undergoes reversible hydrogen desorbing-absorbing reactions when the battery is discharged and recharged. An aqueous solution of potassium hydroxide is the major component of the electrolyte. The overall electrochemical reactions are described in (4). When the battery is discharging, metal hydride in the negative electrode is oxidized to form metal alloy and nickel oxyhydroxide in the positive electrode is reduced to nickel hydroxide. During charge, the reverse reactions occur.

$$\mathrm{MH} + \mathrm{NiOH} \underset{\text{charge}}{\overset{\text{discharge}}{\rightleftarrows}} \mathrm{M} + \mathrm{Ni(OH)_2} \qquad (4)$$

The hydrogen storage metal alloy is a key component of the Ni-MH battery. It is well formulated to maintain stable over a large number of cycles. The rare-earth alloys based around lanthanum nickel, known as the AB5, and the alloys consisting of titanium and zirconium, known as the AB2, are the two major metal alloys used in Ni-MH batteries. Although the AB2 alloys typically have higher capacity than that of the AB5 alloys, the AB5 alloy is widely used because of its superiority in charge retention and stability.

The Ni-MH battery has a nominal voltage of 1.32 V and attains specific energy of 65–110 Wh/kg for EV applications and 45–60 Wh/kg for HEV applications. It operates in a temperature from $-20^{\circ}C$ to $+45^{\circ}C$. A number of battery manufacturers, such as GM Ovonic, GP, GS, Panasonic, SAFT, VARTA, and YUASA, have actively engaged in the development of this battery for HEVs.

Metal/Air Batteries

The rechargeable metal/air batteries include the electrically or mechanically rechargeable zinc/air (Zn/Air) battery and the mechanically rechargeable aluminum/air (Al/Air) battery. These metal/air batteries have very high specific energy and energy density (as high as 600 Wh/kg and 400 Wh/L for Al/Air), low cost, and are environment friendly. In addition, those mechanically rechargeable batteries have two distinct advantages which are very essential for EV applications, namely, fast and convenient refueling (comparable to petrol refueling in a few minutes) and centralized recharging and recycling (most efficient and environmentally sound use of electricity). The disadvantages associated with rechargeable metal/air batteries are low specific power (at most 105 W/kg for Zn/Air), narrow operating temperature window, carbonation of alkaline electrolyte due to carbon dioxide in air, and evolution of hydrogen gas from corrosion in electrolyte.

Zn/Air Battery The Zn/Air battery has been developed as an electrically and mechanically rechargeable battery. Although both of them have been applied to EV applications, the mechanically rechargeable battery is more favorable [24].

The electrically rechargeable Zn/Air battery nominally operates at 1.2 V and has the specific energy of 180 Wh/kg, energy density of 160 Wh/L, and specific power of 95 W/kg. The negative electrode consists of zinc particles and the positive electrode is a bifunctional air electrode. The electrolyte is potassium hydroxide. The simplified electrochemical reactions are described in (5).

$$2Zn + O_2 \underset{\text{charge}}{\overset{\text{discharge}}{\rightleftarrows}} 2ZnO \qquad (5)$$

On discharge, zinc is first oxidized to potassium zincate dissolved in the electrolyte and then to a precipitation of zinc oxide. On charge, the reactions are reversed. However, the zinc electrode generally suffers from the problem of shape change during cycling.

The mechanically rechargeable Zn/Air battery avoids the use of bidirectional air electrode and the shape change problem. Hence, it can offer a higher specific energy of 230 Wh/kg and a higher specific power of 105 W/kg. The depleted zinc negative electrode cassettes can be replaced robotically by a mechanically refueling system at a fleet servicing point or at a public service station. The discharged fuel is then electrochemically recharged at central facilities. There are four steps in a recharging process. Firstly, the discharged cassettes are mechanically taken apart and the zinc oxide discharge product is removed. Secondly, zinc oxide is dissolved in a potassium hydroxide solution to form a zincate solution. Thirdly, the zincate solution is electrolyzed in an electrowinning bath. Finally, the electrowon zinc is compacted onto the negative electrode cassettes.

A mechanically rechargeable Zn/Air battery was developed for field test. A 160-kWh Zn/Air battery was installed and tested in a Mercedes-Benz 180E van in 1994. The driving range at a constant speed of 64 km/h was 689 km.

Al/Air Battery The Al/Air battery has a nominal voltage of 1.4 V. The negative electrode is aluminum metal and the positive electrode is only a simple unifunctional air electrode for discharge. The electrolyte can be either saline solution or alkaline potassium hydroxide solution. The discharge reaction of this mechanically rechargeable battery is described in (6).

$$4Al + 3O_2 + 6H_2O \xrightarrow{\text{discharge}} 4Al(OH)_3 \qquad (6)$$

The Al/Air battery with a saline electrolyte is attractive only for low-power applications. On the other hand, the alkaline Al/Air battery offers high specific energy and energy density of 250 Wh/kg and 200 Wh/L and is suitable for high power applications. Nevertheless, the corresponding specific power is as low as 7 W/kg. Because of its exceptionally low specific power, the Al/Air battery is seldom used as the sole energy source for EVs and it is commonly used in conjunction with other batteries in a battery hybrid system.

Sodium-Beta Batteries

The sodium-beta battery refers to the Na/S and $Na/NiCl_2$ batteries, which have liquid sodium as one reactant and beta-alumina ceramic as the electrolyte.

Na/S Battery The Na/S battery operates at 300–350°C with a nominal cell voltage of 2 V, specific energy of 170 Wh/kg, energy density of 250 Wh/L, and specific power of 390 W/kg. The active materials are molten sodium for the negative electrode and molten sulfur/sodium polysulfides for the positive electrode. The beta-alumina ceramic electrolyte functions as a sodium ion-conducting solid medium and works as a separator for the molten electrodes to prevent any direct self-discharge [25]. The electrochemical reactions of the Na/S battery are described in (7).

$$2Na + xS \underset{\text{charge}}{\overset{\text{discharge}}{\rightleftarrows}} Na_2S_x, \quad x = 2.7 - 5 \qquad (7)$$

On discharge, sodium is oxidized to form sodium ions, which migrate through the electrolyte and combine with the sulfur that is being reduced in the positive electrode to form sodium pentasulfide. Then, the sodium pentasulfide is progressively converted into polysulfides with higher sulfur compositions (Na_2S_x) where x is from 2.7 to 5. On charge, these reactions are reversed.

Barriers to commercialization of the Na/S battery are safety issues (high reactivity and corrosiveness of molten active materials), inadequate freeze-thaw durability (weak ceramic electrolyte subjected to mechanical stress), and need of thermal management (additional energy and thermal insulation).

$Na/NiCl_2$ Battery In $Na/NiCl_2$ battery, the active materials are molten sodium for the negative electrode

and solid nickel chloride for the positive electrode. In addition to the beta-alumina ceramic electrolyte as used in the Na/S, there is a secondary electrolyte, namely, sodium-aluminum chloride, in the positive electrode chamber. The secondary electrolyte conducts sodium ions from the primary beta-alumina electrolyte to the solid nickel chloride positive electrode [26]. The corresponding electrochemical reactions are described in (8)

$$2\mathrm{Na} + \mathrm{NiCl_2} \underset{\text{charge}}{\overset{\text{discharge}}{\rightleftarrows}} \mathrm{Ni} + 2\mathrm{NaCl} \tag{8}$$

On discharge, the solid nickel chloride is converted into nickel metal and sodium chloride crystal. On charge, these reactions are reversed. The $Na/NiCl_2$ battery operates at 155–350°C with a nominal cell voltage of 2.58 V. In a battery system, the system specific energy and specific power can be 86–120 Wh/kg and 150–300 W/kg. Comparing with the Na/S battery, the $Na/NiCl_2$ battery has higher open circuit cell voltage, wider operating temperature, safer products of reaction (less corrosive than molten Na_2S_x), and better freeze-thaw durability (smaller temperature difference).

The AEG ZEBRA (Zero Emission Battery Research Activity) has been the major developer of the $Na/NiCl_2$ battery. The ZEBRA battery, namely, Z12, offered a specific energy of 103 Wh/kg and a specific power of 180 W/kg.

Ambient Temperature Lithium Batteries

There are a number of approaches being taken in the design of rechargeable ambient-temperature lithium batteries. One approach is to use metallic lithium for the negative electrode and a solid inorganic intercalation material for the positive electrode. The electrolyte can be a solid polymer, leading to name as the lithium metal polymer (LiM-Polymer) battery. Another approach is the use of a lithiated carbon material as the negative electrode such that lithium ions move forth and back between the positive and negative electrodes during cycling. The "rocking-chair" movements of Li-Ions lead to the name lithium-ion (Li-Ion) battery [1, 27].

Lithium Metal Polymer Batteries The LiM-Polymer battery uses lithium metal and a transition metal intercalation oxide (M_yO_z) for the negative and positive electrodes, respectively. A thin solid polymer electrolyte (SPE) is used, which offers the merits of improved safety and flexibility in design [28]. The general electrochemical reactions are described in (9).

$$x\mathrm{Li} + \mathrm{M}_y\mathrm{O}_z \underset{\text{charge}}{\overset{\text{discharge}}{\rightleftarrows}} \mathrm{Li}_x\mathrm{M}_y\mathrm{O}_z \tag{9}$$

On discharge, lithium ions formed at the negative electrode migrate through the SPE and are inserted into the crystal structure at the positive electrode. On charge, the process is reversed. By using a lithium foil negative electrode and vanadium oxide (V_6O_{13}) positive electrode, the $Li/SPE/V_6O_{13}$ cell is a typical LiM-Polymer battery. It operates at a nominal voltage of 3 V and has the specific energy of 155 Wh/kg, energy density of 220 Wh/L, and specific power of 315 W/kg. The advantages are high cell voltage (3 V), very high specific energy and energy density (155 Wh/kg and 220 Wh/L), very low self-discharge rate (about 0.5% per month), and capability of fabrication in a variety of shapes and sizes. However, its low-temperature performance is weak [1].

Lithium Ion Batteries Since the commercialization of the Li-Ion battery by Sony Energytec in 1990, the Li-Ion battery has been considered to be the most promising rechargeable battery of the future. The Li-Ion battery has already gained acceptance for HEV applications. The specific energy of Li-Ion battery was 98 Wh/kg in 1990 and increased to 195 Wh/kg in 2008 [27].

The Li-Ion battery consists of two electrodes, a porous separator impregnated with electrolyte, and two current collectors. Lithium cobalt oxide ($LiCoO_2$) typically serves as an active electrode material for the positive electrode. The negative electrode is usually made of lithiated carbon or graphite (LiC_6). Electrodes are electrically isolated by the separator, where the space between them is filled by electrolyte. Copper foil is used for the negative current collector and aluminum for the positive current collector.

The Li-Ion battery employs insertion reactions for both positive and negative electrodes. The Li-Ions are

inserted into the negative electrode when the battery is fully charged and they move between positive and negative electrodes during cycling. Thus, the Li-Ion battery is also called "rocking-chair battery" or "shuttle-cock battery." The main reactions at the positive electrode are described in (10).

$$\mathrm{Li}_{1-x}\mathrm{CoO}_2 + x\mathrm{Li}^+ + xe^- \underset{\text{charge}}{\overset{\text{discharge}}{\rightleftarrows}} \mathrm{LiCoO}_2 \quad 0 \le x \le 0.5 \tag{10}$$

The Li-Ion is extracted from the positive electrode during charging and inserted into the electrode during discharging, where x represents the mol fraction of Li^+ ions inside the positive electrode. For a proper reversible functioning of a Li-Ion battery, not all Li^+ ions can be extracted from the electrode. The corresponding reactions at the negative electrode are described in (11).

$$\mathrm{Li}_z\mathrm{C}_6 \underset{\text{charge}}{\overset{\text{discharge}}{\rightleftarrows}} \mathrm{C}_6 + z\mathrm{Li}^+ + ze^- \quad 0 \le z \le 1 \tag{11}$$

Where z describes the mol fraction of Li^+ ions inside the negative electrode.

The electrolyte is based on a dissociated lithium-containing salt, such as lithium hexafluorophosphate ($LiPF_6$) or lithium perchlorate ($LiClO_4$). Mixtures of ethylene carbonate (EC), diethyl carbonate (DEC), and dimethyl carbonate (DMC) are used as nonaqueous solvents. The ions in the electrolyte are transported by both diffusion and migration, which is induced by the electric field between the electrodes. The overall reactions are described in (12)

$$\mathrm{Li}_{1-x}\mathrm{CoO}_2 + \mathrm{Li}_{z+x}\mathrm{C}_6 \underset{\text{charge}}{\overset{\text{discharge}}{\rightleftarrows}} \mathrm{LiCoO}_2 + \mathrm{Li}_z\mathrm{C}_6 \tag{12}$$

Development of Positive Active Materials The $LiCoO_2$ has been used as positive active material since 1990. Extensive works have been done for new materials with higher energy density and lower cost. Electrode with nickel compounds shows larger capacity than that of $LiCoO_2$. The lithium nickel oxide ($LiNiO_2$) is a potential material for the positive electrode of the Li-Ion battery. The $LiNiO_2$ is a layered oxide with lithium, oxygen, and nickel layers, and it has the same crystalline structure of $LiCoO_2$. The $LiNiO_2$ is not commercialized because the $LiNiO_2$ electrode showed a rapid capacity decay with cycling, due to the movement of nickel to the lithium layer during cycling. In addition, the thermal stability of $LiNiO_2$ at charged state is low such that it goes to thermal runaway easily. Partial substitutions of nickel with Co, Al, and Mn have been studied to enhance thermal stability.

The manganese-based compounds, namely, $LiMnO_2$ and $LiMn_2O_4$ are potential materials for the positive electrode. The three-dimensional structure and spinel $LiMn_2O_4$ is more stable than the $LiCoO_2$ at fully charged state and the cost is lower. The Li-Ion battery with spinel $LiMn_2O_4$ was commercialized in 1996. However, the battery capacity of $LiMn_2O_4$ is lower than that of $LiCoO_2$ and the capacity decays rapidly. Partial substitutions of $LiMn_2O_4$ with Co, Mg, Cr, Ni, Fe, Ti, and Zn improve cycle life of spinel $LiMn_2O_4$.

The positive electrode with polyanions (SO_4^{2-} and PO_4^{2-}) are promising in reducing cost and enhancing thermal stability. The lithium iron phosphate ($LiFePO_4$) is electrochemically active and shows a flat discharge voltage at about 3.5 V. The $LiFePO_4$ electrode is thermally stable, because it does not release oxygen at fully charged state at an elevated temperature. The electric conductivity is enhanced by coating nanosized $LiFePO_4$ particles with ultrathin carbon layer. Moreover, lithium manganese phosphate ($LiMnPO_4$) and lithium cobalt phosphate ($LiCoPO_4$) are under development for enhancements of battery voltage and capacity [29–34].

Development of Negative Active Materials The capacity of negative electrode has increased by replacing coke (non-graphitic carbon) with graphite, which has larger capacity and flat discharge profile. The capacity of graphic carbon used in Li-Ion batteries is close to the theoretical limit. Commercially available graphic carbons are natural graphite, synthetic graphite, and mesocarbon microbead (MCMB). Intermetallic components and lithium titanium oxide are potential materials for negative electrodes of Li-Ion batteries [35].

Vehicle Energy Storage: Batteries. Table 12 Advanced Li-Ion batteries

Positive electrode	Negative electrode	Manufacturers	Key feature
$LiCoO_2$	Graphite	Sony	Mature
$LiMn_2O_4$	Graphite	NEC, GS, Yuasa, LG	High power
NCA/NMC	Graphite	SAFT, Samsung, Sanyo, Evonik	High energy
$LiFePO_4$	Graphite	A123, Valence Tech, BYD	Highly stable
$LiMn_2O_4$	Titanate	Toshiba, Enerdel	High discharge rate

Vehicle Energy Storage: Batteries. Table 13 Key features of promising batteries

Type	Pb-Acid	Nickel-based		Lithium	
Feature	VRLA	Ni-Cd	Ni-MH	Li-Ion	Li-Titanate
Specific energy (Wh/kg)	30–40	40–60	60–70	160	70–90
Cycle life at 100% DoD (cycle)	50–80	300–600	300–500	500–750	25,000
Safety	Fire hazard	Moderate	Fire hazard	Fire hazard	Safest
Charge time (0–90% SoC) (h)	8	2	2	2	0.1
Operating temperature (°C)	−10 to 60	0–50	0–40	0–40	−40 to 70
Environmental impact	Toxic	Toxic	Low	Minimal	Minimal
Memory effect	Very low	High	Moderate	None	None
Power delivery	Good	Moderate	Moderate	Moderate	High
Manufacturability	Easy	Adequate	Adequate	Easy	Easy
Maintenance	Moderate	Moderate	Moderate	Moderate	Moderate
Market position	High volume	Sliding	Modest	Good	Rising
Cost	Low	Tied to Ni	Tied to Ni	Moderate	Moderate

Lithium alloys have been developed for negative electrode since 1970s. Cycle life of lithium alloy was short due to alloy pulverization caused by large volume change during cycling. Intermetallic components, such as Cu − Sn, Cu − Sb, and In − Sb, have been investigated aiming at suppressing volume change in lithium alloys during cycling. In 2005, Sony demonstrated a lithium alloy, composed of Sn, Co, and C, that showed 50% increase in volumetric capacity, comparing with a conventional graphite electrode.

The lithium titanate spinel has been investigated as a negative electrode material since the commercialization of the Li-Ion battery, which uses $LiCoO_2$ cathode and carbon anode. The lithium titanate materials, particularly the $Li_4Ti_5O_{12}$, have demonstrated significant improvements in charge and discharge rates in laboratory and in commercial batteries [36].

Vehicle Applications The Li-Ion battery can be made from different advanced positive electrode and negative electrode materials. The mature positive electrode materials are $LiCoO_2$, $LiMn_2O_4$, $LiFePO_4$, lithium nickel manganese cobalt (NMC) oxide ($LiNiMnCoO_2$), and lithium nickel cobalt aluminum (NCA) oxide ($LiNiCoAlO_2$). The mature negative electrode materials are graphite and titanate. Table 12 shows the potential Li-Ion batteries for vehicle applications. Each Li-Ion battery in Table 12 can only overcome

one of the barriers to EV commercialization. However, these high-power and thermally stable Li-Ion batteries are promising for HEV applications.

Future Directions

The battery is the most significant factor of commercialization of EVs and HEVs. Developments of batteries for EV and HEV applications are continued and accelerated. The key requirements for vehicular applications are safety, high specific energy, high specific power, short recharge time, long life cycle, and low cost.

The mature and promising batteries for EVs and HEVs are VRLA, Ni-Cd, Ni-MH, and Li-Ion batteries. The specific power and specific energy of the batteries are plotted in Fig. 3 and their features are compared in Table 13. The VRLA battery is popular for MHVs and low-cost EVs due to its maturity and cost-effectiveness. Features of the Ni-MH battery are superior to those of the Ni-Cd battery, so the Ni-Cd battery is being superseded by the Ni-MH battery in the market for MHEVs, FHEVs, and PHEVs.

The Li-Ion batteries are the promising batteries in the future. The advanced Li-Ions batteries have demonstrated the potentials of improvements in specific power, specific energy, charge rate, and safety.

Bibliography

Primary Literature

1. Chan CC, Chau KT (2001) Modern electric vehicle technology. Oxford University Press, Oxford
2. Kurzweil P (2009) Secondary batteries. In: Encyclopedia of electrochemical power sources. Elsevier, Amsterdam, pp 565–578
3. Chau KT, Wong YS (2002) Overview of power management in hybrid electric vehicles. J Energy Conver Manage 43:953–1968
4. Chan CC, Wong YS, Bouscayrol A, Chen K (2009) Powering sustainable mobility: roadmaps of electric, hybrid, and fuel cell vehicles. Proc IEEE 97:603–607
5. Chan CC (2007) The state of the art of electric, hybrid, and fuel cell vehicles. Proc IEEE 95:704–718
6. Chan CC, Wong YS (2004) The state of the art of electric vehicles technology. IPEMC 2004 1:46–57
7. Chau KT, Chan CC (2007) Emerging energy-efficient technologies for hybrid electric vehicles. Proc IEEE 95:821–835
8. Chan CC, Bouscayrol A, Chen K (2010) Electric, hybrid, and fuel-cell vehicles: architectures and modeling. IEEE Trans Veh Technol 59:589–598
9. Köhler U (2009) Hybrid electric vehicles: batteries. In: Encyclopedia of electrochemical power sources. Elsevier, Amsterdam, pp 269–285
10. Chau KT, Wong YS (2001) Hybridization of energy sources in electric vehicles. J Energy Conver Manage 42:1059–1069
11. Gutmann G (2009) Electric vehicle: batteries. In: Encyclopedia of electrochemical power sources. Elsevier, Amsterdam, pp 219–235
12. USCAR (2006) Energy storage system goals: USABC goals for advanced batteries for EVs. USCAR. http://www.uscar.org
13. USCAR (2006) Energy storage system goals: power assist HEV battery goals. USCAR. http://www.uscar.org
14. USCAR (2006) Energy storage system goals: 42 V battery goals. USCAR. http://www.uscar.org
15. USCAR (2008) USABC requirements of end of life energy storage systems for PHEVs. USCAR. http://www.uscar.org
16. Rand DAJ, Moseley PT (2009) Lead-acid system overview. In: Encyclopedia of electrochemical power sources. Elsevier, Amsterdam, pp 550–575
17. Weighall MJ (2009) Valve-regulated batteries: absorptive glass mat. In: Encyclopedia of electrochemical power sources. Elsevier, Amsterdam, pp 715–726
18. Kramm F, Niepraschk H (2009) Valve-regulated batteries: gel. In: Encyclopedia of electrochemical power sources. Elsevier, Amsterdam, pp 727–734
19. Loyns AC (2009) Bipolar batteries. In: Encyclopedia of electrochemical power sources. Elsevier, Amsterdam, pp 750–754
20. Lam LT, Furukawa J (2009) Supercap hybrid (UltraBattery™). In: Encyclopedia of electrochemical power sources. Elsevier, Amsterdam, pp 755–763
21. Shukla AK, Venugopalan S, Hariprakash B (2009) Nickel–cadmium: overview. In: Encyclopedia of electrochemical power sources. Elsevier, Amsterdam, pp 452–458
22. Cairns EJ (2009) Nickel–Zinc. In: Encyclopedia of electrochemical power sources. Elsevier, Amsterdam, pp 528–533
23. Hariprakash B, Shukla AK, Venugoplan S (2009) Nickel–metal hydride: overview. In: Encyclopedia of electrochemical power sources. Elsevier, Amsterdam, pp 494–501
24. Haas O, Van Wesemael J (2009) Zinc–air: electrical recharge. In: Encyclopedia of electrochemical power sources. Elsevier, Amsterdam, pp 384–392
25. Holze R (2009) Sodium–sulfur. In: Encyclopedia of electrochemical power sources. Elsevier, Amsterdam, pp 302–311
26. Sudworth JL, Galloway RC (2009) Sodium–nickel chloride. In: Encyclopedia of electrochemical power sources. Elsevier, Amsterdam, pp 312–323
27. Yamaki J (2009) Lithium rechargeable systems – lithium-ion overview. In: Encyclopedia of electrochemical power sources. Elsevier, Amsterdam, pp 183–191
28. Kobayashi Y, Seki S, Terada N (2009) Lithium-ion polymer batteries. In: Encyclopedia of electrochemical power sources. Elsevier, Amsterdam, pp 375–382
29. Goodenough JB (2009) Positive electrode: layered metal oxides. In: Encyclopedia of electrochemical power sources. Elsevier, Amsterdam, pp 243–248

30. Arai H, Hayashi M (2009) Positive electrode: lithium cobalt oxide. In: Encyclopedia of electrochemical power sources. Elsevier, Amsterdam, pp 258–263
31. Zaghib K, Mauger A, Gendron F, Julien CM, Goodenough JB (2009) Positive electrode: lithium iron phosphate. In: Encyclopedia of electrochemical power sources. Elsevier, Amsterdam, pp 264–296
32. Kanno R (2009) Positive electrode: lithium nickel oxide. In: Encyclopedia of electrochemical power sources. Elsevier, Amsterdam, pp 297–306
33. Wohlfahrt-Mehrens M (2009) Positive electrode: manganese spinel oxides. In: Encyclopedia of electrochemical power sources. Elsevier, Amsterdam, pp 318–327
34. Liu DW, Cao GZ, Wang Y (2009) Positive electrode: nanostructured transition metal oxides. In: Encyclopedia of electrochemical power sources. Elsevier, Amsterdam, pp 337–355
35. Inaba M (2009) Negative electrodes: graphite. In: Encyclopedia of electrochemical power sources. Elsevier, Amsterdam, pp 198–208
36. Ariyoshi K, Ohzuku T (2009) Negative electrode: spinel-type titanium oxides. In: Encyclopedia of electrochemical power sources. Elsevier, Amsterdam, pp 209–213

Books and Reviews

Encyclopedia of electrochemical power sources. Elsevier

Vehicle Traction Motors

C. C. Chan[1], Ming Cheng[2]
[1]Department of Electrical and Electronic Engineering, University of Hong Kong, Hong Kong, China
[2]School of Electrical Engineering, Southeast University, Nanjing, China

Article Outline

Glossary

AC motor An electric motor driven by an alternating current. There are two types of AC motors, depending on the type of rotor used. The first is the synchronous motor, which rotates exactly at the supply frequency or a submultiple of the supply frequency. The magnetic field on the rotor is either generated by current delivered through slip rings or by a permanent magnet. The second is the induction motor, which runs slightly slower than the supply frequency. The magnetic field on the rotor of this motor is created by an induced current.

Armature winding The conducting coils that are wound around the armature in which voltage is induced, causing it to rotate within a magnetic field.

Brushless DC motor Also called electronically commutated motors. Synchronous motors powered by direct current supply and having electronic commutation system, rather than mechanical commutators and brushes. The current-to-torque and voltage-to-speed relationships are linear.

CVT Continuous variable transmission is a transmission which can change steplessly through an infinite number of effective gear ratios between maximum and minimum values. This contrasts with other mechanical transmissions that only allow a few different distinct gear ratios to be selected. The flexibility of a CVT allows the driving shaft to maintain a constant angular velocity over a range of output velocities.

DC motor An electric motor that runs on direct current (DC) supply.

DTC Direct torque control is a method used in variable frequency drives to control the torque of three-phase AC motors based on stator flux control in the stator fixed frame using direct control of the inverter switching. It involves estimating the motor's magnetic flux and torque based on the measured voltage and current of the motor.

emf Electromotive force is the force that pushes electrons through a conductor.

Field winding The electric circuit is usually a number of coils wound on individual poles and connected in series, which produces the magnetic field in a motor or generator.

FOC Field-oriented control, also called vector control, is a method used in variable frequency drives to control the torque (and thus finally the speed) of three-phase AC motors by controlling two orthogonal current vectors.

Generator A machine that converts mechanical energy into electrical energy by magnetic induction.

ISG Integrated starter/generator, an advanced electric machine controlled by electronics and is designed for integration with internal combustion engines. It replaces the conventional starter motor and alternator, which are the two indispensable electric units for almost every engine.

mmf Magnetomotive force, also known as magnetic potential, is the property of certain substances or phenomena that give rise to magnetic fields. Magnetomotive force is analogous to electromotive force or voltage in electric field.

Motor A machine that converts one form of energy, such as electricity, into mechanical energy or motion.

Definition of the Subject

The traction motor of EVs is responsible for converting electrical energy to mechanical energy in such a way

M. Ehsani et al. (eds.), *Transportation Technologies for Sustainability*, DOI 10.1007/978-1-4614-5844-9,

Originally published in
Robert A. Meyers (ed.) Encyclopedia of Sustainability Science and Technology, © 2012, DOI 10.1007/978-1-4419-0851-3

that the vehicle is propelled to overcome aerodynamic drag, rolling resistance drag, and kinetic resistance.

Some engineers and even researchers may consider traction motors kindred or similar to industrial motors. However, traction motors usually require frequent start/stop, high rate of acceleration/deceleration, high-torque low-speed hill climbing, low-torque high-speed cruising, and very wide speed range of operation, whereas industrial motors are generally optimized at rated conditions. Thus, traction motors are so unique that they are deserved to form an individual class. Hence, the general requirements of traction motor are significantly different from those of industrial motors. Their major differences in load requirement, performance specification, and operating environment are as follows:

- Traction motors need to offer the maximum torque that is four to five times of the rated torque for temporary acceleration and hill climbing, while industrial motors generally offer the maximum torque that is twice of the rated torque for overload operation.
- Traction motors need to achieve four to five times the base speed for highway cruising, while industrial motors generally achieve up to twice the base speed for constant-power operation.
- Traction motors should be designed according to the vehicle driving profiles and drivers' habits, while industrial motors are usually based on a typical working mode.
- Traction motors demand both high power density and good efficiency map (high efficiency over wide speed and torque ranges) for the reduction of total vehicle weight and the extension of driving range, while industrial motors generally need a compromise among power density, efficiency, and cost with the efficiency optimized at a rated operating point.
- Traction motors desire high controllability, high steady-state accuracy, and good dynamic performance for multiple-motor coordination, while only special-purpose industrial motors desire such performance.
- Traction motors need to be installed in mobile vehicles with harsh operating conditions such as high temperature, bad weather, and frequent vibration, while industrial motors are generally located in fixed places.

Introduction

An electric motor drive is the heart of electric vehicles (EVs). Its job is to interface energy source (such as batteries) with vehicle wheels, transferring energy in either direction as required, with high efficiency, under control of the driver at all times. Hence, the electric motor drives are the core technology for electric, hybrid, and fuel cell vehicles. The major requirements of the traction motor drive are the following: [1–3]:

1. High torque density and power density
2. Very wide speed range, including constant-torque and constant-power regions
3. High efficiency over wide torque and speed ranges
4. High torque for low-speed starting and climbing, and high power for high-speed cruising
5. Fast torque response
6. High intermittent overload capability for overtaking
7. High reliability and robustness for vehicular environment
8. Low acoustic noise
9. Reasonable cost

Typical torque/power-speed characteristics required for traction motor drives are illustrated in Fig. 1.

To satisfy these special requirements, the power rating and torque-speed requirements of the motor drive should be determined on the basis of driving cycles and system-level consideration. New motor design technologies and control strategies are being

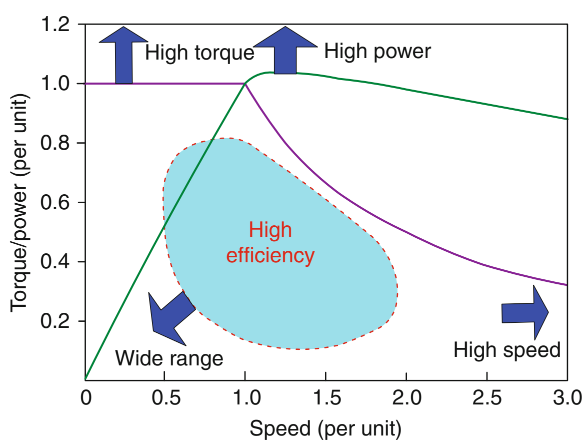

Vehicle Traction Motors. Figure 1
Torque/power requirements for traction motors

pursued to extend the speed range, to optimize the system efficiency, and to enlarge the high-efficiency region. Newly developed electronic products are also adopted to improve the system performance and to reduce the total cost.

From the functional point of view, a traction motor drive system can be divided into two parts – electrical and mechanical. The electrical part consists of the subsystems of motor, power converter, and electronic controller, whereas the mechanical part includes the subsystems of mechanical transmission (optional) and vehicle wheels. The boundary between the electrical and mechanical parts is the air-gap of the motor, where electromechanical energy conversion is taken place. The electronic controller can be further divided into three functional units – sensor, interface circuitry, and processor. The sensor is used to translate the measurable quantities, such as current, voltage, temperature, speed, torque, and flux, into electronic signals. Through the interface circuitry, these signals are conditioned to the appropriate level before being fed into the processor. The processor output signals are usually amplified via the interface circuitry to drive power semiconductor devices of the power converter. The converter acts as a power conditioner that regulates the power flow between the energy source and the electric motor for motoring and regeneration. Finally, the motor interfaces with the vehicle wheels via the mechanical transmission. This transmission is optional because the electric motor can directly drive the wheel as in the case of in-wheel drives. The functional block diagram of a motor drive for EVs is shown in Fig. 2.

Based on the technological growth of electric motors, power electronics, microelectronics, and control strategies, more and more kinds of motor drives become available for EVs. DC motor drives have been traditionally used for EV propulsion because of their ability to achieve high torque at low speeds and easy control. However, the DC motor needs careful maintenance due to its commutator and brushes. Recent technological developments have enabled a number of advanced motor drives to offer definite advantages over those DC motor drives, namely, high efficiency, high power density, efficient regenerative braking,

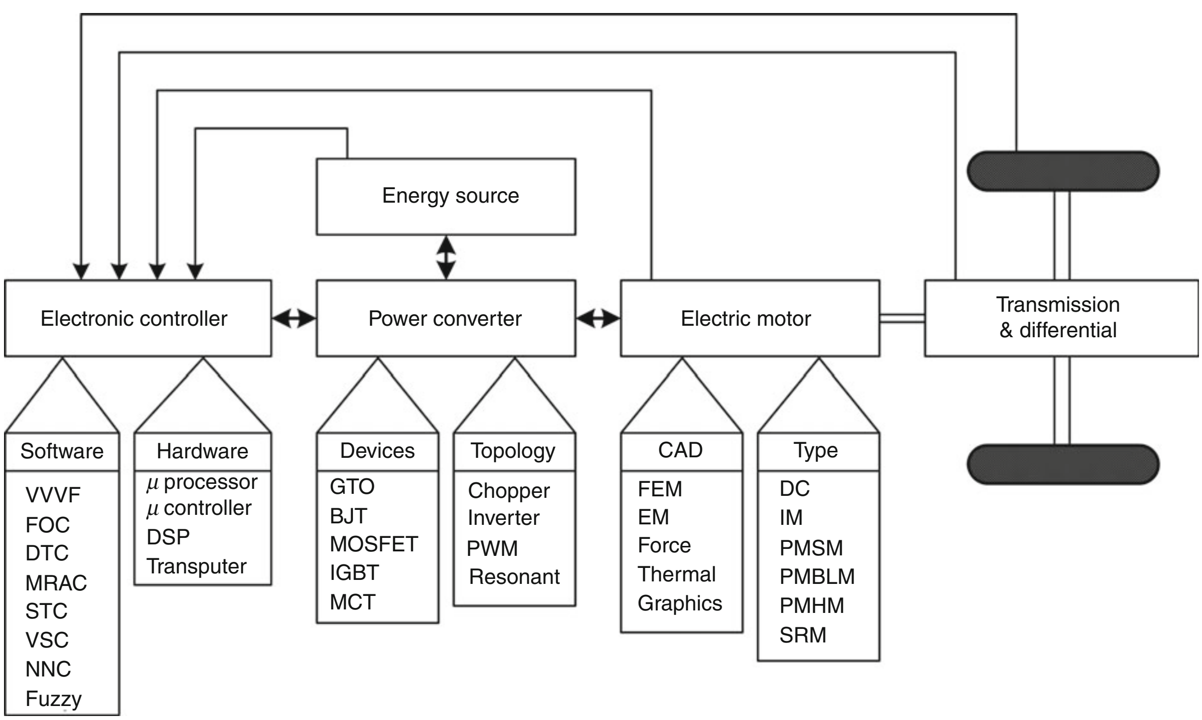

Vehicle Traction Motors. Figure 2
Functional block diagram of an EV drive system

robust, reliable, and maintenance free. Among them, the vector controlled induction motor drive is most popular and mature, though it may suffer from low efficiency at light-load ranges. On the other hand, permanent magnet (PM) brushless motors possess the highest efficiency and power density over the others, but may suffer from a difficulty in flux weakening control for the constant-power high-speed region. The PM hybrid motor is a special type of PM brushless motors. In this motor, an auxiliary DC field winding is so incorporated that the air-gap flux is a resultant of the PM flux and field-winding flux. By adjusting the field-winding excitation current, the air-gap flux can be varied flexibly, hence offering optimal efficiency over a wide speed range. Switched reluctance (SR) motors offer promising features for EV applications due to their simplicity and reliability in both motor construction and power converter configuration, wide speed range, favorable thermal distribution, and efficient regenerative braking. However, they may suffer from torque ripples and acoustic noise problems.

The choice of traction motor drive for EVs mainly depends on three factors – driver expectation, vehicle constraint, and energy source. The driver expectation is defined by a driving profile which includes the acceleration, maximum speed, climbing capability, braking, and range. The vehicle constraint depends on the vehicle type, vehicle weight, and payload. The energy source relates with batteries, fuel cells, capacitors, flywheels, and various hybrid sources. Thus, the process of identifying the preferred features and packaging options for electric motor drive has to be carried out at the system level. The interactions between subsystems and those likely impacts of system trade-offs must be examined.

Classification

Electric motors have been available for over a century. The evolution of motors, unlike that of electronics and computer science, has been long and relatively slow. Nevertheless, the development of motors is continually fuelled by new materials, sophisticated topologies, powerful computer-aided designs (CAD), as well as modern power electronics and microelectronics. Based on the technological growth of electric motors, power electronics, microelectronics, and control strategies, more and more kinds of motor drives become available for EVs. As illustrated in Fig. 3, those traction motors applicable to EVs can be classified as two main groups, namely, the brushed motors and brushless motors. The former simply denote that they generally consist of the commutator and brushes, mainly traditional DC motors, while the latter have no brushes.

DC Motor

Traditionally, DC brushed motors have been loosely named as DC motors. There are typically four types of wound-field DC motors, depending on the mutual interconnection between the field and armature

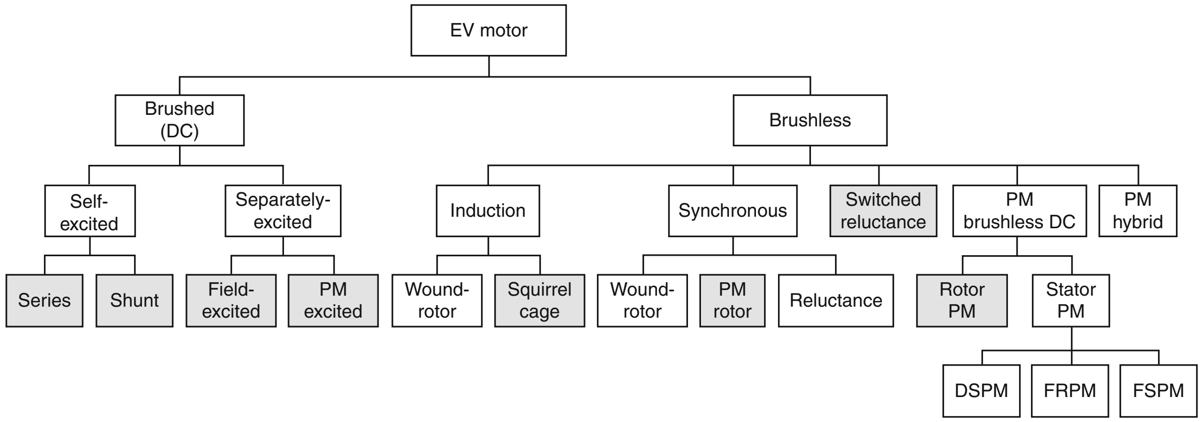

Vehicle Traction Motors. Figure 3
Classification of traction motors for EVs

windings, namely, separately excited, shunt excited, series excited, and compound excited. By replacing the field winding of DC motors with PMs, PMDC motors permit a considerable reduction in stator diameter due to the efficient use of radial space. Owing to the low permeability of PMs, armature reaction is usually reduced and commutation is improved. The control principle of DC motor is simple because of the orthogonal disposition of field and armature mmfs. Figure 4 illustrates the cross section of a wound-field DC motor.

However, the principal problem of DC motors, due to their commutators and brushes, makes them less reliable and unsuitable for maintenance-free operation. Nevertheless, because of mature technology and simple control, DC motors have ever been prominent in electric propulsion. Actually, various types of DC motors, including series, shunt, separately excited, and PM excited, have ever been adopted by recent EVs.

Recently, technological developments have pushed brushless motors to a new era, leading to take the advantages of higher efficiency, higher power density, lower operating cost, more reliable, and maintenance free over DC brushed motors. As high reliability and maintenance-free operation are prime considerations for electric propulsion in EVs, brushless motors are becoming attractive.

Induction Motor

Induction motors (IM) are a widely accepted brushless motor type for EV traction because of their low cost, high reliability, and free from maintenance. There are two types of induction motors, namely, wound rotor and squirrel cage motors. The wound-rotor IMs are less attractive than their squirrel-cage counterparts due to their higher cost, more maintenance, and lack of sturdiness. The most common types of induction motor rotors are the squirrel cage in which aluminum bars are cast into slots in the outer periphery of the rotor, as shown in Fig. 5 [4, 5].

The main advantages of IM include: (1) Robust structure and relatively low cost; (2) Light weight, small volume, and high efficiency. The disadvantages include: (1) The limited constant-power range (only two to three times the base speed); (2) Relatively difficult control schemes due to the variable equivalent parameters.

Conventional control of induction motors such as variable-voltage variable frequency (VVVF) cannot provide the desired performance. One major reason is due to the nonlinearity of their dynamic model. With the advent of microcomputer era, the principle of field-oriented control (FOC) of induction motors has been accepted to overcome their control complexity due to

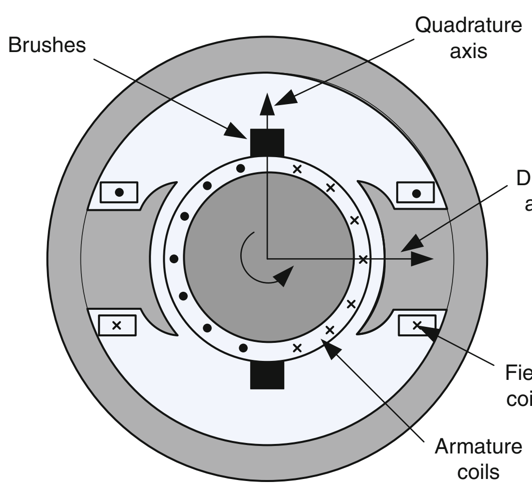

Vehicle Traction Motors. Figure 4
Schematic of DC motor

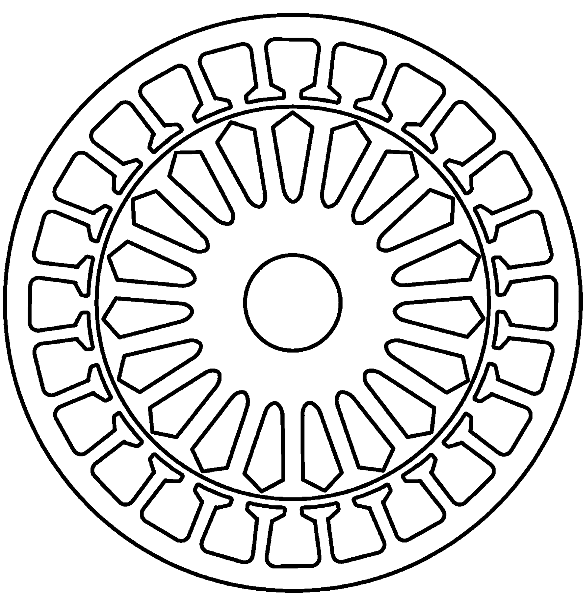

Vehicle Traction Motors. Figure 5
Induction motor with squirrel cage

the nonlinearity. Notice that FOC is also known as vector control or decoupling control. Nevertheless, these EV induction motors employing FOC still suffer from low efficiency at light loads and limited constant-power operating region. On the one hand, an online efficiency-optimizing control scheme has been developed for these EV induction motors [6], which can reduce the consumed energy by about 10% and increase the regenerative energy by about 4%, leading to extend the driving range of EVs by more than 14%. On the other hand, an electrically pole changing scheme has been developed for EV induction motors [7, 8], which can significantly extend the constant-power operating region to over four times the base speed.

Permanent Magnet Brushless Motors

Permanent magnet brushless motors (PMBM) include sinusoidal and trapezoidal back-EMF machines. From the control schemes, they are divided into brushless DC (BLDC) and brushless AC (BLAC) motors. Generally, a trapezoidal back-EMF waveform in BLDC or a sinusoidal back-EMF waveform in BLAC is needed so as to achieve high-torque density and low-torque pulsation. The PM brushless AC motor with sinusoidal back-EMF is also called as the PM synchronous motor. The most obvious advantage of these motors is the removal of brushes, leading to eliminate many problems associated with brushes.

The PM BLAC motor can run from a sinusoidal or PWM supply without electronic commutation. When PMs are mounted on the rotor surface, they behave as non-salient synchronous motors because the permeability of PMs is similar to that of air. By burying those PMs inside the magnetic circuit of the rotor, the saliency causes an additional reluctance torque which leads to facilitate a wider speed range at constant-power operation. Similar to induction motors, those PM synchronous motors usually employ FOC or DTC for high-performance applications. Because of their inherent high power density and high efficiency, they have been accepted to have great potential to compete with induction motors for EV applications. To achieve optimal efficiency throughout the operating region, a self-tuning control has been developed for PM synchronous motors [9].

The PM BLDC motor has surface-mounted magnets on the rotor, and a concentrated fractional stator winding, which results in a low copper loss. Different from PM synchronous motors, these PM BLDC motors generally operate with shaft position sensors. Recently, a phase-decoupling PM BLDC motor has been developed for EVs, which offers the merits of outstanding power density, no cogging torque, and excellent dynamic performance [10]. Also, it can adopt advanced conduction angle control to greatly extend the constant-power operating range [11].

The main advantages of PM brushless motors are: (1) Light weight, small volume, and high power density as the magnetic field is excited by high-energy PMs; (2) High efficiency, high reliability, and good heat dissipation.

The main disadvantages include: (1) A comparatively narrow range of constant-power operation due to the difficultly in weakening the air-gap flux. By using some new schemes, the speed range can reach three times the base speed. However, the PM may suffer from demagnetization and possible fault. (2) Relatively high cost due to PM materials, especially in high power application [5].

Figure 6 illustrates the typical topologies of the PM brushless motors.

It should be emphasized that all the PM machines mentioned above have the magnets located in the rotor, and are referred as "rotor-PM machines," which are predominated in EV applications due to their outstanding advantages. However, the magnets usually need to be protected from the centrifugal force by employing a retaining sleeve, which is made of either stainless steel or non-metallic fiber. The rotor temperature rise may be a problem due to poor thermal dissipation, which may cause irreversible demagnetization of magnets and ultimately limit the power density of the machine. Recently, in contrast, a new type of PM machines having magnets in stator, nominated as "stator-PM machines," have reemerged and developed, which can overcome the problems suffered by rotor-PM counterparts [12]. Conceptually, the stator-PM machines employ the polarized reluctance principle, in which torque and emfs are resultant from the flux-switching action of rotor saliencies on a unipolar flux produced by PMs in the stator. Since the rotor has neither PMs nor windings, these stator-PM machines are mechanically simple and robust, hence very suitable for high-speed

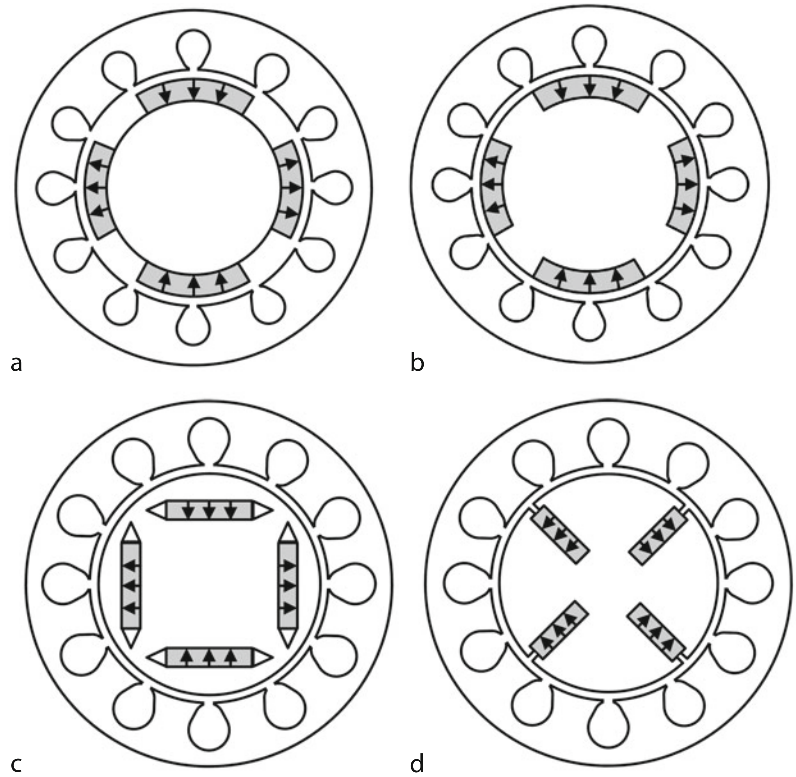

Vehicle Traction Motors. Figure 6

Typical topologies of PM brushless motors. (**a**) Surface mounted; (**b**) surface inset; (**c**) interior radial; (**d**) interior circumferential

operation. Compared with conventional rotor-PM brushless machine topologies, generally, it is easier to limit the temperature rise of the magnets as heat is dissipated more effectively from the stator. According to the location of the PMs in stator, they can be classified as the doubly salient PM (DSPM) machine [13, 14], flux-reversal PM (FRPM) machine [15, 16], and flux-switching PM (FSPM) machine [17–19].

(a) Doubly Salient PM Machine: In this DSPM machine, the PMs are placed in stator back-iron. Figure 7 shows a 12/8-pole DSPM machine topology (with 12 stator poles and 8 rotor poles). For a three-phase machine a magnet is required in the stator back-iron for every three teeth, while for a four-phase machine a magnet is required for every four teeth. The variation of the flux-linkage with each coil as the rotor rotates is unipolar, while the back-EMF waveform tends to be trapezoidal [12]. Thus, this topology is more suitable for BLDC operation. However, a major disadvantage of the DSPM motor is relatively poor torque density as compared to that of other PM brushless machines [20] due to the unipolar flux-linkage, although, as reported in [14], it can still be higher than that of an induction machine.

(b) Flux-Reversal PM Machine: The FRPM machine has the magnets located on the surface of stator teeth and concentrated windings. Figure 8 illustrates a 12/10-pole FRPM machine topology. Each stator tooth has a pair of magnets of different polarity mounted at its surface. When a coil is excited, the field under one magnet is reduced while that under the other is increased, and the salient rotor pole rotates toward the stronger magnetic field. The flux-linkage with each coil reverses polarity as the rotor rotates. Thus, the phase flux-linkage variation

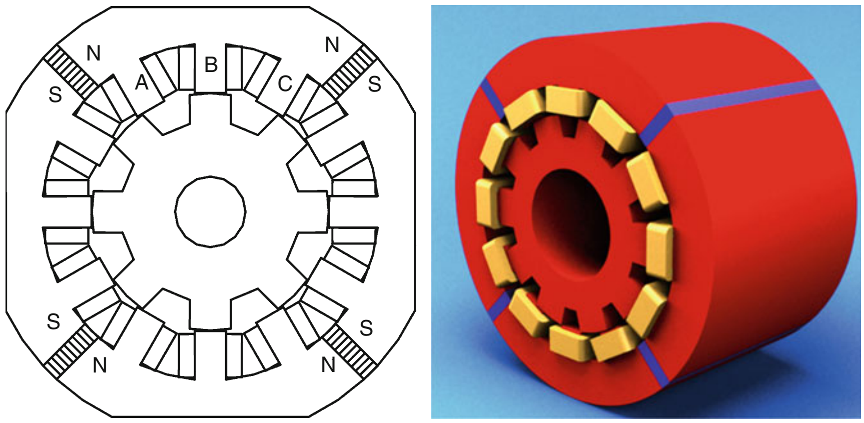

Vehicle Traction Motors. Figure 7
A 12/8-pole DSPM machine

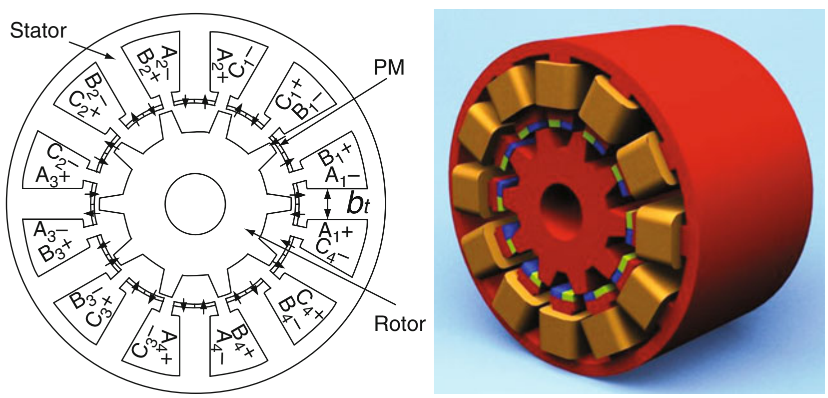

Vehicle Traction Motors. Figure 8
FRPM machine

is bipolar, while the phase back-EMF waveform is, again, essentially trapezoidal. Thus, it is suitable for BLDC operation mode. Additionally, it is found that the FRPM machine exhibits fault-tolerance capability due to its natural isolation between the phases, and the variation of inductances versus rotor position is small. Such a machine topology exhibits a low winding inductance, while the magnets are more vulnerable to partial irreversible demagnetization. In addition, significant eddy-current loss may be induced in the magnets, which also experience a significant radial magnetic force. Further, since the air-gap flux density is limited by the magnet remanence, the torque density may be compromised [2].

(c) Flux-Switching PM Machine: In this FSPM machine, the stator consists of U-shaped laminated segments between which circumferentially magnetized PMs are sandwiched, while the direction of magnetization is being reversed from one magnet to the next. Figure 9 shows a 12/10-pole FSPM machine topology. Each stator tooth comprises two adjacent laminated segments and a PM. Thus, flux-concentration can be readily incorporated, so that low-cost ferrite magnets can be employed [2]. In addition, in contrast to conventional PM brushless machines, the influence of the armature reaction field on the working point of the magnets is minimal. As a consequence, the electric loading of FSPM machines can be very high.

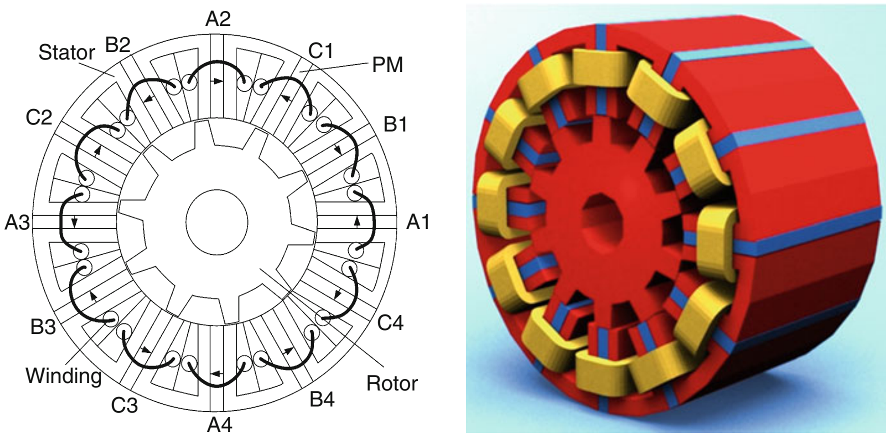

Vehicle Traction Motors. Figure 9
FSPM machine

Therefore, since the phase flux-linkage waveform is bipolar, the torque capability is significantly higher than that of a DSPM machine [20]. Due to the magnetic reluctance difference between the two pairs of coils composing a phase, the resultant phase emf waveforms are essentially sinusoidal without any additional measures [18], which makes them more appropriate for BLAC operation. In addition, since a high per unit winding inductance can readily be achieved, such machines are eminently suitable for constant-power operation over a wide speed range.

PM Hybrid Motor

Although the PM brushless motors possess the highest efficiency and power density over the others, they suffer from a difficulty in flux control. Hence, the current phase angle has to be progressively advanced as the speed is increased above the base-speed so that a demagnetizing d-axis current component is produced which reduces the flux-linkage. Ultimately, however, this may cause partial irreversible demagnetization of the magnets. At the same time, due to the inverter voltage and current limits, the torque-producing q-axis current component has to be reduced correspondingly. Consequently, the torque and power capabilities are limited [2]. Thus, a compromise has to be made between the low-speed torque capability and high-speed power capability. Hybrid PM and field current excitation have been shown to be beneficial in improving the power capability in the extended speed range, enhancing the low-speed torque capability, and improving the overall operational efficiency. Figures 10 and 11 show PM hybrid motors with rotary and stationary PMs, respectively [10, 21]. The PM hybrid motor is a special type of PM brushless motors. In this motor, an auxiliary DC field winding is so incorporated that the air-gap flux is a resultant of the PM flux and field-winding flux. These PM hybrid motors offer many attractive features due to the presence of the hybrid PM field [3]:

1. By varying the polarity and magnitude of the DC field current, the air-gap flux density becomes easily controllable.
2. By realizing flux strengthening, the machine can offer the exceptionally high-torque feature, which is very essential for cold cranking HEVs or providing temporary power for vehicular overtaking and hill climbing.
3. By realizing flux weakening, the machine can offer the exceptionally wide speed constant-power feature, which is very essential for EV cruising.
4. By online tuning the air-gap flux density, the machine can maintain a constant voltage output under generation or regeneration over a very wide speed range, which is very essential for battery charging of various EVs.
5. By online tuning the air-gap flux density, the machine can also offer efficiency-optimizing-control (EOC), which is highly desirable for EVs.

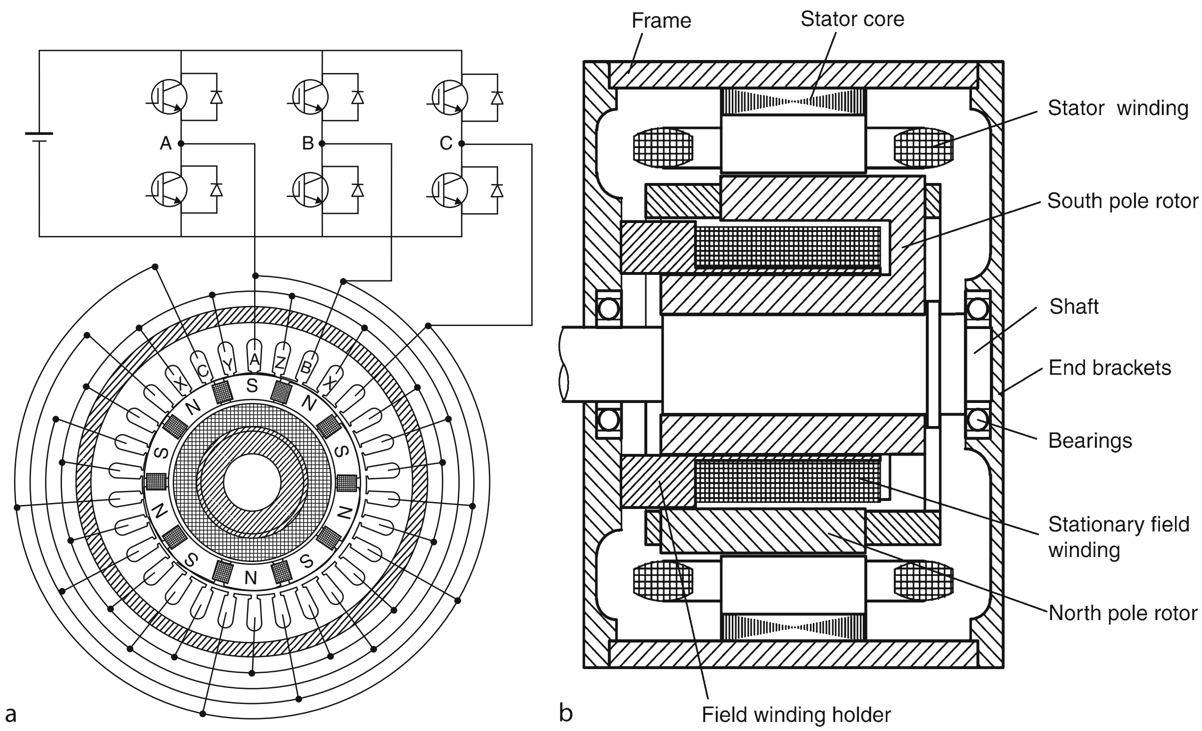

Vehicle Traction Motors. Figure 10
Hybrid PM machine with rotary PMs

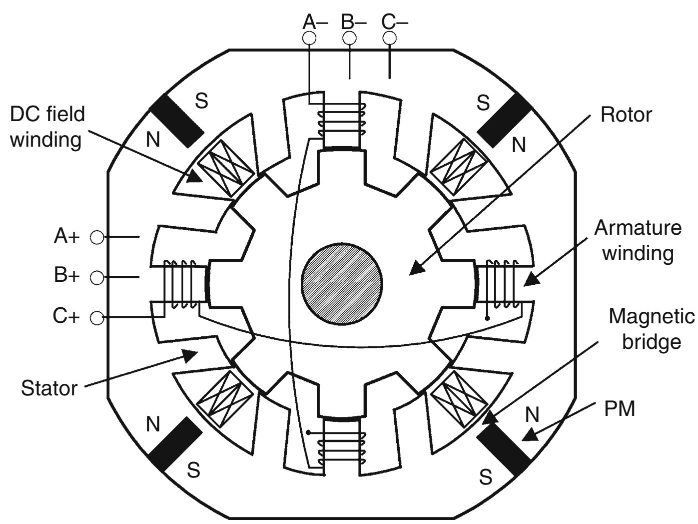

Vehicle Traction Motors. Figure 11
Hybrid PM machine with stationary PMs

Switched Reluctance Motor

SR motors have been recognized to have considerable potential for EV applications. Figure 12 shows the schematic of an 8/6-pole SR motor. SR motors have the definite advantages of simple construction, low manufacturing cost, inherent fault tolerance, and

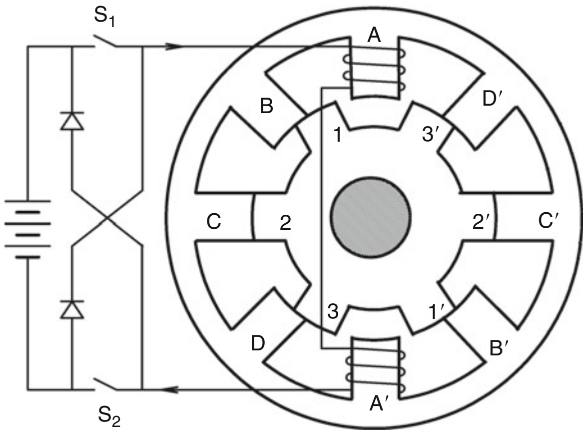

Vehicle Traction Motors. Figure 12
Basic structure of switched reluctance motor drive (only one phase winding shown)

Vehicle Traction Motors. Table 1 Applications of EV motors

EV models	EV motors
Fiat Panda Elettra	Series DC motor
Mazda Bongo	Shunt DC motor
Conceptor G-Van	Separately excited DC motor
Suzuki senior tricycle	PMDC motor
Fiat Seicento Elettra	Induction motor
Ford Th!nk City	Induction motor
GM EV1	Induction motor
Honda EV Plus	PM synchronous motor
Nissan Altra	PM synchronous motor
Toyota RAV4	PM synchronous motor
Chloride Lucas	Switched reluctance motor
Toyota Prius (2005)	PM BLDC motor
Honda Civic	PM BLDC motor

outstanding torque-speed characteristics for EV propulsion. Although they possess the simplicity in construction, it does not imply any simplicity of their design and control. Because of the heavy saturation of pole tips and the fringe effect of poles and slots, their design and control are difficult and subtle. Also, they usually exhibit relatively high acoustic noise, vibration, and torque ripple problems. Recently, an optimum design approach to SR motors has been developed [22], which employs finite-element analysis to minimize the total motor losses while taking into account the constraints of pole arc, height, and maximum flux density. Also, fuzzy sliding mode control has been developed for those EV SR motors so as to handle the motor nonlinearities and minimize the control chattering [23, 24].

The motor types that have ever been adopted by recent EVs are indicated by shaded blocks in Fig. 3. Table 1 also illustrates their recent applications to flagship EVs.

In order to evaluate the aforementioned EV motor types, a point grading system is adopted. The grading system consists of six major characteristics and each of them is graded from one to five points. As listed in Table 2, this evaluation indicates that induction motors and PM brushless motors are relatively most acceptable. When the cost of PM material has significant improvements, the PM brushless (including AC or DC) motors will be most attractive. Conventional DC motors seem to be losing their competitive edges, whereas both SR and PM hybrid motors have increasing potentials for EV propulsion.

Design Consideration

Basic Consideration

The basic consideration of motor design includes magnetic loading – the peak of fundamental component of radial flux density in the air-gap of the motor, electric loading – the total rms current per unit length of periphery of the motor or ampere-turns per unit periphery, power per unit volume and weight, torque per unit volume and weight, flux density at each part of the magnetic circuit, speed, torque and power, losses and efficiency, and thermal design and cooling.

The corresponding key issues are better utilization of steel, magnet, and copper; better electromagnetic coupling; better geometry and topology; better thermal design and cooling; understanding the limits on the motor performance; and understanding the relationship among geometry, dimensions, parameters, and performance, thus to achieve higher power per unit weight, higher torque per unit weight, and better performance.

Traction motor drives for EVs should be designed, as close as possible, to the ideal torque/power-speed characteristics as shown in Fig. 13. In the constant-torque region I, the maximum torque capability is determined by the current rating of the inverter, while in the constant-power region II, flux weakening or commutation phase advance has to be employed due to the inverter voltage and current limits. In region III, the torque and power are reduced due to the increasing influence of the back-emf. However, the power capability and the maximum speed can be enhanced without sacrificing the low-speed torque capability by employing a DC–DC voltage booster [2], a technique which is employed in the Toyota hybrid system, or by employing series/parallel winding connections, i.e., series connection at low speed and parallel connection at high speed, as demonstrated in [25] and [26].

Electrical machine design cannot be undertaken in isolation, but must account for the control strategy and the application requirements, both static and dynamic. Hence, a system-level design approach is essential.

Vehicle Traction Motors. Table 2 Evaluation of EV motors

	DC motor	Induction motor	PM brushless motor	SR motor	PM hybrid motor
Power density	2.5	3.5	5	3.5	4
Efficiency	2.5	3.5	5	3.5	5
Controllability	5	4	4	4	4.5
Reliability	3	5	4	5	4
Maturity	5	5	5	4	3
Cost	4	5	3	4	3
Total	22	26	26	24	23.5

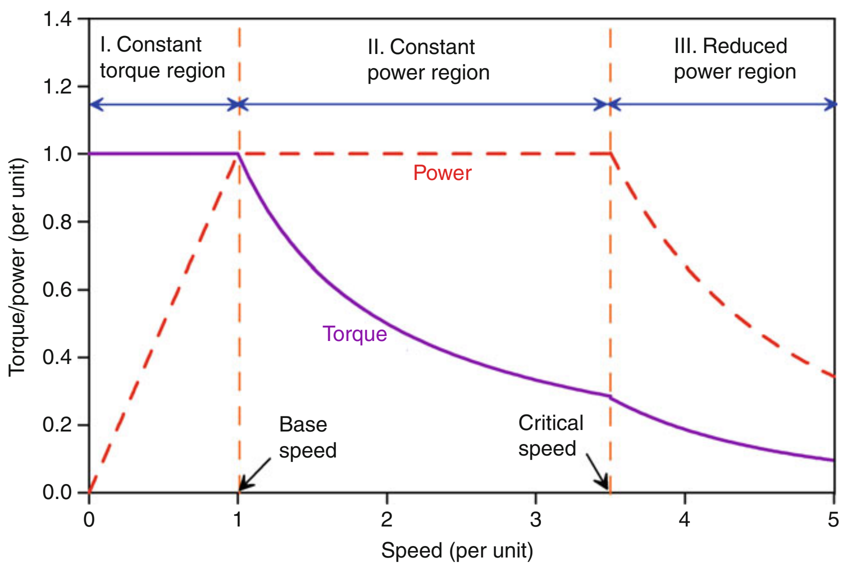

Vehicle Traction Motors. Figure 13
Ideal torque/power-speed characteristics

System Consideration

Vehicle operation consists of three main segments. They are: (1) the initial acceleration; (2) cruising at vehicle rated speed; and (3) cruising at the maximum speed. These three operations provide the basic design constraints for the EV and HEV drive train.

Apart from satisfying the aforementioned special requirements, the design of traction motors also depends on the system technology of EVs. From the technological point of view, the following key issues should be considered:

1. Single- or multiple-motor configurations. One adopts a single motor to propel the driving wheels, while another uses multiple motors permanently coupled to individual driving wheels. The single-motor configuration has the merit of using only one motor which can minimize the corresponding size, weight, and cost. On the other hand, the multiple-motor configuration takes the advantages to reduce the current/power ratings of individual motors and evenly distribute the total motor size and weight. Also, the multiple-motor one needs additional precaution to allow for fault tolerance during the electronic differential action. The functional block diagrams of single- and dual-motor configurations are shown in Fig. 14, while their comparison is listed in Table 3. Since these two configurations have their individual merits, both of them have been employed by modern EVs. For example, the single-motor configuration has been adopted in the GM EV1 while the dual-motor configuration has been adopted in the NIES Luciole. Nevertheless, as reliability is of utmost importance for EVs, the use of single-motor configuration is rekindling, especially for commercialization.
2. Fixed- or variable-gearing transmissions. It is also classified as single-speed and multiple-speed transmissions. The former adopts single-speed

Vehicle Traction Motors. Table 3 Comparison of single- and dual-motor configurations

	Single motor	Dual motor
Cost	Lower	Higher
Size	Lumped	Distributed
Weight	Lumped	Distributed
Efficiency	Lower	Higher
Differential	Mechanical	Electronic
Reliability	Higher	Lower
Failure modes	Better	Worse

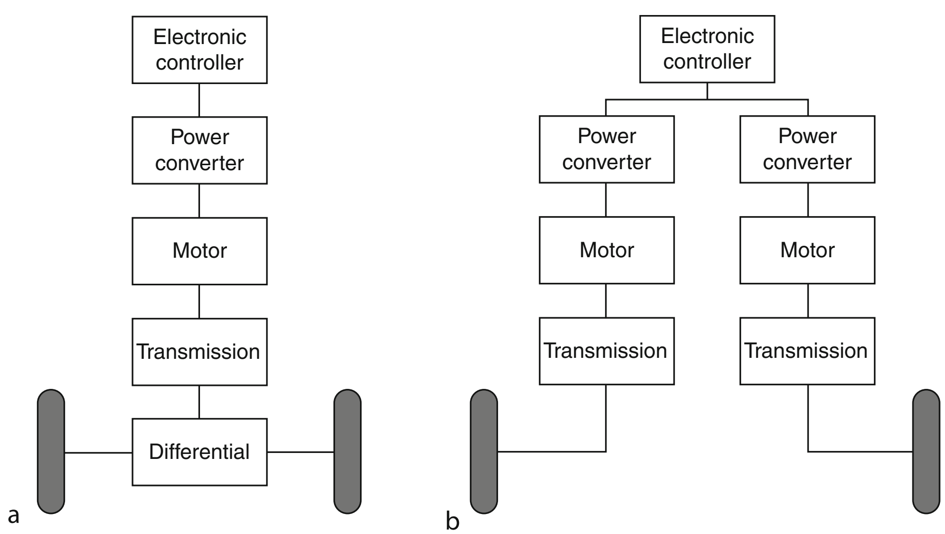

Vehicle Traction Motors. Figure 14
(**a**) Single-motor and (**b**) dual-motor configurations

fixed-gearing, while the latter uses multiple-speed variable gearing together with the gearbox and clutch. Based on fixed-gearing transmission, the motor should be so designed that it can provide both high instantaneous torque (three to five times the rated value) in the constant-torque region and high operating speed (three to five times the base speed) in the constant-power region. On the other hand, the variable-gearing transmission provides the advantage of using conventional motors to achieve high starting torque at low gear and high cruising speed at high gear. However, there are many drawbacks on the use of variable gearing such as the heavy weight, bulky size, high cost, less reliable, and more complex. Table 4 gives a comparison of fixed-gearing and variable-gearing transmissions. Actually, almost all the modern EVs adopt fixed-gearing transmission.

Vehicle Traction Motors. Table 4 Comparison of fixed- and variable-gearing transmissions

	Fixed gearing	Variable gearing
Motor rating	Higher	Lower
Inverter rating	Higher	Lower
Cost	Lower	Higher
Size	Smaller	Larger
Weight	Lower	Higher
Efficiency	Higher	Lower
Reliability	Higher	Lower

3. Geared or gearless. The use of fixed-speed gearing with a high gear ratio allows EV motors to be designed for high-speed operation, resulting high power density. The maximum speed is limited by the friction and windage losses as well as transaxle tolerance. On the other hand, EV motors can directly drive the transmission axles or adopt the in-wheel drive without using any gearing (gearless operation). However, it results the use of low-speed outer-rotor motors which generally suffer from relatively low-power density. The breakeven point is whether this increase in motor size and weight can be outweighed by the reduction of gearing. Otherwise, the additional size and weight will cause suspension problems in EVs. The functional block diagrams of geared and gearless in-wheel motor configurations are shown in Fig. 15. Both of them have been employed by modern EVs. For examples, the high-speed geared inner-rotor in-wheel motor has been adopted in the NIES Luciole while the low-speed gearless outer-rotor in-wheel motor was adopted in the TEPCO IZA. Nevertheless, with the advent of compact planetary gearing, the use of high-speed planetary-geared in-wheel motors is becoming more attractive than the use of low-speed gearless in-wheel motors.

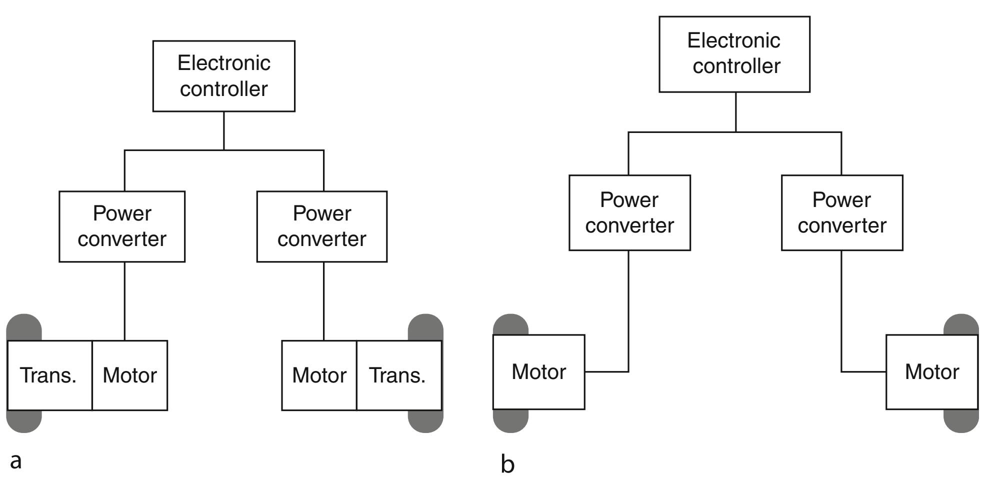

Vehicle Traction Motors. Figure 15
In-wheel motor configurations. (**a**) Geared motor; (**b**) Gearless motor

4. System voltage. The design of traction motors is greatly influenced by the voltage level of the EV system. Reasonable high-voltage motor design can be adopted to reduce the cost and size of inverters. If the desired voltage is too high, a large number of batteries will be connected in series, leading to the reduction of interior and luggage spaces, the increase in vehicle weight and cost, as well as the degradation of vehicle performances. Since different EV types adopt different system voltage levels, the design of EV motors needs to cater for different EVs. Roughly, the system voltage is governed by the battery weight which is about 30% of the total vehicle weight. In practice, higher power motors adopt higher voltage levels. For examples, the GM EV1 adopts the 312-V voltage level for its 102-kW motor, whereas the Reva EV adopts the 48-V voltage level for its 13-kW motor.
5. Integration. The integration of the motor with the converter, controller, transmission and energy source is prime important consideration. The EV motor designer should fully understand the characters of these components, thus to design the motor under these given environments. It is quite different with the normal standard motors under standard power source for normal industrial drives.

Efficiency

The efficiency may be classified into two types, namely, energy efficiency and power efficiency. The energy efficiency η_e is the ratio of energy output to energy input, while the power efficiency η_p is the ratio of power output to power input. So, they can simply be expressed as:

$$\eta_e = \frac{E_{out}}{E_{in}}$$

$$\eta_p = \frac{P_{out}}{P_{in}}$$

For industrial operation, these two efficiencies may not be necessarily distinguishable. On the contrary, for vehicular operation, there is a significant difference because the power efficiency varies continually during the operation of most vehicles. Thus, it is necessary to delineate the power efficiency associated with the speed and torque conditions. Instead of using a particular operating point (such as rated power at rated torque and rated speed) to describe the power efficiency of a vehicle subsystem or component, an efficiency map is generally adopted. Figure 16 shows typical efficiency maps of a three-phase induction motor and a PM BLDC motor for propelling an EV. Hence, the energy efficiency can be derived by summing powers over a given time period.

Regenerative braking is a definite advantage of EVs over internal combustion engine vehicles (ICEVs). During braking, the motor operates in the regenerative mode which converts the reduction of kinetic energy during braking into electrical energy, hence recharging the batteries. On average, the amount of convertible

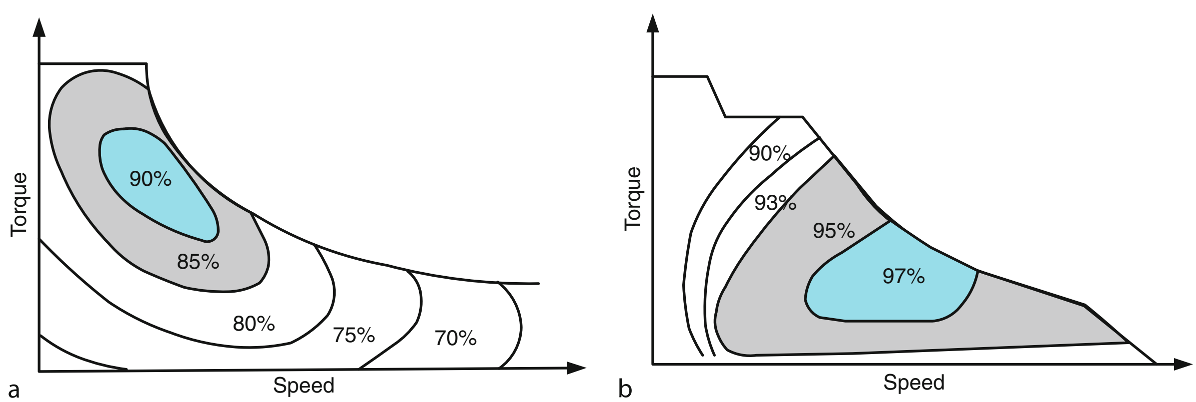

Vehicle Traction Motors. Figure 16
Typical power efficiency maps of EV traction motors. (**a**) Induction motor; (**b**) PM BLDC motor

energy is only about 30–50% as there is significant dissipation in road load. Assuming that the in/out efficiency of the drivetrain and energy source is about 70%, the amount of energy actually stored in the batteries is about 21–35%. This is known as the regenerative braking efficiency. Similar to the previous case, in order to depict the value at different loads, a regenerative braking efficiency map should be adopted.

Design Methodology

To keep up with the stringent requirement and fast changing motor topologies, the design of motors has turned to CAD. Basically, there are two major design approaches – circuit and field. In essence, the circuit approach is based on equivalent circuit analysis while the field approach depends on electromagnetic field analysis. The field approach takes the advantages of more accurate results, greater knowledge of the critical areas, as well as capabilities of handling complicated machine geometry and nonlinear materials. Recently, the finite-element method (FEM) has been regarded as one of the most powerful tools for electromagnetic field analysis of EV motors. The FEM outranks other numerical methods because of its flexibility and applicability in stress and thermal field analyzes.

The performance of a motor drive depends on not only the motor, but also the control circuits. And there are strong coupling between the magnetic circuit and electric circuit of a motor drive. Traditionally, magnetic circuit and electric circuit of electric machines, however, are separately dealt with in dynamic simulations. To evaluate accurately the performance of a motor drive in design procedure, the co-simulation method for the motor drive may be required. In co-simulation, the magnetic circuit and the electric circuit are coupled in time-domain, providing the possibility of system-level simulation. Finite-element time-domain modeling coupled with the equations of circuit and motion is an accurate and detailed approach of simulating drive system performance. Figure 17 illustrates the field-circuit-motion coupled method. The modeling tools for the co-simulation consist of two separate packages, namely, the magnetic solver, Maxwell 2D® and the circuit solver, Simplorer®. The magnetic solver calculates two-dimensional transient magnetic problem of motor drive, while electric circuit

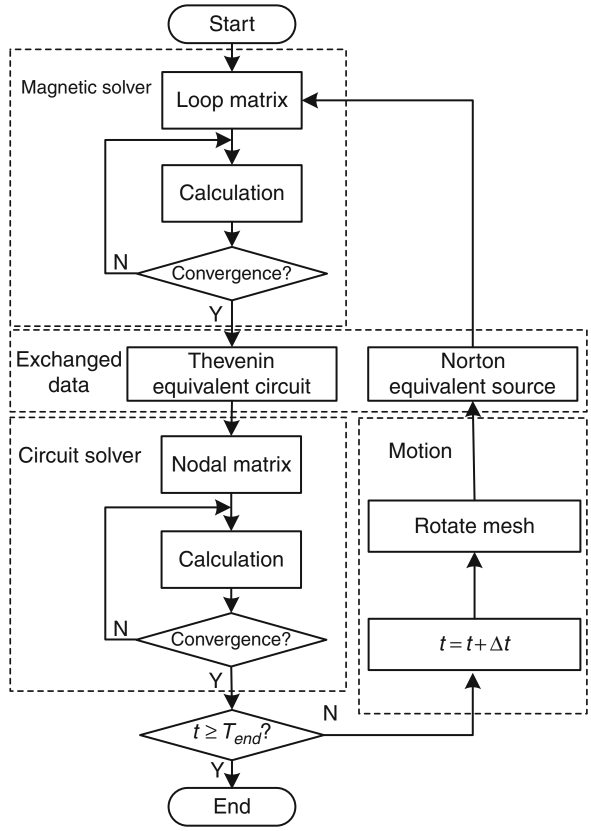

Vehicle Traction Motors. Figure 17
Flowchart of a co-simulation method

and controller are supplied by the circuit solver. Incorporating electric circuit equations into equations of the finite-element system, the magnetic solver uses a loop form of the magnetic equations. At the same time, the circuit solver uses a nodal form of the circuit equations. In each time step, the circuit solver forms a Norton equivalent source of the drive circuit at the coupling pins between the motor and the rest of the drive system. The magnetic solver converts it to a loop matrix and solves the finite-element equations. Finally, the magnetic solver outputs a Thevenin equivalent circuit for the next time step of the circuit solver. This parameter-based coupling enhances the solution accuracy and stability. When the simulation runs in the circuit solver, the magnetic solver will start automatically in a co-simulation mode. At each co-simulation time step, both the simulators exchange the calculated data, and results achieved by one solver will be

exported to the other solver in the next step. The co-simulation model allows an easy access to all available components such as linear or nonlinear resistances, capacitances, inductances, various diodes, controlled switches, independent sources, voltages, and current probes [27, 28].

Control Consideration

Power Electronics

EV Power Devices In the past decades, power semiconductor device technology has made tremendous progress. These power devices have grown in power rating and performance by an evolutionary process. Among existing power devices, the power diode behaves as an uncontrolled switch, whereas the others, including the thyristor, gate turnoff thyristor (GTO), power bipolar-junction transistor (BJT), power metal-oxide field-effect transistor (MOSFET), insulated-gate bipolar transistor (IGBT), static-induction transistor (SIT), static-induction thyristor (SITH), and MOS-controlled thyristor (MCT), are externally controllable. Active research is still being pursued on the development of high performance power devices.

Before selecting the preferred power devices for electric propulsion, the following requirements have to be considered:

- Ratings. The voltage rating is based on the battery nominal voltage, maximum voltage during charging, and maximum voltage during regenerative braking. On the other hand, the current rating depends on the motor peak power rating and number of power devices connected in parallel. When paralleling these devices, on-state and switching characteristics have to be matched.
- Switching frequency. Switching at higher frequencies can bring down the filter size and help to meet the electromagnetic interference (EMI) limitation requirements. Over the switching frequency of 20 kHz, there is no acoustic noise problem.
- Power losses. The on-state conduction drop or loss should be the minimum while the switching loss should be as low as possible. Since higher switching frequencies increase the switching loss, switching the device at about 10 kHz seems to be an optimum for efficiency, power density, acoustic noise, and EMI considerations. The leakage current should also be less than 1 mA to minimize the off-state loss.
- Base/gate driveability. The device should allow for simple and secure base/gate driving. The corresponding driving signal may be either triggering voltage/current or linear voltage/current. The voltage-mode driving involves very little energy and is generally preferable.
- Dynamic characteristics. The dynamic characteristics of the device should be good enough to allow for high dv/dt capability, high di/dt capability, and easy paralleling. The internal antiparallel diode should have similar dynamic characteristics as the main device.
- Ruggedness. The device should be rugged to withstand a specific amount of avalanche energy during overvoltage and be protected by fast semiconductor fuses during over-current. It should operate with no or minimal use of snubber circuits. Since EVs are frequently accelerated and decelerated, the device is subjected to thermal cycling at frequent intervals. It should reliably work under these conditions of thermal stress.
- Maturity and cost. Since the cost of power devices is one of the major parts in the total cost of electric propulsion systems, these devices should be economical. Some recent power devices such as the high power MCT are not yet mature for EV applications.

Taking into account the above requirements, the GTO, power BJT, power MOSFET, IGBT, and MCT are considered for electric propulsion. The thyristor is not considered because it requires additional commutating components to turn off and its switching frequency is limited to 400 Hz. The SIT and SITH are also excluded because of their normally turn-on property and limited availability. In order to evaluate their suitability, a point grading system is adopted, which consists of eight major characteristics and each of them is graded from one to five points. From Table 5, the power MOSFET, IGBT, and MCT score high points which indicate that they are particularly suitable for EV propulsion. Due to its highest score, the IGBT is almost exclusively used for modern EVs. Nevertheless, the power MOSFET has also been accepted for those relatively low-power electric tricycles and bikes.

Vehicle Traction Motors. Table 5 Evaluation of EV power devices

	GTO	BJT	MOSFET	IGBT	MCT
Ratings	5	4	2	5	3
Switching frequency	1	2	4	4	4
Power losses	2	3	4	4	4
Base/gate driveability	2	3	5	5	5
Dynamic characteristics	2	3	5	5	5
Ruggedness	3	3	5	5	5
Maturity	5	5	4	4	2
Cost	4	4	4	4	2
Total	24	27	33	36	30

EV Power Converters The evolution of power converter topologies normally follows that of power devices, aiming to achieve high power density, high efficiency, high controllability, and high reliability [29]. Power converters may be AC–DC, AC–AC at the same frequency, AC–AC at different frequencies, DC–DC or DC–AC. Loosely, DC–DC converters are known as DC choppers while DC–AC converters are known as inverters, which are respectively used for DC and AC motors for electric propulsion.

Initially, DC choppers were introduced in the early 1960s using force-commutated thyristors that were constrained to operate at low switching frequency. Due to the advent of fast-switching power devices, they can now be operated at tens or hundreds of kilohertz. In electric propulsion applications, two-quadrant DC choppers are desirable because they convert battery DC voltage to variable DC voltage during the motoring mode and revert the power flow during regenerative braking. Furthermore, four-quadrant DC choppers are employed for reversible and regenerative speed control of DC motors. A four-quadrant DC chopper is shown in Fig. 18.

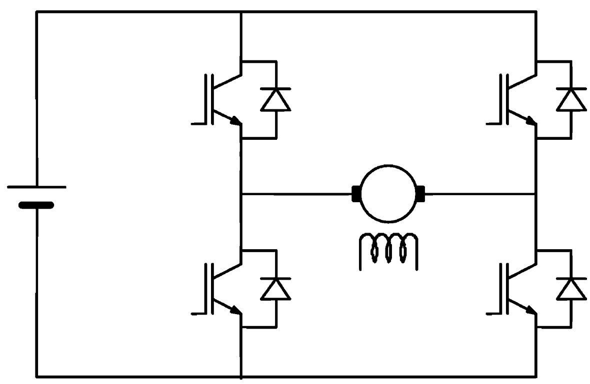

Vehicle Traction Motors. Figure 18 Four-quadrant DC chopper

Inverters are generally classified into voltage-fed and current-fed types. Because of the need of a large series inductance to emulate a current source, current-fed inverters are seldom used for electric propulsion. In fact, voltage-fed inverters are almost exclusively used because they are very simple and can have power flow in either direction. A typical three-phase full-bridge voltage-fed inverter is shown in Fig. 19. Its output waveform may be rectangular, six-step or PWM, depending on the switching strategy for different applications. For example, a rectangular output waveform is produced for a PM BLDC motor, while a six-step or PWM output waveform is for an induction motor. It should be noted that the six-step output is becoming obsolete because its amplitude cannot be directly controlled, and its harmonics are rich. On the other hand, the PWM waveform is harmonically optimal and its fundamental magnitude and frequency can be smoothly varied for speed control.

Starting from the last decade, numerous PWM switching schemes have been developed

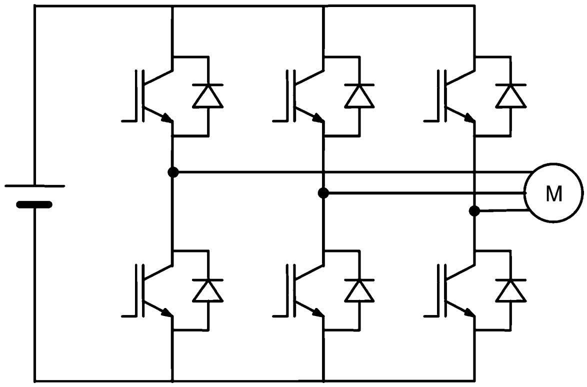

Vehicle Traction Motors. Figure 19
Three-phase full-bridge voltage-fed inverter

for voltage-fed inverters, focusing on the harmonic suppression, better utilization of DC voltage, tolerance of DC voltage fluctuation, as well as suitability for real-time and microcontroller-based implementation [29]. These schemes can be classified as voltage-controlled and current-controlled PWM. The state-of-the-art voltage-controlled PWM schemes are natural or sinusoidal PWM, regular or uniform PWM, harmonic elimination or optimal PWM, delta PWM, carrierless or random PWM, and equal-area PWM. On the other hand, the use of current control for voltage-fed inverters is particularly attractive for high-performance motor drives because the motor torque and flux are directly related to the controlled current. The state-of-the-art current-controlled PWM schemes are hysteresis-band or band–band PWM, instantaneous current control with voltage PWM, and space vector PWM.

Soft-Switching EV Converters Instead of using hard or stressed switching, power converters can adopt soft or relaxed switching. The key of soft switching is to employ a resonant circuit to shape the current or voltage waveform such that the power device switches at zero-current or zero-voltage condition. In general, the use of soft-switching converters possesses the following advantages:

- Due to zero-current or zero-voltage switching condition, the device switching loss is practically zero, thus giving high efficiency.

Vehicle Traction Motors. Table 6 Comparison of hard switching and soft switching for EV converters

	Hard switching	Soft switching
Switching loss	Severe	Almost zero
Overall efficiency	Norm	Possibly higher
Heat-sinking requirement	Norm	Possibly lower
Hardware count	Norm	More
Overall power density	Norm	Possibly higher
EMI problem	Severe	Low
Dv/dt problem	Severe	Low
Modulation scheme	Versatile	Limited
Maturity	Mature	Developing
Cost	Norm	Higher

- Because of low heat sinking requirement and snubberless operation, the converter size and weight are reduced, thus giving high power density.
- The device reliability is improved because of minimum switching stress during soft switching.
- The EMI problem is less severe and the machine insulation is less stressed because of lower *dv/dt* resonant voltage pulses.
- The acoustic noise is very small because of high frequency operation.

On the other hand, their key drawbacks are the additional cost of the resonant circuit and the increased complexity. Although soft-switching DC–DC converters have been widely accepted by switched-mode power supplies, the corresponding development for EV propulsion is much slower. As the pursuit of power converters having high efficiency and high power density for EV propulsion is highly desirable, the development of EV soft-switching power converters is in progress [30–32]. Table 6 gives a comparison between hard-switching and soft-switching converters for EV propulsion.

Although there have been many soft-switching DC–DC converters developed for switched-mode

power supplies, these converters cannot be directly applied to DC motors for EV propulsion. Apart from suffering excessive voltage and current stresses, they cannot handle backward power flow during regenerative braking. It should be noted that the capability of regenerative braking is very essential for EVs as it can extend the vehicle driving range by up to 25%. Recently, a new soft-switching DC–DC converter, having the capability of bidirectional power flow for motoring and regenerative braking as well as the minimum hardware count, has been developed for EV DC motors [33].

The development of soft-switching inverters for AC motors (including induction motors, PM brushless motors, and PM hybrid motors) has become a research direction in power electronics. Figure 20 shows a milestone of soft-switching inverters, namely, the three-phase voltage-fed resonant DC link inverter developed in 1986 [34]. Consequently, many improved soft-switching topologies have been proposed, such as the quasi-resonant DC link, series resonant DC link, parallel resonant DC link, synchronized resonant DC link, resonant transition, auxiliary resonant commutated pole, and auxiliary resonant snubber inverters. A number of development goals of soft-switching inverters for EV propulsion have been identified, namely, efficiency over 95%, power density over 3.5 W/cm^3, switching frequency over 10–20 kHz, *dv/dt* below 1,000 V/μs, zero EMI, zero failure before the end of the vehicle life, and redundant with "limp-home" mode. Recently, the delta-configured auxiliary resonant snubber version has satisfied most of these goals, and has been demonstrated to achieve an output power of 100 kW.

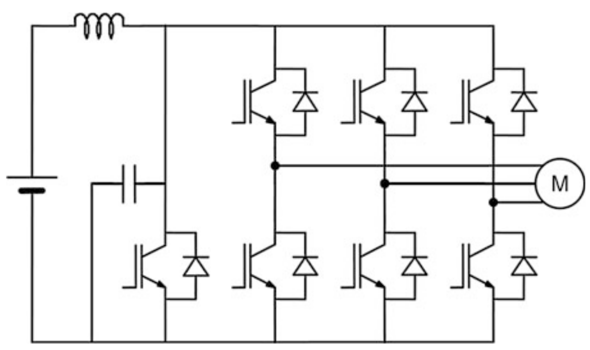

Vehicle Traction Motors. Figure 20
Three-phase voltage-fed resonant DC link inverter

Compared with the development of soft-switching inverters for AC motors, the development for SR motors has been very little [35]. Recently, a new soft-switching converter, so-called the zero-voltage-transition version, has been particularly developed for SR motors [36]. This new converter possesses the advantages that all main switches and diodes can operate at zero-voltage condition, unity device voltage and current stresses, as well as wide operating range. Moreover, it offers simple circuit topology, minimum hardware count, and low cost, leading to achieve high switching frequency, high power density, and high efficiency.

Microelectronics

Since the introduction of microcomputers in 1970, the microelectronics technology has gone through an intense evolution in last 5 decades. Modern microelectronic devices can generally be classified as microprocessors, microcontrollers, and digital signal processors (DSPs).

Microprocessor technology has been used to recognize the milestone of the development of microelectronics, such as the 8086, 80186, 80286, 80386, 80486, Pentium, Pentium II, Pentium III, Pentium IV, Pentium M, and so on. Microprocessors are the CPU of microcomputer systems, which decode instructions, control activities, as well as perform all arithmetic and logical computations. Unlike microprocessors, microcontrollers, such as the 8096, 80196, and 80960, include all resources (CPU, ROM or EPROM, RAM, DMA, timers, interrupt sources, A/D and D/A converters, and I/O ports) to serve as stand-alone single-chip controllers. Thus, microcontroller-based electric propulsion systems possess definite advantages of minimum hardware and compact software. Digital signal processors (DSPs), such as the TMS320C24x/LC24x, TMS320C28x, etc., include several microcontroller peripherals such as Memory, Pulse Width Modulation (PWM) generator, Analog to Digital Converters (ADC), and Event Manager module, and have the capability of high- speed computation to implement sophisticated control algorithm for high performance motor drives for electric propulsion.

By integrating microelectronic devices and power devices on the same chip (like the integration of brain and muscle), power ICs (PICs), loosely named as "smart power," aim to further reduce the cost, minimize the size, and improve the reliability. The PIC may include the power module, control, protection, communication, and cooling. The main problems in PIC synthesis are the isolation between high-voltage and low-voltage devices as well as cooling. Nevertheless, this technology has promising applications to electric propulsion in near future. The key is the integrating and packaging.

Control Strategies

Conventional linear control such as PID can no longer satisfy the stringent requirement placed on high-performance motor drives. In recent years, many modern control strategies have been proposed. The state-of-the-art control strategies that have been proposed for motor drives are direct torque control (DTC), efficiency optimizing control (EOC), artificial intelligent control, position-sensorless control (PSC), and so on [3].

Direct Torque Control DTC is becoming attractive for EVs, particularly for those equipped with dual-motor propulsion which desires fast torque response. It does not rely on current control and depends less on parameters. For the PM BLAC drives, the DTC controls both the torque and the flux-linkage independently [37, 38]. The controller outputs provide proper voltage vectors via the inverter in such a way that these two variables are forced to predefined trajectories.

Efficiency-Optimizing Control (EOC) EOC of motor drives is highly desirable for EVs since their on-board energy storage is very limited. Different types of motor drives may employ different ways for efficiency optimization. For the rotor-PM BLAC drives, the EOC can be achieved by online tuning the input voltage or the d-axis armature current I_{2d} to minimize the total losses P_{loss} [9], [39]

$$P_{loss}(I_{2d}, T, \omega) = P_{cu}(I_{2d}, T, \omega) + P_{Fe}(I_{2d}, T, \omega)$$

where P_{Cu} is the copper loss, and P_{Fe} is the iron loss for the given torque T and speed ω. It can be found that there is a unique optimal operating point. In particular, the minimum total losses occur at a lower d-axis armature current than that of the minimum copper loss, hence illustrating that the maximum torque per ampere control cannot maximize the efficiency of the PM BLAC drives. For the hybrid PM BLAC drive incorporated with an additional DC field winding [40], the EOC can be easily achieved by tuning the polarity and magnitude of the DC field current.

Artificial Intelligent Control All artificial intelligence-based control strategies, such as fuzzy logic control, neural network control, neuro-fuzzy control, and genetic control, are classified as artificial intelligent control (AIC). Among them, the fuzzy logic control [41] and the neural network control [42] are most mature and attractive since they can effectively handle the system's nonlinearities and sensitivities to parameter variations.

Position-Sensorless Control In order to achieve high performance for EV drives, position feedback is almost mandatory. In order to get rid of the costly and bulky position encoder, position-sensorless control (PSC) is becoming attractive [43–45]. There are various PSC techniques which can be classified as motional EMF, inductance variation, and flux-linkage variation. Basically, the position information is derived by online analysis of the voltages and currents in the machine windings.

It should be noted that the PSC can be readily incorporated into other control strategies such as the EOC, the DTC, and the AIC.

Comparison of Control Strategies As shown in Table 7, the aforementioned control strategies are compared in terms of their major advantages, major disadvantages, and typical techniques [3]. Since there are many possible strategies for the AIC, the self-tuning fuzzy PI control [41] is used for exemplification. The corresponding control block diagrams are shown in Fig. 21. Finally, some sample results of these control strategies have illustrated that the EOC can achieve the minimum total losses [39], the DTC can provide direct bang–bang control of torque [38], the AIC can achieve fast and accurate response [41], and the PSC can offer accurate estimation of rotor position [44].

Vehicle Traction Motors. Table 7 Comparison of control strategies

	Advantage	Disadvantage	Techniques
DTC	Fast torque response; no need for current control; less parameter dependence	Cause errors due to drift flux-linkage estimation and variation of stator resistance	Generate the voltage vectors using independent torque and flux computations
EOC	Minimize the overall losses; no need for accurate loss model; work for wide speed and torque range	Originate system oscillation or convergence problem	Control the input voltage or d-axis armature current; control DC field current
AIC	Flexible control algorithms; adapt nonlinearities and parameter variations	Require expert knowledge or intensive computation and sophisticated hardware	Incorporate fuzzy logic, neural network, and other AI into traditional controls
PSC	Eliminate position sensor, hence reduce system size and cost; readily merge into other controls	Require intensive computation and sophisticated hardware	Estimate the position based on motional EMF, inductance variation, or flux- linkage variation

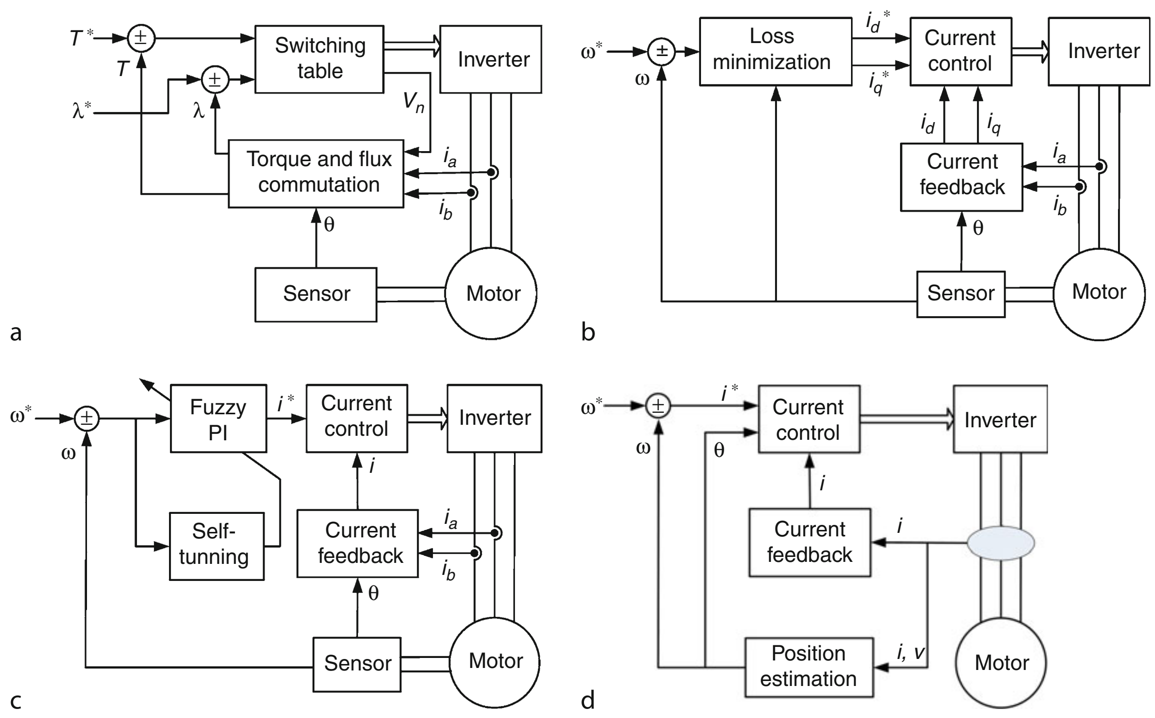

Vehicle Traction Motors. Figure 21
Control block diagrams. (**a**) DTC; (**b**) EOC; (**c**) AIC; (**d**) PSC

Future Directions

Thanks to persistent hard work of both academic and industrial communities in the past years, the performance of traction motors for EVs has been improved greatly. With quick development of industry technology, motor drives in EVs would meet with new renovations.

The development of traction motor drives is no longer limited to the design and operation of a single

motor or drive. The research trends of the traction motor drive in EVs may be concluded as follows.

1. High-speed motors. By increasing speed, the size of electric motors may be reduced greatly, namely, higher power from smaller machines and redesigning for increased material utilization [3, 46]. Some companies have started to focus on high speed of 16,000 r/min PM motors that can achieve field weakening within the structure of the motor and eliminate the need for a DC–DC boost converter [47].
2. System integration. It is necessary for the designers to take electrical machine, power electronics, such as converter, and energy source into consideration altogether. Furthermore, control methods will be analyzed during the machine design so as to extend the constant-power speed range, increase the starting torque, and etc.
3. Redundant and fault-tolerant motor structure. Continued operation of motor drive is an essential requirement in EV application. Therefore, the need for high degree of reliability in motor drive system has inspired much research in the area. To achieve high reliability, redundant or conservative design techniques have been employed in many motor drives. Figure 22 illustrates a 6-phase 8-pole rotor-PM motor [48] and a flux-switching motor.
4. Novel manufacture techniques. To achieve high power density, high efficiency, and low-cost motors for EVs, the manufacture technique of motors is being improved. The segmented stator and concentrated winding are examples [49]. In addition, using flat wire to replace round wire in motor windings can increase slot filling factor, enabling both a higher torque constant and a lower copper loss.
5. Novel machine topologies with composite structures and new materials. For traditional machines, each has its own merits and demerits. The composition of different machines may significantly improve the performance. Hence, the traction machines consist of different structures may be noticed in the next step.

EVT Systems

In 1997, Toyota developed the first EVT system for its flagship HEV, Prius, which is a full hybrid. The schematic configuration of this EVT is shown in Fig. 23, which is mainly composed of a planetary gear, a motor, and a generator. The internal combustion engine (ICE) is attached to the planet carrier, the motor is coupled with the driveline shaft so that both are attached to the ring gear, and the generator is mounted to the sun gear [50].

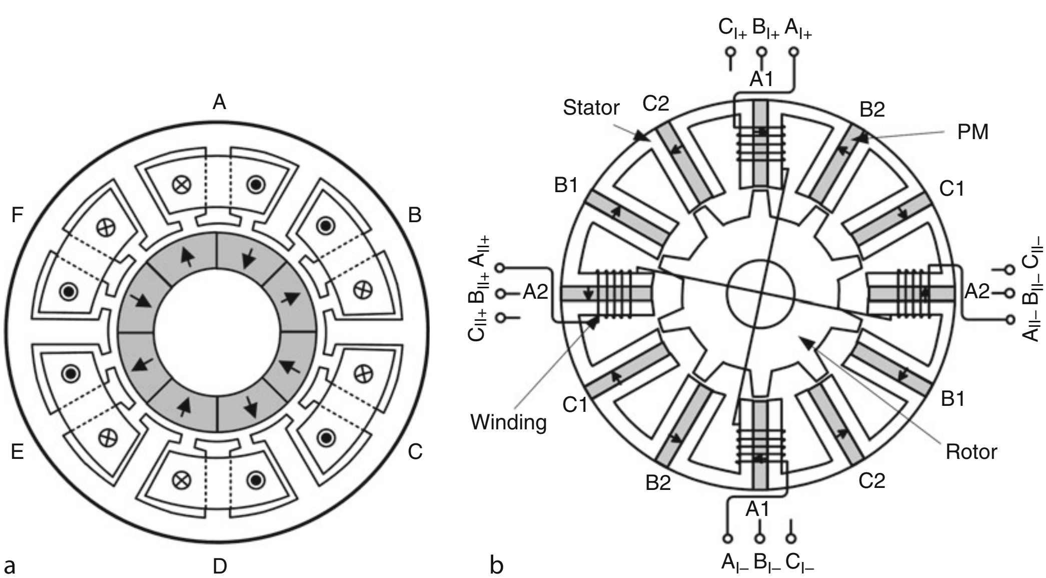

Vehicle Traction Motors. Figure 22
Fault-tolerant motor topologies. (**a**) 6-phase 8-pole rotor-PM motor; (**b**) Flux-switching PM motor

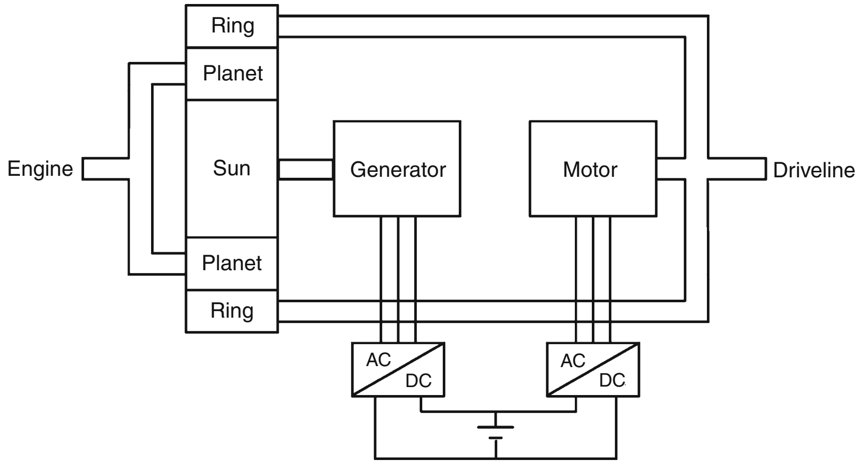

Vehicle Traction Motors. Figure 23
Planetary-geared EVT system

By controlling the power taken by the generator and then feeding back into the motor, the ICE speed can be maintained constant when the driveline-shaft speed is varying. Thus, a continuously variable ratio between the ICE speed and the wheel speed can be achieved. Hence, this EVT system takes the following advantages.

1. Because of the absence of clutches or shifting gears, it can significantly improve the transmission efficiency and reduce the overall size, hence increasing both the energy efficiency and the power density.
2. In the presence of continuously variable ratio between the ICE speed and the wheel speed, the ICE can always operate at its most energy-efficient operating point, hence resulting in a considerable reduction of fuel consumption.
3. The system can fully enable the idle stop, electric launch, regenerative braking, and full-throttle acceleration features, which are particularly essential for the full hybrids.

However, this planetary-geared EVT system inherits the fundamental drawbacks of planetary gearing, namely, transmission loss, gear noise, and need of regular lubrication.

In recent years, active research works have been conducted to eliminate this mechanical planetary gear while retaining the EVT propulsion. One viable approach is the use of the dual mechanical port (DMP) machine to realize power splitting for the full hybrids [51]. Figure 24 shows the EVT system

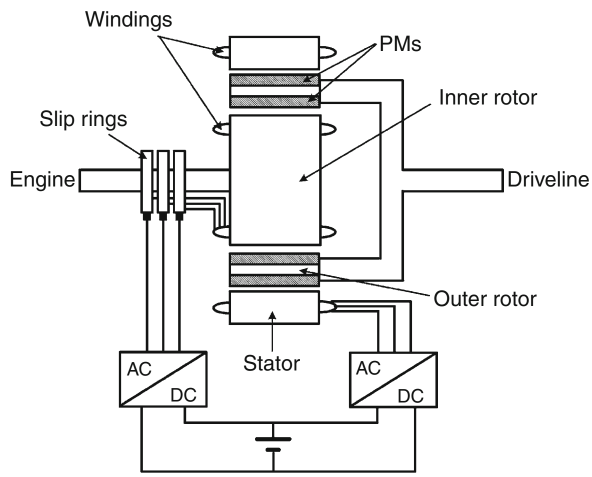

Vehicle Traction Motors. Figure 24
EVT system using integrated DMP machine for HEVs

integrated with the DMP machine. When installing this EVT system in a full hybrid, it offers four modes of operation, namely, cranking, charging, launching, and continuous variable transmission (CVT) [52].

1. In the cranking mode, the battery delivers the power to crank the ICE via the primary machine until the ICE reaches the speed for ignition.
2. In the charging mode, the battery is either charged by the ICE via the inner-rotor winding when the vehicle stops motion or by the stator winding during regenerative braking.

3. In the launching mode, the battery delivers the power to launch the vehicle via the stator winding without using the ICE.
4. In the CVT mode, the input and output shafts are controlled to change the speed and the torque, respectively, so that the optimal operating line of the ICE can be achieved.

Magnetic-Geared PM Brushless Drives

For EVs, in-wheel motor drives are very attractive since they play the role of electronic differential [1]. As the wheel speed is only about 600 r/min, the in-wheel motor drive is either a low-speed gearless outer-rotor one or a high-speed planetary-geared inner-rotor one.

Although the former one takes the advantage of gearless operation, its low-speed operation causes bulky size and heavy weight. On the other hand, although the latter one takes the merits of reduced overall size and weight, the planetary gear inevitably involves transmission loss, acoustic noise, and regular lubrication. Magnetic gearing is becoming attractive since it offers the advantages of high efficiency, reduced acoustic noise, and maintenance free [53]. By artfully integrating the magnetic gear into a motor drive, the low-speed requirement for direct driving and the high-speed requirement for machine design can be achieved simultaneously [54]. Figure 25 shows the detailed configuration of a magnetic-geared in-wheel PM BLDC motor. The artfulness is the share of a common PM rotor, namely, the outer rotor of a PM BLDC motor and the inner-rotor of a concentrically arranged magnetic gear. The operating principle of this magnetic-geared PM BLDC drive is similar to that of a high-speed planetary-geared inner-rotor drive, but with the difference that this one is an outer-rotor drive. That is to say, the motoring operation is the same as the PM BLDC drives. First, the stator is fed by three-phase voltages, which are rated at 220 Hz, to achieve the rated speed of 4,400 r/min. Then, the magnetic gear steps down the rated speed to 600 r/min, which in turn boosts up the torque for direct driving. The torque transmission is based on the modulation of the air-gap flux density distributions along the radial and circumferential directions. The space harmonic is modulated by the 25 stationary steel pole pieces from three pole pairs in the inner air-gap to 22 pole pairs in the outer air-gap. Hence, the torque in the outer rotor can be significantly amplified to about seven times that of the inner-rotor.

ISG Systems

In conventional automobiles, the starter motor and generator are separately coupled with the ICE, hence providing high starting torque for cold cranking and generating electricity for battery charging, respectively.

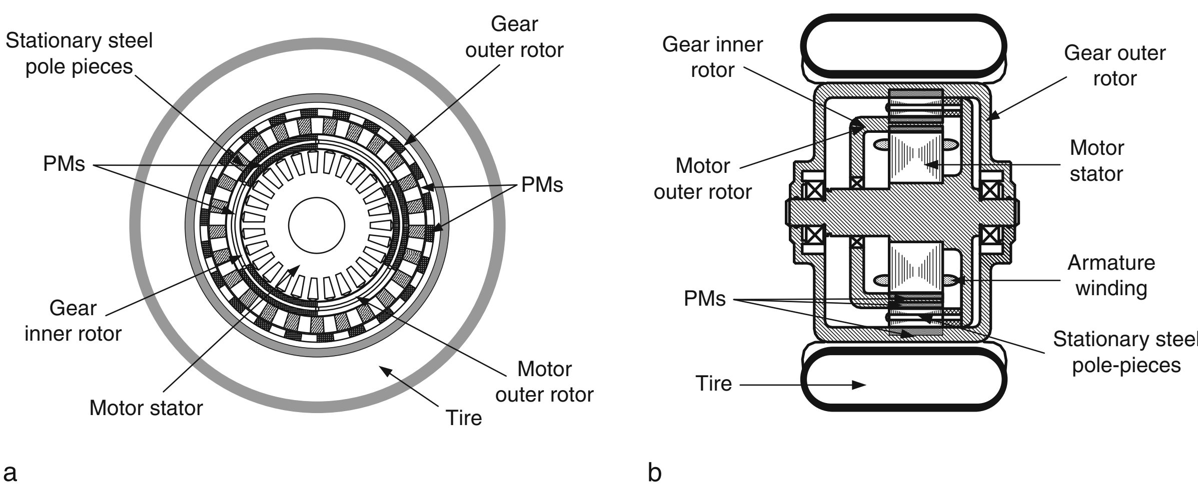

Vehicle Traction Motors. Figure 25
Magnetic-geared in-wheel motor drive. (**a**) Elevation view; (**b**) Side view

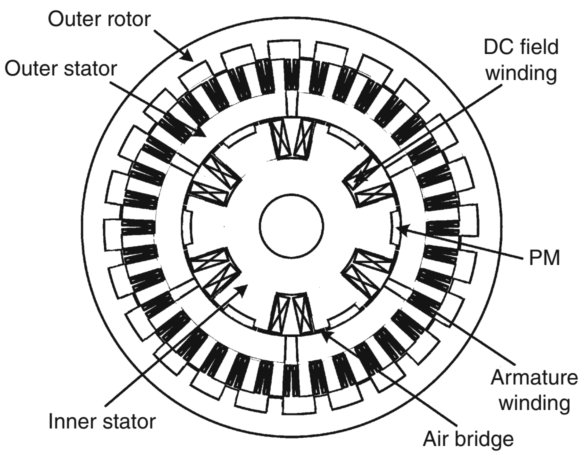

Vehicle Traction Motors. Figure 26
ISG system based on a stator doubly fed DSPM machine

This arrangement takes the advantage of simplicity but suffers from the poor utilization of both machines, hence resulting in heavy weight and bulky size. In order to incorporate both functions in a single unit, the development of integrated starter-generator (ISG) systems is accelerating.

By incorporating the inherent merits of PM brushless machines into the ISG, the resulting PM brushless ISG system is attractive for the latest micro- and mild HEVs. The stator doubly fed DSPM brushless machine [55] is a particular type of the aforementioned PM hybrid brushless machine topologies, which is promising for application to the ISG system. Its configuration is shown in Fig. 26, in which there are two magnetic field excitations, namely, the PMs and the DC field windings, air bridges in shunt with the PMs in the inner stator, AC armature windings in the salient-pole outer stator, and the salient-pole outer rotor with no PMs or windings.

This stator doubly fed DSPM brushless ISG system offers several distinct advantages:

1. The DC field current can be bidirectionally controlled to strengthen and weaken the air-gap flux density, hence offering high starting torque for cold cranking and constant output voltage over a wide speed range for battery charging. Meanwhile, the air bridge amplifies the effect of flux weakening.
2. The outer-rotor topology can fully utilize the space of the inner stator to accommodate the PMs and the DC field windings, hence reducing the overall size of the machine.
3. Since the outer rotor does not involve any windings or PMs, it can provide high mechanical integrity which is essential to handle the high starting torque during cold cranking.
4. Since the stator adopts fractional-slot concentrated windings, it can effectively reduce the cogging torque which usually occurs in the PM BLDC machines. In addition, it can shorten the length of end windings, hence saving the copper material and improving the power density.

Memory Brushless Machine Topologies

Although the DC field winding in PM hybrid motors enables the air-gap flux controllable, the use of DC field current inevitably causes additional power loss and degrades the efficiency. Hence, a new class of flux controllable PM machines, namely, the memory brushless machine was advent, which has the distinct ability to change the intensity of magnetization and also memorize the flux-density level in the PMs [56]. Figure 28 shows the topologies of memory brushless machines. In Fig. 27(a), it consists of aluminum nickel cobalt (AlNiCo) PMs sandwiched by soft iron, which are then mechanically fixed to a nonmagnetic shaft. The online magnetization is achieved by properly applying a short DC current pulse flowing through the stator armature winding to change the magnetization level of the AlNiCo PMs in the rotor. Figure 27(b) is a memory DSPM motor that adopts two-layer inner stator and outer rotor. In the stator, the armature windings are located in the outer layer, while both the PMs and magnetizing windings are placed in the inner layer, hence achieving a compact structure. Since the outer rotor is simply composed of salient poles without PMs or windings, it is very robust. The PM material used in the motor is an AlNiCo alloy [57]. Due to its direct magnetization of PMs by a temporary current pulse in the magnetizing windings, the flux control is highly effective and highly efficient.

Transverse Flux Machine

PM transverse flux machine (TFM) [58, 59] is claimed to exhibit a higher torque density compared to the induction motor, SR motor, PM BLDC motor, and normal PM

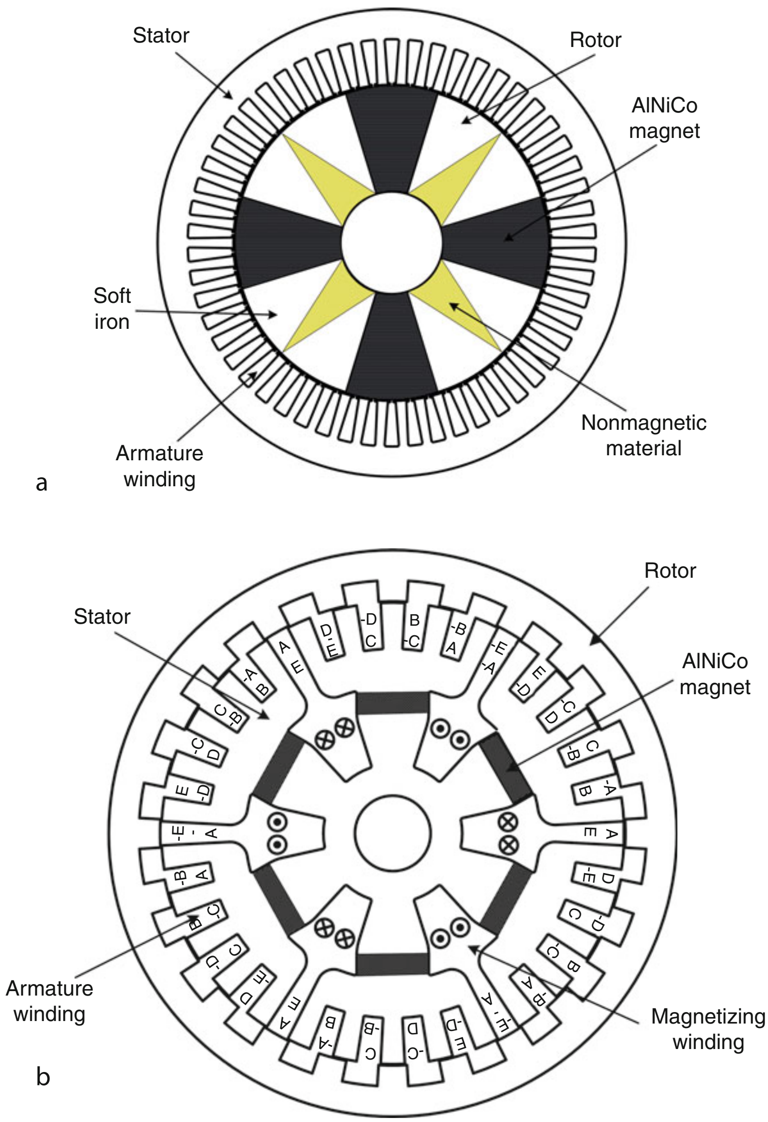

Vehicle Traction Motors. Figure 27
Memory brushless machines. (**a**) Rotor-PM; (**b**) Stator-PM

synchronous motor. In the TFM, the flux enters segments of stator core in transverse, i.e., perpendicular to the direction of rotor movement in the cross section plane, therefore, it is called transverse flux machine. The TFM stator iron core has two basic structures: (1) U-shape poles which have both teeth in the same axial plane and (2) claw-poles. Figure 28 shows the schematic configurations of the TFM. For each phase, a toroidal winding is placed inside the stator teeth or poles. Generally, TFMs have a relatively large number of poles, all of which interact with the total ampere-conductors of each phase. This enables very high electric loadings and, hence, high-torque densities to be achieved. Hence, it is especially suited for in-wheel direct drive. However, they have a significant leakage flux and a relatively high winding inductance, as well as a poor power factor. This impacts significantly on the associated VA rating of the power electronics converter.

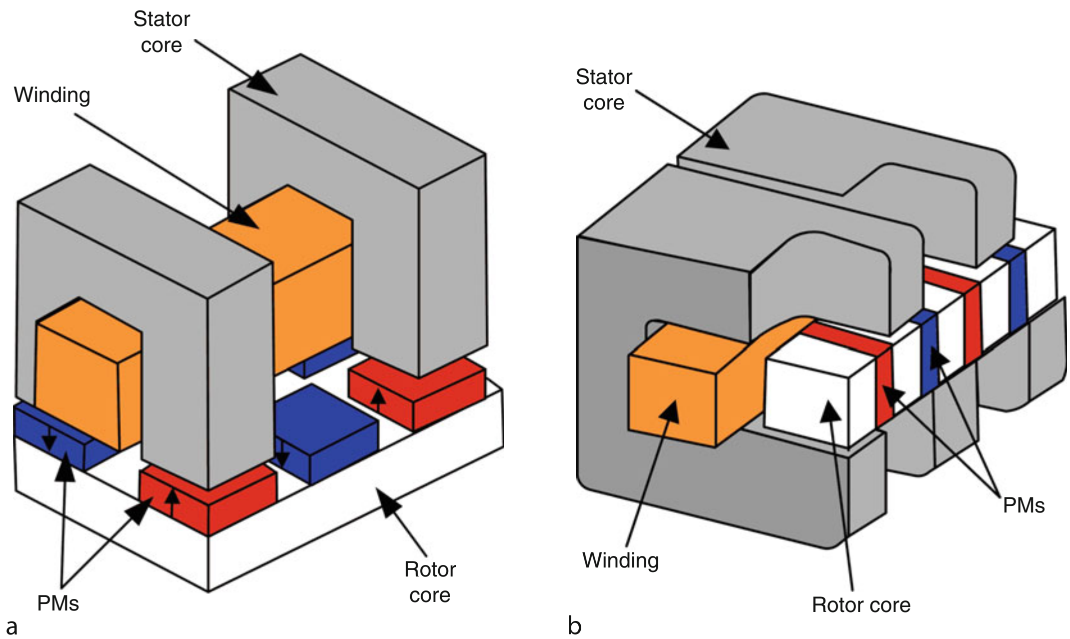

Vehicle Traction Motors. Figure 28
PM transverse flux motor. (**a**) Surface PMs; (**b**) Flux concentrated PMs

Bibliography

Primary Literature

1. Chan CC, Chau KT (2001) Modern electric vehicle technology. Oxford University Press, Oxford, UK
2. Zhu ZQ, Howe D (2007) Electrical machines and drives for electric, hybrid, and fuel cell vehicles. Proc IEEE 95:746–765
3. Chau KT, Chan CC, Liu C (2008) Overview of permanent-magnet brushless drives for electric and hybrid electric vehicles. IEEE Trans Ind Electron 55:2246–2257
4. Fuhs A (2008) Hybrid vehicles and the future of personal transportation. CRC, Boca Raton
5. Xu W, Zhu J, Guo Y et al (2009) Survey on electrical machines in electrical vehicles. In: IEEE international conference on applied superconductivity and electromagnetic devices, Chengdu, 25–27 Sept 2009, pp 167–170
6. Yamada K, Watanabe K, Kodama T et al (1996) An efficiency maximizing induction motor drive system for transmission less electric vehicle. In: Proceeding the 13th international electric vehicle symposium, Osaka, vol II, pp 529–536
7. Jiang SZ, Chau KT, Chan CC (2002) Performance analysis of a new dual-inverter pole-changing induction motor drive for electric vehicles. Electr Power Compon Syst 30:11–29
8. Jiang SZ, Chau KT, Chan CC (2003) Spectral analysis of a new six-phase pole-changing induction motor drive for electric vehicles. IEEE Trans Ind Electron 50(1):123–131
9. Chan CC, Chau KT (1996) An advanced permanent magnet motor drive system for battery-powered electric vehicles. IEEE Trans Veh Technol 45:180–188
10. Chan CC, Chau KT, Jiang JZ et al (1996) Novel permanent magnet motor drives for electric vehicles. IEEE Trans Ind Electron 43:331–339
11. Chan CC, Jiang JZ, Xia W, Chau KT (1995) Novel wide range speed control of permanent magnet brushless motor drives. IEEE Trans Power Electron 10:539–546
12. Cheng M, Hua W, Zhang J, Zhao W (2011) Overview of stator-permanent magnet brushless machines. IEEE Trans Ind Electron. doi:10.1109/TIE.2011.2123853
13. Liao Y, Liang F, Lipo TA (1995) A novel permanent magnet machine with doubly salient structure. IEEE Trans Ind Appl 3(5):1069–1078
14. Cheng M, Chau KT, Chan CC (2001) Static characteristics of a new doubly salient permanent magnet motor. IEEE Trans Energy Convers 16(1):20–25
15. Deodhar RP, Andersson S, Boldea I, Miller TJE (1996) The flux-reversal machine: a new blushless doubly-salient permanent-magnet machine. In: Proceedings of the IEEE IAS Annual Conference. San Diego, 6–10 Oct 1996, pp 786–793
16. Kim TH, Jang KB, Chun YD et al (2005) Comparison of the characteristics of a flux reversal machine under the different driving methods. IEEE Trans Magn 41(5):1916–1919

17. Hoang E, Ben-Ahmed AH, Lucidarme J (1997) Switching flux permanent magnet polyphased machines. In: Proc. Eur. Conf. Power Electron. Appl., Trondheim, pp 903–908
18. Hua W, Cheng M, Zhu ZQ et al (2008) Analysis and optimization of back EMF waveform of a flux-switching permanent magnet motor. IEEE Trans Energy Convers 23(3):727–733
19. Zhu ZQ, Chen JT (2010) Advanced flux-switching permanent magnet brushless machines. IEEE Trans Magn 46(6): 1447–1453
20. Hua W, Zhu ZQ, Cheng M et al (2005) Comparison of flux-switching and doubly-salient permanent magnet brushless machines. In: Proc. Int. Conf. electrical machines and systems, Nanjing, pp 165–170
21. Zhu X, Cheng M (2010) Design, analysis and control of hybrid excited doubly salient stator-permanent-magnet motor. Sci China Tech Sci 53(1):188–199
22. Chan CC, Jiang Q, Zhou E (1995) A new method of dimension optimization of switched reluctance motors. In: Proceedings of Chinese international conference on electrical machines, Hangzhou, pp 1004–1009
23. Chan CC, Jiang Q, Zhan YJ, Chau KT (1996) A high-performance switched reluctance drive for P-star EV project. In: Proceedings of 13th international electric vehicle symposium, Osaka, vol II, pp 78–83
24. Zhan YJ, Chan CC, Chau KT (1999) A novel sliding-mode observer for indirect position sensing of switched reluctance motor drives. IEEE Trans Ind Electron 46:390–397
25. Krishnan R (1996) Review of flux-weakening in high performance vector controlled induction motor drives. In: Proc. IEEE Int. Symp. Industrial Electronics, Warsaw, pp 917–922
26. Miller JM, Gale AR, McCleer PJ et al (1998) Starter/alternator for hybrid electric vehicle: comparison of induction and variable reluctance machines and drives. In: Proceedings of the industry applications Society Annual Meeting, Oct 1998, St Louis, pp 513–523
27. Zhu X, Cheng M, Zhao W et al (2007) A transient co-simulation approach to performance analysis of hybrid excited doubly salient machine considering indirect field-circuit coupling. IEEE Trans Magn 43(6):2558–2560
28. Zhao W, Cheng M, Zhu X et al (2008) Analysis of fault tolerant performance of a doubly salient permanent magnet motor drive using transient co-simulation method. IEEE Trans Ind Electron 55(4):1739–1748
29. Bose BK (1992) Modern power electronics: evolution, technology, and applications. IEEE, New York
30. Chan CC, Chau KT, Chan DTW, Yao JM (1997) Soft switching inverters in electric vehicle. In: Proceedings of the 14th international electric vehicle symposium, CD-ROM, Orlando
31. Lai JS (1997) Resonant snubber-based soft-switching inverters for electric propulsion drives. IEEE Trans Ind Electron 44:71–80
32. Murai Y, Cheng J, Yoshida MA (1997) Soft-switched reluctance motor drives circuit with improved performances. In: Proc of IEEE power electronics specialists conference, 22–27 June 1997, St Louis, pp 881–886
33. Chau KT, Ching TW, Chan CC, Chan DTW (1997) A novel two-quadrant zero-voltage transition converter for DC motor drives. In: Proceedings of IEEE international conference on industrial electronics, New Orleans, pp 517–522
34. Divan DM (1986) The resonant DC link converter – a new concept in static power conversion. In: Proceedings of IEEE industry application society annual meeting, Denver, pp 648–656
35. Cho JG, Kim WH, Rim GH, Cho KY (1997) Novel zero transition PWM converter for switched reluctance motor drives. In: Proceedings of IEEE power electronics specialists conference, St Louis, pp 887–891
36. Ching TW, Chau KT, Chan CC (1998) A new zero-voltage-transition converter for switched reluctance motor drives. In: Proceedings of IEEE power electronics specialists conference, Fukuoka, pp 1295–1301
37. Rahman MF, Haque ME, Tang L, Zhong L (2004) Problems associated with the direct torque control of an interior permanent-magnet synchronous motor drive and their remedies. IEEE Trans Ind Electron 51(4):799–809
38. Pascas M, Weber J (2005) Predictive direct torque control for the PMsynchronous machine. IEEE Trans Ind Electron 52(5):1350–1356
39. Cavallaro C, Tommaso AOD, Miceli R et al (2005) Efficiency enhancement of permanent-magnet synchronous motor drives by online loss minimization approaches. IEEE Trans Ind Electron 52(4):1153–1160
40. Shu Y, Cheng M, Kong X (2008) Online efficiency optimization of stator-doubly-fed doubly salient motor based on a loss model. In: Proceedings of 11th international conference on electrical machines and systems, Wuhan, pp 1174–1178
41. Cheng M, Sun Q, Zhou E (2006) New self-tuning fuzzy PI control of a novel doubly salient permanent-magnet motor drive. IEEE Trans Ind Electron 53(3):814–821
42. Pajchrowski T, Zawirski K (2007) Application of artificial neural network to robust speed control of servo drive. IEEE Trans Ind Electron 54(1):200–207
43. Acarnley PP, Watson JF (2006) Review of position-sensorless operation of brushless permanent-magnet machines. IEEE Trans Ind Electron 53(2):352–362
44. Silva C, Asher GM, Sumner M (2006) Hybrid rotor position observer for wide speed-range sensorless PM motor drives including zero speed. IEEE Trans Ind Electron 53(2):373–378
45. Angelo CD, Bossio G, Solsona J et al (2006) Mechanical sensorless speed control of permanent-magnet AC motors driving an unknown load. IEEE Trans Ind Electron 53(2):406–414
46. Emadi A, Young Joo L, Rajashekara K (2008) Power electronics and motor drives in electric, hybrid electric, and plug-in hybrid electric vehicles. IEEE Trans Ind Electron 55(6):2237–2245
47. U.S. Department of Energy (2007) Plug-in hybrid electric vehicle R&D plan. http://www1.eere.energy.gov/vehiclesandfuels/pdfs/program/phev_rd_plan_june_2007.pdf
48. Mecrow BC, Jack AG, Haylock JA, Coles J (1996) Fault-tolerant permanent magnet machine drives. IEEE Proc Electric Power Appl 143(6):437–442

49. Akita H, Nakahara Y, Miyake N, Oikawa T (2003) New core structure and manufacturing method for high efficiency of permanent magnet motors. In: Conference record of IEEE IAS annual meeting, Amagasaki, 12–16 Oct 2003, pp 367–372
50. Miller JM (2006) Hybrid electric vehicle propulsion system architectures of the e-CVT type. IEEE Trans Power Electron 21(3):756–767
51. Xu L, Zhang Y, Wen X (2007) Multi-operational modes and control strategies of dual mechanical port machine for hybrid electrical vehicles. In: Proceedings of the IEEE IAS Annual meeting, New Orleans, pp 1710–1717
52. Cheng Y, Cui S, Song L, Chan CC (2007) The study of the operation modes and control strategies of an advanced electromechanical converter for automobiles. IEEE Trans Magn 43(1):430–433
53. Atallah K, Howe D (2001) A novel high performance magnetic gear. IEEE Trans Magn 37(4):2844–2846
54. Chau KT, Zhang D, Jiang JZ, Liu C, Zhang Y (2007) Design of a magnetic-geared outer-rotor permanent-magnet brushless motor for electric vehicles. IEEE Trans Magn 43(6):2504–2506
55. Chau KT, Li YB, Jiang JZ, Liu C (2006) Design and analysis of a stator doubly fed doubly salient permanent magnet machine for automotive engines. IEEE Trans Magn 42(10):3470–3472
56. Ostovic V (2003) Memory motor. IEEE Ind Appl Mag 9(1):52–61
57. Yu C, Chau KT, Liu X et al (2008) A flux-mnemonic permanent magnet brushless motor for electric vehicles. J Appl Phys 103(07103):1–3
58. Henneberger G, Bork M (1997) Development of a new transverse flux motor. In: IEE Colloq. new topologies for permanent magnet machines, London, pp 1/1–1/6
59. Baserrah S, Orlik B (2009) Comparison study of permanent magnet transverse flux motors (PMTFMs) for in-wheel applications. In: Proceedings of the international conference on power electronics and drive systems, Taipei, pp 96–101

Books and Reviews

Chan CC (2002) The state of the art of electric and hybrid vehicles. Proc IEEE 90:247–275

Chan CC, Chau KT (1997) An overview of power electronics in electric vehicles. IEEE Trans Ind Electron 44:3–13

Chau KT, Ming C (2010) New drive technology for electric vehicles. China Machine, Beijing (In Chinese)

Ehsani M, Rahman KM, Toliyat HA (1997) Propulsion system design of electric and hybrid vehicles. IEEE Trans Ind Electron 44:19–27

Ehsani M, Gao Y, Gay SE, Emadi A (2005) Modern electric, hybrid electric, and fuel cell vehicles: fundamentals, theory, and design. CRC, Boca Raton

Husain I (2003) Electric and hybrid vehicles-deign fundamentals. CRC, Boca Raton

Rashid MH (2005) Modern electric, hybrid electric, and fuel cell vehicles: fundamentals, theory, and design. CRC, Boca Raton

Vehicular Ad Hoc Networks, Enhanced GPSR and Beacon-Assist Geographic Forwarding in

Ping Wang, Fuqiang Liu, Wenjie Shu, Wenqiang Xu
Department of Information and Communication Engineering, Tongji University, Shanghai, China

Article Outline

Glossary

BGF Beacon-Assist Geographic Forwarding, one of the approaches for enhanced GPSR in packet-forwarding strategy to enable nodes to forward packets by considering their neighbors' beacon interval in neighbor list.

Geographical routing A kind of routing protocol in VANET that uses geographic information to help complete packets delivery. This kind generally contains two parts: location server and packets forwarding.

GPSR The famous geographical routing protocol, named greedy perimeter stateless routing, uses greedy forwarding strategy to select a next hop and perimeter forwarding strategy to cope with routing failure caused by local minimum.

ITR Inaccuracy-Tolerant Range represents the inaccurate degree of location information.

Local minimum No neighbor exists which is closer to the destination than the intermediate node itself.

NUR Neighbor-Awareness position Update, one of the approaches for enhanced GPSR in beaconing to set the position update interval dynamically.

SDR The Successful Date Rate defines as the ratio of packets successfully delivered to the destination node to those generated by the sender.

VANET The VehiculAr NETwork is a special communication network comprising of radio-enabled vehicles and roadside units, including vehicle-to-vehicle communication and vehicle-to-roadside unit communication.

Definition of the Subject

In vehicular network (VANET), moving vehicles always have a high speed and a frequent change of their moving direction. These make the network topology highly dynamic. Because of the highly dynamic nature of the mobile nodes, finding and maintaining routes is very challenging in VANET.

GPSR is considered as a promising geographical routing protocol applicable for VANET. In order to cope with the problem of highly dynamic topology, it makes routing decisions at the intermediate nodes instead of building a constant route. Under this strategy, routing failure caused by nodes disconnection in constant routing approach can be efficiently mitigated. However, there are still some problems in GPSR. As in greedy forwarding strategy, the intermediate node always selects the next hop node that lies close to the relaying nodes' transmission range border; the selected one has high possibility to leave the transmission range because of the high speed node movement. GPSR does not take this into consideration. Another problem comes from the constant beacon interval strategy. Such principle may lead to high routing overhead and poor performance in various nodes density environment.

Introduction

Researches on routing protocol in VANET come from the bases of earlier researches on routing protocol in Mobile Ad hoc network (MANET). They share the characteristics of self-organization, self-management, low-bandwidth, and short radio transmission range. However, VANET differs from MANET by its highly dynamic topology. The traditional topology-based routing strategies in MANET, such as AODV (Ad hoc On-demand Distance Vector) and DSR (Dynamic Source Routing), are not approving enough to be used

M. Ehsani et al. (eds.), *Transportation Technologies for Sustainability*, DOI 10.1007/978-1-4614-5844-9,

Originally published in
Robert A. Meyers (ed.) Encyclopedia of Sustainability Science and Technology, © 2012, DOI 10.1007/978-1-4419-0851-3

in VANET. These routing protocols are under the principle of building a constant route table and maintaining the pre-build route table. Due to the highly dynamic mobility, routing protocols under such principle are unable to quickly find, maintain, and update long routes in VANET. The route will become invalid if some intermediate nodes disconnected. Thus, frequent route recovery will make the whole performance inefficient. Take AODV for example. It has been tested in real-world experiments. Results show that packets are excessively lost due to route failures.

Vehicles are not only simply mobile nodes, but also they have characteristics of high speed, limited movement along roads, and capability to equip with GPS system. As GPS systems are widely used in vehicles now, the mobile nodes can easily get their position information. This trend brings a new type of routing protocol, geographical routing, or position-based routing, which uses the position information to help deliver packets. Position-based routings mainly content two parts: location server and forwarding strategy. Location server is responsible for providing location information of the destination nodes to the source nodes. After getting location information of the destination nodes, different kinds of forwarding strategies will be used at the intermediate nodes to make the forwarding decisions in order to select an appropriate next hop. As introduced above, one of the main characteristics of position-based routings is that they do not try to build a constant route table. In this way, it makes position-based routings more applicable to VANET with highly dynamic mobility. Researchers see position-based routing as a more promising approach and do researches on them.

GPSR is one of the most typical position-based routing protocols. It uses the positions of routers and a packet's destination to make packet forwarding decisions. It contains two modes of forwarding strategy: greedy forwarding mode and perimeter forwarding mode. GPSR makes greedy forwarding decisions using only information about a router's immediate neighbors in the network topology. When a packet reaches a region where greedy forwarding is impossible, the algorithm recovers by routing around the perimeter of the region. By keeping state only about the local topology, GPSR scales better in per-router state than shortest-path and topology-based routing protocols as the number of network destinations increases. Under mobility's frequent topology changes, GPSR can use local topology information to find correct new routes quickly.

Although GPSR shows a much higher performance than the traditional topology-based routing protocols in VANET, it still has some drawbacks within its routing strategy. GPSR uses a fixed period beaconing mechanism to send HELLO messages. Such mechanisms may lead to several problems such as wasted bandwidth, delaying of data packet, and increased network congestion. As GPSR adopts greedy forwarding algorithm, in which the intermediate node always selects the next hop node that lies close to the relaying nodes' transmission range border. The selected route may be not stable enough for the chosen next hop nodes have a high possibility to move away from the relaying nodes. One more drawback comes from the perimeter forwarding strategy. GPSR lacks considering the usage of road topology that restricts nodes' movements. Under such perimeter approach, the select route path may be not the most efficient and shortest one.

Describing Enhanced GPSR Using Neighbor-Awareness Position Update and Beacon-Assist Geographic Forwarding

The enhanced GPSR is modified by the algorithm called GPSR-N&B. It includes two parts: Neighbor-Awareness position Update (NAU) and Beacon-Assist Geographic Forwarding (BGF). GPSR-N&B uses NAU to set the position update interval dynamically, according to the neighbors' number and position of the relaying nodes. And BGF strategy enables nodes to forward packets by considering their neighbors' beacon interval in neighbor list. This algorithm aims to reduce beacon overhead and medium access control (MAC) layer collisions in different densities and velocities of VANET, while ensuring the Successful Date Rate (SDR) performances well.

Neighbor-Awareness Position Update (NAU)

GPSR-N&B is based on the following assumptions (a) all links are bidirectional and (b) all nodes can easily get their current location information and velocity.

In VANET, a vehicle's movement has effect on its neighbors' movement. NAU adapts the beacon update intervals according to the number, position, and

velocity of the nodes in the neighborhood. The Neighbor-Awareness position Update (T_i) is shown as follows:

$$T_i = \frac{1}{2}T_i' + \frac{1}{2}T_i''. \tag{1}$$

T_i' is affected by the neighbors' position, while T_i'' is affected by the number of neighbors.

1. T_i'

In GPSR-N&G, an aspect of inaccuracy-tolerant range (ITR) is supposed to represent the inaccurate degree of location information that can be accepted. Intuitively, within maximum transmission range, the larger the distance between two nodes is and the more the probability the link may break, the shorter the beacon interval should be.

Figure 1 demonstrates the inaccuracy-tolerant range around node A. For example, node E which is located between the maximum transmission range (250 m) and ITR threshold (240 m) will not forward packets from node A, because of the changeable environment and distance between them, which may often lead to link breakdown.

As node D is within the range of 200–240 m, ITR equals to 240-d, where d is the distance between nodes A and D: $d = \sqrt{(x_A - x_D)^2 + (y_A - y_D)^2}$. The relative beacon interval time T_{AD} will be set to be $\mathrm{Max}\left[\frac{(240-d)T_{\mathrm{MINbeacon}}}{240-175}, T_{\mathrm{MINbeacon}}\right]$.

As node B is within the range of 175 m, the default beacon interval $T_{\mathrm{MINbeacon}}$ is then used as T_{AB}, instead of calculating the effect of ITR.

In Fig. 2, node A and B are neighbors. After considering A and B, a relative beacon interval T_{AB} will be got as well as T_{AC} and T_{AD} in a similar way. Then T_A' can be set as:

$$T_A' = \frac{T_{AB} + T_{AC} + T_{AD}}{3}. \tag{2}$$

Then, $T_i' = \frac{\sum_{j=2}^{k} T_{ij}}{K}$, where K is the number of node I's neighbors.

2. T_i''

T_i'' is set as $T_i'' = wK$, in which w is computed in simulation test. Finally, node i's new beacon interval is shown in Eq. 3:

$$T_i = \frac{1}{2}\frac{\sum_{j=2}^{k} T_{ij}}{K} + \frac{1}{2}wK \tag{3}$$

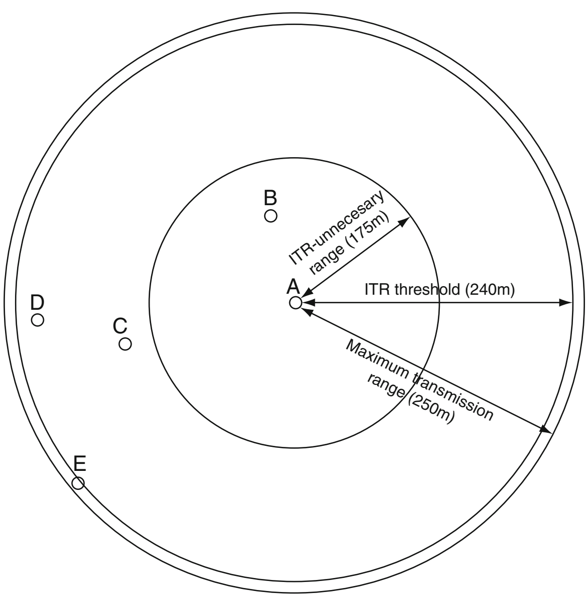

Vehicular Ad Hoc Networks, Enhanced GPSR and Beacon-Assist Geographic Forwarding in. Figure 1 Inaccuracy-tolerant range

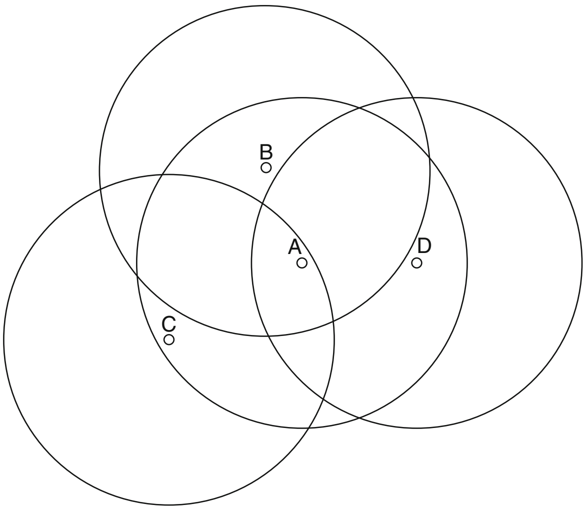

Vehicular Ad Hoc Networks, Enhanced GPSR and Beacon-Assist Geographic Forwarding in. Figure 2 Neighbor-awareness position update

Upon initialization, each node broadcasts a beacon informing its neighbors about its current location (x_i, y_i) and velocity (v_{xi}, v_{yi}) using default beacon interval $T_{\mathrm{DEFbeacon}}$, which is set to $\frac{175}{V_{\mathrm{MAX}}}$ in the following simulation. Here, V_{MAX} is the maximum node velocity.

After initialization, each node replaces its own beacon interval by T_i.

Beacon-Assist Geographic Forwarding (BGF)

In NAU, the way to set position update time is based on the change of relative distance, instead of change of position. The neighbor list is changed by using relative distance in x and y directions, instead of the position as Table 1 shows.

In Table 1, X-Distance and Y-Distance are the distance between current node and its neighbor in x direction and y direction. V_x and V_y are the relative velocity of current node and its neighbor in x direction and y direction. T_{beacon} is the neighbor's beacon interval time.

As in NAU, each neighbor's T_{beacon} includes the topology information in its vicinity. So the neighbors' T_{beacon} can be used as the topology information of the next hop in choosing the efficient forwarding node. In BGF, a routing metric is defined which depends on (a) relative distance and (b) T_{beacon} as follows:

$$M_j(l_j, T_{j\mathrm{beacon}}) = \alpha g(l_j) + \beta h(T_{j\mathrm{beacon}}) \tag{4}$$

$$g(l_j) = \exp(-(l_j - l_i)) \tag{5}$$

$$h(T_{j\mathrm{beacon}}) = \exp\left(-(T_{j\mathrm{beacon}} - T_{\mathrm{DEFbeacon}})\right) \tag{6}$$

Here α and β are the weights to distance and T_{beacon}. l_i is the distance between the destination and node i. l_j is the distance between the destination and node j in node i's neighborhood, and $T_{j\mathrm{beacon}}$ is node j's beacon interval.

Vehicular Ad Hoc Networks, Enhanced GPSR and Beacon-Assist Geographic Forwarding in. Table 1 Node A's neighbor list

	X-distance	Y-distance	V_x	V_y	*Tbeacon*
B	−50	210	10	15	2
C	−202	−45	−20	5	3
–	–	–	–	–	–

Simulation Results

Performance of GPSR-N&B is evaluated by simulation varying the beacon interval, the maximum speed of mobile nodes and the network density for freeway models. NS-2 is used to estimate the effect of inaccurate location information with different beacon intervals, speeds, and densities on GPSR, which has been proven to perform efficiently with accurate location information.

1. Set w in T_i''
   In the simulation, w of 1/5,2/5,3/5,4/5,5/5 is tested in different number of nodes (20,40,60). In Fig. 3, w equaling to 3/5 outperforms the others in terms of the SDR. As a result, in following simulation, w is set to 3/5.
2. Results and Analysis
   The results represented here are averaged over ten runs, each using a different random seed. Nodes are randomly placed over a 1,000*50 m^2 freeway created by sumo and move.

Performance of various beacon intervals (0.5, 1, 2, 4, 8) is compared as well as GPSR-N&B by varying maximum moving speed (10, 20, 30 m/s) and different number of nodes (20, 40, 60). Each simulation lasts 100 simulation seconds. The size of data packets is 32 bytes.

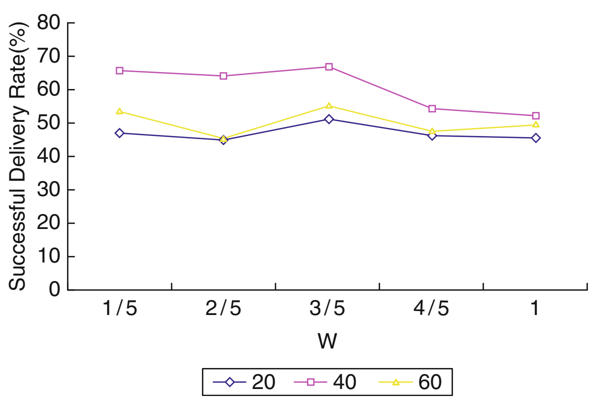

Vehicular Ad Hoc Networks, Enhanced GPSR and Beacon-Assist Geographic Forwarding in. Figure 3 SDR of different w

Five random source–destination pairs, using CBR as the traffic flows and lasting about 20 s, are selected. Different aspects of the performance of the routing protocol are evaluated using the following metrics:

Successful date rate (SDR): The ratio of packets successfully delivered to the destination node to those generated by the sender.
Routing overhead: The total number of beacon packets transmitted.
Number of MAC layer collisions: The number of collisions in MAC layer due to the beacon packets.

Figure 4a, b, and c illustrates that GPSR-N&B outperforms from GPSR with fixed beacon interval with various numbers of nodes and maximum node speed. GPSR with fixed beacon interval results in low SDR, and cannot cope with the topology change with high mobility.

Firstly PSR-N&B controls the routing overhead and decreases the MAC layer collisions to leave more channel resource for the CBR packets which will be discussed later. Secondly, GPSR-N&B using BGF makes use of the beacon intervals of neighbors for estimating the next hop topology, which makes the greedy forwarding more stable and efficient. The greedy forwarding is extended to two-hop area.

Figure 5a, b, and c shows that the routing overhead of GPSR-N&B is very low in all the simulations. The most important thing is that routing overhead of GPSR-N&B does not increase a lot with the increasing density of nodes, so GPSR-N&B fits the large number of nodes. In NAU, the node beacon interval is set according to the number of neighbors.

GPSR-N&B makes lower MAC layer collisions as shown in Fig. 6a, b, and c, due to the different beacon intervals of nodes in the network compared with GPSR using fixed beacon intervals. The overhead packets in high-density neighbor area are less than in low-density neighbor area due to the addition of T'' in NAU.

Survey of Different Strategies to Enhance GPSR

GPSR does not take cars' mobility characteristics into consideration which limits the performance in VANET. The movement of nodes is assumed to be arbitrary in MANET while bound to a street in VANET. It makes sense that many researchers are going to exploit the different characteristics to increase packet-forwarding performance. Going from simple to complex, scenarios of cars movement can be classified as highway and city scenario.

Considering these characteristics in highway and city scenario, which will be discussed in following sections, researchers have developed other approaches to improve the routing performance in VANET compared with GPSR.

Strategies of Enhancement in Highway Scenario

Definition of the Subject In highway scenario, cars may move in different directions or in different lanes, but the main extent of movement is along the road, not across, which makes the movement one dimensional. This makes packet forwarding fairly easy but much sensitive to speed because cars may move in highway very fast.

Advanced Greedy Forwarding (AGF)

V. Naumov, R. Baumann, and T. Gross in [1] proposed the Advanced Greedy Forwarding (AGF) algorithm to significantly improve GPSR performance in VANETs.

Both the source and the destination nodes inform each other with the help of the location discovery service (e.g., reactive location service [2]) about their moving directions and speeds – velocity vectors. Velocity vector information is also added into HELLO beacons of all nodes. Velocity vector requires two additional bytes to store the information about nodes' speed and direction. The first byte encodes the direction in the range of 0–127. The second byte stores the speed in km/h (enough for representing the allowed maximum speed in most countries).

Also the information about the packet travel time is added in a data packet header. Every node forwarding a data packet adds its own processing time into packet header. A next hop node is chosen based on the velocity vectors information stored in the neighbor tables.

A node receiving a data packet checks if the destination is listed in its neighbor table and the entry is still valid, taking into account the packet travel time and the node's and the destination's velocity vectors. If this is the case, the node sends the packet directly to the destination. If the destination is in the neighbor table, but the new position estimation tells that the

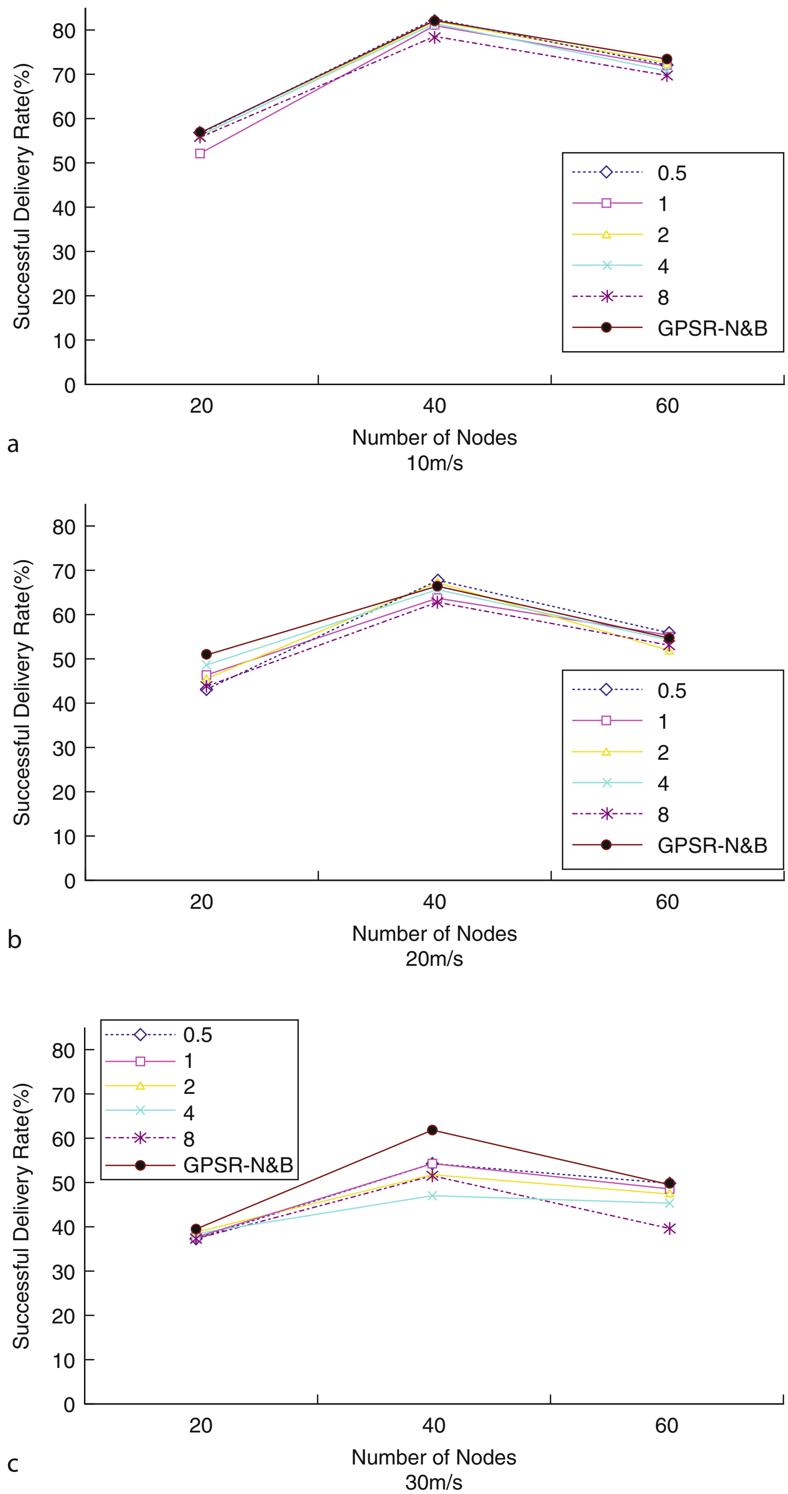

Vehicular Ad Hoc Networks, Enhanced GPSR and Beacon-Assist Geographic Forwarding in. Figure 4
SDR varying maximum node speed

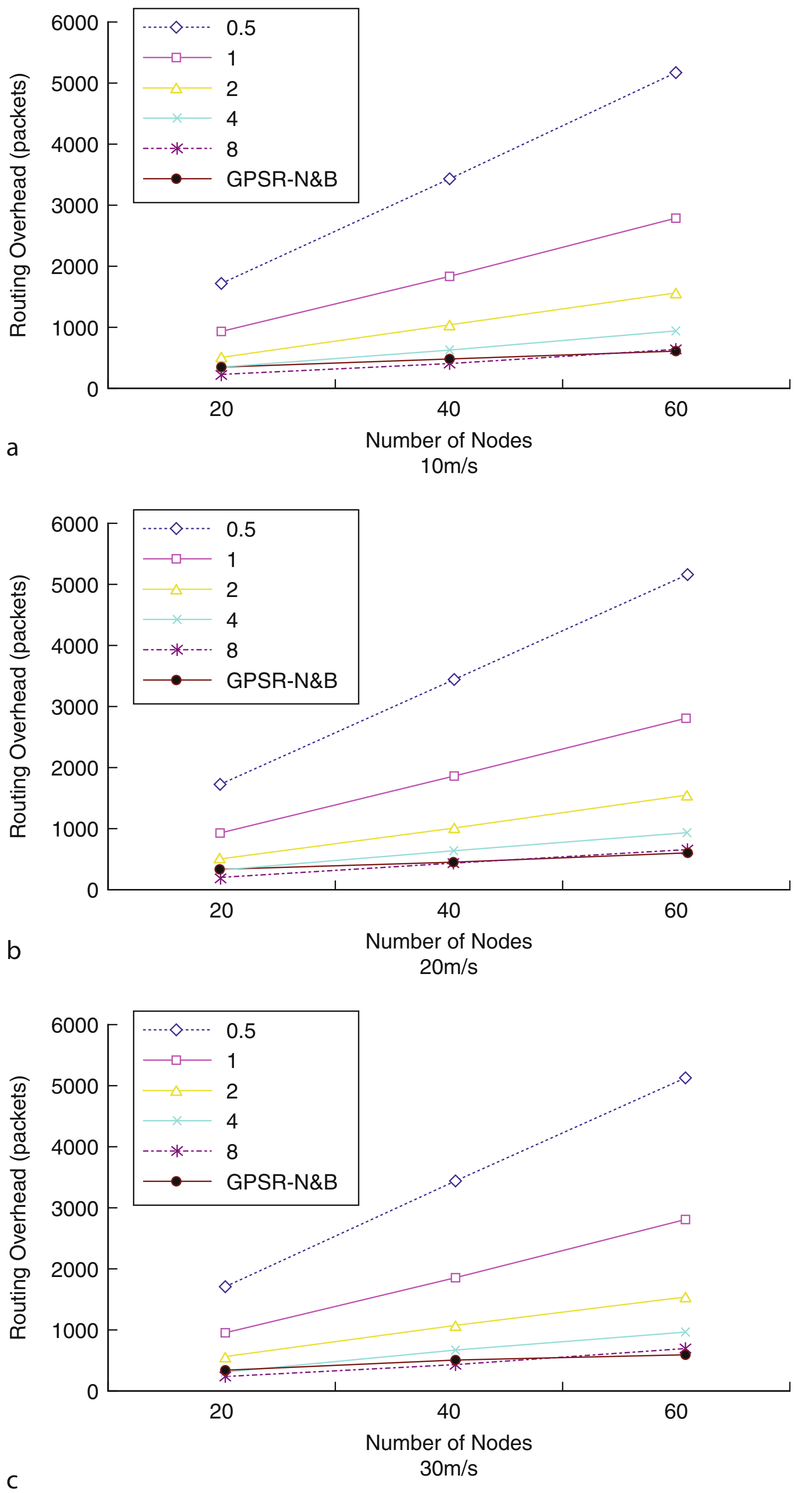

Vehicular Ad Hoc Networks, Enhanced GPSR and Beacon-Assist Geographic Forwarding in. Figure 5
Routing overhead varying maximum node speed

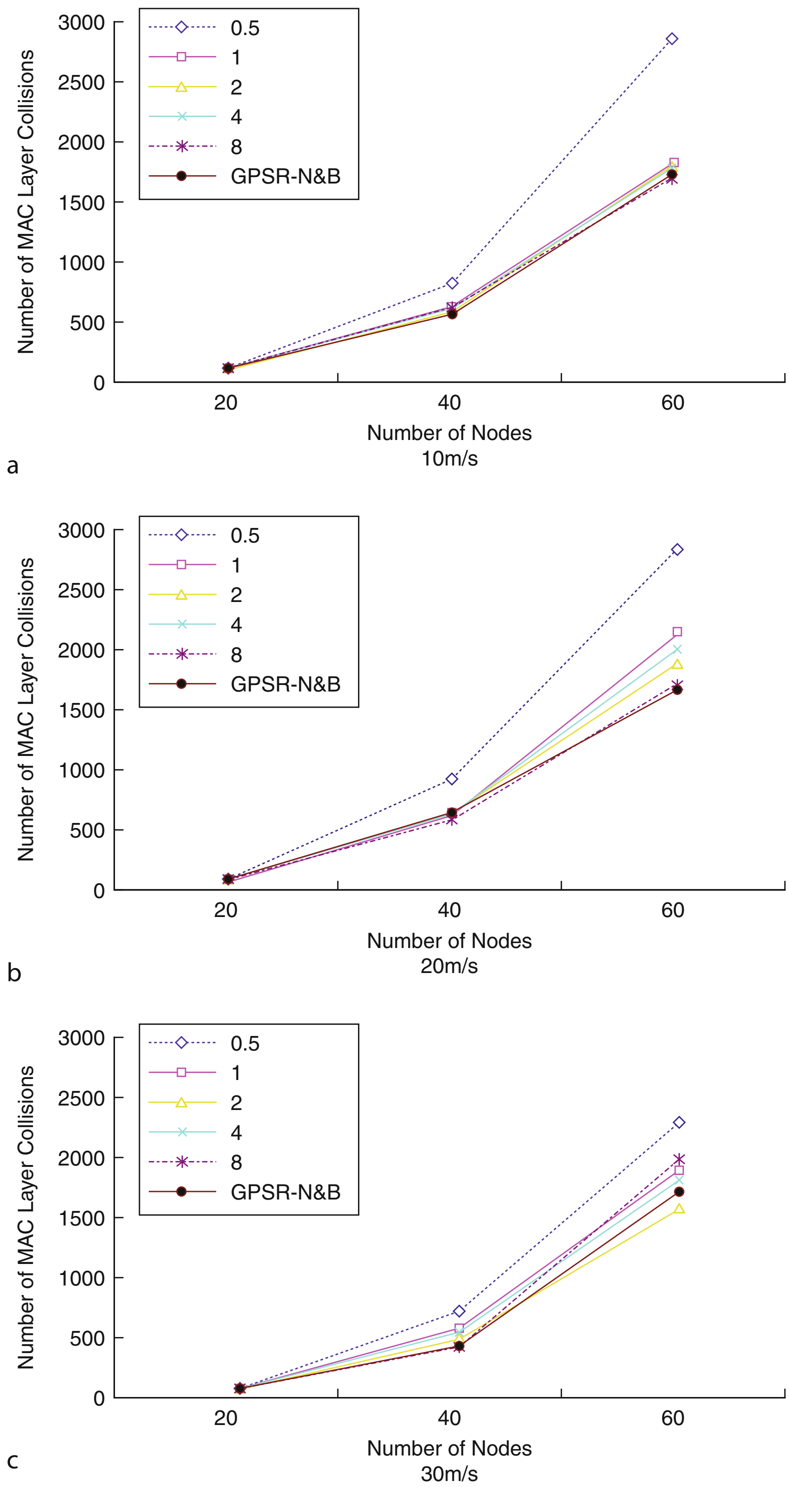

Vehicular Ad Hoc Networks, Enhanced GPSR and Beacon-Assist Geographic Forwarding in. Figure 6
Number of MAC layer collisions varying maximum node speed

destination is most likely already out of the range, then the node closest to the new position of the destination is chosen as a next hop.

If no destination is found in the neighbor table, the node consults the packet travel time and estimates whether it may potentially reach the position of the destination recorded in the packet header within one hop, taking into account a distance potentially traveled by the destination node within the packet travel time. If yes, the non-propagating broadcast is sent around, with the search for the destination. If no answer is received (either from the destination or the node that has the destination in its table and is closer to the destination than the current node), then the next closest to the destination node is chosen, and the process repeats.

Movement Prediction–Based Routing

This routing concept, based on vehicles movement prediction, estimates the stability of each communication link in the network in terms of communication lifetime, and then selects the most stable route composed by the most stable intermediate links from the source till the destination. This concept can be applied to position-based routing protocols and has been implemented with GPSR under the network simulator NS2. By this way, GPSR's performance is improved.

Movement Prediction-Based Routing (MOPR) [3] determines the most stable path from a source to a destination in terms of communication lifetime by selecting the most stable intermediate links, then, the best intermediate vehicles. For example, assuming there is a network protocol which is capable to provide several unicast paths to a destination, one of those paths can result to be more stable with respect to the others. A stable path can increase the probability that link failures will be avoided during the whole communication. MOPR, based on vehicles' movement information, guarantees the selection of the best next hop for data forwarding. Using MOPR, each vehicle estimates the Link Stability (LS) for each neighboring vehicle before selecting the next hop for the data forwarding/sending. The LS is a relation between the link communication lifetime and a constant value (σ) which represents in general cases the routing route validity time, and it depends on the used routing protocol. Figure 7 shows how link lifetimes are estimated based on neighbors' movement information. The lifetime of the link (i, j) (LifeTime[i,j]) corresponds to the estimated time $\Delta t = t_1 - t_0$ with t_1 is

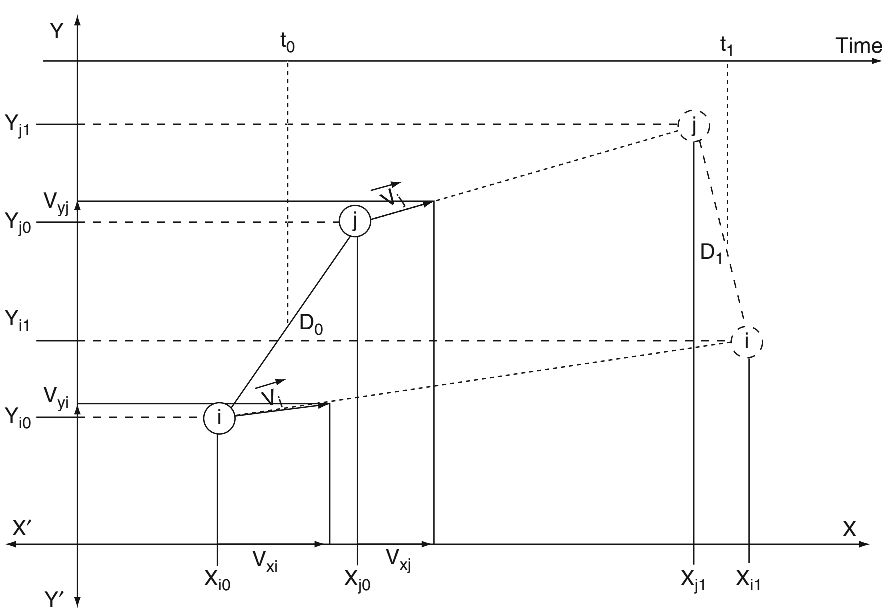

Vehicular Ad Hoc Networks, Enhanced GPSR and Beacon-Assist Geographic Forwarding in. Figure 7
Link lifetime estimation

the time when D_1 becomes equal or bigger than the communication range R (i.e., the time when j goes out of the communication rage of i). D_1 and Δt are estimated using the initial positions of i and j ((X_{j0}, Y_{j0}), and their initial speeds $\bar{V}_j$ and $\bar{V}_j$, respectively):

$$D_1^2 = ((X_{i0} + Vx_i\Delta t) - (X_{j0} + Vx_j\Delta t))^2 + ((Y_{i0} + Vy_i\Delta t) - (Y_{j0} + Vy_j\Delta t))^2$$

$$D_1^2 = A\Delta t^2 + B\Delta t + C$$

$$\text{with} \begin{cases} A = (Vx_i - Vx_j)^2 + (Vy_i - Vy_j)^2 \\ B = 2[(X_{i0} - Y_{j0})(Vx_i - Vx_i) \\ \qquad + (X_{i0} - Y_{j0})(Vy_i - Vy_i)] \\ C = (X_{i0} - X_{j0})^2 + (Y_{i0} - Y_{j0})^2 \end{cases}$$

By solving the equation $A\Delta t^2 + B\Delta t + C - R^2 = 0$ it is easy to get Δt which corresponds to the LifeTime[i,j]. LS is calculated as follows:

$$LS[i,j] = \frac{\text{Life Time}[i,j]}{\sigma}, \text{ with } LS\,[i,j] = 1 \text{ when Life Time } [i,j] \geq \sigma$$

Once LS is calculated for each neighboring vehicle, MOPR selects as a next hop for data forwarding/sending the one corresponding to the highest LS (corresponding to the most stable neighboring link).

This approach should help as well in minimizing the risk of broken links and in reducing data loss and link-layer and transport retransmissions.

F. Granelli et al. have proposed a Movement-Based Routing Algorithm (MORA) [4] for vehicular ad hoc networks. It is applied to GPSR. MORA takes into account the physical location of neighboring vehicles and their movement direction when selecting the next hop for sending/forwarding packets. MOPR believes that considering only the position and the movement direction is not enough for a best next hop selection in VANETs. The vehicle's driving speed is important and should be taken into account as well. A vehicle which is almost out of communication range should not be selected as a next hop, which cannot be guaranteed without taking into account the speed. Thus, with MOPR, a vehicle which is estimated to go out of communication range in a short duration will not be selected as a next hop for data routing if a better candidate is available.

To show the performance improvements of MOPR over position-based routing protocols, it is applied over GPSR. It is not suitable to apply MOPR to GPSR as it is done to unicast routing [3, 5], where MOPR tries to select the path with the longest lifetime. When applying MOPR to GPSR as it is, the selected paths should be same or longer in terms of number of hops when compared to basic GPSR. And the calculation of neighboring links' LS before sending/forwarding each packet takes a considerable time. All this decreases the routing performances. To face this problem, MOPR is applied in a different way. When a vehicle wants to send or forward data, it first estimates the future geographic location after a duration time T in seconds for each neighbor. T is counted in seconds, and it is fixed to 1 s in the simulations. Then, it selects as next hop the closest neighbor to the destination which does not have a future location out of its communication rage after the time T.

By doing this, MOPR-GPSR avoids the case when a next hop goes out of communication range during a data packet transmission, thus, decreasing data loss and link-layer and transport retransmissions, which increases the routing performances.

To evaluate the performances of MOPR over position-based routing protocols, it is implemented on top of GPSR, named MOPR-GPSR. A Hierarchical Location Service (HLS) is used to provide the exact position information of the neighboring and the destination vehicles. More information on HLS is given in [6].

The simulations use a 5,000 m length highway scenario, with 200 vehicles moving on it as shown in Fig. 8. In each direction, there are three lanes with different speed ranges starting from a minimum speed value of 70 km/h and a maximum speed value which is increased from 120 to 220 km/h. In each direction there is a density of five vehicles every 150 m. The classical 802.11 Medium Access Control (MAC) functionalities are used. Traffic type was CBR with 1,024 Bytes of packet size and a 512 bps of maximum CBR rate. A transmitting source and a destination vehicle are selected randomly along the middle lane (normal vehicles' lane) in each direction.

Figure 9 shows the Packet Delivery Ratio (PDR) obtained for each routing protocol as function of vehicles' maximum speed. It is clearly shown that both MOPR and MORA guarantee a better PDR when

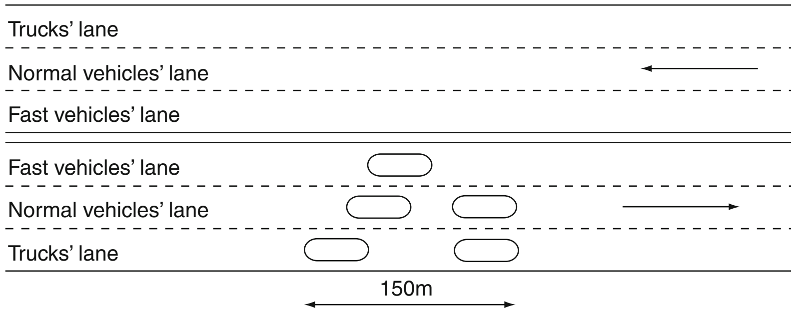

Vehicular Ad Hoc Networks, Enhanced GPSR and Beacon-Assist Geographic Forwarding in. Figure 8
The highway scenario in simulations

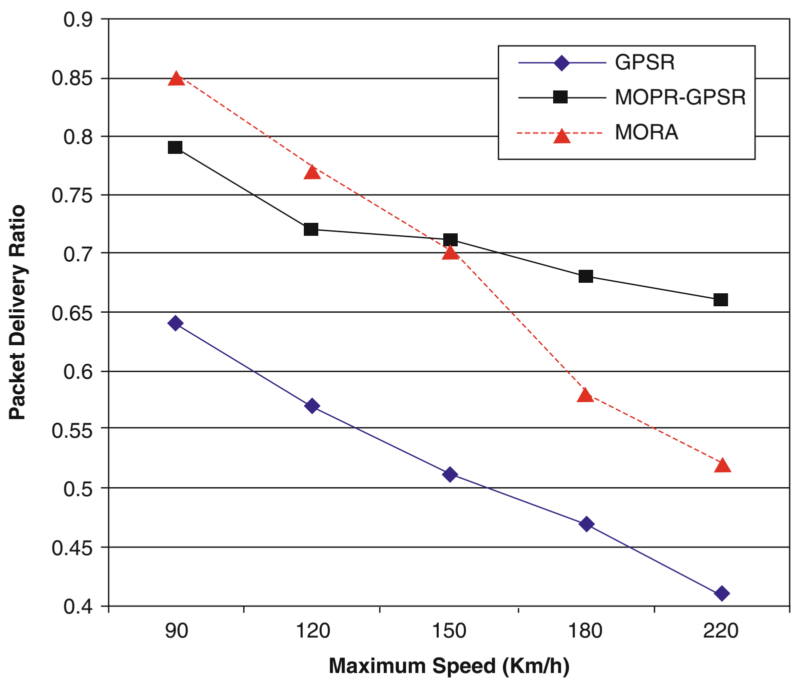

Vehicular Ad Hoc Networks, Enhanced GPSR and Beacon-Assist Geographic Forwarding in. Figure 9
Packet delivery ratio comparison between GPSR, MOPR, and MORA

compared to basic GPSR. As shown, higher the vehicles' maximum speed, higher the PDR of MOPR when compared to MORA. This means that MOPR guarantees the best PDR when speed is higher.

Figure 10 shows the delay for each routing protocol as a function of vehicles' maximum speed. MOPR improves the delay by at least two times when compared to both basic GPSR and MORA.

Figure 11 shows the routing overhead as a function of vehicles' maximum speed. MOPR decreases the routing overhead when compared to basic GPSR, but MORA decreases the routing overhead more. That means that MORA is the best in terms of routing overhead. But, in Fig. 12 the Hierarchical Location Service (HLS) overhead caused in the network which should be taken into account to evaluate the real performance of this routing

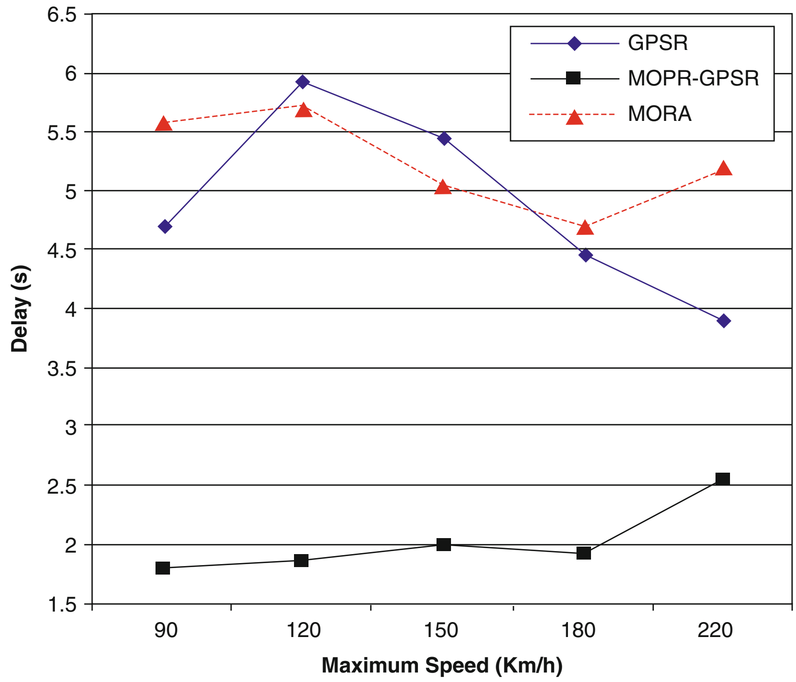

Vehicular Ad Hoc Networks, Enhanced GPSR and Beacon-Assist Geographic Forwarding in. Figure 10
Delay comparison between GPSR, MOPR, and MORA

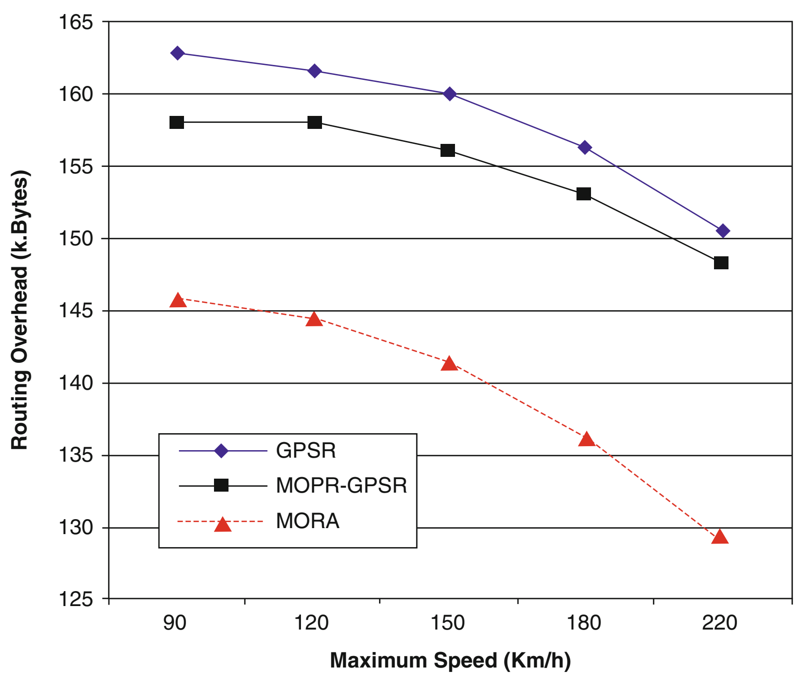

Vehicular Ad Hoc Networks, Enhanced GPSR and Beacon-Assist Geographic Forwarding in. Figure 11
Routing overhead comparison between GPSR, MOPR, and MORA

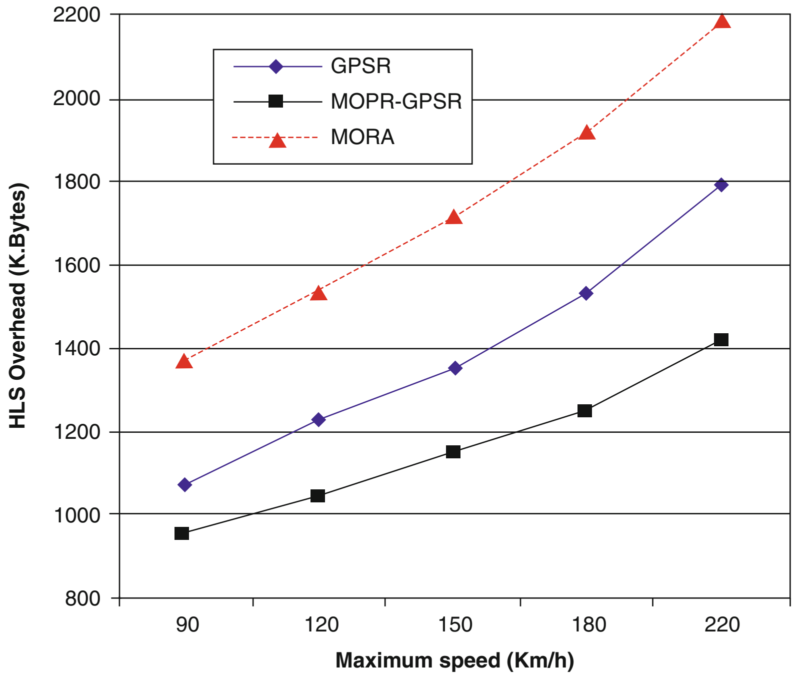

Vehicular Ad Hoc Networks, Enhanced GPSR and Beacon-Assist Geographic Forwarding in. Figure 12
HLS overhead comparison between GPSR, MOPR, and MORA

protocol in terms of routing overhead. And it is clearly shown that MOPR is the best in terms of HLS overhead when compared to both basic GPSR and MORA.

To evaluate the performance of any routing protocol in terms of routing overhead, it is important to calculate the Routing Overhead Ratio (ROR). Figure 13 shows the ROR caused in the simulation network while taking into account only the routing overhead (i.e., without counting the HLS overhead). It is clearly shown that both MOPR and MORA improve the ROR when compared to basic GPSR. And MOPR shows an almost stable ROR compared to MORA which increases when the maximum speed increases.

The ROR is important, but in such kind of routing protocol, the global ROR overhead, while taking into account the HLS overhead as well, is more important. Figure 14 shows clearly how MOPR improves the network performance in terms of global ROR by about two times when compared to both basic GPSR and MORA.

All simulation results presented in this section show that MOPR improves the routing performances from all sides. Consequently, MOPR shows a big potential for position-based routing in VANETs.

Strategies of Enhancement in City Scenario

Definition of the Subject A city scenario is much more complicated. Communication between cars driving in a city environment creates different challenges, largely due to the more complex geometry of the scenario. The challenges can be summarized as follows:

Geometric two-dimensionality: Cars change their movement direction all the time and can move at any relative angle to each other allowed by the street geometry. This weakens the correlation of the destination position to a suitable next hop.

Obstacles: A city is usually characterized by the presence of radio obstacles, which creates problems with position-based next hop selection because the nodes are not able to communicate whenever the line of sight between two nodes goes through an obstacle. And multipath propagation and complex obstacle surfaces create a much more complicated situation in reality.

Node density: the node density can be expected to be rather high with respect to the radio range, especially at “density hot spots” like junctions. Node density

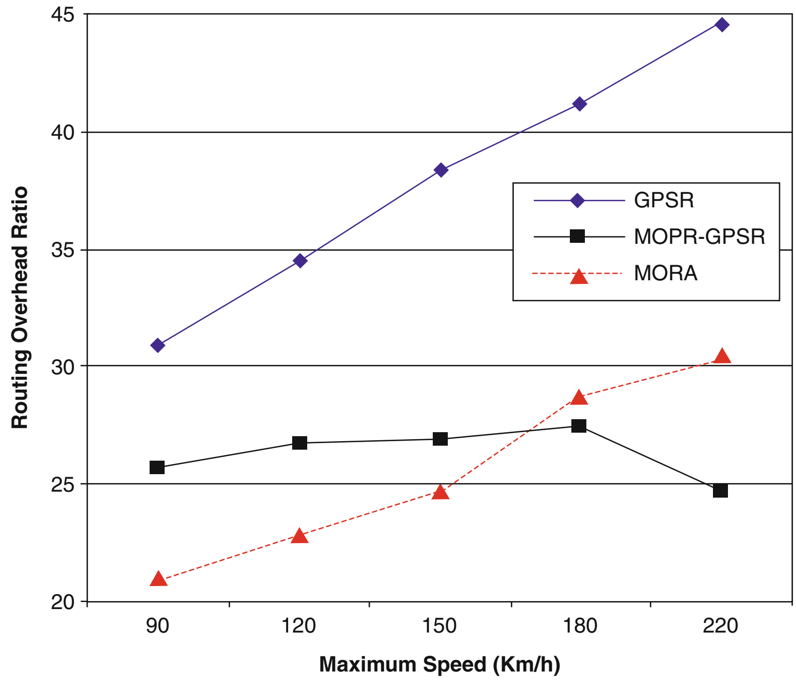

Vehicular Ad Hoc Networks, Enhanced GPSR and Beacon-Assist Geographic Forwarding in. Figure 13
Routing overhead ratio comparison between GPSR, MOPR, and MORA

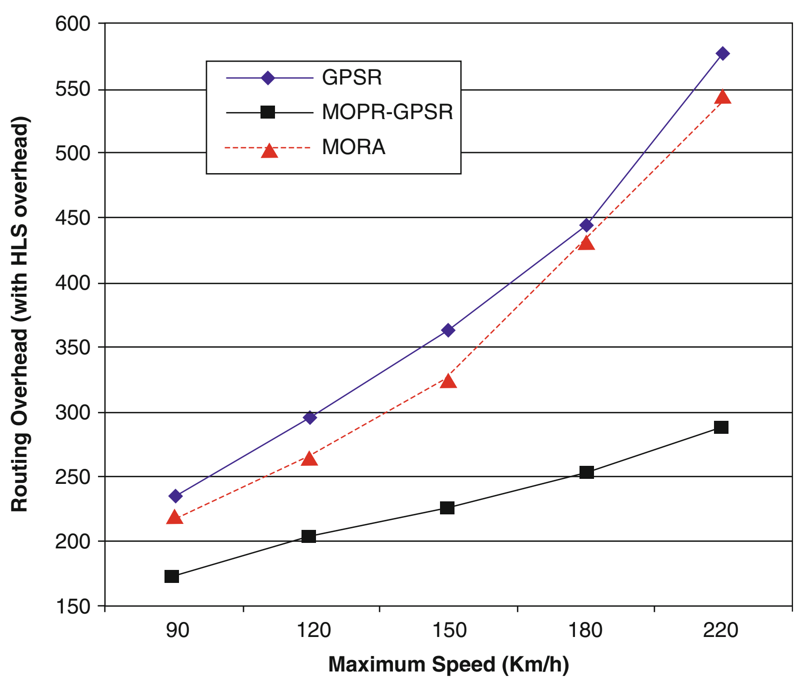

Vehicular Ad Hoc Networks, Enhanced GPSR and Beacon-Assist Geographic Forwarding in. Figure 14
Global routing overhead (routing + HLS) ratio comparison between GPSR, MOPR, and MORA

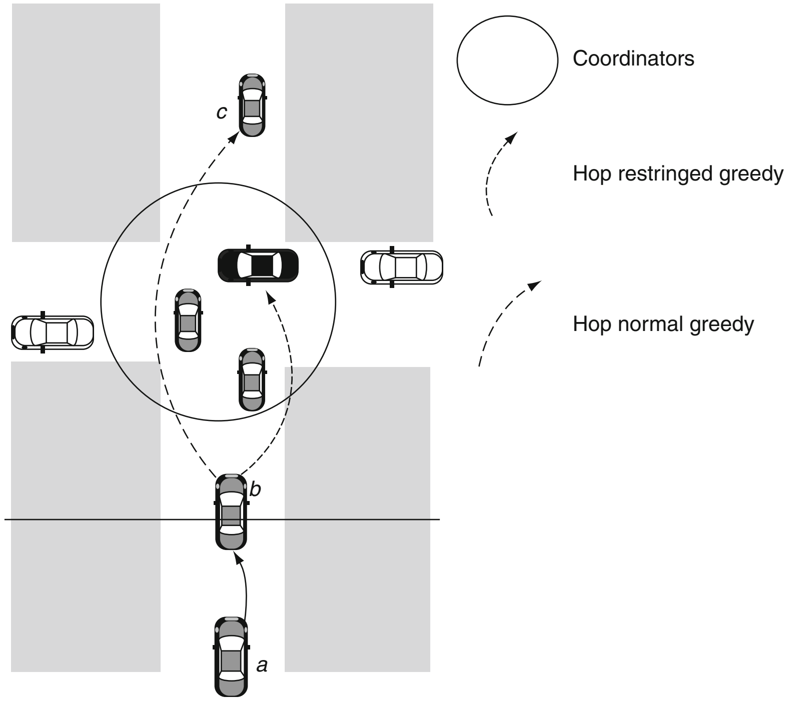

Vehicular Ad Hoc Networks, Enhanced GPSR and Beacon-Assist Geographic Forwarding in. Figure 15
Preference coordinator nodes in GPCR

creates better ad hoc connectivity while it also poses a challenge to flooding mechanisms that need to be very efficient.

Low mobility: Compared to highway scenarios, nodes move at lower speeds, influenced by node density and are constrained by speed limits.

Greedy Perimeter Coordinator Routing

Greedy perimeter coordinator routing (GPCR) [7] does not use map information or densities in the streets, nor does it use the idea of a list of junctions that a packet must pass until it reaches the destination. It aims to avoid overhead. GPCR proposes a position-based algorithm. The main idea is to take into account the fact that the streets and junctions form a natural planar graph and, hence, it is possible to apply geographic routing directly. GPCR consists of two parts: restricted greedy routing and repair strategy.

Restricted greedy routing. Data packets should be routed along streets because they cannot get through buildings. The junctions are the only places where actual routing decisions are taken. Therefore, packets should always be forwarded to a node on a junction rather than being forwarded across a junction. This is illustrated in Fig. 15, where node *b* would forward the packet beyond the junction to node *c* if greedy forwarding is used. But by forwarding the packet to any of the nodes in the corner it finds an alternative path to the destination without getting stuck in a local optimum. A local optimum is produced when a forwarding node does not find a neighbor closer to the destination than itself. A node on a junction usually has more available options to route a message. Nodes that are located close to a junction are called coordinators. A coordinator broadcasts its role into its beacon packets. Thus, its neighbors will know its role when they have to forward these beacons. As a node must know whether it is a coordinator or not, two methods have been proposed to learn that.

The first one consists of including neighbors' locations and identifiers in beacons, so that each node can have information about the two-hop distance. Then, a node is considered to be in a junction when it has two neighbors that are within transmission range to each other but do not list each other as neighbors.

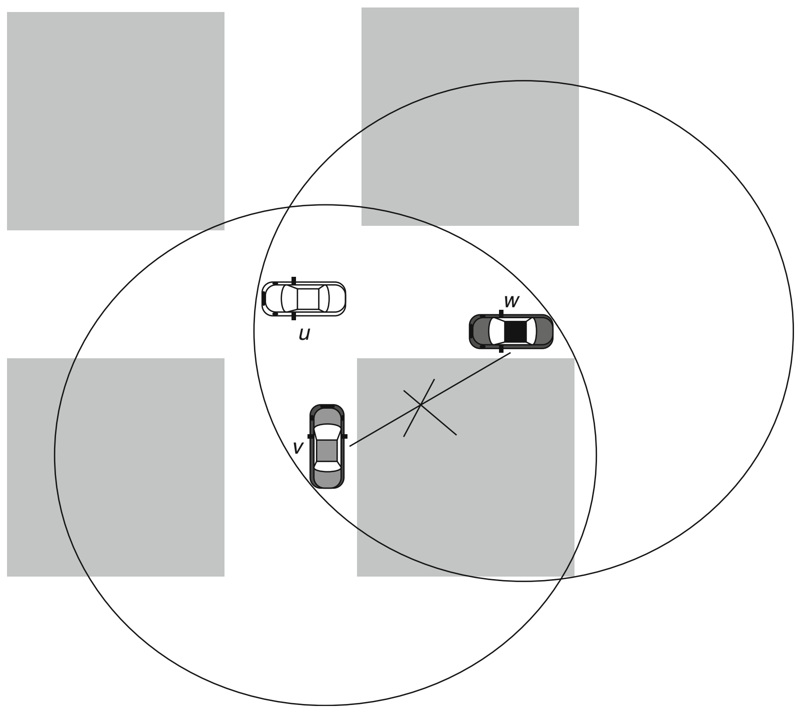

Vehicular Ad Hoc Networks, Enhanced GPSR and Beacon-Assist Geographic Forwarding in. Figure 16
Discovery method of coordinators in GPCR

Figure 16 shows v and w are neighbors of node u but they do not list each other as neighbors. This method might have problems. In Fig. 17 the requirement is correct but node u is not really a coordinator because it is located in a curve.

The second one consists of calculating the correlation coefficient (CC) with respect to the position of the neighbors. In this method, it is not necessary to include additional information into beacon messages. Let x_i and y_i be the (x, y) coordinates of a node i. Also let $\bar{x}$ and $\bar{y}$ be the mean of x-coordinates and y-coordinates, respectively. σ_{xy} indicates covariance of x and y. σ_x and σ_y indicates the standard deviation of x and y, respectively. Finally, the correlation coefficient is defined in Eq. 7:

$$\rho_{xy} = \left|\frac{\sigma_{xy}}{\sigma_x \sigma_y}\right| = \left|\frac{\sum_{i=1}^{n}(x_i - \bar{x})(y_i - \bar{y})}{\sqrt{\left(\sum_{i=1}^{n}(x_i - \bar{x})^2\right)\left(\sum_{i=1}^{n}(y_i - \bar{y})^2\right)}}\right| \quad (7)$$

with $\rho_{xy} \in [0,1]$. If the value is close to 1 it indicates a linear coherence that is normally found when a vehicle is located in the middle of a street (Fig. 18). On the other hand, a value close to 0 might indicate a linear coherence and, hence, a vehicle can be determined to be located in a junction. By adjusting a threshold $\in$, a node can evaluate the correlation coefficient and assume with $\rho_{xy} \geq \in$ that it is located on a street and then the node is a coordinator. But if $\rho_{xy} \leq \in$, it can be concluded that the node is close to a junction. 0.9 is considered to be a good value for 2, but it may be arbitrary.

If the forwarding node is located on a street and not on a junction, the packet is forwarded along the street toward the next junction. To achieve this, the forwarding node draws a line between the forwarding node's predecessor and the forwarding node itself. The neighbors that approximate the extension of the line will be candidates. The farthest candidate node is selected. In Fig. 18, node w is selected based on the

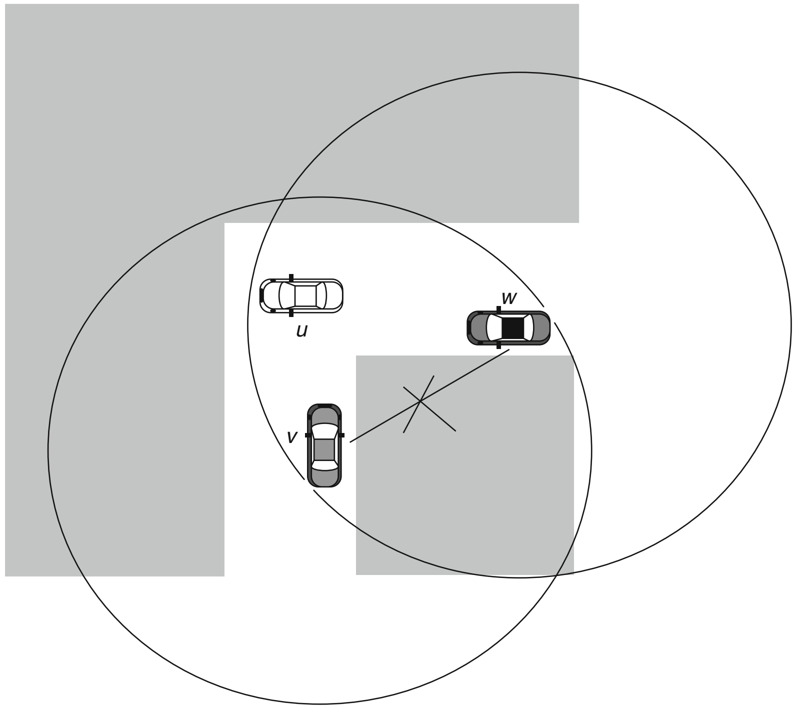

Vehicular Ad Hoc Networks, Enhanced GPSR and Beacon-Assist Geographic Forwarding in. Figure 17
Failed discovery coordinator in GPCR

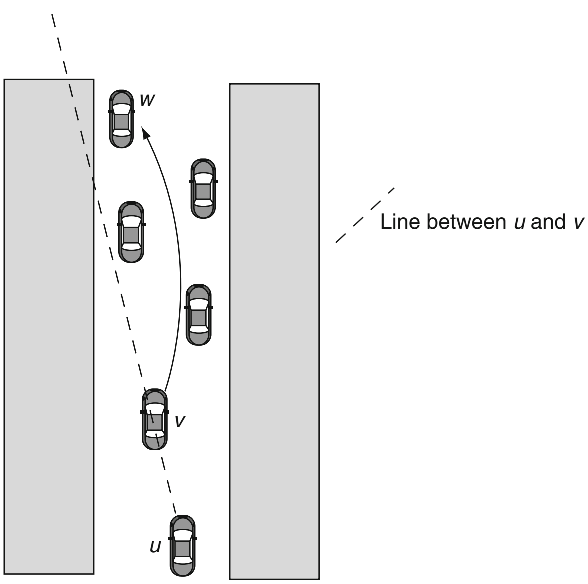

Vehicular Ad Hoc Networks, Enhanced GPSR and Beacon-Assist Geographic Forwarding in. Figure 18
Restricted greedy in a street

line between *u* and *v*. In the event that some candidate node is a coordinator it will be selected before any non-coordinator node. If there were more coordinators, one of them is randomly selected (Fig. 15). This prevents a packet from crossing a junction. Once a packet reaches a coordinator, a decision has to be made about the street that the packet should follow. This is done in a greedy mode: the neighbor with the largest progress toward the destination is chosen. This implies a decision on the street that the packet should follow (Fig. 19).

Repair strategy. Despite the new greedy routing model, there exists the risk that a packet gets stuck in a local optimum. Hence a repair strategy is required. The vehicle tries to infer the topology of the roads by applying the recovery strategy over the set of neighbors. If the forwarding node is a coordinator and the packet is in repair mode, then the node needs to determine which street the packet should follow next. To this end the right-hand rule [8] is applied (Fig. 20). Using the right-hand rule it chooses the street that is the next one

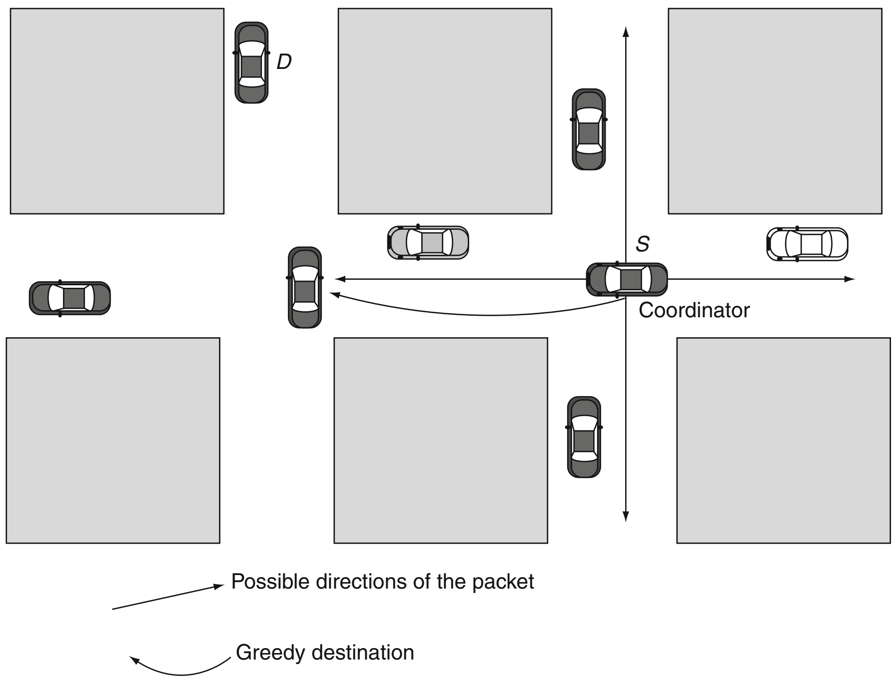

Vehicular Ad Hoc Networks, Enhanced GPSR and Beacon-Assist Geographic Forwarding in. Figure 19
Restricted greedy in a street

counterclockwise from the street the packet has arrived on. But if the forwarding node with a packet in repair mode is not a coordinator, then the node applies restricted greedy routing.

In GPCR, there exists a risk that a packet could be forwarded back over the same street from which the packet has arrived. When a packet is being forwarded in repair mode and reaches a coordinator node, it applies perimeter routing. In Fig. 21, it shows how if the node *u* applies the right-hand rule (in this case left-hand rule) from the line formed between nodes *u* and *v*, the coordinator chooses the node *w* as the next hop, instead of the node *x* which is located along the next street. Therefore, the packet does not turn the junction, but it remains on the same street.

Simulation of GPCR is implemented with the ns-2 simulator version ns-2.1b9a. In the simulation, a real city topology is used, which is a part of Berlin, Germany. The scenario consists of 955 cars (nodes) on 33 streets in an area of 6.25 × 3.45 km. The movement of the nodes was generated with a dedicated vehicular traffic simulator and represents a real-world movement pattern for this given scenario [9]. IEEE802.11 was used as MAC with a transmission rate of 2 Mbps. The transmission range was set to 500 m. Real-world tests with cars have shown this to be a reasonable value when using external antennas. For each simulation run ten sender–receiver pairs are randomly selected. Each pair exchanges 20 packets over 5 s. Figure 21 shows the achieved packet delivery rate versus the distance between the two communication partners and Fig. 22 shows the number of hops. The communication distance between two nodes is calculated as the minimal distance based on the street topology at the beginning of the communication.

Figure 21 also depicts how the delivery rate is influenced by the algorithms used for junction detection. It shows that calculating the correlation coefficient (CC) is slightly better than relying on the comparison of the neighbor tables (NT). A compound decision consisting of the neighbor table comparison and correlation coefficient is also analyzed, concatenated by logical OR as well as by logical AND. The latter one outperforms the other approaches slightly but it does not come for free: the size of the beacon packets increases for each of the two

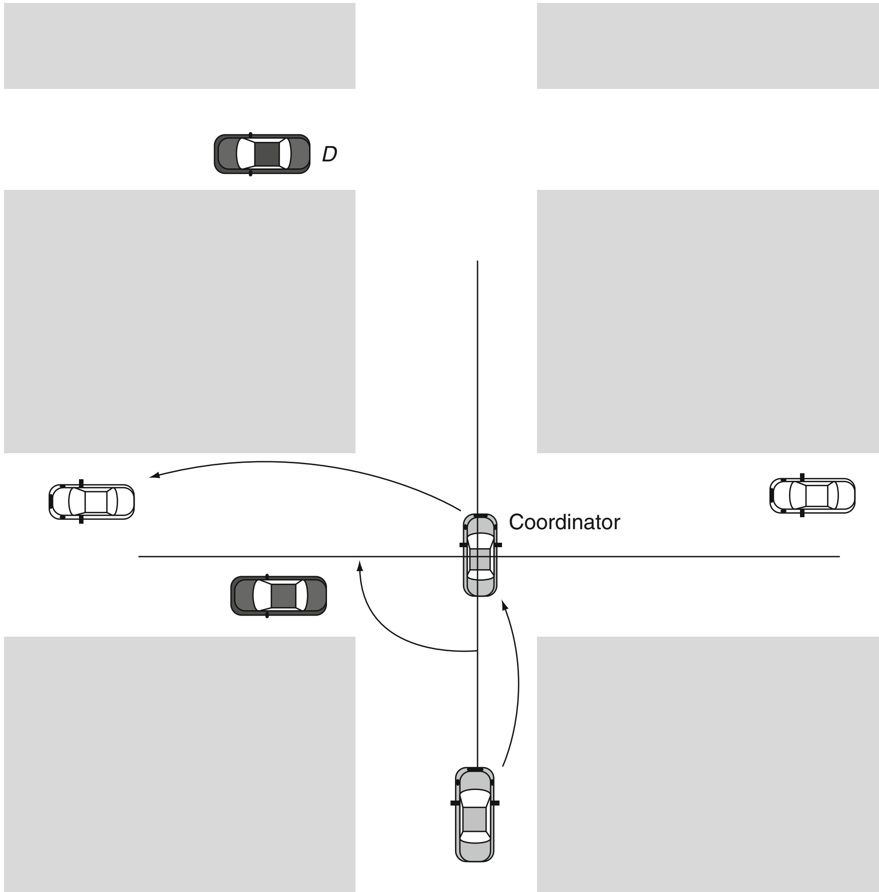

Vehicular Ad Hoc Networks, Enhanced GPSR and Beacon-Assist Geographic Forwarding in. Figure 20
Coordinator applying perimeter in GPCR

approaches. Therefore, GPCR simply uses the correlation coefficient. In general, the study on achievable packet delivery rate (Fig. 21) shows good results for the approach compared to GPSR. This improvement in performance comes at the expense of a higher average number of hops and a slight increase in latency. This increase in hop counts and latency is mainly caused by those packets that could not be delivered at all by GPSR and thus did not impact the hop-count and latency for GPSR.

Connectivity-Aware Routing

Connectivity-aware routing (CAR) [10] is a position-based routing scheme. The protocol is aimed at solving the problem of determining connected paths between source and destination nodes. VANETs' nodes present a high degree of mobility, and nodes cannot know the position of the rest of the vehicles due to several well-known scalability problems. This lack of information makes it impossible to determine a priori which streets have enough vehicles to allow messages to be routed through them.

CAR's algorithm is designed to deal with these problems, and to do that it is divided into three stages: (1) finding the location of the destination as well as a connected path to reach it from the source node, (2) using that path to relay messages, and (3) maintaining the connectivity of the path in spite of the changes in the topology due to the mobility of vehicles.

In the first stage, the source node broadcasts a route request message. The idea behind this initial broadcast

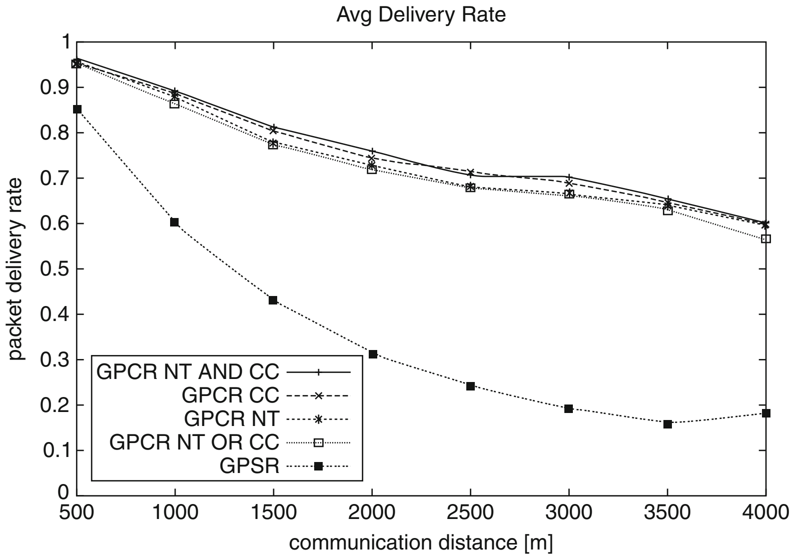

Vehicular Ad Hoc Networks, Enhanced GPSR and Beacon-Assist Geographic Forwarding in. Figure 21
GPCR versus GPSR – delivery rate

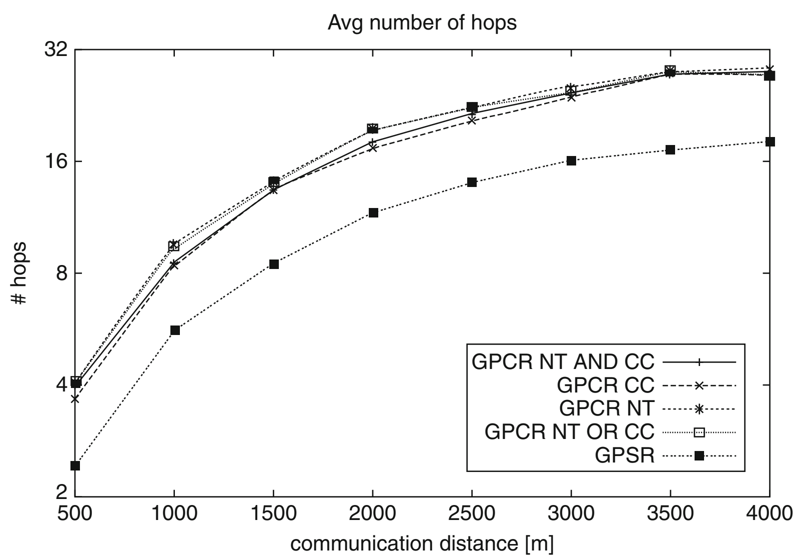

Vehicular Ad Hoc Networks, Enhanced GPSR and Beacon-Assist Geographic Forwarding in. Figure 22
GPCR versus GPSR – average number of hops

is the following: The reception of, at least, one of these route request messages at the destination means that at least one connected path exists. The destination node answers the route request message with a response message including its current location so that the first problem is solved. But the source node also needs to know the path to reach the destination.

In CAR, it is proposed to include in the header of every route request message the list of junctions (called anchor points) traversed by that message in its way

toward the destination. Thus, adding that list to the response message issued by the destination solves the second problem. Besides, nodes periodically transmit short messages including the issuer's identifier, location, and current velocity vector. These short messages (called beacons) keep the neighbor's tables updated. Moreover, the determination of junctions is made by means of comparing the direction of the vehicles. That is, a node determines if it is currently located at a junction when the angle between its velocity vector and one of the neighbors is not parallel. Two velocity vectors are parallel if the smallest angle between the vectors is less than α (equal to 18°). Otherwise the velocity vectors are nonparallel. Nodes that have neighbors with nonparallel velocity vectors identify themselves as being near a crossing or road curve and can serve as relays.

Additionally, to select not only a connected path between the source and the destination but also a short one, the destination does not respond immediately. Instead, it waits a predefined amount of time and then the path selected is the shortest one among those included in the different route request messages received. CAR uses the preferred group broadcast (PGB) [2] protocol to reduce as much as possible the overhead of flooding.

Once the source node has determined a path to reach the destination, data messages are routed geographically from an anchor node to the next one until the destination is reached. To do that, the source node uses a source routing approach. The full list of anchor nodes is included as a header in every data message transmitted. CAR uses the advance greedy forwarding (AGF) [2] algorithm to deliver messages between each pair of anchor nodes. In AGF, relay nodes select as next hop the neighbor located closest to the destination. In this case, it is the vehicle located closest to the next anchor point.

CAR defines the concept of "guards" (see Fig. 23) to help nodes determine if a message has reached a certain anchor point. A guard is a set of information tied to a geographical area. That area is defined by the location of the anchor point and a radius. Thus, guards contain both the location and the radius. Nodes create guards when they identify a new anchor point. A node creating a guard is the first one including it on its beacon messages. Nodes store the guards received during beaconing periods, but only nodes located inside the area defined in the guard retransmit it on their beacons.

A node receiving a message being routed toward the anchor point *a* can determine that the message has reached *a* by checking if it has already received a guard for *a*. Moreover, the mobility of vehicles causes constant topology changes. Thus, the connected path found at the beginning of a data transmission can become disconnected over time. To overcome this issue, CAR uses the guards to help maintain the connectivity of the path, or at least to dynamically auto-adjust it on the fly without resorting to a new route discovery process.

Concretely, it is assumed that there cannot be disconnection problems between anchor points, so that only the movement of the destination node represents an issue. Therefore, when a destination node changes its direction, then a new guard is generated including also the new velocity vector of the destination node. When a data message arrives to the old destination node's location, the guarding nodes (those interchanging that guard) can retransmit the packet toward the new estimated location of the destination. Of course, this assumption may not hold in general, which means that the protocol may fail to maintain the path connected.

Finally, as CAR makes extensive use of beacons, an adaptive beaconing mechanism is proposed to reduce control overhead while keeping neighbor tables as accurate as possible, especially when the number of neighbors or their mobility makes them very unstable. The idea is to adapt the beaconing rate to the nodes density, so that the fewer the number of neighbors, the higher is the beaconing frequency. By this way, several drawbacks, such as wasted bandwidth, delaying of data packet, increased network congestion, coming from fixed period beacon strategy, can be mitigated.

In CAR, there are two possibilities for routing error to occur. First, the AGF algorithm may fail to forward a packet between two anchor points due to (a) a temporary gap between vehicles (or raised interference level), such gaps may appear and disappear with time at any place on a road; or (b) long-term disconnections due to a suddenly closed road or an unusually big gap in the vehicular traffic. Second, a packet may reach the estimated destination position after passing the last anchor point but fails to find the

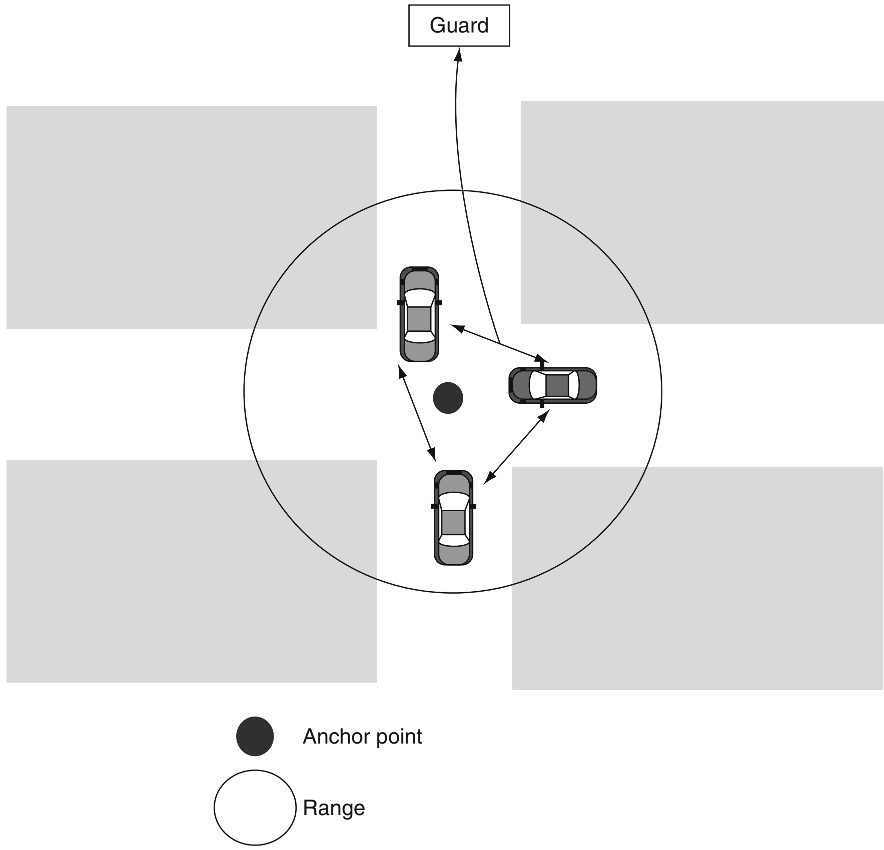

Vehicular Ad Hoc Networks, Enhanced GPSR and Beacon-Assist Geographic Forwarding in. Figure 23
Three vehicles interchanging a guard about an anchor point.

destination there. The reason for that event could be that the destination changed direction but could not activate a guard due to lack of neighbors within communication range, or the guard was activated but later could not be retransmitted due to the same problem. CAR uses two approaches to handle these routing errors: (1) *Timeout algorithm with active waiting cycle* – One approach to tackle temporary gaps (or a raised interference level) is the use of timeout with packet buffering and an active waiting cycle. The forwarding node suspends the packet and periodically checks if the next hop neighbor has appeared. A long-term disconnection recovery algorithm should be invoked when a simple timeout approach failed. (2) *Walk-around error recovery* – If the AGF algorithm fails to find the destination at its estimated position (case 1), or the timeout algorithm could not find the next hop host (case 2), the node that detected the problem informs the source about the error and starts a local destination location discovery process. In case (1) the scope of this discovery is limited to half the number of anchor points in the old source–destination path. The broadcast is allowed to travel no more than one half of the old path length. In case (2) the scope is limited to the number of anchor points in the old path to the destination (from the current node) plus 50%. The same applies to the path length.

Simulations are made under version 2.28 of the ns-2 simulator with the probabilistic Shadowing model. The performances of CAR protocol without and with enabled walk-around error recovery (CAR + WA) are compared with GPSR and GPSR + AGF. Three different densities of nodes (low – less than 15 vehicles/km of road, medium – 30–40 vehicles/km, and high – more than 50 vehicles/km) are used in the following movement scenarios: highway (averaged over three different

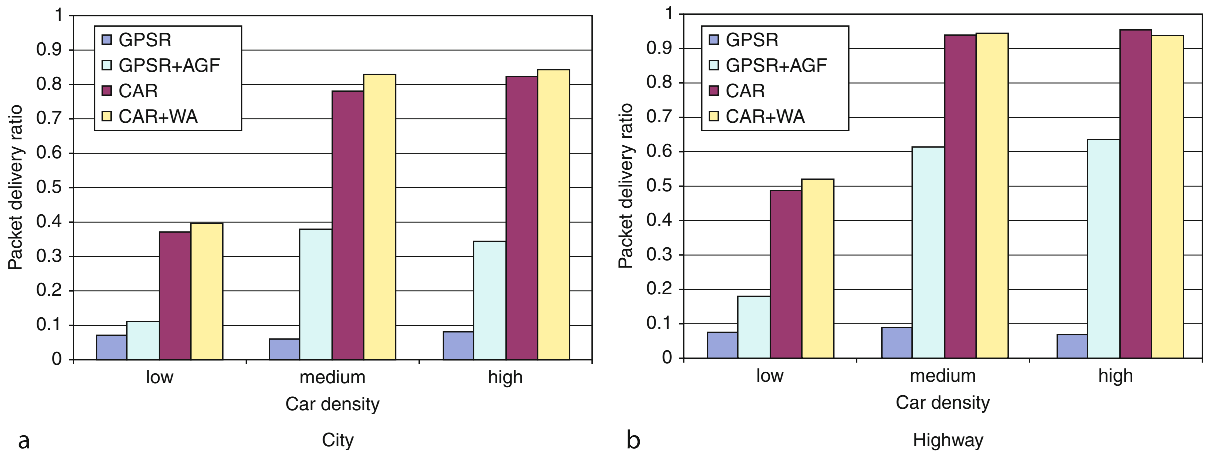

Vehicular Ad Hoc Networks, Enhanced GPSR and Beacon-Assist Geographic Forwarding in. Figure 24
Packet delivery ratio

highway areas, ten sub-scenarios each for every density of vehicles) and city (averaged over three different city areas, ten sub-scenarios each for every density of vehicles) [2]. 20 CBR traffic sources with a sending rate of 4 packets/s are considered. Sources stop generating data packets 50 s before the simulation ends. Source/sink nodes stay inside the simulated area (do not leave the area and do not park) for the duration of the simulations (300 s).

Figure 24 shows packet delivery ratio for city and highway scenarios with different densities of vehicles. For all traffic densities, GPSR performs very poorly in the city scenario, with 5–7% of data packets delivered. Also, the advanced greedy forwarding algorithm (GPSR + AGF) shows moderate performance (up to only 38% of data packets delivered), although performance is noticeably higher than for standard GPSR. Note that GPSR and GPSR + AGF use an idealized location service in the simulation: source nodes obtain the true location of destinations each time a data packet is originated. Despite the additional overhead to discover the real paths and to obtain destination coordinates, CAR and CAR + WA demonstrate much better results than GPSR + AGF. The highway scenarios are geographically less sophisticated than the city scenarios, thus all studied protocols show better PDR in highway areas. Again, CAR and CAR + WA outperform GPSR and GPSR + AGF, despite the need to obtain and maintain paths between source–destination pairs.

In terms of the average data packet delays (Fig. 25), the original GPSR and the GPSR + AGF are always worse than CAR and CAR + WA. For CAR, the route discovery process precedes every first data transmission to an unknown destination, this step adds to the delay of the first data packets. However, the average delay of the data packet for CAR and CAR + WA is much lower than for GPSR and GPSR + AGF. This result is a consequence of CAR's use of real connected paths between source and destination pairs, whereas GPSR and GPSR + AGF often fail due to local maximum resolution encountered by the perimeter mode. CAR easily tolerates short-term disconnections due to gaps or a temporary high interference level (e.g., frequent MAC collisions).

Figure 26 shows the total routing protocol overhead, measured in total number of routing packets sent network-wide during the entire simulation. For the CAR protocol, the overhead is presented as accumulative contribution of (1) beaconing, (2) path discoveries, and (3) path maintenance with the help of guards. The use of adaptive beaconing allows CAR to keep the average beaconing overhead from 1.5 to 3 times lower than the beaconing overhead of GPSR, without harming the performance.

GpsrJ+

GpsrJ+ is a position-based routing protocol which consists of two modes, yet using a special form of

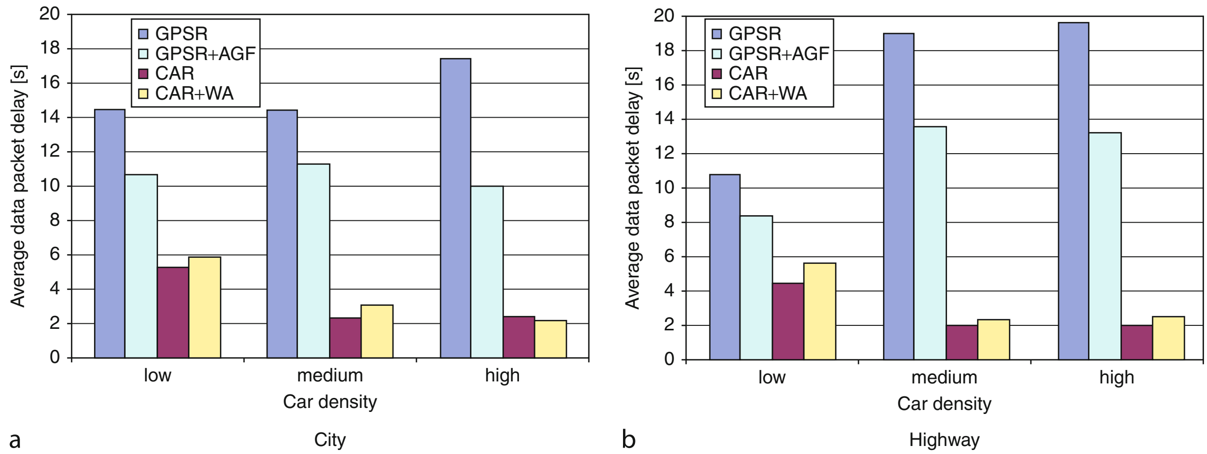

Vehicular Ad Hoc Networks, Enhanced GPSR and Beacon-Assist Geographic Forwarding in. Figure 25
Average delay of a data packet

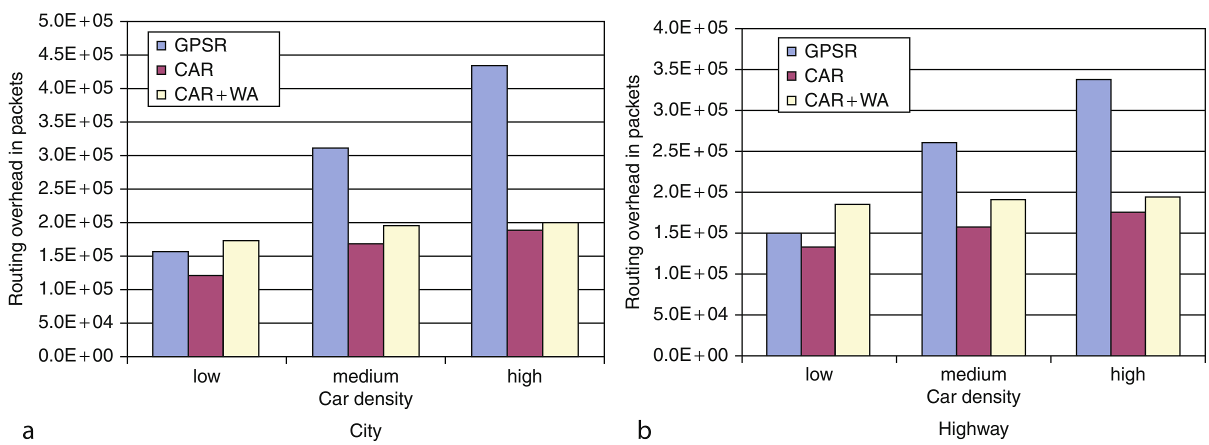

Vehicular Ad Hoc Networks, Enhanced GPSR and Beacon-Assist Geographic Forwarding in. Figure 26
Routing overhead in packets

greedy forwarding. As obstacles (e.g., buildings) block radio signals, packets may only be greedily forwarded along road segments as close to the destination as possible. Accordingly, the major directional decisions are made at junctions. When packets reach a local maximum, a point at which there is no node closer to the destination, the node switches to GpsrJ+'s recovery mode.

In recovery mode, packets are greedily backtracked along the perimeter of the roads. GpsrJ+ removes the unnecessary stop at a junction while keeping the efficient planarity of topological maps. It is not necessary to back forward in small steps through planarized links, for reasons that the general direction of the right-hand rule always results in the opposite direction of where packets were going before recovery, and the objective is to come back as fast as possible to a junction. Unlike GPCR, where packets must be sent to a junction node since junction nodes coordinate the next forwarding direction, GpsrJ+ lets nodes that have junction nodes as their neighbors predict on which road segment its junction nodes would forward packets

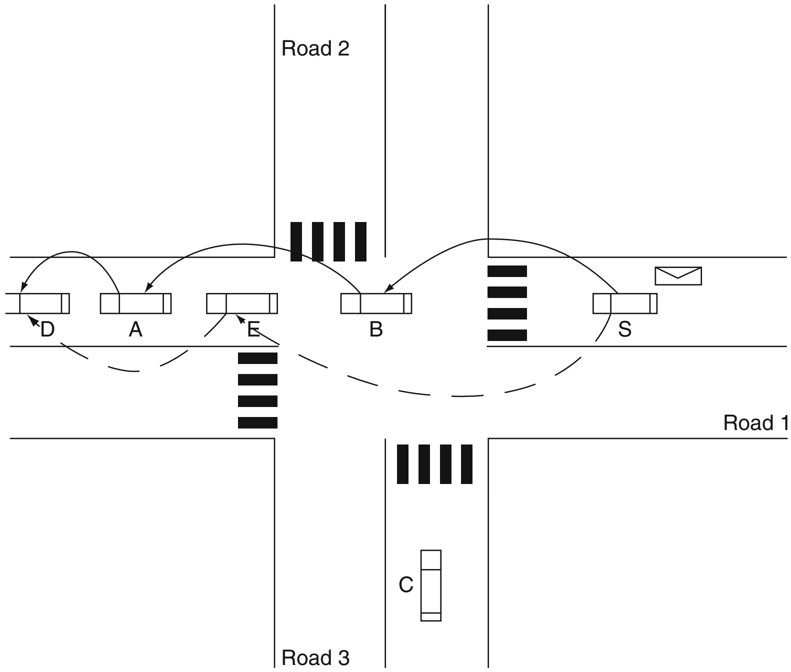

Vehicular Ad Hoc Networks, Enhanced GPSR and Beacon-Assist Geographic Forwarding in. Figure 27
Dashed arrows are GpsrJ+ and *solid arrows* are GPCR

onto, and thus may safely overpass them if not needed. GpsrJ+ uses the right-hand rule to determine the best direction (as opposed to final destination direction) and thereby the best forwarding node. That is, if the furthest node is in the same direction as the best direction, the best forwarding node is the furthest node; otherwise, the best forwarding node is a junction node. Figure 27 illustrates the advantage of prediction. The figure shows that GpsrJ+ can bypass the junction area and forward the packet to node *E* directly, yet GPCR forwards it to the junction node *B*, thus causing more transmissions.

Moreover, GpsrJ+ uses a two-hop neighbor enhanced beaconing. In addition to the node's position in the beacon, each node also broadcasts the road segments that its neighbors are on. In the neighbor list, each node has its neighbor's location and the associated road segments on which its neighbor's neighbors are.

GpsrJ+ is analyzed by comparing it with GPSR and GPCR under Qualnet 2.95 simulator software, with 75 nodes up to 175 nodes, with a 25-node increment. Generally, GpsrJ+ improved recovery strategy brings significant results compared to GPSR and GPCR. In the simulation, an urban topology is employed, which is a user-defined Manhattan-grid of 1,500 $\times$ 1,500 m.

Figure 28 shows the packet delivery ratio (PDR) between GPSR, GPCR, and GpsrJ+. Clearly, taking aggressive hops in the recovery mode along the perimeter improves the PDR. This is further verified by the fewer hops GpsrJ+ needs compared to GPSR as shown in Fig. 29a. A higher number of hops imply an increased probability of channel contention; therefore, there is a higher probability that a packet gets dropped along the way. Although GPCR and GpsrJ+ stop at each junction node in greedy mode, this is not sufficient to increase the hop count dramatically. The total hop count of GPCR and GpsrJ+ is still lower than that of GPSR. Figure 29b shows the number of hops a packet experiences before being dropped. GPSR's failed hop is twice as much as GPCR and GpsrJ+. This is consistent with that planarization of nodes produces too many hops. The undeliverable packets, as a result of disconnections between the source and destination, engage in perimeter forwarding most of the time and explore all possible perimeters in a limited way caused by

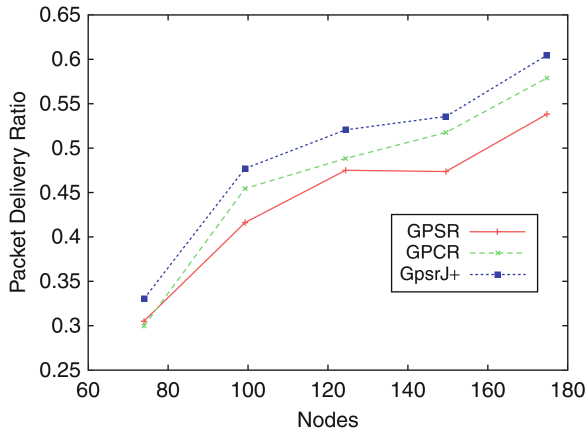

Vehicular Ad Hoc Networks, Enhanced GPSR and Beacon-Assist Geographic Forwarding in. Figure 28
PDR among GPSR, GPCR, and GpsrJ+

planarization. Since more nodes are involved in forwarding, there is a lot of resource wastage. The situation worsens for undeliverable packets as they create a loop and the same route formed by the same nodes in the same hops is visited again. In summary, the inefficiency of node planarization strategies in urban vehicular scenarios to forward packets in perimeter mode not only affects the delivery ratio but also impacts the hop count and network resources as packets stay longer in the network before being dropped.

Figure 28 also shows that GpsrJ+ possesses a higher PDR than GPCR thanks to prediction. The slight increase in hop count and latency in Fig. 29a and c, respectively, is the result of packets that do not get delivered to the destination and thus do not contribute to GPCR's hop count and latency. The reason is that the

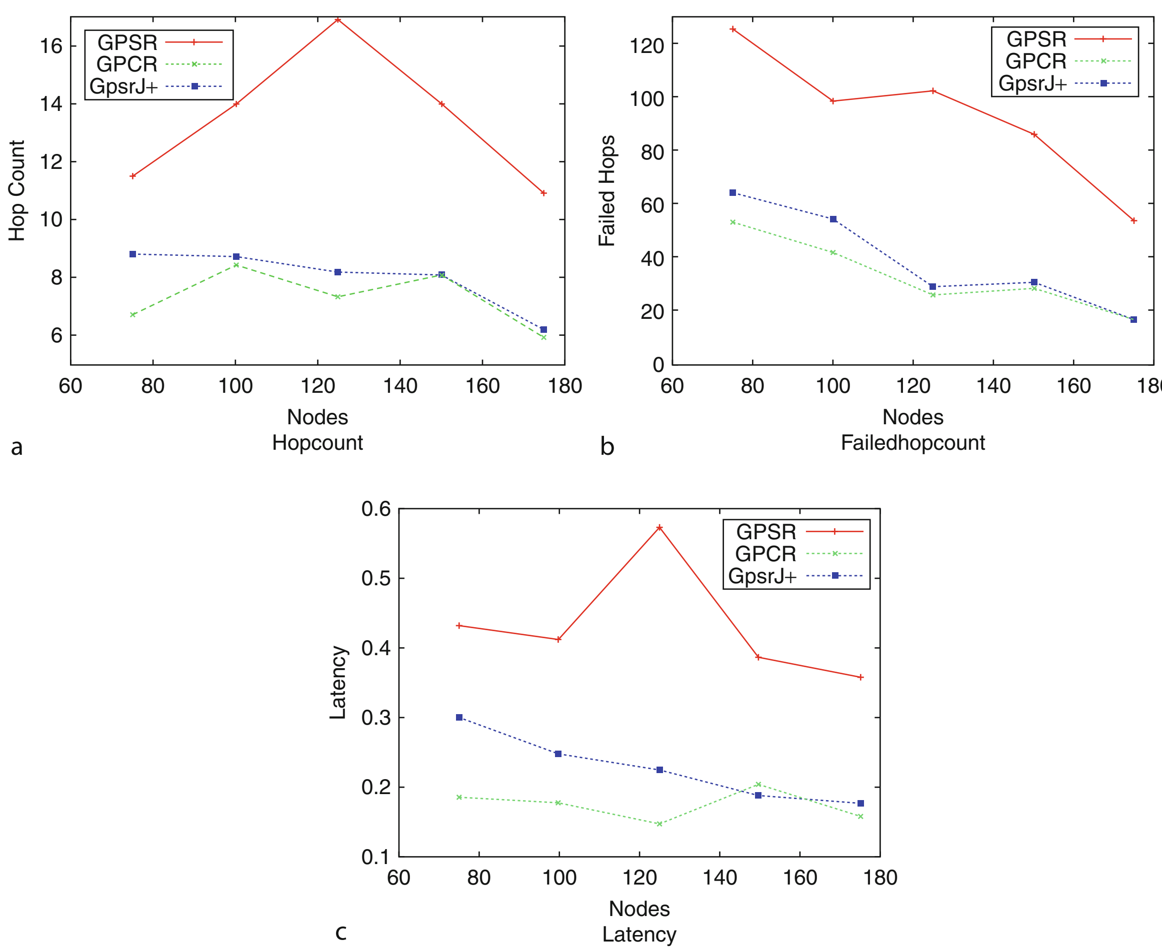

Vehicular Ad Hoc Networks, Enhanced GPSR and Beacon-Assist Geographic Forwarding in. Figure 29
Hop count and latency among GPSR, GPCR, and GpsrJ+

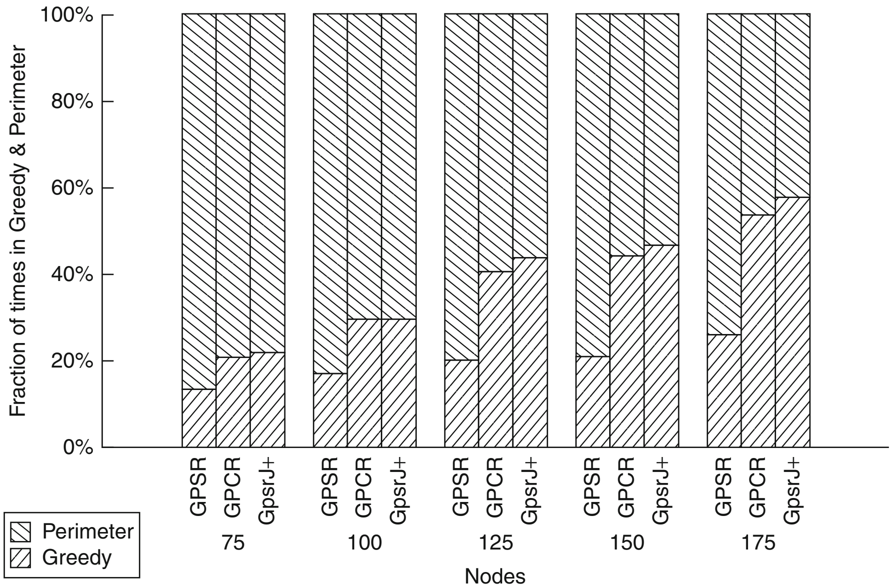

Vehicular Ad Hoc Networks, Enhanced GPSR and Beacon-Assist Geographic Forwarding in. Figure 30
Fraction of times in greedy and perimeter

smoother decrease in hop count in GpsrJ+ compared to GPCR is due to the fact that nodes do not necessarily have to go through junction nodes, which might be heavily used for forwarding in GPCR. Consequently, the interference and collision of multiple packet transmission cause packets either to be dropped or to be forwarded on a longer route. The slight increase in failed hops in GpsrJ+ compared to GPCR in Fig. 29b illustrates a longer expectancy of packets as GpsrJ+ makes a better effort to deliver them. Once again, the ability not to rely on junction nodes that get flooded with traffic prolongs the life expectancy of a packet before it gets dropped. The improved PDR in GpsrJ+ also brings in the advantage of the fraction of times a packet travels in greedy mode.

Figure 30 indicates that GpsrJ+ is in greedy mode a higher fraction of time than GPCR, and implies that GpsrJ+ minimizes the number of times a packet gets into a local maximum and maximizes the number of times a packet gets out of a local maximum.

Vehicle-Assisted Data Delivery

Zhao and Cao [11] proposed several vehicle-assisted data delivery (VADD) protocols. All of them share the idea of storing and forwarding data packets. That is, nodes can decide to keep the message until a more promising neighbor appears on their coverage range, but trying always to forward them as soon as possible. Additionally, decisions about which streets must be followed by the packet are made using vehicle and road information such as current speed, distance to the next junction, and maximum speed allowed. These routing decisions are dynamically taken at junctions because the authors state that precomputed optimal paths used by other protocols might rapidly lose their optimality due to the unpredictable nature of VANETs.

In VADD, the main goal is to select the path with the smallest packet delivery delay. The behavior of the protocol depends on the location of the node holding the message. Two cases are considered: when nodes routing the message are located in the middle of a road and when they are located in a junction. The first case (also called routing in straight way) presents less alternatives: forwarding the packet toward the next junction or to the previous one. However, the second case (also called routing in intersections) is much more complicated because at junctions, the routing decision must consider the different roads, so that the number of options is higher.

Both cases use the same approach, determining the next road the message must follow, and then selecting

the next relay among the current neighbors. In VADD, a common way of determining the next road is proposed, while the determination of the next hop remains different. Concretely, the outgoing road with the lowest estimated delay would be selected. In the "straightway" case, there are two possible outgoing roads, the two segments of the roads in which the node divides the current road. In the "intersection" case, each road starting in that junction represents a different option.

The authors call roads to the street segments delimited by two consecutive junctions. The estimation of the delay of routing a message through a certain road takes into account the road's length, its maximum speed, the mean traffic density, and other traffic-specific parameters. But, to estimate the delay to the destination, the authors also incorporate the estimated delay of the next possible roads along with the probability of choosing them. Figure 31 depicts the delay model used in VADD. A car located near intersection I_m computes the delay for the road between I_m and I_n (D_{mn}) accounting also the estimated delay of choosing the road between I_n and I_a, the one between I_n and I_b, or the one between I_n and I_c.

To estimate message delays for the different roads, the authors propose to solve an $n \times n$ linear equation system using the Gaussian elimination algorithm [$\Theta(n^3)$], n being the number of junctions. To limit the complexity of this computation, a boundary area around the current location is defined, so that only the junctions inside that area are considered in the equation system.

Once the next road has been selected, it is time to determine which neighbor must be the next relay. In the "straightway" the decision is simple, the one located closest to the next junction according to the next road selected. In this case, the next junction can be the next one in the direction of the current vehicle or the one the vehicle has just passed by. In both cases, the packet is stored only if no neighbors are available at the moment.

The "intersection" case is more complex. Obviously, if no neighbor is available, or every outgoing road has a longer estimated delay than the current one, the decision taken consists of storing the message waiting for the next forwarding opportunity. Additionally, the authors propose three alternative ways to select the next forwarder when more than one candidate neighbor is available:

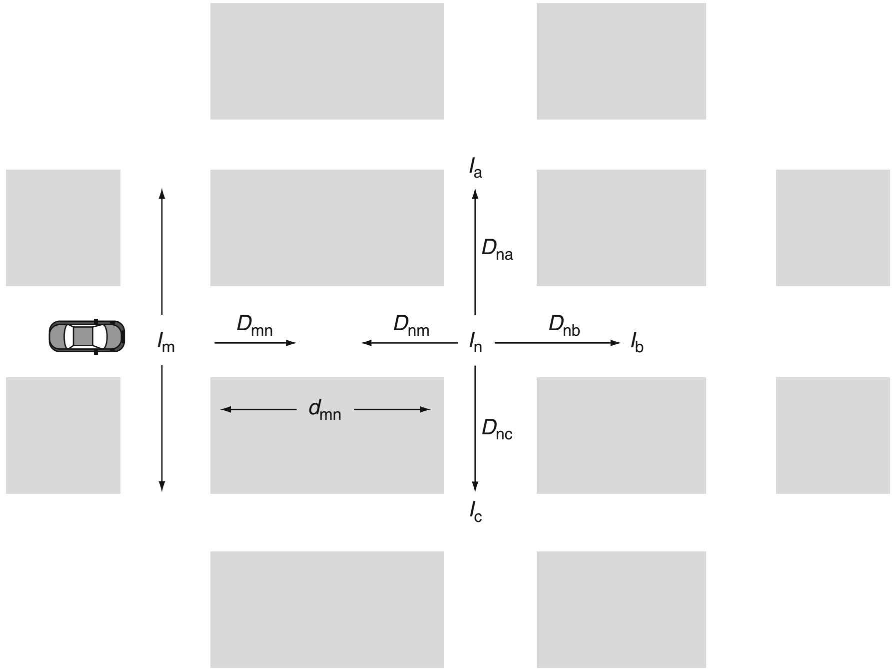

Vehicular Ad Hoc Networks, Enhanced GPSR and Beacon-Assist Geographic Forwarding in. Figure 31
Example of VADD model

Location first: The node located closest to the next selected junction in the most promising road is chosen. This scheme presents routing loops.

Direction first: The node located closest to the next selected junction in the most promising road among the ones moving in the right direction.

Hybrid: Location first is applied unless a cycle is detected, in that case direction first scheme is used. This scheme seems a little bit unrealistic due to the difficulty of detecting routing loops.

VADD's main drawbacks are its complexity and difficulty of parameterization. The size of the bounding area is by far the most important parameter and, at the same time, it is responsible for the complexity of the computation needed at every node. Determining a value for this parameter to achieve a good trade-off between computational complexity and accuracy can be a hard task. Additionally, the authors claim that their hybrid scheme achieves the best performance; however, it is not clear how to implement this scheme due to the difficulty of detecting cycles.

Future Directions

The ways of strategies to enhance or extend performance of GPSR routing protocol have been introduced. The density of vehicles in each possible route as well as the travel direction and movement of the vehicles have been taken into account to improve the forwarding algorithm performance, and thus increasing the packets delivery ratio. Beaconing strategy has also been modified by these facts, and finally decreasing the route overhead.

Although data dissemination and routing have been extensively addressed, many unique characteristics of VANET together with the diversity in promising applications offer newer research challenges. Authors in [12, 13] have focused on the problems of radio obstacle during data transmission in city scenario. They use an intersection-based approach to forward packets along successions of road from the source to destination in order to find robust and optimal routes. And the digital map information is used in these routing strategies to get information of intersections.

A VANET may exhibit a bipolar behavior, i.e., the network can either be fully connected or sparsely connected depending on the time of day or on the market penetration rate of the wireless communication devices. Authors in [14] have mentioned the issue when routing is within sparse vehicular ad hoc wireless networks. Simulation results show that the network re-healing time can vary from a few seconds to several minutes. This suggests a new ad hoc routing protocol will be needed as current routing protocol may not work with such long re-healing times for most of them are designed under an assumption that the networks are full and well connected.

Bibliography

Primary Literature

1. Naumov V, Baumann R, Gross T (2006) An evaluation of inter-vehicle ad hoc networks based on realistic vehicular traces. In: Proceedings of ACM MOBIHOC'06, Florence, pp 108–119
2. Lochert C et al. (2003) A routing strategy for vehicular ad hoc networks in city environments. In: IVS'03, pp 156–161
3. Menouar H, Lenardi M, Filali F (2005) A movement prediction-based routing protocol for vehicle-to-vehicle communications. In: First international vehicle-to-vehicle communications workshop, co-located with MobiQuitous 2005, V2VCOM 2005, San Diego
4. Granelli F, Boato G, Kliazovich D (2006) MORA: a movement-based routing algorithm for vehicle ad hoc networks. In: IEEE workshop on automotive networking and applications (AutoNet 2006), San Francisco
5. Menouar H, Lenardi M, Filali F (2006) An intelligent movement-based routing for VANETs. In: ITS world congress 2006, London
6. Kieß W, Füßler H, Widmer J, Mauve M (2004) Hierarchical location service for mobile ad-hoc networks. Proc ACM SIGMOBILE Mobile Comput Commun Rev 8:47–58
7. Christian L, Martin M (2005) Geographic routing in city scenarios. ACM SIGMOBILE Mobile Comput Commun Rev Arch 9(1):69–72
8. Frey H, Stojmenovic I (2006) On delivery guarantees of face and combined greedy face routing in ad hoc and sensor networks. In: Proceedings of the ACM annual international conference on mobile computing and networking (Mobicom), Los Angeles
9. Lochert C, Hartenstein H, Tian J, Füßler H, Hermann D, Mauve M (2003) A routing strategy for vehicular ad-hoc networks in city environments. In: Proceedings of IEEE IV'03, Columbus, pp 156–161
10. Naumov V, Gross TR (2007) Connectivity-aware routing (CAR) in vehicular ad-hoc networks. In: Proceedings of 26th IEEE international conference on computer communications (INFOCOM'07), Anchorage, pp 1919–1927

11. Zhao J, Cao G (2006) VADD: vehicle-assisted data delivery in vehicular ad hoc networks. In: Proceedings of 25th IEEE international conference on computer communications (INFOCOM'06), Barcelona
12. Nzouonta J, Rajgure N, Wang G, Borcea C (2009) VANET routing on city roads using real-time vehicular traffic information. IEEE Trans Veh Technol 58(7):3609–3626
13. Jerbi M, Senouci S-M, Rasheed T, Ghamri-Doudane Y (2009) Towards efficient geographic routing in urban vehicular networks. IEEE Trans Veh Technol 58(9):1–1
14. Wisitpongphan N, Bai F, Mudalige P, Sadekar V, Tonguz O (2007) Routing in sparse vehicular ad hoc wireless networks. IEEE J Sel Area Commun 25(8):1538–1556

Books and Reviews

Lee KC, Haerri J, Uichin L, Gerla M (2007) Enhanced perimeter routing for geographic forwarding protocols in urban vehicular scenarios. In: 2007 IEEE Globecom workshops, 26–30 Nov 2007, pp 1–10